Novel Fluorescence Techniques for Real-Time Mineral Identification

Jillian Elizabeth Moffatt
July 2020
Institute of Photonics and Advanced Sensing
School of Physical Sciences
Department of Physics
The University of Adelaide
PhD Thesis

Supervisors:
Professor Nigel A. Spooner
Professor David J. Ottaway
Doctor Barnaby W. Smith

Table of Contents

Abstract

Fluorescence is the rapid emission of light after photon absorption. The absorption and emission characteristics of a sample depend on both the fluorescent species and the surrounding lattice. Fluorescence can thus be used to identify particular materials, even in a complicated environment.

Upconversion fluorescence is a process wherein the sample absorbs one or more photons of a lower energy than the photons of fluorescence emission. Upconversion fluorescence wavelengths are much less likely to excite upconversion from multiple samples at once, which can provide greater sample specificity for sample identification.

There is great need for real-time mineral sensors to enable real-time ore sorting and mineral processing controls, which are required for the application of mining optimisation techniques such as grade engineering. Fluorescence is real-time, non-contact and non-destructive by nature, and does not require pre-treatment of samples. This makes it interesting for sensor development. An advantage for deployment over other sensor techniques include the comparative safety of even high-energy excitation sources over radiation-based techniques. Another is the fact that fluorescence is a material-dependent phenomenon, and so has the ability to enable the creation of mineral-specific rather than element-specific sensors. Light-based excitation sources can also be much cheaper than other excitation sources currently used.

Before prototypes can be made, mineral fluorescence signals must be discovered, identified and tested for use in mineral identification. This thesis describes the development of a new, state-of-the-art system designed for dual-wave excitation, providing the capability to find and characterise novel conventional and upconversion signals. This Dual-Wavelength System is characterised and tested on multiple mineral specimens, then applied to the search for previously unknown signals for further study.

Quantitative upconversion fluorescence measurements using rare earth dopants found in minerals are conducted in synthetic ZBLAN glass, providing both context for natural mineral upconversion signals and direct experimental measurements of a fibre-based upconversion kinetic parameter for the first time.

Upconversion signals are described and characterised in natural mineral samples for the first time. An additional lattice defect-based conventional fluorescence signal is discovered and characterised, highlighting the flexibility and broad capabilities of the Dual-Wavelength System and the great potential for such "novel" fluorescences to open new possibilities for real-time, non-contact material sensing. These new signals are assessed for their potential for mineral discrimination and abundance measurements.

Declaration of Authorship

I certify that this work contains no material which has been accepted for the award of any other degree or diploma in my name, in any university or other tertiary institution and, to the best of my knowledge and belief, contains no material previously published or written by another person, except where due reference has been made in the text. In addition, I certify that no part of this work will, in the future, be used in a submission in my name, for any other degree or diploma in any university or other tertiary institution without the prior approval of the University of Adelaide and where applicable, any partner institution responsible for the joint-award of this degree. I give permission for the digital version of my thesis to be made available on the web, via the University's digital research repository, the Library Search and also through web search engines, unless permission has been granted by the University to restrict access for a period of time. I acknowledge the support I have received for my research through the provision of an Australian Government Research Training Program Scholarship and a Cooperative Research Centre for Optimising Resource Extraction (CRC ORE) Grant and Scholarship.

Jillian Elizabeth Moffatt

Signed: Jillian Elizabeth Moffatt

Acknowledgements

Firstly I would like to acknowledge my supervisors, Prof. Nigel Spooner, Prof. David Ottaway, and Dr Barnaby Smith. Without them I would not have been able to do my experiments, and my thesis would have made very little sense.

Secondly I would like to acknowledge the Upconversion Team: Dr Georgios Tsiminis, Dr Elizaveta Klantsataya, Thomas de Prinse, Thomas Payten, and Lewis Teixeira. Without the support of this team I would not have an experimental system, let alone experiments to write about.

In specific, I am very grateful to the people below for the following contributions:

Chapter Two: I would like to thank Georgios and Liz for building the Dual-Wavelength System, and the whole Upconversion Team for maintaining it. Milad Abou Dakka helped characterise the detection side of the system, and Dr. Owen Williams and the Upconversion Team helped with the blackbody radiation calibration.

Chapter Three: I would like to thank Dr Ori Henderson-Sapir for his advice throughout the experiment. Ori, Dr Christopher Kalnins, and Georgios allowed me to borrow equipment to undertake the experiment. Liz prepared and polished all my fibres to a level much greater than what I could have achieved. Georgios taught me how to align a laser into a fibre. Donald Creighton helped fix the laser when a capacitor failed. Ori and Liz checked all my code for this chapter to ensure there were no errors. Professor Stewart Jackson provided a sample fibre.

Chapter Four: This chapter could not have occurred without the Upconversion Team's diligence in maintaining the Dual-Wavelength System.

Chapter Five: This chapter benefitted greatly due to experiment suggestions from Georgios and Thomas Payten, who also helped identify many near-infrared signals. Discussions about mineral processing with Tom also gave much needed context to experimental design and structure. Kathryn McDonnell taught and assisted me with a clay separation experiment.

I would like to acknowledge the CRC ORE for our grant and scholarship, which allowed the vast majority of the experiments in this thesis to take place. In particular I would like to thank Dr Greg Wilkie and Vicki Askew for samples and support throughout my thesis.

Further equipment such as the near-infrared spectrometer was funded by a Defence Next Generation Technology Fund grant (Project CIT-186).

On a personal note, I would like to thank all the people in my office, past and present, and my family and friends (in particular Bruce, Sheila, Jamie and Tegan), who cheered me on throughout my PhD and gave me good advice.

This work could not have occurred without the support and encouragement of Andrew Cunningham.

List of Abbreviations and Jargon

CCD

-"Charge Coupled Device", a sensor that uses coupled capacitors to detect and read light input.

"dual excitation", "dual wavelength"

-excitation with two different wavelengths.

DWS, "Dual-Wavelength System"

-The fluorescence detection setup created during this thesis in order to excite samples with two wavelengths and detect higher-energy emission output.

"energy level", "electronic/atomic energy level", "excited state"

-a potential energy at which an excited electron or hole is metastable, due to the balance of electromagnetic forces upon it.

ET, "energy transfer"

-when one ion or defect in an excited state transfers energy equivalent to the difference between the excited state and a lower state to another ion via resonant effects.

"fibre"

-an optical device much longer than it is wide used to transfer light within it using internal reflection characteristics.

FWHM

-"Full Width Half Maximum", the spectral range over which half an output is present, centred on the peak of the output.

"gangue"

-parts of an ore deposit with no commercial significance.

"ion inclusion"

-the inclusion of an ion in a lattice in which it is usually not present.

"ionise"

-to give electrons (or holes) in a material enough energy that they are able to move freely and are not bound to a certain atomic or lattice position.

IR, "infrared"

-wavelengths lower in energy than 1.77 eV (> 700 nm) and higher than approximately 0.06 eV (20,000 nm).

"lattice defect"

-a deviation from the normal crystal structure of a mineral.

LP, "longpass"

-a filter that passes lower-energy photons and blocks higher-energy photons.

"nanoparticle"

-a small particle below 100 nm in diameter.

NIR, "near-infrared"

-the region of the IR around 700-2000 nm, near the visible.

"ore"

-a mixture of minerals containing a commercially significant product.

OPO

-"Optical Parametric Oscillator", a nonlinear device which changes the energy of incoming photons by a ratio determined by the angle of the OPO.

OSL, "optically stimulated luminescence"

-luminescence sensitised by ionising radiation and excited by visible wavelengths.

"pellet"

-a crushed or powdered sample pressed into a certain shape.

"phonon"

-a quantised unit of vibrational energy.

"photon"

-a quantised unit of electromagnetic energy

"power"

-the energy per unit time, usually of an excitation source.

"pump"

-an excitation source.

"quench"

-a decay pathway which serves to counter a specific fluorescence.

"radiative pathway"

-a de-excitation pathway that requires the output of a photon to release energy.

"real-time"

-within the reaction timeframe of a human, device, or process.

REE, "rare earth element"

-elements in the lanthanide group of the periodic table.

SP, "shortpass"

-a filter that passes higher-energy photons and blocks lower-energy photons.

"spectra"

-an output arranged by wavelength.

"spectrofluorimeter"

-a detection setup designed for measuring fluorescence spectra, including excitation, emission, and monochromator devices.

"spectrometer"

-a device that separates input light by wavelength, for intensity per wavelength to be read individually.

"Stokes' emission"

-An emission that is of lower photon energy than the input photon.

TL, "thermoluminescence"

-luminescence sensitised by ionising radiation and excited by increased temperature.

TM, "transition metal"

-an element whose ionic form has a partially filled d electron shell, excluding the lanthanide and actinide groups.

UC, UCF, "upconversion, "upconversion fluorescence"

-the process of successive excitations of electrons or holes via multiple electronic energy levels, and the fluorescence created.

UV, "ultraviolet"

-photons of a higher energy than 3.1 eV (> 400 nm), terminating at approximately 24 eV (50 nm).

"visible"

-photons of an energy between 1.77 eV and 3.1 eV (400-700 nm).

"weathering"

-chemical processes, especially oxidation, that occur when a material is exposed to ambient temperature, light, pressure, and atmospheric conditions.

X-ray

-photons between 124 eV and 124,000 eV.

XRD, "X-ray diffraction"

-the technique of using the diffraction pattern of x-rays to determine the crystal structure of a material.

1. — Background Information

1.1. Introduction

Mining is an energy- and resource-intensive process, and many deposits around the world are only economically viable to run when product prices are near their peak. One proposed way of making mines more efficient and therefore more economical to run is called grade engineering, which is implemented by pre-sorting of ores into different grades before further processing. Grade engineering only becomes quick and reliable, however, if real-time information about mine ore output is available. X-ray fluorescence (XRF), Laser-Induced Breakdown Spectroscopy (LIBS) and Magnetic Resonance Imaging (MRI) have been successfully trialled, but MRI is only useful on a certain subset of minerals, and XRF and LIBS are element-specific and not mineral-specific. There remains, therefore, a need for strong mineral-specific identifiers for real-time scanning of mine output. Mineral fluorescence is a strong contender for this type of process.

Fluorescence occurs when a material is excited to a higher energy state by a photon, and subsequently emits a photon in order to move to a lower energy state. In solid lattice structures such as minerals, the excited energy state is usually a potential energy state of electrons or holes in the material (Kasha, 1950) (for brevity I will only talk about electrons here). These electrons become excited to either the conduction band of the material, potential energy states within the ions making up the lattice, or potential energy states within a defect site in the material. The defect could be an ion inclusion, a lattice vacancy or deformity, or the interaction between two types of defects. The defect produces a different set of potential electronic energy levels in the material, isolated from the bulk lattice energy levels. It is this isolation that prevents other non-radiative pathways of energy dissipation to dominate the decay, allowing photon emission to occur.

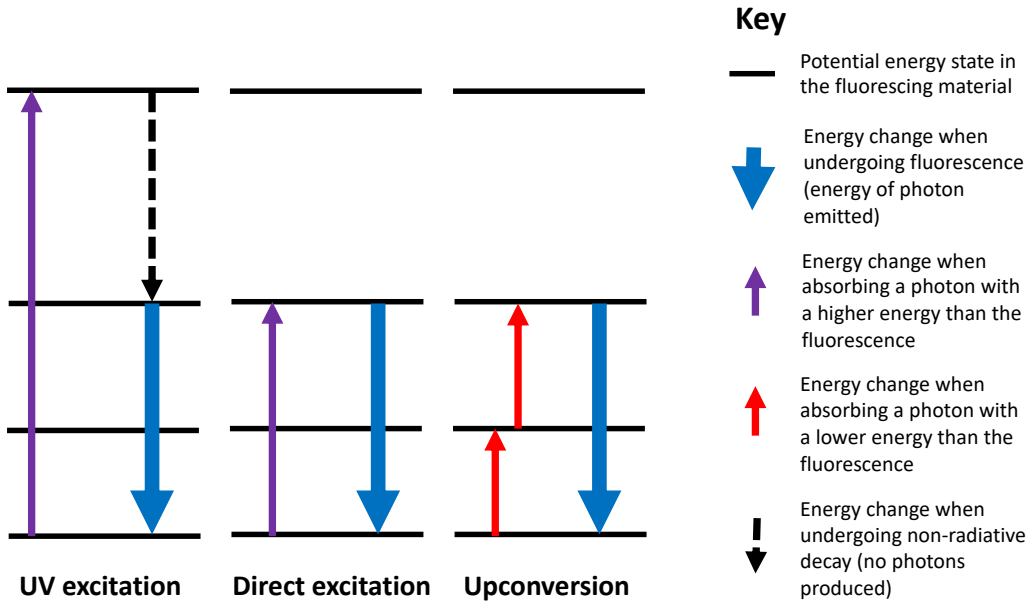

Figure 1: Band diagrams showing UV excited fluorescence, directly excited fluorescence, and upconversion fluorescence.

Direct fluorescence (Figure 1) is an energy-efficient way of producing a signature response from a mineral, but can have multiple drawbacks in real-time fluorescence studies. The bulk of emitted photons will be of a lower energy than the excitation photon, but this energy difference can be very small. At room temperature, it is possible for the emission wavelength peak to overlap the excitation line. While emissions energetically close to excitation energies can be resolved in the laboratory, the small differences preclude cheap and simple technologies for use in mining and mineral processing.

One way to prevent excitation/emission overlap is to excite fluorescence from much higher energy levels than the emission level: for visible and near-infrared (NIR) emission, ultra-violet (UV) excitation is typically used. From this higher level, the electron decays in energy until reaching the emission level (Figure 1). At higher energies, the gap between atomic energy levels decreases, and the photon energies of UV excitation are above the energy of the conduction band for many minerals. This means that at room temperature UV excitation can produce multiple emissions from a variety of materials even using a reasonably narrow excitation bandwidth. This spectral richness can be useful for laboratory diagnosis of samples, but decreases the signal-to-noise ratio for any one emission signature and can prevent real-time identification of species in complex mixtures of materials unless complex peak finding algorithms are used.

One means to excite fluorescence in a more specific way with greater wavelength separation from the emission response is by using upconversion fluorescence (UCF). In this type of fluorescence the electron is excited two or more times in order to reach the emission excitation level (Figure 1). While this is a more photon-intensive process (in general two or more photons are required to excite an emission rather than one), it has advantages over direct and UV fluorescence. Similar to UV induced fluorescence, the energy of the emission

will be removed from the energy of excitation. Upconversion fluorescence also typically requires an intermediate energy level to be available for the excited electron, which greatly assists making UCF far more mineral-specific than either direct or UV excited fluorescence.

1.2. Thesis synopsis

In this thesis fluorescence signatures suitable for identifying minerals in real time will be sought and explored, with a focus on upconversion fluorescence.

- Chapter One: A review of theory and literature, and an outline of the project.
- Chapter Two: A new upconversion fluorescence experimental facility will be described.
- Chapter Three: Upconversion experiments with a known synthetic material will introduce and explore different types of upconversion processes and kinetics.
- Chapter Four: Fluorescence from selected minerals of economic significance will be investigated.
- Chapter Five: Natural fluorine-bearing minerals will be analysed for conventional and upconversion fluorescence, and these fluorescence signatures will be tested for their ability to determine ore grade.
- Chapter Six: Summary and conclusions as to the viability of fluorescence identification in real time mineral analysis.

1.3. Real-time mineral and elemental detection

This section briefly describes other techniques that either are in use or have the potential for real-time mineral analysis. Their advantages and disadvantages in mine-site deployment are briefly discussed.

1.3.1. X-ray techniques (XRF, XRL, XRT)

There are three commonly-used X-ray technologies in ore sorting: x-ray fluorescence (XRF), x-ray luminescence (XRL), and x-ray transmission (XRT). In XRF, a sample is exposed to an x-ray source, which ionises individual atoms within the material and causes fluorescence as electrons de-excite to their original states (Barkla, 1915). The quantity of each atom present is relative to the intensity of the fluorescence peak corresponding to that atom's emission.

Current XRF technologies deployable in the field are not capable of identifying light elements such as oxygen, phosphorous, and sulphur, and so identification of many minerals of interest is not possible from elemental ratios. To obtain accurate quantification of signal, XRF requires a flat surface, and so without sample preparation XRF is more a qualitative technique. XRF is used successfully to measure changes in metal content in ore on a number of mine sites (Gleeson, 2019).

X-ray luminescence (XRL) uses the same types of in-system rather than ionising luminescence pathways as conventional fluorescence, but are excited by an x-ray source instead of UV-IR energy photons. This luminescence is used commonly to sense diamonds(Knapp et al., 2014) which are highly fluorescent under XRL.

X-ray transmission (XRT) works similarly to a medical x-ray scan, in which atomically denser ore members absorb more x-rays as they pass through the sample. This technique is used

when the mine product ore is atomically much lighter or heavier than gangue (non-useful) ore, as is the case with coal and the tungsten-bearing ore scheelite(Knapp et al., 2014).

1.3.2. Prompt Gamma Neutron Activation Analysis (PGNAA)

PGNAA uses a source of neutrons to bombard the sample. If an atom in the sample captures a neutron, the atom emits a gamma-energy photon as it returns to a stable energy state. In principle this allows detection of the presence of any atom in the periodic table, but current deployable technologies only allow the detection of certain elements (Lindstrom and Révay, 2017).

PGNAA is used extensively in the mining industry. Disadvantages include the quantity of shielding needed to protect plant and workers from the neutron source. A great advantage of PGNAA compared to XRF is that it is a volumetric rather than surface technique, as both neutrons and gamma rays are capable of penetrating through the rock surface. This provides a larger statistical reliability for element concentration results.

1.3.3. Magnetic Resonance (MR)

Magnetic resonance occurs when a magnetic field induces a radio-frequency response from a material, or vice-versa. This effect can be significant in specific minerals such as chalcopyrite (Bennett et al., 2009). Magnetic resonance has the advantage, like PGNAA, that it is a volumetric rather than surface technique. While only available as a technique for a few specific minerals, it shows promise as a field-deployable technology.

1.3.4. Laser-Induced Breakdown Spectroscopy (LIBS)

LIBS is a technique that uses high intensity laser light to induce a highly excited plasma of the atomic components of the sample. As with XRF, the emission from the highly ionised atomic states are detected and the emission peaks analysed for elemental composition (Loree and Radziemski, 1981). A crucial advantage of LIBS compared to XRF is the ability to sense light elements, allowing sensing of elements of interest such as lithium, phosphorous, fluorine, and sulphur. Mineralogical or molecular composition results are obtained using fits to ratios of elements (El Haddad et al., 2019). This can be very accurate when grain sizes are larger than the spot size of the laser, but more complex computational analysis is needed in intergrown and fine grained ores.

The main disadvantage of LIBS is the small laser spot size needed to induce plasma and ensure the plasma is small enough to prevent self-absorption and maintain ratiometric accuracy of the atomic peaks. Applicability and ease of use in conveyor-belt-type scenarios depends on the variability of sample across the width of the conveyor belt and the sampling needed to create the required statistical accuracy. In less time-sensitive applications such as rock face and in-bucket analysis, the laser can be comprehensively scanned across the sample to ensure statistical reliability of results.

1.3.5. Reflectometry and Absorption

Reflectometry and absorption rely on the different absorption and reflection properties of different minerals to distinguish them in the field. This technique is extensively used in satellite and aircraft-based surveys for bulk analysis (2020c), and in hand-held hyperspectral imaging devices (2018a). Reflectometry and absorption are mineral rather than elemental

detection techniques, making them valuable for analysis of elementally similar but mineralogically distinct species. A main advantage is that it does not require unsafe levels of radiation or laser light. The main disadvantage is that it uses reasonably precise light return level changes for analysis, and so in conveyor belt scenarios where relatively large rocks are present at different orientations, the technique can be imprecise. Additionally, even small amounts of weathering can drastically change the absorption and reflection characteristics of a sample, and so inaccurate readings can occur if the sample is not fresh.

1.3.6. Radiation detectors

Radioactive ores such as uranium-bearing ore are able to be detected by the radiation they emit. Gamma radiation detectors are currently used to sort high-grade ore from low-grade and gangue materials (Knapp et al., 2014). As different radioactive elements emit different energies of gamma rays, the radioactive element is able to be identified with a suitable detector. The technique cannot, however, distinguish between the same element in different mineral phases.

1.4. Mineral fluorescence signatures

1.4.1. Fluorescence in minerals

There are hundreds of minerals known to fluoresce, in most part due to defects or ion inclusions (Baramin, 2010, MacRae et al., 2016). Most mineral fluorescence investigated historically has used UV excitation and visible emission. Newer silicon CCD-based spectrometers with extended ranges have increased investigations in NIR emission to around 1000 nm although the published data for these NIR bands are still relatively sparse. Most fluorescence investigated has been attributed to rare earth or transition metal ion inclusions, though some defect-related emission has also been seen (Letz and Parthier, 2006).

The incorporation of rare earth or transition metal ions in a mineral depends on both the presence of these ions at mineral formation and the surrounding matrix of minerals, as particular defect ions are preferentially taken up by particular minerals. This preference generally depends on how well the impurity ion can fit into the matrix of the mineral. This is influenced by the:

-ion charge. If the charge of the impurity ion is similar to the charge of the ions in the matrix, it will more easily substitute into that matrix, otherwise charge compensation effects like defect creation or clumping can occur (Joshi et al., 2010, Baira et al., 2018).

-atomic radius. If the radius of the impurity ion is much greater or lesser than the radius of an ion it is substituting in the matrix, it will deform the structure of the mineral and be less stable within it (Yu and Yu, 2013, Li et al., 2013).

-crystal structure of the mineral. A more densely packed crystal structure will be less likely to allow impurity ions that do not closely fit the charge and radius criteria above (Li et al., 2013).

Ion impurities can occur in two ways without unduly modifying the mineral lattice structure: by substitution or interstitial inclusion. Substitutions occur when an ion occupies a site usually occupied by a similarly-charged ion of the matrix. Interstitial inclusions occur when an ion is held in a place in the matrix which usually holds no ion. This can allow for better incorporation

of ions of differing radii, but creates structural deformation of the matrix around the ion to account for the different charge and physical dimensions.

Due to the variability of ion presence in mineral samples from different sample sites, any ion-impurity-based signals seen in natural samples may not be present for all samples. Even for very common ions, there may be site variability in impurity populations and therefore in the intensity of signals. If we rely on impurity-based signals, therefore, any detection process will have to be assessed on a site-by-site basis, and potentially calibration will be needed from samples across a complex ore body.

Whether or not an ion impurity will produce fluorescence depends on the mineral matrix surrounding it. Similar to the case in synthetic materials, large potential phonon energies and transition energies matching energies of the host material will decrease the likelihood of fluorescence. It is known that when making optical materials, charge and radius differences between ions and their matrix will cause lattice defects, which have their own absorption characteristics and can quench fluorescence pathways. While this is usually a detriment, as detailed in section 1.13.1, upconversion fluorescence has been known to be produced by these ion-induced defects. These matrix-specific defects may represent a more mineral-specific signature than fluorescence from the ions themselves, and therefore represent an important class of target UCF signals for material detection and identification.

1.4.1. Real-time fluorescence sensing

UV-excited fluorescence has already been tested successfully at mine sites for a variety of minerals. Scheelite (Robben and Wotruba, 2019), phosphorous-bearing minerals, clay, and diamond (Broicher, 2005) have been candidates for fluorescence sensing. Specific mine sites that have higher-than usual fluorescence due to high fluorescent impurity concentrations also occasionally use fluorescence for sorting, such as the Franklin mine in New Jersey, USA (Cyr and Moritz, 2016). UV-excited fluorescence is also commonly used to identify low-grade opal in the South Australian opal fields when "noodling" (fossicking) (2018c, 2020b).

Limitations noted for UV-excited fluorescence sorting include the inability to penetrate through small surface coatings, large fluorescence bandwidths (~100-300 nm), and the reliance on ion inclusions that may change in concentration from sample to sample (Broicher, 2000). As fluorescence is a surface technique, if the fluorescent ore is not well-represented on the surface of the sample it cannot be used for sensing (Robben and Wotruba, 2019). While many of these limitations remain with all fluorescence sensing, the proposed excitation and emission wavelengths in this thesis may have advantages over UV-excited fluorescence. Excitation wavelengths investigated are in the visible and near-infrared, which often penetrate further into materials than ultraviolet light, and so may be more useful in situations where coatings such as dust are present on the sample. Broad emission bands are generally a disadvantage when confounding signals from other minerals may be present, which are less likely when using upconversion fluorescence. While lattice-based emission is preferable, ion impurity emission may still give important information about mineral presence. In a conveyor-belt sensing system, even if ion impurity changed drastically between samples under the same growing conditions, an average grade could be identified for a section of ore by averaging 'sensed presence' data over a period of time.

1.4.2. Minerals of interest

In mining and mineral processing, minerals of interest for real-time detection and identification fall into three main categories:

- Minerals of economic interest: this includes many sulphide species (Cu, Zn, Fe, Pb) that are mined directly for their metal content. These minerals are monitored to identify the grade of the mined ore. If more than one significant mineral is present (e.g. different copper sulphides) information on the abundance ratio enables optimising processing parameters when the metal is extracted.
- Minerals that are detrimental: highly reactive minerals such as fluorides, clays, and carbonates can interfere with extraction processes such as leaching. Hard minerals such as quartz can in large quantities interfere with crushing processes, increasing energy costs. Some minerals can pass through most process and refining stages, contaminating the final product. Monitoring these minerals can aid decision making in either changing process parameters or discarding parts of the ore body before processing the remainder.
- Minerals that inform overall mineralogy: some minerals or ratios of minerals give information about the type of conditions the ore deposit has been subjected to as well as the initial conditions of the deposit at formation. This can help in determining variability, spatial resolution, and mineral content of a deposit, and in some cases aid in mineral exploration.

1.5. Fluorescence in solids

1.5.1. Signal-to-noise in conventional and upconversion fluorescence

Fluorescence occurs when an electron is raised to an excited state, and emits a photon in the process of de-exciting to a more stable energy state. Direct fluorescence (noted in section 1.1) provides the most efficient way of exciting to a potential energy state, but excitation cannot be easily filtered from emission. UV excitation is a common way to excite visible and near-infrared emission from higher potential energy states, but it is equally possible to excite in the visible, as is often used when exciting rare earth element-based emission (Czaja et al., 2012). For exciting specific signals, visible excitation is useful as any one visible wavelength is less likely than any UV wavelength to excite multiple sources of emission. Exciting in the visible and emitting in the near-infrared has an additional advantage in sensor creation, as the solar flux at the emission wavelength is less than in the visible. This aids in increasing signal-to-noise. While some UV-excited emission is shown in this thesis, "novel" conventional fluorescence (previously unreported Stokes' fluorescence) signals that emit in the near-infrared and are excited by visible wavelengths are the focus of signals for potential sensor development.

Upconversion fluorescence excitation has in general greater spectral separation from emission than conventional fluorescence, and so can be easily filtered from emission. As it needs a minimum of two specific excited potential energy states to be present in the material rather than a minimum of one as in conventional fluorescence, upconversion fluorescence is inherently more material-specific, and especially so if the potential energy states are due to the host material rather than inclusions.

The upconversion fluorescence emission studied in this thesis is predominantly excited in the near-infrared to produce emission in the visible. This does not have the background advantage that visible-to-near-infrared emission does, but can take advantage of cheaper and more sensitive detectors. As upconversion fluorescence needs higher powers than conventional fluorescence in order to observe a signal, focusing on the more sensitive detector ranges is more important for signals to be used in developing mineral sensors.

1.5.2. Electronic Energy Levels

Fluorescence in solids requires electronic energy levels to which electrons are excited to and radiatively decay from. By far the most common energy level structure used in upconversion fluorescence studies to date has been the energy structure of dopant ions embedded in a surrounding material (Wilhelm, 2017, Gamelin and Güdel, 2001). Dopant ions provide a set of electronic energy levels that are energetically different to those of the surrounding lattice, decreasing the chance of non-radiative decay pathways. To de-excite after absorbing a photon, then, the ion-associated electron has an increased likelihood of decay via photon emission. Dopant ions can also create new potential energy levels by distorting the surrounding lattice (Campbell et al., 1997), or by interacting with lattice components to create dimers and other non-lattice groupings. In the same way as dopant-intrinsic emission, the resulting potential energy levels can be sufficiently isolated from the lattice energy states to undergo radiative decay.

Intrinsic lattice defects can also produce potential energy levels (Johnson et al., 1982). Common defects include vacancies, where a lattice component is absent (Gibart et al., 1996); lattice perturbation (such as at a crystal boundary or due to an inclusion of a larger or smaller size than the replaced ion) (Yu and Yu, 2013); and interactions between adjacent defects (Rix, 2011). The conduction band of the material can also be counted as a potential energy level, in which electrons are relatively free to move to more isolated defect sites for radiative recombination.

1.6. Upconversion fluorescence in solids

Upconversion fluorescence (UCF) occurs when an electron is raised to an excited state of higher energy than the energy of any single absorbed photon, and subsequently emits a photon of shorter wavelength. There are multiple pathways an electron can take to emit upconversion fluorescence, described below.

1.6.1. Sequential absorption upconversion

The simplest case of upconversion fluorescence is two-photon sequential absorption upconversion, also known as ground state absorption/excited state absorption (GSA/ESA). In this process, an electron is first excited to an intermediate excited state, and then is further excited directly by a photon to the final higher excited state before subsequent radiative decay (Figure 2). This process was theorised in solids by Bloembergen (Bloembergen, 1959) for use in quantum counter applications (see section *History and applications*). Sequential absorption of more than two photons is possible; however the likelihood of the full upconversion process occurring is much smaller for every additional excited state absorption. Without the occurrence of long-lived intermediate excited states or the use of high power excitation sources, two-photon GSA/ESA is the most commonly seen variant.

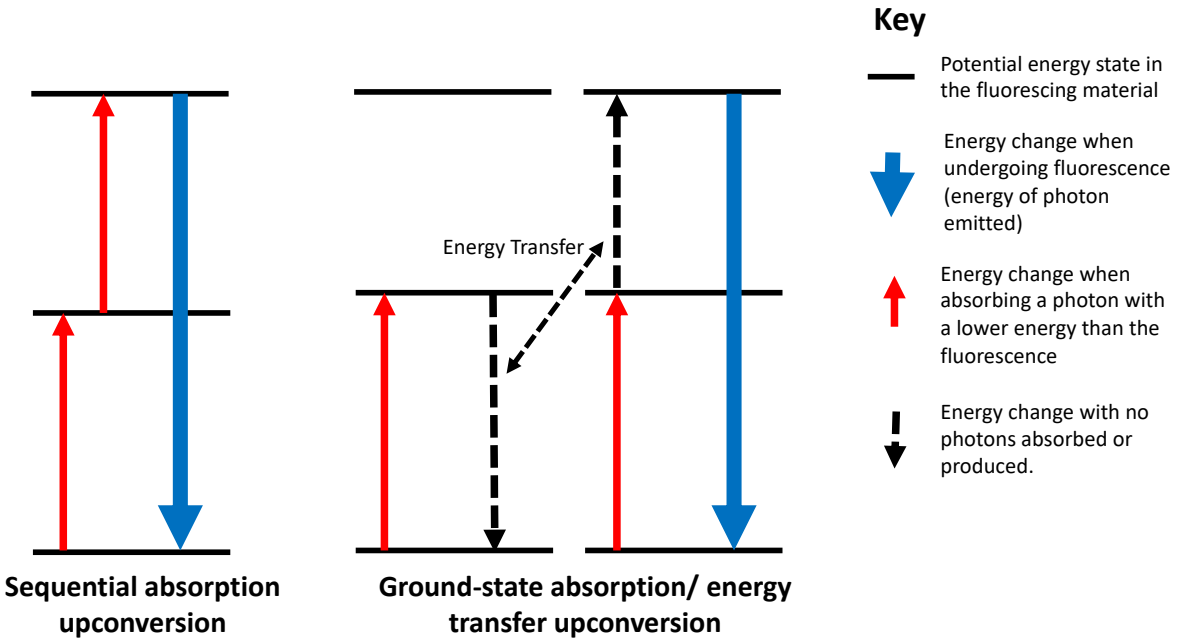

Figure 2: Band diagrams depicting the sequential absorption upconversion process and the GSA/energy transfer upconversion process.

1.6.2. Energy transfer upconversion

The most commonly used upconversion fluorescence emission in modern applications is energy transfer upconversion (Tanner et al., 2018), which for two-photon excitation processes include ground state absorption/energy transfer upconversion (GSA/ET) (Golding et al., 2000), Additions de Photons par Transfert d'Energie (APTE) (Auzel, 1966b), donor-acceptor energy transfer upconversion (Meng et al., 2004), and simultaneous or cooperative energy transfer (Feofilov and Ovsyankin, 1967). In these processes, energy is absorbed in creating one excited energy state, and via resonant energy transfer processes such as dipole-dipole interactions that energy is then transferred to a different excited state. For this to occur the two potential energy states must be close enough together to enable interactions. Energy transfer is thus usually seen in high-doped samples or samples in which the dopants naturally clump together, such as to minimise the effect of lattice deformation and to balance ion charge. More details on different energy transfer combinations and processes are below:

GSA/Energy Transfer: In this simple case, two ions are excited to excited states: one then transfers energy to the other, exciting it to a higher-energy excited state, while itself de-exciting to a lower energy state (Figure 2).

Additions de Photons par Transfert d'Energie: In this case, two ions are excited, and sequentially transfer their energy to a third ion (Figure 3).

Donor-Acceptor Energy transfer: This occurs when one type of ion is able to absorb the excitation photon with higher efficiency than the emitting ion. The donor sequentially absorbs excitation photons and transfers energy to the emitter (Figure 3).

Simultaneous/Cooperative Energy Transfer: This can be described as the energy transfer equivalent of multi-photon absorption (see section 1.7). In the two-photon case, two ions are excited, and their energy is simultaneously transferred to an ion that does not have a suitable intermediate energy state (Figure 3).

Many combinations of direct absorption and energy transfer can occur in multi-level energy state interactions. Both mathematical and experimental tests can be needed to identify the full process that produces emission from an unknown sample.

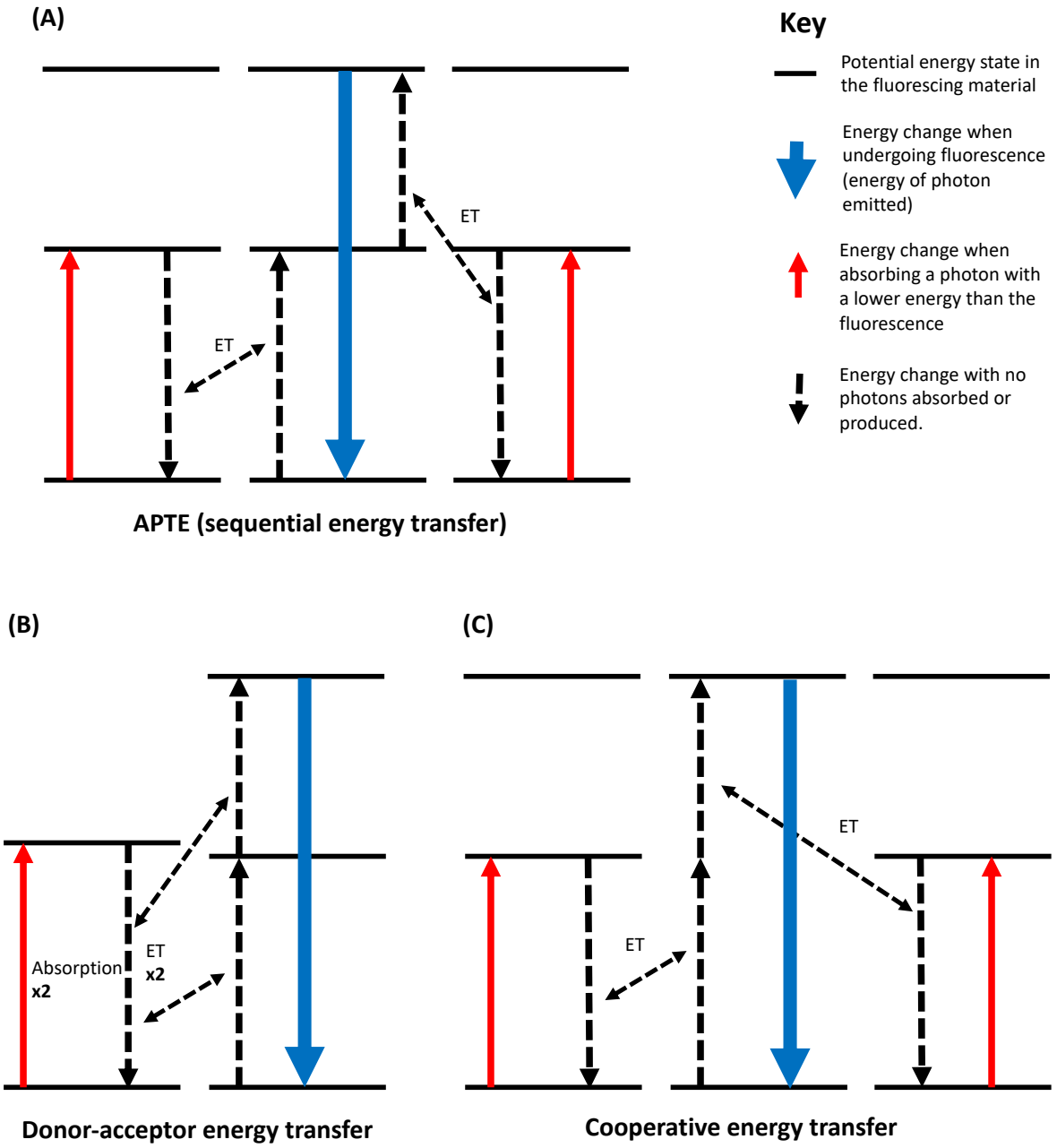

Figure 3: Band diagrams depicting (A) APTE upconversion; (B) donor-acceptor energy transfer upconversion; (C) cooperative energy transfer upconversion.

1.7. Shorter-than-excitation wavelength emission processes

Upconversion fluorescence belongs to a subset of shorter-than-excitation processes using electronic transitions. While upconversion fluorescence is in general one of the most efficient of these processes, there is also a possibility of seeing other shorter-than-excitation

wavelength emission processes when exciting samples with high powered sources. A summary of these processes and how to distinguish them from UCF follows.

1.7.1. Sum frequency generation

These processes include second and third harmonic generation, and three-wave mixing. In these processes, the excitation light perturbs the electromagnetic field of the material, creating detectable harmonics at high energies (Kleinman, 1962). They only occur when the excitation light is not absorbed, so are unlikely to occur for high absorptive samples. A typical test to distinguish these processes from fluorescence emission is to vary the excitation wavelength--for sum frequency generation, the emission will remain a fixed energy ratio of the excitation, whereas for processes using electronic transitions the emission will vary in intensity but not wavelength.

1.7.2. Inelastic scattering

Anti-Stokes scattering such as anti-Stokes Raman and anti-Stokes Brillouin scattering absorb energy already in the material in order to create a shorter-than-excitation wavelength emission. In the case of Raman scattering, this is from vibrational bonds in the material; in the case of Brillouin scattering, it is from acoustic waves (Shen and Bloembergen, 1965). Similar to sum frequency generation, emission will remain a fixed energy from the excitation photon energy when the excitation frequency is varied, but phenomena such as resonant Raman can create a sharp change in intensity over an excitation wavelength range, mimicking electronic transition processes. A clearer test is to keep the excitation wavelength fixed and measure the emission intensity while varying the power of the excitation light--scattering processes will have a linear power dependence, unlike processes that require more than one photon to occur.

1.7.3. Photon-induced radiative emission

This emission occurs when an excitation wavelength is highly absorptive within the incident material, and subsequently raises the material's temperature. This creates thermal radiation (Robinson et al., 2002). If the local temperature increases enough, the peak wavelength of the thermal radiation can become shorter than the excitation wavelength (Wang et al., 2014). This type of emission can easily be distinguished by either varying the wavelength of excitation or the power: when off-band to the absorption peak of the material, the peak of the radiation will shift to longer wavelengths; the same shift will occur at lower powers.

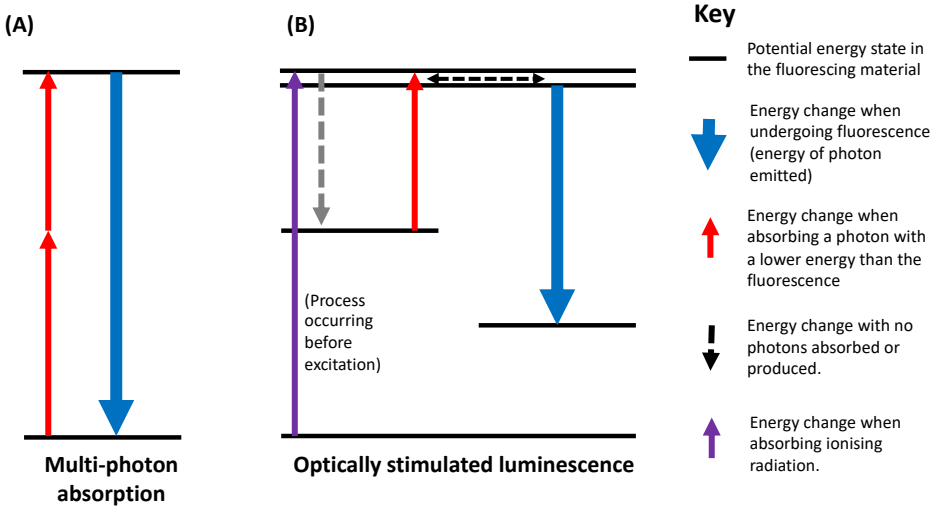

Figure 4: Band diagrams showing (A) multi-photon absorption and (B) optically stimulated luminescence

1.7.4. Non-UCF electronic transitions

These include multi-photon absorption, and optically stimulated luminescence (Figure 4). Multi-photon absorption uses a final real electronic level, but is distinguished from upconversion fluorescence by not using intermediate energy levels and instead absorbing all needed photons at the same time (Kaiser and Garrett, 1961). It can occasionally be difficult to distinguish between multi-photon absorption and upconversion fluorescence unless the absorption profile of the sample material is known. In general, if there is absorption at an intermediate stage accessible by an excitation photon, then multi-photon absorption is unlikely to occur.

Optically stimulated luminescence (OSL) occurs when a previous ionising radiation event creates an electron and hole pair in the material which then become trapped at metastable excited states. Subsequent excitation allows the electron or hole to exit the metastable state and radiatively decay, through recombination with a trapped charge of opposite type (Huntley et al., 1985). OSL is distinguished by its decay in intensity over time unless continually exposed to an ionising radiation source.

1.8. Rate equations

Electronic transition processes can be expressed as rate equations. For conventional fluorescence, the following equations show the change in populations of states 0 and 1 over time in a material (the equivalent band diagram is shown in Figure 5). Note that these equations neglect saturation effects and apply to two coupled states (e.g. a population of identical dopant ions).

$$\frac{dN_0}{dt} = -N_0 E_{ex} \alpha_{01} + N_1 A_{10}$$

$$\frac{dN_1}{dt} = +N_0 E_{ex} \alpha_{01} - N_1 A_{10}$$

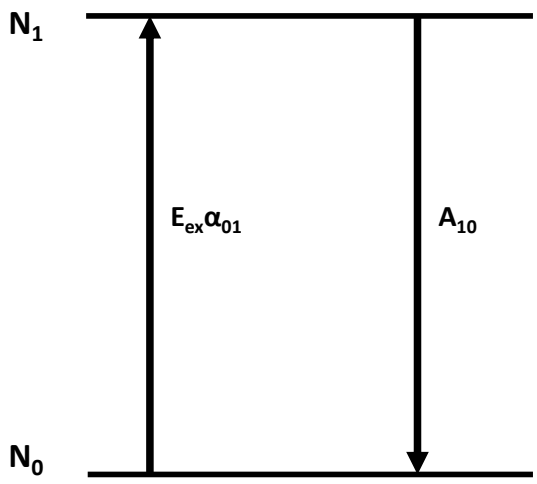

Figure 5: Band diagram depicting processes in the two-population rate equations.

N_0 is the number of ions in the ground state per volume, N_1 is the number of ions in the excited state per volume, α_{01} is the absorption coefficient of the dopant ion to the excitation wavelength per area, E_{ex} is the energy of the incident excitation , and A_{10} is the reciprocal of the total fundamental lifetime of the transition N_1 -> N_0. The equations for GSA/ESA (Figure 6) are similar:

$$\frac{dN_0}{dt} = -N_0 E_{ex1}\alpha_{01} + N_1 A_{10} + N_2 A_{20}$$

$$\frac{dN_1}{dt} = +N_0 E_{ex1}\alpha_{01} - N_1 E_{ex2}\alpha_{12} - N_1 A_{10} + N_2 A_{21}$$

$$\frac{dN_2}{dt} = +N_1 E_{ex2}\alpha_{12} - N_2 A_{21} - N_2 A_{20}$$

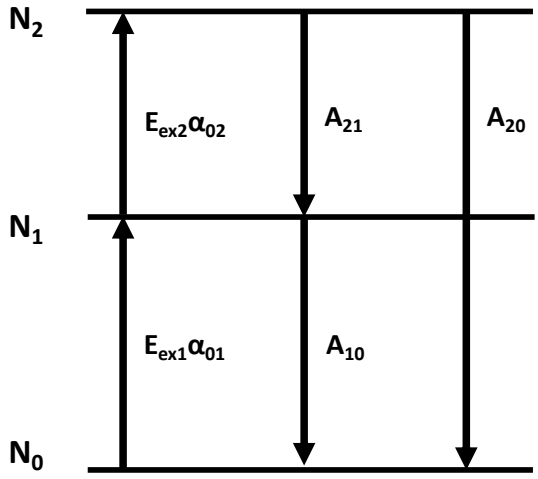

Figure 6: Band diagram depicting processes in the GSA/ESA three-population rate equations.

Where α_{12} is the absorption coefficient of a dopant ion in the excited state to the second excitation wavelength. Further ESA steps progress similarly.

For energy transfer from one ion to another (Figure 7), the following set of rate equations applies:

$$\frac{dN_{0donor}}{dt} = -N_{0donor}E_{ex}\alpha_{01(d)} + N_{1donor}A_{10(d)} + N_{1donor}N_{0acceptor}W_{da}$$

$$\frac{dN_{1donor}}{dt} = +N_{0donor}E_{ex}\alpha_{01(d)} - N_{1donor}N_{0acceptor}W_{da} - N_{1donor}A_{10(d)}$$

$$\frac{dN_{0acceptor}}{dt} = -N_{1donor}N_{0acceptor}W_{da} + N_{1acceptor}A_{10(a)}$$

$$\frac{dN_{1acceptor}}{dt} = +N_{1donor}N_{0acceptor}W_{da} - N_{1acceptor}A_{10(a)}$$

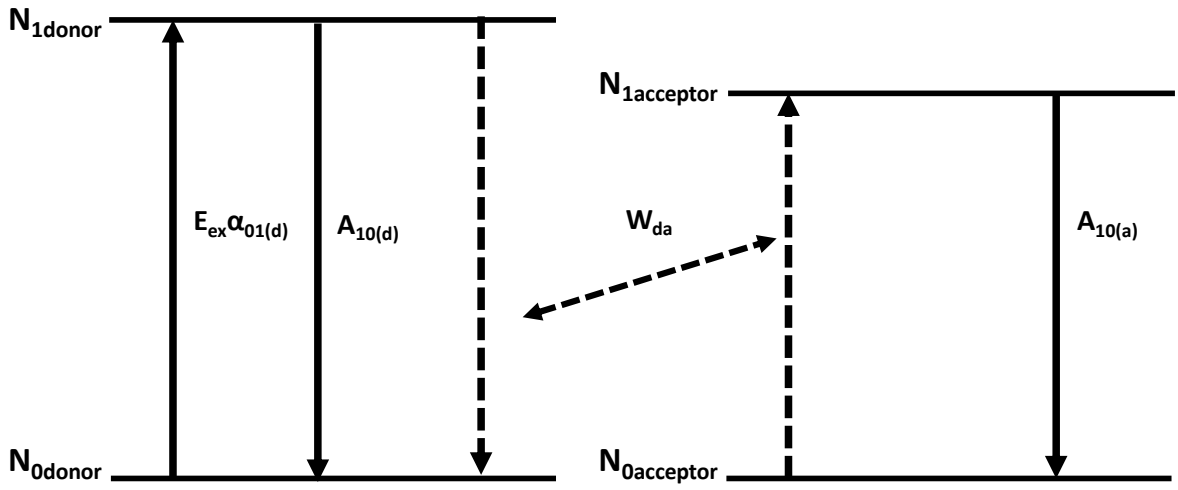

Figure 7: Band diagram depicting processes in the donor-acceptor energy transfer four-population rate equations.

where W_{da} is the energy transfer rate. This energy transfer rate has units of volume per second, as unlike ESA, energy transfer depends on the proximity between two ions. The energy transfer rate increases when ions are more likely to be close together, as is the case when there is clumping of doping ions or the doping percentage is increased.

Using a combination of absorption and energy transfer parameters, one can model the rate of change of different energy states over time by solving the differential equation set.

1.9. Upconversion fluorescence experimental behaviour

While rate equations can provide valuable insights into the behaviour of different processes, identifying the process is more reliably done by experimental means, especially with complicated or unknown samples. The following section describes different experimental variables and how they shed light on the upconversion processes that are producing emission.

1.9.1. Emission and excitation wavelength

The peak wavelength of emission can give information as to its origin, especially if the emission comes from a known dopant or defect. The relative width of the emission peak can give more general information about the emission origin—rare earth element-based emissions tend to have a narrow emission width (Freed, 1931), while transition metal and lattice defect-based emissions tend to be broad. Behaviour when varying excitation wavelength is similar, with broader excitation peaks for transition metal and lattice defect-based emissions, and narrower excitation peaks for rare earth element transitions.

1.9.2. Power dependence

The power dependence of an upconversion emission depends on a number of different aspects:

a) The regime of power-to-population ratio (less incident photons than dopants in a population, excited state population near saturation, etc.)
b) The processes involved (energy transfer vs excited state absorption)
c) How many pathways are available other than upconversion emission (when looking at two-photon emission, is there a three-photon emission pathway available, etc.)

At very low powers, the effect of different pathways on the intensity of emission is low, and the intensity of emission is proportional to P^N, where P is the excitation energy incident on the material, and N is the number of photons needed to complete the upconversion process (Auzel, 1966b). At very high powers near or at saturation, the trend in emission intensity increase flattens to a slope of 0.

The behaviour of simple excited state absorption and energy transfer upconversion processes at middle power ranges is detailed thoroughly in (Pollnau, 2000). In more complicated materials with multiple different transition pathways, changes in power can change the probability of particular pathways, drastically changing the slope of the energy-emission dependence. Increasing energy incident on a material can also locally heat the area, compounding this issue—for instance, increasing the temperature can increase the likelihood of phonon-assisted energy transfers. One example of a power-dependent pathway change is the photon avalanche upconversion emission process (Chivian et al., 1979). In this process, single photons induce excited state absorption to a second excited state from a small population of thermally excited ions in the first excited state. The electrons in the second excited state can decay via two methods: either decaying to the first excited state and transferring energy to a nearby ion, thereby raising a second electron to the first excited state; or by fluorescence emission (Figure 8). In highly doped samples where energy transfer is efficient, at higher powers the population of the first excited state quickly increases, greatly increasing the rate of all other processes.

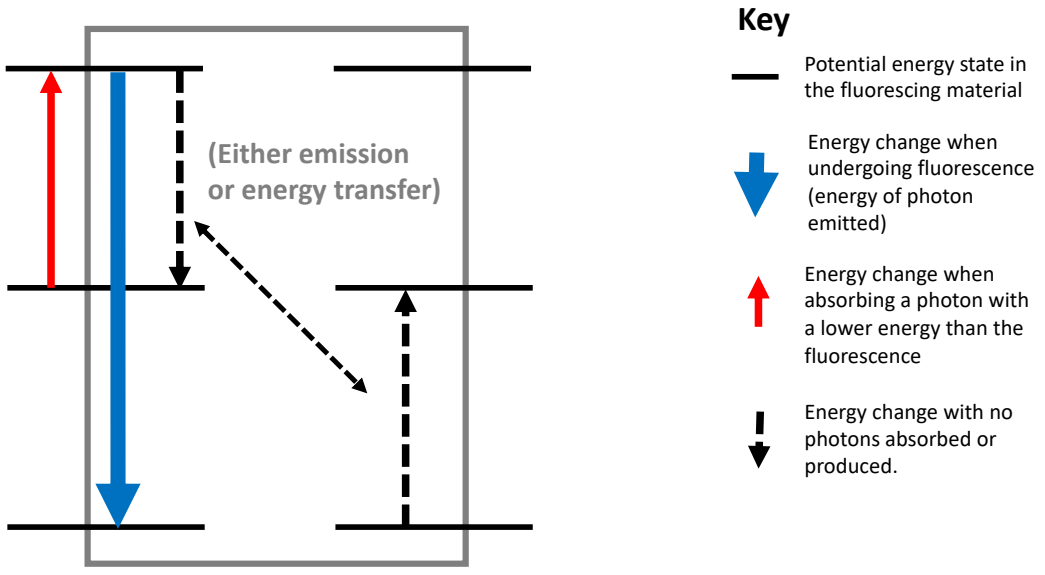

Figure 8: Band diagram of the photon avalanche upconversion process.

1.9.3. Time dependence

Time-resolved data can shed light on different processes causing an emission. After an initial ground state absorption, excited state absorption and energy transfer processes can be distinguished between one another through time-resolved data. Upconversion emission via energy transfer will have a longer lifetime, as the energy transfer process can occur after excitation has stopped—the population of ions undergoing energy transfer depends on the lifetime of the excited donor state. Changes in lifetime can also be caused by different upconversion or transfer processes in a material, and so the presence of codopants can be identified via a faster-than-expected lifetime. The usefulness of lifetime measurements often requires the fundamental lifetime of the emission state and the first excited state to be known in advance, usually via direct excitation measurements or by theoretical calculations such as Judd-Olfelt theory (Judd, 1962, Olfelt, 1962).

1.9.4. Temperature dependence

In general, lowering the temperature of a sample narrows the absorption bands of potential excited states in the material and lowers the maximum available phonon energy of the material (Jean Weigle, 1945). Both of these phenomena can cause a decrease in energy transfer upconversion efficiency. Narrowing absorption bands can increase mismatch between energy states, which can prevent resonant energy transfer. Decreasing the set of available phonon energies can prevent phonon-assisted energy transfer. For GSA/ESA, more precise excitation wavelengths may be needed as the potential absorbed wavelengths decrease. However, if these precise excitation wavelengths are available, GSA/ESA process may increase in efficiency, as the increase in energy difference between states due to the narrowing of bands and the lack of phonon assisted energy transfer decreases the efficiency or possibility of various non-radiative pathways within the material.

1.10. History and applications

While historically upconversion fluorescence has had limited applications, the advent of nanoparticles and high-powered lasers have opened up the potential uses for UCF. A brief summary of current and past applications and areas of research is below.

1.10.1. Quantum Counters

Upconversion luminescence was theorised as a possible way to create infrared quantum counters (infrared photon detectors) in 1959 (Bloembergen, 1959). While J. F. Porter (Porter, 1961) showed that sequential two-step fluorescence was possible using La-doped $PrCl_3$, the fluorescence emission was not true anti-Stokes emission, as Porter used 2300 nm and 558 nm wavelength photons to induce fluorescence at 618 nm. In 1963 Brown and Shand created shorter-than-excitation wavelength upconversion emission using Pr^{3+}-doped LaF_3, SrF_2, CaF_2 and BaF_2 at liquid nitrogen temperatures to produce blue 485 nm fluorescence from various excitations including infrared, red, orange and green wavelengths (Brown and Shand, 1963).

Others made similar discoveries using different host materials and rare-earth dopants in the following years (Bakumenko et al., 1965). It was assumed that the upconversion fluorescence was created from the sequential absorption of two photons by the one dopant ion, as was theorised by Bloembergen. In 1966 it was separately demonstrated that in much of the

previous work the mechanism of upconversion was ion-ion energy transfer, and not sequential absorption (Auzel, 1966b, Feofilov and Ovsyankin, 1967, Ovsyankin and Feofilov, 1966).

1.10.2. Lasers

Ion-ion energy transfer is important in the creation of upconversion laser crystals, which require high-efficiency upconversion output. While in the past upconversion (or more specifically excited state absorption) was considered a detriment due to reducing the Stokes luminescence output (Young, 1969), upconversion lasers were soon developed out of the need for short-wavelength lasers and the availability of near-infrared pump lasers. The first upconversion lasers were created in 1971 (Johnson and Guggenheim, 1971), and used co-doping to provide efficient ion-ion transfer in Yb,Er:BaY_2F_8, and Yb,Ho:BaY_2F_8. An advantage of co-doping is that by choosing the material and codopant carefully, one can gain upconversion using only one light source, and both of Johnson and Guggenheim's lasers were pumped with a single Si-doped GaAs luminescent diode.

When semiconductor laser diodes increased in power and became cheap and efficient, upconversion lasers pumped with more than one wavelength were developed (Nguyen et al., 1989, Hebert et al., 1992, Szela and Mackenzie, 2012). While normally using only one pump wavelength is preferred for energy efficiency, optimising the excitation wavelengths used greatly increases the quantum yield of the output (Krämer et al., 1998). The base material of an upconversion laser is chosen in order to minimise phonon energies and therefore minimise non-radiative transitions; the dopants are chosen for their ability to provide multiple metastable states and to minimise phonon-ion energy transitions. Due to these requirements, when looking for upconversion materials the dopant chosen is usually a rare-earth element, although sometimes transition metals are used instead (Jacobsen and Güdel, 1989), or as co-dopants (Cresswell et al., 1978).

1.10.3. 3D Displays

3D display designs require an invisible input and a visible output in a transparent medium, thus two-photon two-step excitation has been theorised and researched for this application since the early 1900s (Luzy and Dupuis, 1914). Methods that require two excitation sources are needed to enable one voxel of the three-dimensional display to be targeted. Sequential two-photon absorption has been widely used, which in the anti-Stokes case is upconversion fluorescence.

Upconversion 3D display designs involve a solid crystal or glass matrix (Downing et al., 1996, Langhans et al., 2003) or nanoparticles suspended in a liquid or polymer (Koudsi et al., 2015, Deng et al., 2015). To get different colours, researchers use different materials or dopants (Deng et al., 2015, Downing et al., 1996). Deng et al. produced RGB output with only two lasers by making use of the different lifetimes of the excited states of the dopants. In their experiment, differently timed pulses produce differently coloured emissions from their multi-layered upconversion nanocrystals.

1.10.4. Medical Imaging

Upconversion fluorescence was first used in the medical field for laser scanning fluorescence microscopy (Denk et al., 1990). Upconverting organic molecules or nanoparticles are placed

in a sample or animal in addition to fluorescent markers which can either be attached to the upconverter or be activated by the upconversion light. An infrared laser is scanned across the surface of the sample, and the fluorescence emission is collected. In this way, one creates a spatially resolved image of the fluorescence of the material.

Upconversion for scanning fluorescence microscopy is considered highly advantageous as the long-wavelength excitation source does not damage biological tissue as much as a UV source (Denk et al., 1990), which is generally the alternative excitation source in fluorescence microscopy techniques. In addition, longer wavelength light can travel further through biological material than UV light (on the order of cm rather than mm), enabling beyond-surface resolution and in-vivo analysis, and greatly reduces interfering autofluorescence signals.

1.10.5. Medical tracking and dosing

Upconversion nanoparticles (UCNPs) can be used to track chemical or drug delivery in tissues or cells (Wang et al., 1999). When attached to a drug or large molecule, UCNPs can be used in the same way as markers in scanning fluorescence microscopy to observe the movement of the chemical within a cell or tissue over time.

Research has also been done on the potential of UCNPs for use with photon-stimulated dosing particles. Since the 1970s, molecules have been developed that either expose or release a previously encapsulated medicinal agent when exposed to light (Diamond et al., 1972) which enables spatially targeted dosing. The wavelength of the stimulation light needed is often of blue-UV photon energy, meaning that it does not travel far through biological material and can damage healthy cells. Combining these light-stimulated dosers with UCNPs enables the external stimulation light to be infrared and therefore able to be transmitted further through the body (Chatterjee and Yong, 2008). It also minimises the flux of photons of damaging energies the healthy tissue is exposed to.

1.10.6. Chemical Sensors

There are a number of ways UCNPs are used in chemical sensors. A common method is to bind the UCNP to a fluorescent marker (Zhang et al., 2006), as in fluorescence scanning microscopy. Upon stimulation, the UCNPs emit the right wavelength needed to induce the activated fluorescent markers to fluoresce. This method is used both if activating the fluorescent markers directly is infeasible, and to reduce background noise.

UCNPs have been used in the creation of upconversion pH sensors (Sun et al., 2009): upconversion nanoparticles can be combined with a pH sensitive dye that absorbs different wavelengths depending on the pH of the sample. Sun et al. excited $NaYF_4$:Er,Yb nanoparticles that emit in both green and red, and the pH could be calculated by measuring the ratio of absorption of the two peaks.

Many different ways to use UCNPs in chemical sensors have been developed, though most fit into one of three categories:

- sensors wherein the presence of the target molecule activates a fluorophore that is stimulated by UC emission;

- sensors in which the presence of the target molecule inhibits UC emission detection; and
- sensors in which the presence of the target molecule changes the chemistry or position of molecules near the UCNP in order to allow UC emission to be sensed (Wu et al., 2015).

1.10.7. Temperature Sensors

Upconversion temperature sensors rely on the fact that different kinetic pathways become more probable at different temperatures, as various resonant, thermal coupling, and phonon effects come into play. Common dopants are Yb/Er (Berthou and Jörgensen, 1990), Er (Maciel et al., 1995), Ho (Singh et al., 2006), and Ho/Tm (Savchuk et al., 2018). Some use the total emission intensity as an indication of temperature (Singh et al., 2006) (non-radiative pathways compete more strongly at higher temperatures, decreasing emission intensity), while others use a ratio between two different emission peaks (Berthou and Jörgensen, 1990). Using upconversion to sense temperature is useful as upconversion sensors can be more robust than conventional sensors, and can be made much smaller, such as nanoparticles for in-situ medical temperature sensing (Savchuk et al., 2018).

1.10.8. Solar cell development

Conventional solar cells only make use of a limited bandwidth of the solar spectrum, and so upconverting materials have been studied in order to try to develop solar cells that make use of the near-infrared spectral region (Trupke et al., 2002) as well as the visible region. Studies first looked at one- and two-wavelength excitations (Gibart et al., 1996, Jiang et al., 2013), but later studies used broadband near-infrared sources (Chen et al., 2015). Upconversion for solar cells requires a very efficient process with reasonably long-lived metastable states involved, as unlike in medical and laser technologies, the excitation wavelengths are not coming into the material at a very high photon flux. While UCNPs have been researched due to their efficient upconversion, they have proved too unstable for long term use (Jiang et al., 2013), and suitable bulk materials are still being researched.

1.11. Aspects of solid upconversion materials: dopant ions

Most upconversion fluorescence solid materials synthesised for research or commercial use rely on two parts to be effective: the dopants and the bulk material. The dopants are responsible for the electronic energy states involved in the upconversion fluorescence, and thus what wavelengths can be used to excite electrons. There are three main concerns to consider when doping a material:

1.11.1. Choice of dopant ion

The dopant is responsible for the energies of photons that are absorbed by metastable states in the material. Rare earth ions are often used as dopants, as they have multiple potential excited states that decay via radiative transitions. They also have the advantage that the optically active electrons in the ion are well shielded from the effect of positive ions in the lattice by other electron shells. This means that when using rare earth ions for UCF there is less energy loss and a greater likelihood of UCF. The well-shielded nature of the rare earth ions also means the energy scheme of the electronic energy states remains almost independent of the host material (Eichhorn, 2008a), which allows easier selection of dopant

and host when creating an UCF material for a particular purpose. Rare earth ions used include praseodymium (Pr) (Brown and Shand, 1963), dysprosium (Dy) (Brown and Shand, 1964a), erbium (Er) (Brown and Shand, 1964c), holmium (Ho) (Brown and Shand, 1964b), ytterbium (Yb) and thulium (Tm) (Auzel, 1966a).

Transition metals are also sometimes used for doping upconversion materials, as they have similar energy level complexities and advantages as rare earths. However the optically active electrons in transition metals are less shielded from the host lattice than rare earth ions—rare earth elements have 5s, 5p, and 6s shells beyond the 5f optically active area, while transition metals only have the 5s shell. This leads to a greater chance of electron-phonon coupling and non-radiative energy transfer (Wermuth and Güdel, 1997). Their subsequent broader absorption characteristics (Wenger et al., 2002), however, can be an advantage. Transition metals used include nickel (Ni) (Moncorgé and Benyattou, 1988), titanium (Ti) (Jacobsen and Güdel, 1989), osmium (Os) (Wermuth and Güdel, 1997); molybdenum (Mo), and rhenium (Re) (Gamelin and Güdel, 1998). Both rare earth and transition metal ions previously used for upconversion processes are highlighted in Table 1.

H																	He
Li	Be											B	C	N	O	F	Ne
Na	Mg											Al	Si	P	S	Cl	Ar
K	Ca	Sc	Ti	V	Cr	Mn	Fe	Co	Ni	Cu	Zn	Ga	Ge	As	Se	Br	Kr
Rb	Sr	Y	Zr	Nb	Mo	Tc	Ru	Rh	Pd	Ag	Cd	In	Sn	Sb	Te	I	Xe
Cs	Ba	La	Hf	Ta	W	Re	Os	Ir	Pt	Au	Hg	Tl	Pb	Bi	Po	At	Rn
Fr	Ra	Ac	Rf	Db	Sg	Bh	Hs	Mt	Ds	Rg	Cn	Uut	Fl	Uup	Lv	Uus	Uuo

Ce	Pr	Nd	Pm	Sm	Eu	Gd	Tb	Dy	Ho	Er	Tm	Yb	Lu
Th	Pa	U	Np	Pu	Am	Cm	Bk	Cf	Es	Fm	Md	No	Lr

Table 1: Periodic table with elements reported in upconversion fluorescence doped materials highlighted. Yellow elements are dopants, green elements are common anions for bulk materials, and blue elements are common cations.

1.11.2. Concentration of dopant

For most applications, it is preferable to maximise the output of UCF materials. While maximising the amount of dopant in the material maximises the chance a photon will be absorbed by a metastable state, fluorescence quenching effects can take place when the dopant concentration is large. In addition, different fluorescence pathways can preferentially take place depending on the dopant concentration (Zhou et al., 2010). To balance these requirements and effects, the dopant concentration is generally between 0.3 % and 15 %, and usually between 1 % and 5 % (Joubert, 1999).

1.11.3. Codopants

Codoping the UCF material with more than one type of ion is common, as codopants can create the right conditions for energy transfer upconversion (Auzel, 1966a). It can also minimise quenching effects (Yu and Yu, 2013), or create lattice defects that maximise emission (Maciel et al., 2009). Codoping is often used in applications where high efficiencies

are needed, such as solar cell NIR harvesting, laser crystals, and nanoparticles for medical imaging. This is because codoping can minimise quenching and create opportunities for more efficient energy transfer upconversion. Ytterbium is the most common rare earth codopant, paired with erbium (Schulze and Schmidt, 2015) in solar cell research, praesodymium (Joubert, 1999) and erbium (Johnson and Guggenheim, 1971) in upconversion lasers, and gadolinium, erbium, and thulium in nanoparticles for medical research (Xu et al., 2015).

1.12. Aspects of solid upconversion materials: surrounding lattice

The matrix of the upconversion material is responsible for providing an environment that is both suitable for the application and enables radiative transitions from the dopant. The main requirements for an upconversion matrix material are listed below:

1.12.1. Phonon energies and multi-phonon relaxation

Whether an electron in an excited metastable state loses its energy radiatively or non-radiatively greatly depends on how likely multi-phonon relaxation occurs between the matrix and the metastable state. This is partly governed by how well the energy levels of a dopant ion match to the phonon energies of the matrix (Reisfeld et al., 1975). In general, it is more likely for multi-phonon relaxation to be suppressed in low phonon materials (Riedener et al., 1995).

Multi-phonon relaxation can in the most severe case prevent radiative transitions from occurring, and in less severe cases lower the energy of the upconversion fluorescence photon output or 'smear' the upconversion fluorescence by broadening the emission peak. In general, when creating an upconversion fluorescence material, the lowest phonon energy host material suitable for the application is chosen.

1.12.2. Size of complete structure

While some upconversion fluorescence applications require large-scale crystals or glasses (such as upconversion lasers), for medical applications the upconversion materials need to be small, and so can take advantage of the small-size effect, which suppresses phonon energies due to the lack of space for multiple resonant frequencies (Zheng et al., 2015). Upconversion nanoparticles can also utilise surface effects. Changing ligand and surface effects can create changes in absorption and emission properties (Liao et al., 2013), which can create multi-step upconversion that is usually impossible in bulk materials (Zheng et al., 2015).

For nanoparticle upconversion materials, the optimum atomic radius of the dopant ion is of a similar size to the ion it is substituting in the lattice. Mismatches between atomic radii can create crystal defects that deform nanoparticle growth and prevent uniform distribution of dopants. $NaYF_4$, therefore, is the most common upconversion nanocrystal used with rare earth doping, with NaF, CaF_2, YF_3, SrF_2, Ba_2LaF_7, $KGdF_4$, and other fluorides combined with relatively high atomic radius cations also being used (Xu et al., 2015).

1.12.3. Application-dependent properties

While the lower the phonon energy the more likely the occurrence of upconversion fluorescence with minimum energy loss, choosing a material purely for its UCF properties ignores the material properties needed for its application, such as stability in the application

environment. Bromides, for instance, have very low phonon energies, and can provide much more efficient UCF than a similar chloride crystal (Riedener et al., 1995). However, as bromide crystals are generally less stable under heat, light, and humidity, fluorides are usually chosen for UCF laser applications. Similarly, while upconversion nanoparticles can provide much more efficient upconversion than bulk materials, they are too unstable for solar cell applications (Jiang et al., 2013). Medical applications require upconversion nanoparticles to be non-toxic, thus fluorides are generally chosen for their stability and low toxicity.

Opacity is also an important property dependent on the application. Surface-only excitation is possible using nanoparticles, as collectively they have a very large surface area. In contrast for laser applications an upconversion crystal must be transparent to both excitation and emission wavelengths, in order for efficient excitation and for emission wavelengths to exit the crystal without being absorbed.

In general, while oxides (Maciel et al., 2009), bromides (Riedener et al., 1995) and chlorides (Cresswell et al., 1978) have been extensively studied for their upconversion properties, fluorides are by the far the most widely used in practice. An exception is $Y_3Al_5O_{12}$ (YAG), which is a common laser crystal that has good upconversion properties (Pollack and Chang, 1988) and is stable in most laser environments.

1.13. Upconversion from Lattice Defects

Defects are less common in artificial materials than natural minerals due to their regulated growth conditions; despite this, there are a number of reported cases of upconversion from, or aided by, defect-created metastable states. These defects are created by a non-compatible ion being substituted into the lattice (Yu and Yu, 2013, Joshi et al., 2010), deformation processes being applied to the material (Qin et al., 2004, Wang et al., 2015), or intrinsic defects due to irregularities in crystal formation (Johnson et al., 1982, Wang et al., 2007, Chen et al., 2012, Wang et al., 2018). Anomalous upconversion wavelengths not able to be explained by the dopant ions are generally attributed to lattice defects (Maciel et al., 2009, Yıldırım and Birer, 2014). Maciel et al. found anomalous upconversion at 845 nm and 869 nm in Pr^{3+}, Yb^{3+}: Al_2O_3 when exciting at 980 nm. Yıldırım and Birer found a number of small anomalous peaks in Tm^{3+}:$NaYF_4$ crystals when exciting at 965 nm. Other workers have gone into further detail about the nature or cause of the potential defects involved, as outlined below.

1.13.1. Ion-induced defects

Attempting to dope a lattice with ions that are of a much larger or smaller atomic radius than the major lattice constituents can deform the lattice and create defect-derived metastable states. These defects are commonly associated with quenching effects because their closeness to the dopant ion allows for efficient energy transfer from the ion. In some cases however upconversion enhancement has been seen. Co-doping Er:Al_2O_3 with Sc^{3+} ions can enhance erbium upconversion by providing lattice asymmetry around Er^{3+}, sensitising it to excitation transitions (Yu and Yu, 2013). Four anomalous upconversion peaks have also been found in Er:$Cs_2NaEr_xY_{1-x}Cl_6$ at low temperatures, which were attributed to oxygen ions substituting for chlorine ions near the erbium dopant (Campbell et al., 1997).

Doping lattices with ions that are electronically different to the ions they are substituting can also create upconversion defects. In 2010 it was discovered that when Yb^{3+} substituted for Ca^{2+} in $Yb^{3+}/Yb^{2+}:Ca_{12}Al_{14}O_{33}$, a broad defect-related peak at 500 nm was seen when the material was excited at 976 nm (Joshi et al., 2010).

1.13.2. Lattice deformation and defects

Physically deforming a lattice can lead to upconverting metastable states. Qin et al. created nano- and micro-crystals of Tm^{3+},$Yb^{3+}:ZnF_2$ using pulsed laser ablation, a technique in which a pulsed laser is focused beyond the surface of a material (Qin et al., 2004). The high power of the laser creates an explosive reaction at the focus point, vaporising a volume of internal material and thereby expelling surface material which is then recovered. The crystals showed upconversion peaks that were not seen in bulk material or in material milled to an equivalent size. In 2015, it was shown that pumping a Yb:YAG crystal with a femtosecond laser formed Yb^{2+}-F^{+} defect centres that produced upconversion (Wang et al., 2015). Natural lattice defects can also create upconversion: a 565 nm peak from a defect in hexagonal boron nitride was shown to be excited by photon-phonon upconversion techniques (Wang et al., 2018).

1.13.3. Upconversion in semiconductors

Defect-derived upconversion in semiconductors often use the conduction band as the second excited state, as electrons can freely travel in this band to recombination sites otherwise isolated from the original defect site. (Johnson et al., 1982) observed upconversion in GaAs at 8 K; exciting at 892 nm, they discovered a number of peaks, some attributed to ion substitution but one attributed to the defect caused when an As ion replaces a Ga ion in the lattice (arsenic antisite defect).

More extensively studied are the upconversion properties of ZnO. In 2007, Wang et al. (Wang et al., 2007) found two anti-Stokes luminescence peaks at room temperature when exciting at 800 nm with a femtosecond laser. One peak, at 500 nm, they attributed to two-photon simultaneous absorption, and the other at 395 nm they attributed to three-photon upconversion. The metastable states involved were attributed to defect pairs. Chen et al. found two-photon upconversion at 5 K, and attributed it to Zn vacancies (Chen et al., 2012). They proposed the upconversion process started with metastable state electrons being excited to the conduction band, and then valence band electrons being excited to the metastable state, leaving a hole in the valence band that is filled during the radiative transition. This upconversion fluorescence was analysed in more detail in 2014 (Stehr et al., 2014), and more data was found to support the zinc vacancy defect theory.

Overall, upconversion via defects are reported to have much broader emission and absorption spectra. While it also tends to be weaker than doped-ion upconversion in reported upconversion materials, this may be due to the greater numbers of dopant ions as compared to defect sites in these materials.

1.14. The relationship between bulk and electronic properties

While dopant ion and lattice behaviour are discussed separately above, fluorescence is greatly influenced by the interaction between the two. Ions or defect structures in a material

fluoresce when there is an energy 'gap' in the potential energy structure between the upper and lower energy states large enough that non-photonic forms of de-excitation (non-fluorescent) are insufficient to bridge the gap. The size of the energy gap, and the number of non-photonic pathways available, are highly influenced by the interaction of the bulk properties of the material to the potential energy structure.

Most fluorescent ions have an optically active energy levels that are 'shielded' from the surrounding lattice by having initially filled electron shells at higher energies. Despite this, the electromagnetic structure of the lattice does have an effect on the potential energy bands of the optically active area of the ion. The potential energy levels of electrons in an ion in isolation are determined by the attractive forces of the nucleus being balanced by the repellent forces of the other electrons in the ion. In a lattice, these energy levels are also dependent on balancing the attractive and repellent forces of the lattice members. This generally serves to broaden the width of the potential energy levels. This can be advantageous for fluorescence, as a broader range of excitation energies can be absorbed; however broad emission can be harder to detect, especially if other fluorescence emission is present. Broader energy levels also reduces the gap between the two energy levels used for fluorescence, increasing the chance that a non-photonic pathway will be available to bridge the energy gap.

The lattice itself also has potential electronic energy levels, and these can have an effect on the fluorescent pathways. If the lattice potential energy levels are similar to the levels in the fluorescent ion or defect, the energy is likely to be transferred to the lattice, rather than be emitted as a photon. This occurs in a similar way as energy transfer to a different dopant ion.

The lattice also has vibrational energy states, radiated by phonons, which occur at vibrational resonant frequencies of the host. These frequencies depend on the 'vibrational potential' of the lattice members (dependent on bond strength and lattice temperature), the physical distance between lattice members, and how many lattice members are present. This means that both the lattice properties and the overall size of the host lattice is important. In a similar way to lattice electronic potential energies, if a potential energy gap has a similar energy to a host phonon energy, that energy is likely to be transferred to vibrational energy in the lattice rather than be emitted as a photon. Phonon energies can in some cases aid fluorescence; if energy transfer cannot in general occur between two ions due to an energy mismatch, energy can be added or taken away via phonon interactions in order to allow the energy transfer to occur.

1.15. Thesis aim

This study aims to do the following:

1. Develop and characterise a dual-wavelength upconversion fluorescence facility.
2. Apply the facility to explore and identify upconversion fluorescence previously unknown in minerals.
3. Assess the viability of these newly-discovered fluorescences—both upconversion and "conventional" single-photon fluorescence—as real-time, non-contact mineral detection, identification and quantification techniques.

To this end, this thesis shall take the following shape:

Chapter Two will describe the apparatus used in this thesis, including the description of the world's first fluorescence facility specifically designed for the purpose of identifying upconversion fluorescence signatures from natural minerals and artificial materials.

Chapter Three will show upconversion fluorescence behaviour in a known synthetic material, including quantitative results of kinetic parameter measurements.

Chapter Four will show conventional, ultra-violet-induced, and upconversion fluorescence results from selected minerals of economic significance, including copper and zinc sulphides and uranium oxides.

Chapter Five will identify conventional and upconversion fluorescence in natural minerals known to be highly fluorescent, and show the potential of fluorescence for mineral discrimination and abundance measurements.

Chapter Six will discuss the previous results in light of our aims and give conclusions on the viability of different fluorescence signatures for use in mineral identification and quantification.

2. — Experimental Details

A novel Dual-Wavelength System was created for the purpose of conducting two-wavelength investigations, and applied to the two-wavelength excitation experiments reported in this thesis. In addition, other one-wavelength measurements, where specified, were conducted on an Edinburgh Instruments F980 spectrofluorimeter. Specifications of these two systems, as well as sample preparation and experimental sequences, are given below.

2.1. The Dual-Wavelength System

The Dual-Wavelength System (DWS) was built in order to scan for two-wavelength-excited upconversion luminescence. It includes two synchronised, tuneable lasers that illuminate a sample on a thermally controllable stage. Emission is detected by a supplementary silicon EMCCD camera situated above the sample stage for image and total intensity measurements, and in addition optical fibres lead to two spectrometers, operating in the ultra-violet-visible-near-infrared and the short-wavelength infrared, for simultaneous real-time spectral measurement across the 300 nm to 1,700 nm range.

The inputs and outputs in any measurement are as follows:
Inputs:

1. Excitation Wavelength 1
2. Excitation Wavelength 2
3. Delay of Wavelength 2 from Wavelength 1
4. Power Wavelength 1
5. Power Wavelength 2
6. Temperature of sample

Outputs:

7. Emission Intensity
8. Emission Wavelength

Initial measurements were made at room temperature. To simplify initial measurements and lower the parameter space, the pulses are set in typical operation mode to arrive at the same time. OPO pulse energy is wavelength dependent, and was not controlled for initial measurements.

To allow complicated sequences of measurements to be done in a reproducible and timely manner, the different parts of the system have been integrated in a National Instruments LabView TestStand program, developed by a software contractor "Resonate Systems" (Level 1, 21 Peel Street, South Australia, Australia, +61 08 7200 5700).

In this section the excitation and emission parts of the system will be discussed separately. Figure 9 shows the complete system in schematic form to illustrate the beam-line layouts and sample presentation, while Figure 10 and Figure 11 show on photographs the beamline and different elements.

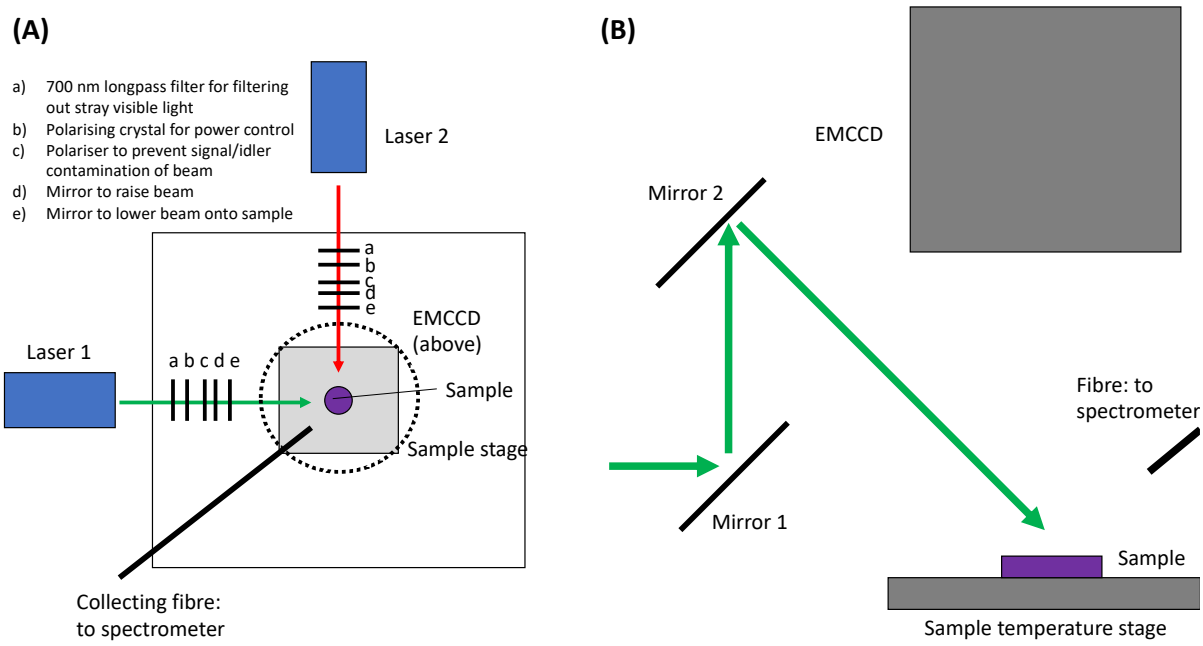

Figure 9: (A) Schematic plan view of the Dual-Wavelength System. (B) The EMCCD and sample stage setup.

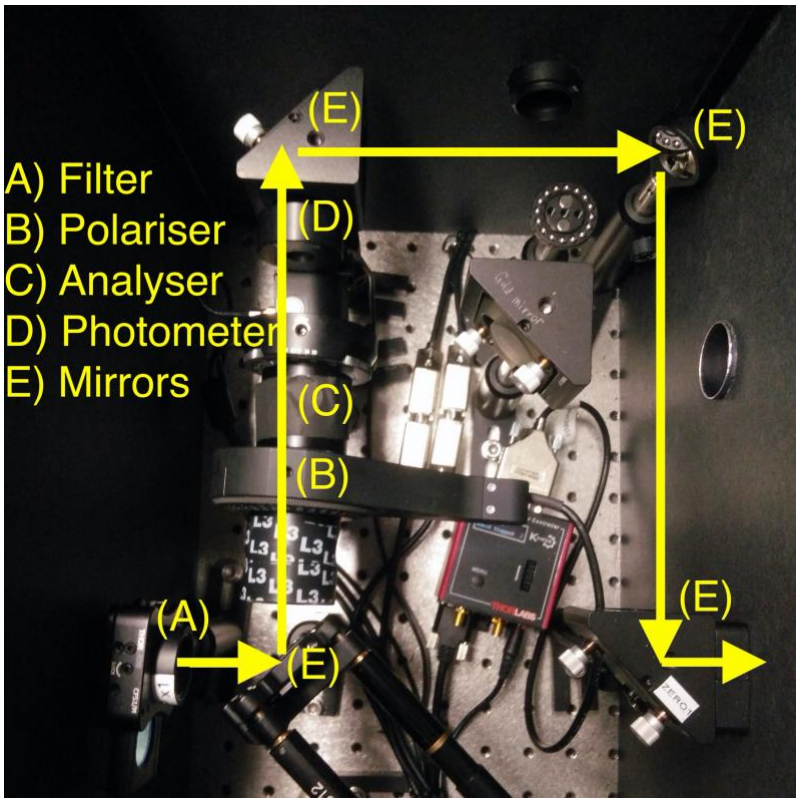

Figure 10: Annotated photo of the external beamline in the current Dual-Wavelength System setup, used for power control and filtering stray 'leaked' light from OPO function.

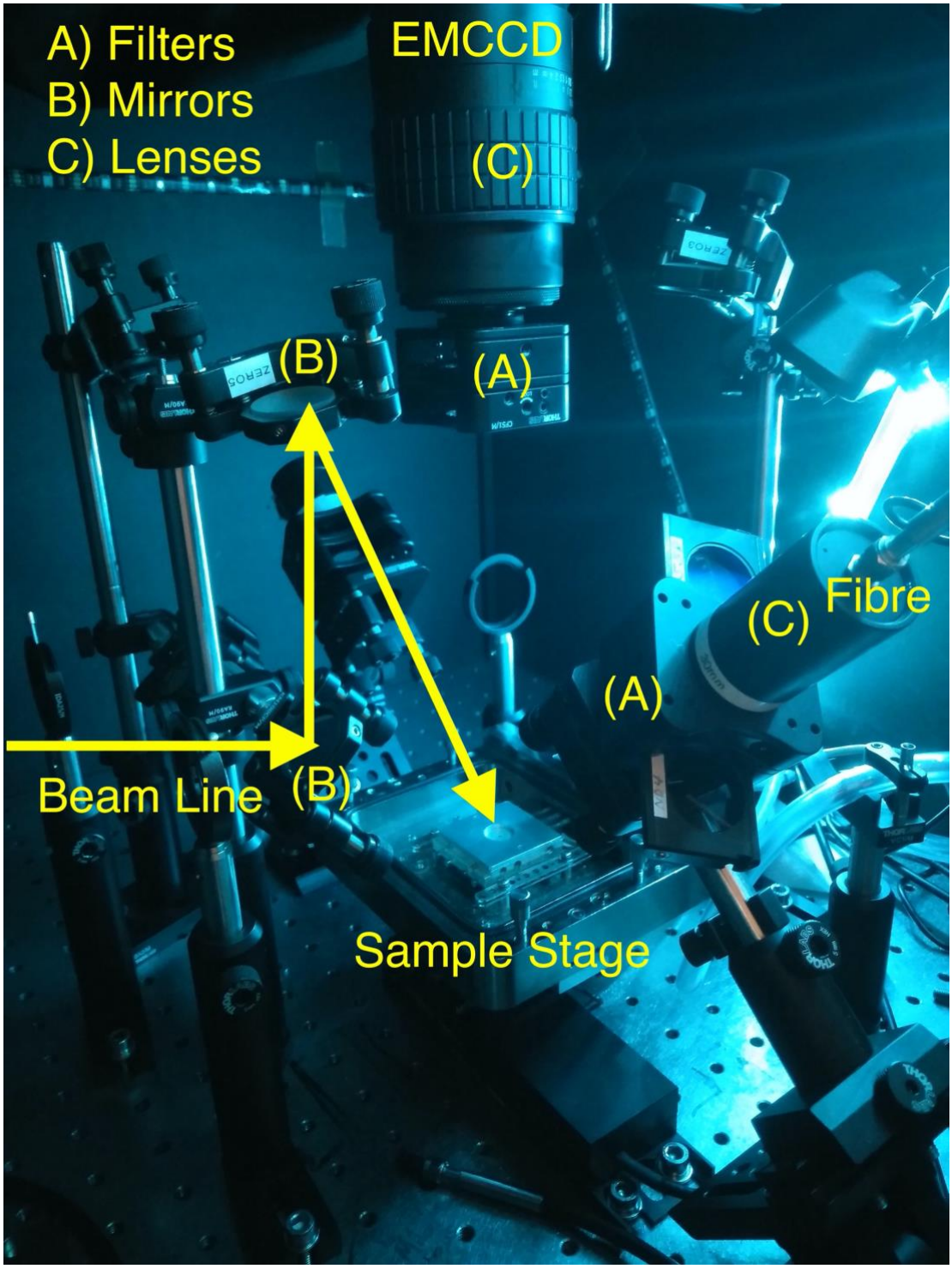

Figure 11: Annotated photograph of the optical layout inside the current Dual-Wavelength System chamber, including delivering excitation to the sample, EMCCD setup, spectrometer fibre setup, and detection filtering.

2.1.1. Excitation sources

2.1.1.1. Introduction

The Dual-Wavelength System uses two optical parametric oscillators (OPOs) to provide excitation light. OPOs use a nonlinear crystal to split the photon energy of an incoming beam into two, with the ratio of the split dependent on the angle of the crystal (a formal description

can be found in (Yariv and Louisell, 1966)). These lasers are independently tuneable from 200 nm to 2500 nm. Some details are provided below:

Manufacturer: Opotek, USA
Model: Radiant 355 HE UV
OPO wavelength ranges: 210-255 nm ("HUV"); 255-410 nm ("UV"); 410-710 nm ("Signal"); 710-2500 nm ("Idler")
Pulse frequency: 10 Hz
Pulse duration: 7 ns
Pulse trigger: Q-switch
Pulse peak energy: 50-70 mJ at 450 nm

The lasers are pumped by 1064 nm Nd:YAG pump lasers of approximately 100 mJ pulse peak energy. The 1064 emission is passed through two doubling crystals, to get 532 and then 355 nm output. The 355 nm emission is passed through the OPO crystal, a birefringent non-linear crystal that splits the incoming photons into two separate photons of differing polarisations. By convention, the light polarised in the same direction as the 355 nm light is called the signal, and the light polarised at right angles is called the idler. OPO ranges "UV" (ultraviolet) and "HUV" (high ultraviolet) are both in the ultraviolet, but are acquired by different processes. To acquire the 255-410 nm "UV" wavelength range, signal photons are mixed within a non-linear crystal with residual 532 nm output from the Nd:YAG pump. To acquire the 210-255 nm "HUV" wavelength range, signal photons are passed through a doubling crystal (Figure 12).

Block diagram of the Opotek Radiant 355 Optical Parametric Oscillator

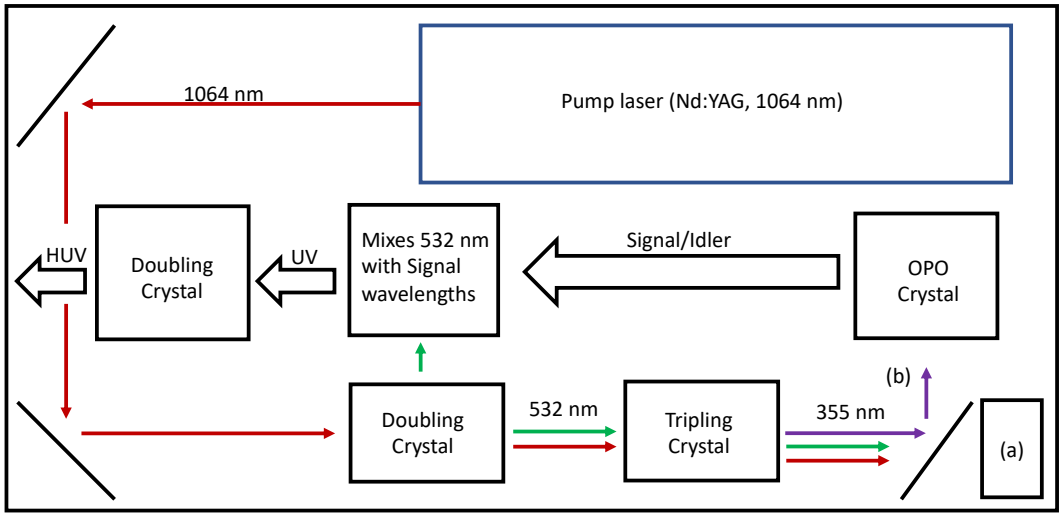

(a) spectrometer; (b) dichroic filter

Figure 12: Diagram of the Radiant 355 HE UV laser system and how it creates signal (410-710 nm) idler (710-2500 nm) UV (255-410 nm) and HUV (210-255 nm) wavelengths.

The Nd:YAG pump laser is excited by a flashlamp/Q-switch arrangement. A flashlamp is first triggered, exciting the laser cavity. This excitation slowly decays over a number of milliseconds. A Q-switch triggers the cavity to release its energy in a 7 ns pulse. The minimum

externally triggered safe delay of the lasers between the flashlamp trigger and the Q-switch trigger is 320 μs for one laser and 323 μs for the other. The delay can be greater values, though due to the decay in the cavity this will result in smaller pulse energies.

2.1.1.1. List of System Elements

The following elements are in the beam path between laser output and the sample, with relative positions shown in Figure 9:
1) Mirror. This element only occurs for one laser, due to table size constraints.
2) 715 nm longpass/shortpass filters. These are in place when the idler/signal frequencies respectively are used in order to filter out unwanted wavelengths from the laser.
3) Rotating polariser. This polariser rotates to let through more or less of the full beam to control the pulse energy.
4) Clean-up polariser. This polariser cleans up any stray light of changed polarisation, and helps to minimise signal/idler leaked wavelengths. Its position can be changed depending on whether the signal or idler light is being used.
5) Power meter. This is only flipped into place when an energy measurement is needed.
6) Two mirrors. These raise the beam then target it to the sample position.

Outside of the beam path, the following elements are used:
1) Signal generator to synchronise the pulses of the two lasers. This involves four cables of paired lengths to transmit the signal pulses.

2.1.1.2. Purity of Frequency

There are some potential wavelength 'leaks' from the laser due to the processes involved in the creation of the output wavelength. Formation of most of the UV wavelengths can be prevented by removing the UV mixing crystal. When exciting in the NIR (idler frequencies), this leaves the following potential 'noise' wavelengths:
-The Idler frequency's corresponding signal frequency (3.49 eV-idler energy = signal energy). This is minimised by the clean-up polariser shown in Figure 9, but may still be present.
-The 355 nm OPO pump wavelength.
-The 532 nm doubled Nd:YAG pump wavelength.
-The 1064 nm initial Nd:YAG pump wavelength.

Two 715 nm longpass filters are placed at the laser's input port to the chamber, which filter out the signal wavelength, the 355 nm OPO pump wavelength, and the 532 nm wavelength. With the filters in place, no leaked signal is seen at the sample area. When using the signal part of the spectrum, the longpass filters are replaced with two 715 nm short pass filters, which likewise prevent leaked idler frequencies reaching the sample area. Tests indicated that with these filters in place the pump wavelengths were not detected in the final wavelength output using the EMCCD with a rough aluminium plate at the sample position to scatter the incoming light. This also indicates that if fluorescence excited by these pump wavelengths is present, it will also not interfere with measurements as fluorescence excited by these wavelengths would be less bright than the signals themselves.

2.1.1.3. Pulse Synchronisation

In order for two-photon excited state absorption upconversion to occur, the second photon must be absorbed before the electron or hole at the first excited state can decay. In the simplest case, this requires both photons to reach the target material at near the same time. For our excitation pulses, the flash lamp and Q-switch of each laser is externally triggered by a Standford Research Systems DG645 Digital Delay Generator. This pulse generator can provide high-accuracy pulses of different widths, times, shapes, and voltages. For use with the OPO, narrow-width, square pulses of less than 5 V are used.

Initial experiments are conducted with the pulses fully synchronised with one another: the apparatus is physically positioned on the optical table to assist the ease with which the OPOs are placed on the bench so that the path length of each pulse from the laser output to the sample position is approximately the same, ensuring that pulses triggered at the same time will arrive at approximately the same time at the sample. The flashlamps of both lasers are triggered by the same pulse, travelling to the flashlamp trigger input ports by BNC cables of the same length. The Q-switch for each laser is triggered separately. While delays between the flashlamp and the Q-switch that are longer than the optimum delay can change the power of the laser output and affect stability, the small changes to the delay needed to synchronise the pulses (~ 10 μs) in this case do not affect the beam more than the normal pulse-to-pulse energy stability.

To synchronise the arrival time of the two laser pulses at the sample position, two identical fast photodiodes are pointed at the sample position, with different filters in front of each. The lasers are tuned to different wavelengths, selected so that each filter blocks one wavelength. The output of the photodiodes are analysed by an oscilloscope. The Q-switch delay for one laser is adjusted until the signal response peaks overlap. At this point, as the photodiodes are approximately the same distance from the sample position as each other, and the cables used to take the responses to the oscilloscope are of the same length, the two pulses should be synchronised. As the pulses are 7 ns in length, errors in the path length from the OPO output to the photodetectors would have to be greater than 2.1 m for the pulses to not overlap. The error in path position is in fact approximately 10 cm, giving an error of less than 5 %.

2.1.1.4. Pulse Energy

Pulse energy varies from pulse to pulse; in general the pulse-to-pulse stability is around 20%. Upconversion processes increase in photon production efficiency non-linearly, and so pulse variability needs to be taken into account when undertaking measurements, and any power-dependent measurements need to include enough pulses to give a stable average power. This may mean averaging over many seconds worth of data for time resolved and varying power measurements. For initial scans, the laser power will be set high enough that any variance in pulse energy will not affect detection of an emission from the sample, and so only a small number of pulses will be needed for each measurement.

To enable control of the power incident on the sample, polarising crystals are placed between the laser and the sample. Pulses come out of the laser polarised: the signal wavelengths in one plane, and the idler wavelengths at ninety degrees to the signal. By rotating the polarising crystal, more or less light proportionally hits the sample. While initial scans do not change the

polariser while scanning, the power of the OPOs is wavelength dependent (Figure 13) and this functionalisation will be useful for future excitation scans.

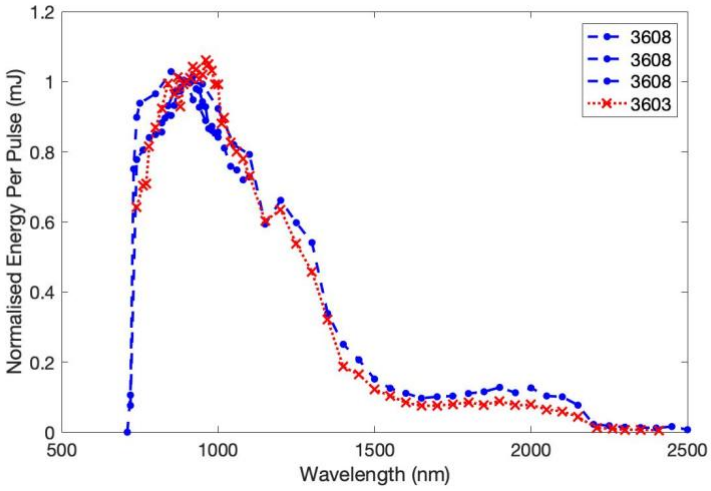

Figure 13: Graph of normalised pulse energy vs wavelength for idler frequencies. Blue circles indicate data from laser one (serial number 3603), and red crosses indicate data from laser two (serial number 3608). The total energy for each wavelength can change over time due to flashlamp wear and replacement, but the relative energy between different wavelengths of a given OPO will remain the same.

When the laser is turned on, it emits heat that has an effect on the efficiency of the laser crystal. Because of this the laser is subject to optical power 'drift', especially when the laser has just been turned on. Allowing the laser to reach thermal equilibrium before doing measurements is essential for reasons of pulse power and pulse stability. However, even after more than two hours the power is not stable. Figure 14 shows the power drift after an hour of stabilising time; this power change will not unduly influence short scans, but for longer ones it may have an effect on results, particularly for photon production efficiency quantification.

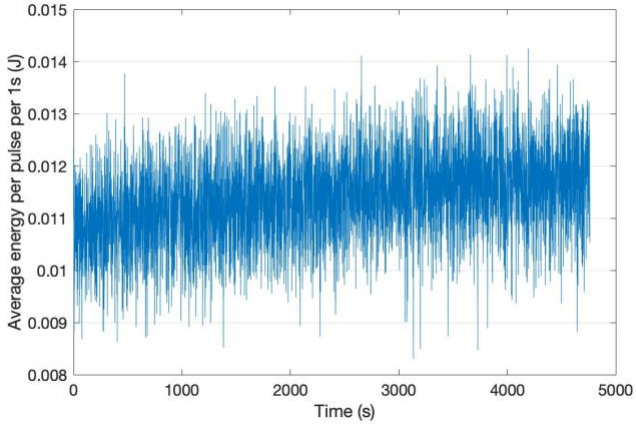

Figure 14: Graph of pulse energy of an OPO laser vs time with t=0 after an hour of stabilisation time. A drift in energy is still seen up to 2500 s, implying that approximately one hour 40 minutes is needed for stabilisation of laser beam energy.

Due to small temperature differences within the pump laser and the laser path, the optimum angle for the doubling crystals to be in order to acquire the most power out of the laser changes slightly from day to day. The laser software comes with a harmonic optimisation option, which changes the angle of the crystals in order to produce the most power. In theory this peak power should be the same every time, but changes in room temperature, humidity, and cavity temperature produce differences in this peak power. When turned on, the laser has a heating and cooling function to keep the crystals at their optimal temperature. When turned off, the laser cools and can undergo changes in cavity length and condensation. To minimise this, the temperature control of the laser is kept on as much as possible.

For measurements in which we need to know the pulse energy of the lasers, in each laser path is a flip mount with a 20 mm Thorlabs ES220C pyroelectric energy meter (www.thorlabs.com), which can automatically take an energy reading before each measurement. However, dual wavelength experiments in this thesis have been made as qualitative "survey" explorations, being in almost all cases the first ever made, and do not take pulse energy into account but are instead concentrated on "yes/no" discovery of new fluorescence emissions.

2.1.2. Detection of upconversion emission

2.1.2.1. Introduction

The Dual-Wavelength System has three main devices for looking at the upconversion emission. One is an electron multiplied CCD (EMCCD): a CCD that amplifies the signal it observes using electron cascade techniques, enabling low-emission detection. The other two are spectrometers, which enables spectral information to be obtained for brighter emissions. The specifications of the devices are detailed in Table 2:

Specifications of Dual-Wavelength System detection devices						
Device	**EMCCD**		**Visible Spectrometer**		**Near-infrared Spectrometer**	
Part	EMCCD	Camera Lens	Spectrograph	CCD	Spectrograph	CCD
Manufacturer	Princeton Instruments	Coastal Optics	Princeton Instruments (USA)		Princeton Instruments (USA)	
Model	ProEm 1024BX3	60 mm UV-VIS-IR APO Macro Lens	Acton SpectraPro SP-2300	PIXIS 100	Acton SpectraPro HRS-300	PyLoN-IR
Wavelength range	200-1100 nm	310-1100 nm	0-1400 nm	300-1000 nm	700-2500 nm	800-1700 nm
Pixel size	13 x 13 µm			20 x 20 µm		25 x 500 µm
Pixel array	1024 x 1024			1340 x 100		1024 x 1
Operational temperature	-70°C			-80°C		-100°C

Table 2: Table of specifications for the three detection devices used in the Dual-Wavelength System: the EMCCD, the visible spectrometer, and the near-infrared spectrometer.

2.1.2.2. EMCCD

The EMCCD is positioned vertically above the sample, focused onto the centre of the sample stage by the Coastal Optics camera lens. Light from the sample passes one of a selection of short pass filters, enabling the scattered excitation light to be excluded from detection in order to only observe the higher-energy upconverted emission. Passing into the EMCCD, the upconversion fluorescence emission hits an array of pixels. Each pixel output is individually electron multiplied, and then the ensemble is output as an enhanced image (Figure 15).

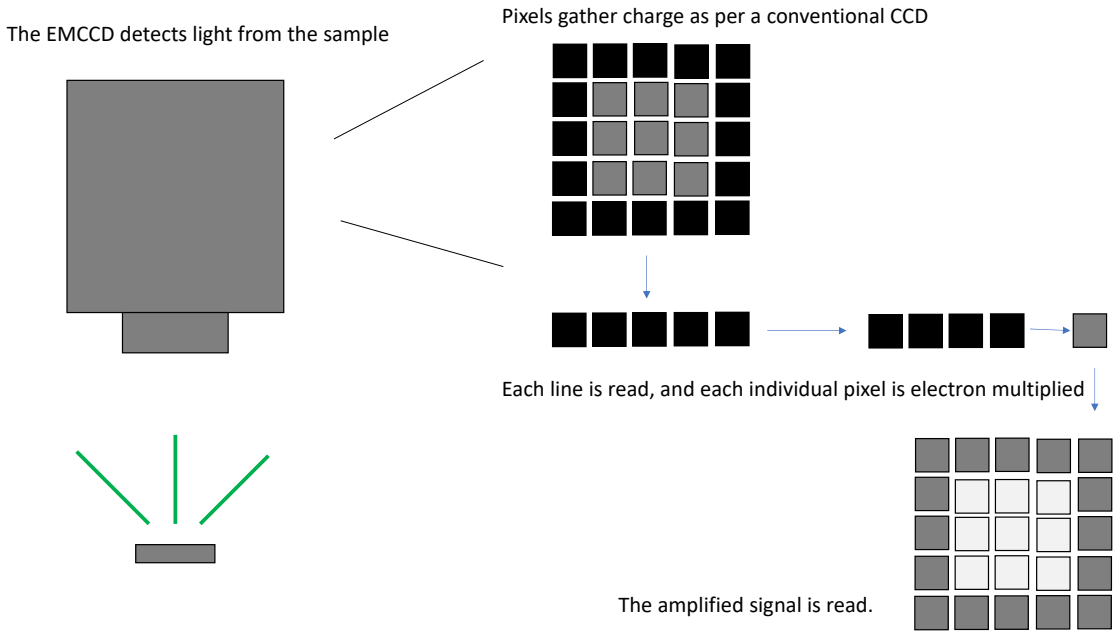

Figure 15: Diagram of EMCCD functionality, showing how pixels are charged before electron multiplication.

The EMCCD collects emission as per a normal CCD before electron multiplication. This limits the total number of counts the EMCCD can detect to below the damage threshold of the EMCCD, unlike in other electron multiplied detection systems such as photomultipliers. This gives the EMCCD a very large dynamic range, able to deal with room light illumination with electron multiplied gain set to zero, and near photon counting ranges with the electron multiplied gain set to maximum. To make use of this feature, we need to carefully select the right EMCCD gain for each sample. Samples with very bright signals will saturate the EMCCD at gain levels needed to detect samples with very dim signals. Due to different fluorescence efficiencies, two fluorescence peaks in the same sample may not be seen with the same settings. Certain settings such as the detection time will stay the same for each 3D scan, but the amount of electron multiplication (the gain) can be programmed by the Resonate Systems Labview code to change depending on the light levels seen. The new gain settings are recorded and the output normalised by this gain in the data processing stage.

2.1.2.3. Spectrometers

Emission light is transmitted to each spectrometer via a separate bundle of nineteen 200 μm diameter fused silica optical fibres arranged in a circular pattern and having a total bundle entrance diameter of about 1 mm. A short pass filter is placed before the bundle. At the

spectrograph, the nineteen fibres are arranged in a linear pattern 3-4 mm in length to physically approximately match the input slit. The light from the fibre bundle is passed through the monochromator slit, and down the monochromator grating path that changes the emission path dependent on its wavelength. The emission is passed through a slit onto the EMCCD, and the position on the EMCCD the light falls onto corresponds to the wavelength of light (Figure 16). Due to the lack of electron multiplication by the detector chip and the dispersion of the light across gratings, the spectrometers cannot detect very dim sources. However, detection levels can be enhanced by long integration times and summing or averaging over a number of measurements.

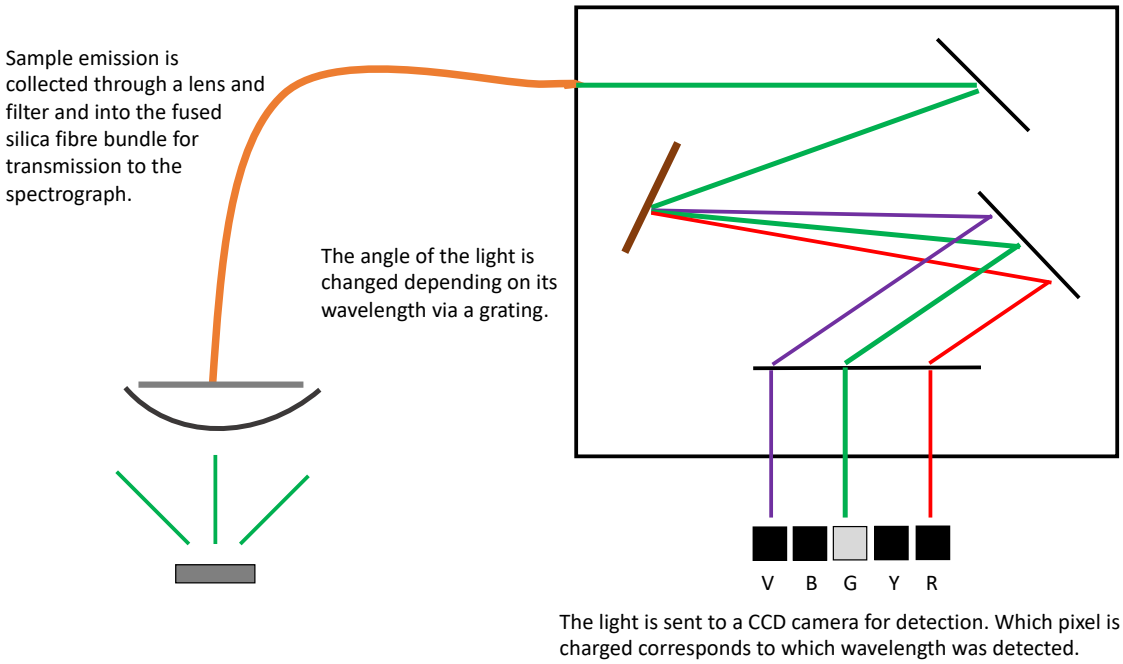

Figure 16: Diagram of spectrometer functionality, showing beam path through the spectrograph.

2.1.2.4. Filters

A range of filters, both long-pass and short-pass have been analysed using a Cary Spectrophotometer in order to observe filter behaviour over the entire operating range of the Dual-Wavelength System. This filter data, collected by Georgios Tsiminis, Jillian Moffatt, Thomas de Prinse, and Thomas Payten is available through an app created by Georgios Tsiminis at the following address: <https://upconversion.shinyapps.io/uc_filters/>. The main filters used in this thesis are Semrock 700 nm short-pass filters for the detectors <www.semrock.com> and Thorlabs 715 nm long-pass filters <www.thorlabs.com> for the excitation sources.

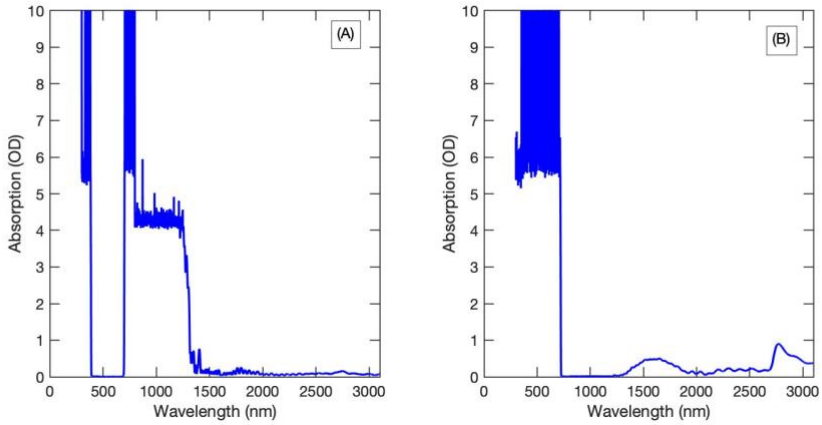

Figure 17: Filter optical densities for A) 700 nm short-pass and B) 715 long-pass filters used in most experiments on the Dual-Wavelength System. Measurements were conducted on a Cary Spectrophotometer by Thomas de Prinse. Filters have a specific operational range, as seen in (A) by the sudden increase in absorption at 400 nm and the step decreases near 900 nm and 1400 nm. The spectrophotometer is unable to measure absorption greater than OD 6, but we can tell from these measurements that the optical density in the operational range does not decrease beyond 5.5.

Figure 17 shows the Cary Spectrophotometer data for a 700 nm short-pass filter and a 715 nm long-pass filter used in two-wavelength excitation experiments in this thesis. When exciting from 750-1500 nm, the 700 nm short-pass filters are placed on the detectors and the 715 nm long-pass filters are placed in the OPO beamline in order to prevent 'signal' leakage interfering with experiments. Two filters are stacked in each case, and all four filters of each type show near-identical absorption data.

2.1.2.5. Noise and spurious signal: low level

The main types of low-level noise and spurious signal found in our experiments are discussed below:

- Thermal detector background: This is the random background output of the detector which cannot be changed in a detector with a single operating temperature. Increasing the integration time of a measurement increases this background, but lowers the relative error, 'flattening' the background and allowing for better subtraction.
- Ambient light sources: This is the spurious signal coming from room lights, indicator lights, and other light sources within the lab. This interference can be reduced by turning off unnecessary lights, and ensuring the sample chamber is light proof.
- Equipment readout noise: This is electronic noise added to the data as the signal is read from the detector. This can be reduced by increasing integration times (lowering the readout speed of the detector). Another technique that can be used by the EMCCD is hardware pixel binning. In this technique, instead of each pixel being read by itself, it is read at the same time as a set number of its neighbours. This decreases overall noise, though decreases picture or wavelength resolution at the same time.

2.1.2.6. Spurious signal: high level

High level signal interference, or spurious signal that is near the same magnitude as bright signal emissions, comes from two different sources--scatter from excitation light, and cosmic rays.

Scattered excitation light: Under most circumstances in the Dual-Wavelength System setup, scattered excitation light is suppressed to background levels by short-pass filters for upconversion measurements, or long-pass filters for Stokes luminescence measurements. However, if the filter is not as efficient at the excitation wavelength being used, or the sample is an efficient scatterer, then to the EMCCD the sample will appear bright, similar to if it is emitting luminescence.

In order to distinguish between emission and scatter while testing the system, a scatterer was placed partially over the sample. When scattered light is seen, both the sample and the scatterer light up, while when there is only emission, the scatterer remains dark (Figure 18). When there is both scattered light and emission the scattered light may be subtracted by calibrating the beam profiles of the excitation sources to the signal from the scatterer, and subtracting this from the sample section. This is a complex process and introduces more uncertainties in the data, so it is best to first review the filters being used to exclude noise for maximised signal/noise. Tests have shown that for the initial sequences, the filters used are adequate to prevent scattered light being detected by the EMCCD. For the spectrometer, unless the scattered light is bright enough to produce saturation effects, scattered light will only effect measurements at the laser wavelength or half, a quarter, etc. of its photon energy.

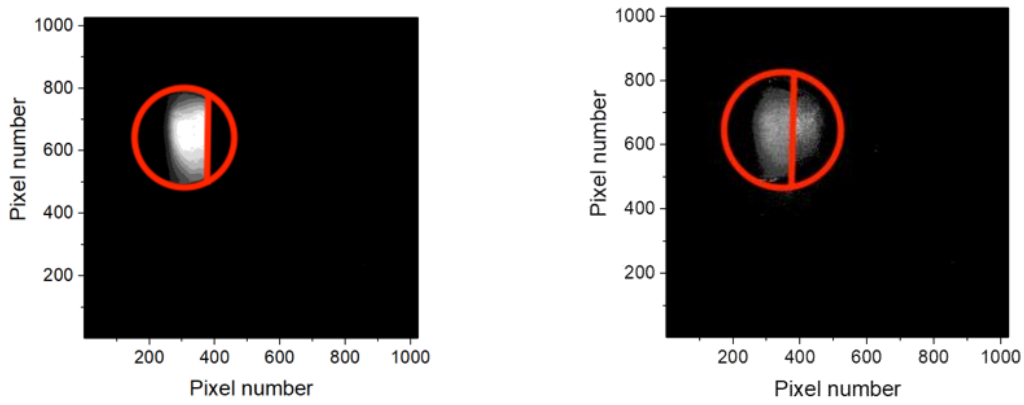

Figure 18: Emission from the sample (left), and scattered light from both the sample and the scatterer (right). The red circle depicts the edge of the disk, and the red line depicts the edge of the scatterer.

Cosmic rays: Cosmic ray hits are an independent source of signal interference. When a cosmic ray hits the EMCCD or spectrometer CCD directly, it causes high-to-saturated signal output in a small number of pixels (Figure 19). While the pixels impacted by the cosmic ray hit are small, the high counts can affect total count analysis in dim samples for EMCCD data and produce anomalous spikes in spectrometer data. Cosmic rays can be identified when preprocessing data due to the small number of pixels they influence, but methods to reduce their effect are helpful as they can lower preprocessing time. Cosmic ray hits to our CCDs are relatively low (around 115 counts per hour), so averaging over multiple measurements

reduces the effect of cosmic rays. Pixel binning has the same effect, as the counts are spread out over a larger area. Averaging in general is more useful for negating and identifying false positives potentially generated by cosmic rays, especially when the expected emission is low, as it lowers the peak pixel count while still 'quarantining' the effect of the cosmic ray within a small number of pixels. An inbuilt cosmic ray removal algorithm was provided with the spectrometer output software, but this was not used in measurements reported in this thesis as it is possible that bright, sharp signals such as from rare earths may be altered by this algorithm.

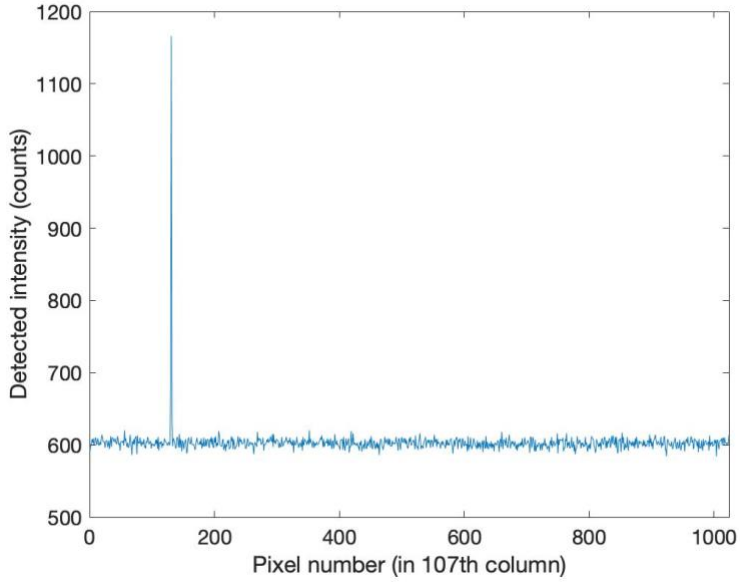

Figure 19: Pixel output from one column of the EMCCD output when detecting in darkness. A cosmic ray 'spike' affecting one pixel can be seen.

2.1.2.7. Saturation effects

In CCD measurements, saturation has a number of negative effects. In the long-term it can degrade the pixels being saturated. When taking a measurement, information about the magnitude of the signal is lost. Spatial resolution can also be reduced. Saturation in one pixel can 'bloom' into a neighbouring pixel, which can bloom into the next, causing a smeared gradient effect. On the EMCCD, this appears as streaks on the image. On the spectrometer, it can appear as a saw-tooth or plateau-like appearance on the spectrum (
Figure 20).

Since some signals will likely be bright and others dim, finding a balance beforehand between saturation and not being able to detect the signal can be difficult. In order to keep most variables the same, while doing EMCCD measurements within a DW scan integration time, analogue gain, and hardware binning settings are kept the same, but the EM gain can be changed if needed in order to avoid saturation and enhance dim signals. Changing just this one variable allows inter-comparison of EMCCD measurements of the same sample.

Spectrometer:
Unsaturated scattered laser light (left), saturated signal (middle) and highly saturated signal (right)

EMCCD:
Highly saturated signal from one pixel (top), unsaturated signal (left) and saturated signal (right). The circle represents the spot size of the excitation.

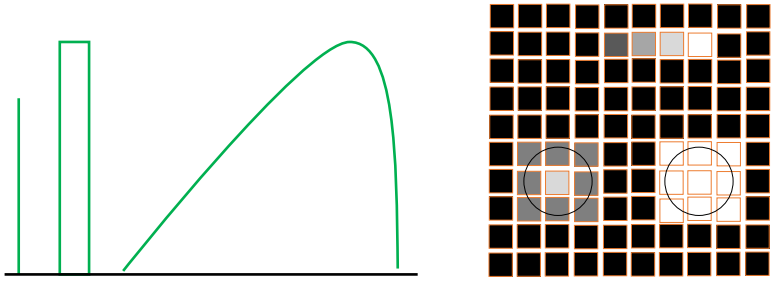

Figure 20: Diagram of the shape of saturation effects seen in the spectrometer and EMCCD data.

2.1.2.8. EMCCD Characterisation

Using a "beta" light, a steady light source comprising tritium-doped scintillator plastic with drift in photon count measured in months or years (see Figure 21 for emission spectrum), EMCCD settings were changed and the change in detection count measured. The following results are for Gain settings, Exposure Time, and Lens Aperture.

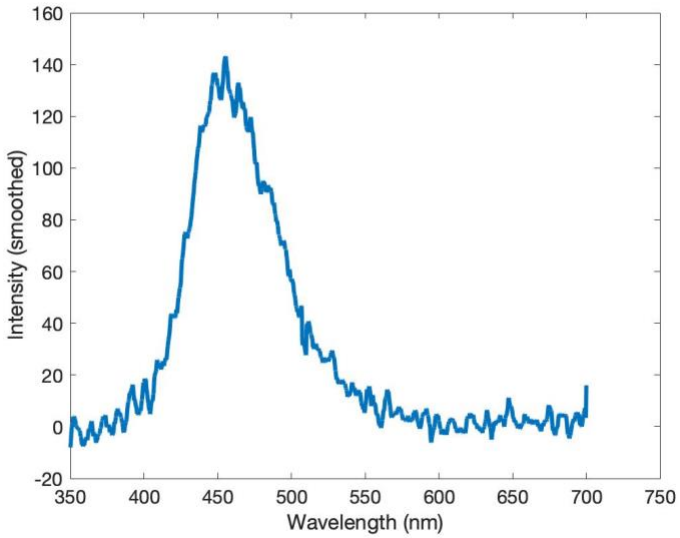

Figure 21: Emission spectrum of the "beta light" used to calibrate EMCCD settings. The emission peaks around 460 nm. Data is smoothed to remove cosmic ray hits.

Gain Settings: Changing the electron-multiplying (EM) gain gave linear increases in detection output, with the analogue gain changing the slope of the increase. Plots of detection counts and linear fits to the EM gain variations are below in Figure 22 and Table 3 respectively.

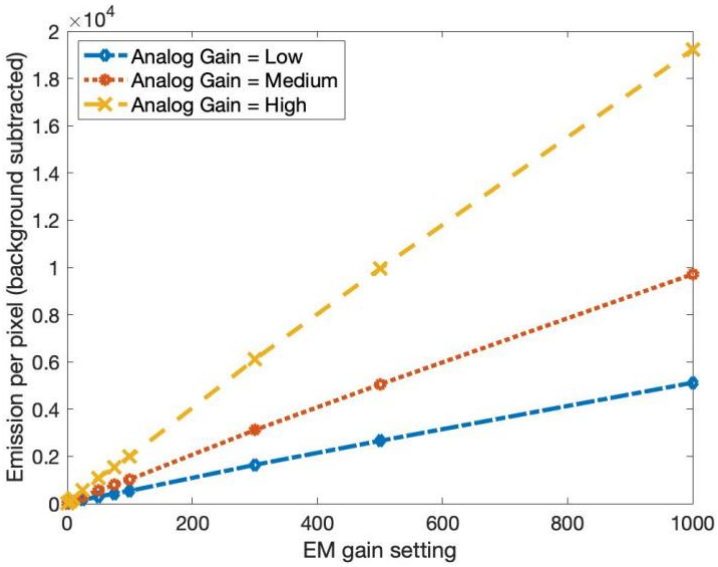

Figure 22: The impact of different gain settings on the EMCCD to the total detected count output using the beta light with no filters.

Analogue Gain	**Linear Fit to the Data**			
Low	y=	5.1	*x +	32.3
Medium	y=	9.7	*x +	62.0
High	y=	19.3	*x +	96.0

Table 3: Linear fits to the different gain setting outputs on the EMCCD, seen in Figure 22.

Exposure Time: As expected, the relationship between exposure and detected counts is linear. Different gains change the offset of the slope—the 'zero' count increases with increased gain. From Figure 23 and Figure 24 we can see that the relationship remains linear both at low counts and at high counts until saturation at 65,000 counts per pixel.

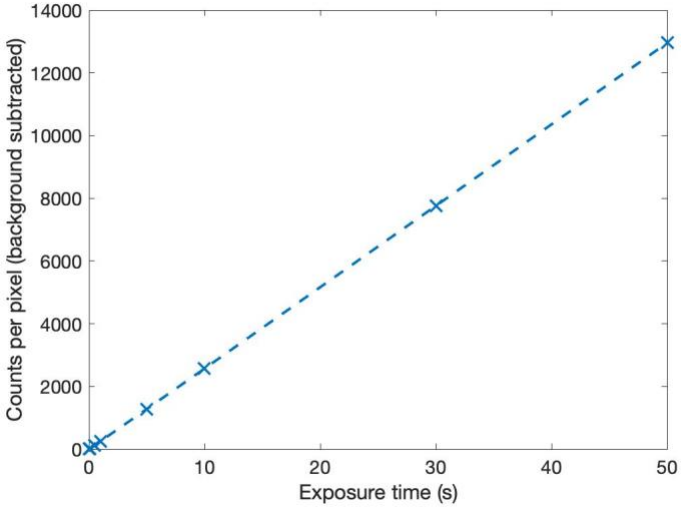

Figure 23: Detected emission vs exposure on the EMCCD using a gain of 1. The exposure increases the detected counts per pixel linearly at low gains.

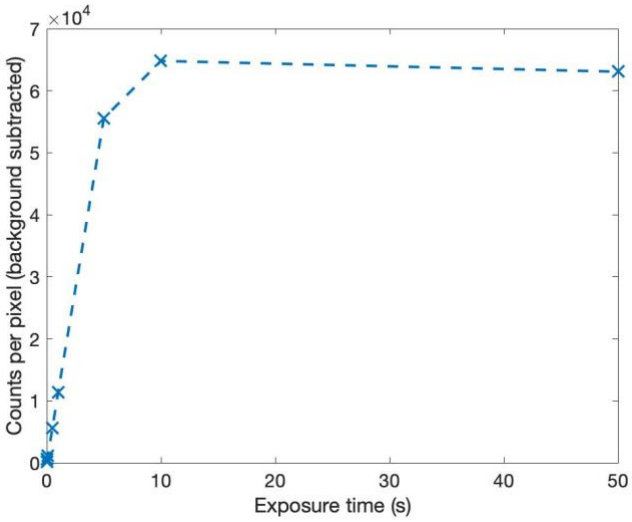

Figure 24: Detected emission vs exposure time for the EMCCD output using a gain of 50. The exposure increases the detected counts per pixel linearly until pixel saturation at around 65,000 counts.

Lens Aperture: The lens has an aperture that can be changed from F/45 to F/4. Each aperture position is designed to let in half the amount of light as the one before it when the light source is a certain distance away. For our sample setup, fitting a power equation to the result gives us a power dependence of -1.5 (Figure 25).

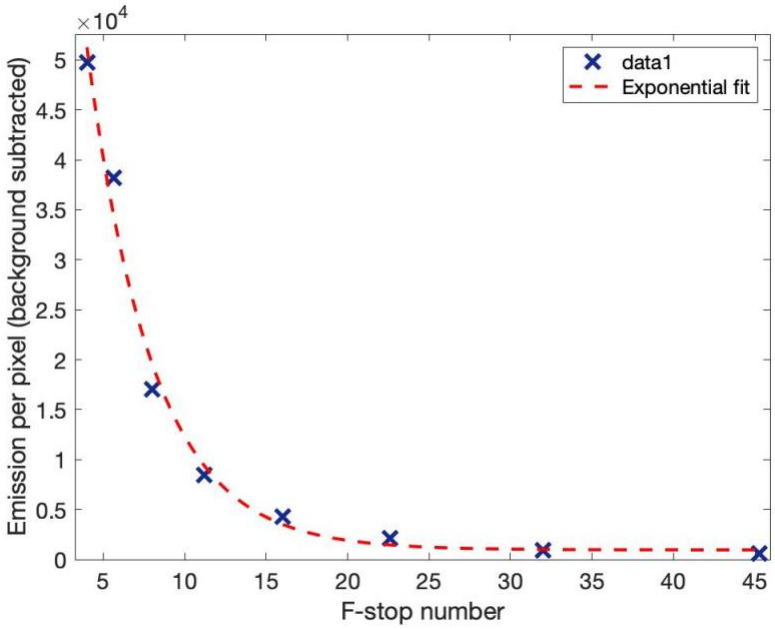

Figure 25: The emission per pixel of the EMCCD using different lens aperture positions.

2.1.2.9. Calculated total efficiency

The absolute efficiency of the detection setup can be estimated by calculating the proportion of light that will hit the detector. The efficiency of the detection setup depends on the following:

- *Detector position:* this determines the total number of photons incident on the detector optics, by both distance (changes the solid angle incident on the detector), and by detector angle incident to the emitting surface (as the emitter is not a point source, the emission follows Lambert's Cosine Law). All samples are approximately of a similar size, so this measurement should be similar for all samples.
- *Lens transmission (for the EMCCD) and filter transmission losses:* Lenses and filters have a certain transmission loss per wavelength. Filter losses have been measured as in Figure 17.
- *Fibre transmission losses (for the spectrometers).*
- *Slit losses (for the spectrometers):* Not all light from the fibres travel through the slit. The loss is minimised by careful alignment of the fibres to the slit.
- *Grating losses (for the spectrometers):* Each grating in the spectrograph (see Figure 16) has a particular loss.
- *CCD quantum efficiencies:* These are different for each CCD used.

Product specifications give the transmission efficiency of all mirrors, lenses, filters, and gratings that are in the fluorescence path, and the quantum efficiency of the detectors. However, the quantum efficiencies are usually measured at room temperature rather than operating temperature by the product suppliers, and so given values are an overestimation of values in experiment. Additionally, all optical elements degrade over time. It is also difficult to estimate losses through the monochromator slit of the spectrometers. An experimental method of determining absolute efficiency of the setup is therefore useful, both for initial measurements and for later measurements to record the degradation of the components over time.

Blackbody emission was chosen as a good approximation to fluorescence from the sample. Blackbody emission from a point source is isotropic, like fluorescence, and an emitting surface follows Lambertian geometry. A blackbody emitter the same shape as a fluorescing emitter should follow the same geometry. This estimation fails when the excitation energy—heat for the blackbody and light for the fluorescer, is not distributed in the same way for each. Heat in the blackbody experiment is expected to be evenly distributed across the sample. Excitation in the fluorescence measurements in this thesis is from a Gaussian profile beam. As the beam diameter is large (approximately the size of the sample), this is not expected to change the outcome significantly, and the blackbody experiment is still considered a good estimation of the detection setup behaviour.

A 11 mm x 12 mm piece of pressed graphite was placed on the sample stage and heated to 350 °C, 400 °C, and 450 °C using the Instek sample stage (see next section). Graphite does not have strong molecular absorption peaks over the visible and near-infrared, and so its thermal emission output can be approximated by a blackbody. The blackbody radiation emission of a sample can be determined by Planck's thermal radiation law:

$$I(T,\lambda) = \frac{2\pi hc^2\lambda^{-5}}{e^{hc/\lambda kT} - 1}$$

Where I is the energy over a hemisphere per area of emitting body, h is Planck's constant, k is Boltzmann's constant, c is the speed of light, λ is the wavelength of light, and T is the temperature. For a physical sample, we add:

$$Ph(T,\lambda) = \frac{2\pi hc^2\lambda^{-5}}{e^{hc/\lambda kT} - 1}\epsilon A\frac{\lambda}{hc}\Delta\lambda$$

Where Ph is now the number of photons per wavelength range Δλ emitted from the sample, ϵ is the emissivity of the sample (for pressed graphite, 0.98), A is the surface area of the sample. This gives the number of photons in a hemisphere for each wavelength—i.e. the number of photons available to be seen by the detectors. This experiment gives us a value of emission detected vs emission produced without filters, but with the sample stage spectral window. The spectral window transmission is very high (near 100%) for the ranges observed here, so is not taken into account. The graphite sample is approximately the same shape as the samples used in this thesis, so the Lambertian shape of the emission does not need to be taken into account. The code used for the following results is given in appendix A1.

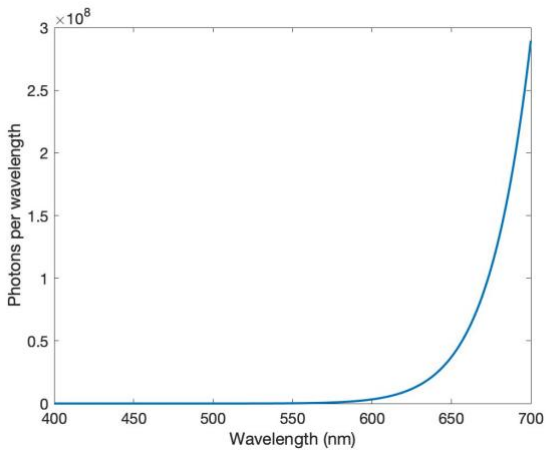

Figure 26: Calculations showing expected photons per wavelength from blackbody radiation from a 11 mm x 12 mm diameter piece of graphite. The temperature was taken to be 400°C.

In Figure 26, we see that at 400 °C, even though the blackbody radiation peaks far later, there are significant photons in the visible and near-infrared range. This allows blackbody radiation to be used as an efficiency calculator for all detectors while using the sample stage for heating. While the sample stage can heat up to 600 °C, going beyond 450 °C will need vacuum capabilities to prevent oxygen from degrading heating stage components, while from 200°C to 450 °C only a nitrogen gas purge is needed.

Spectrometer measurements were conducted with no filters, in order to find the efficiency of the spectrometers for different wavelengths. Δλ was taken to be the bin size of the spectrometer output. The EMCCD had two 745 SP filters in place. Gain settings were at 1, and the iris was set at maximum.

Figure 27 shows that the detected emission did not follow a black body curve for all wavelengths, and so analysis was done with the ranges 400-930 nm for the visible spectrometer emission and 850-1150 nm for infrared spectrometer emission.

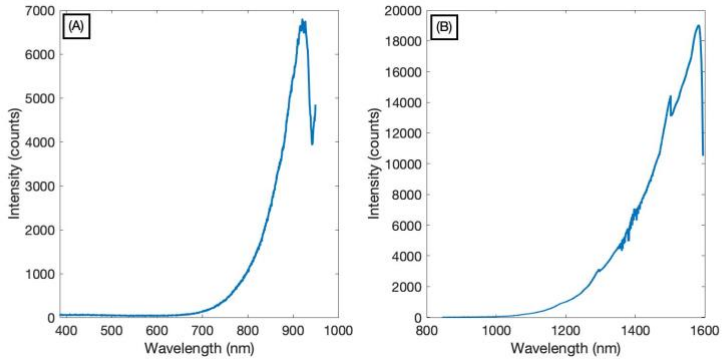

Figure 27: Experimental results showing emission from graphite at 45°C, using A) the visible spectrometer, and B) the infrared spectrometer.

Figure 28 shows the ratio of detected counts vs calculated emission at 450 °C for the infrared spectrometer. The lower counts at shorter wavelengths is responsible for the large scatter (that can lead to negative count numbers in background subtracted counts) at these

wavelengths, but the average ratio remains approximately 1-2 x 10^{-9} throughout the range observed. By contrast the ratio in Figure 29 showing results from the visible spectrometer trend down, indicating a decrease in sensitivity at longer wavelengths. The visible spectrometer results indicate much larger sensitivities overall however, which is expected from the specifications of each system.

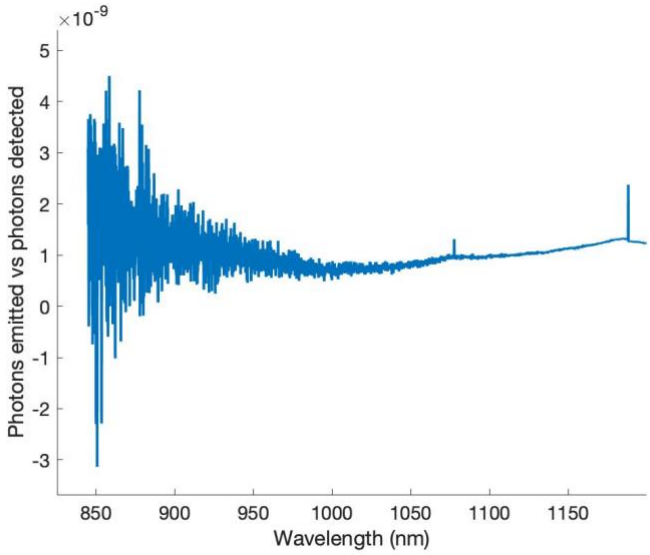

Figure 28: Ratio of detected counts on the infrared spectrometer vs calculated blackbody emission of graphite at 450°C. Negative numbers are due to low count rates at 850-900 nm allowing negative numbers after background subtraction because of scatter in the data.

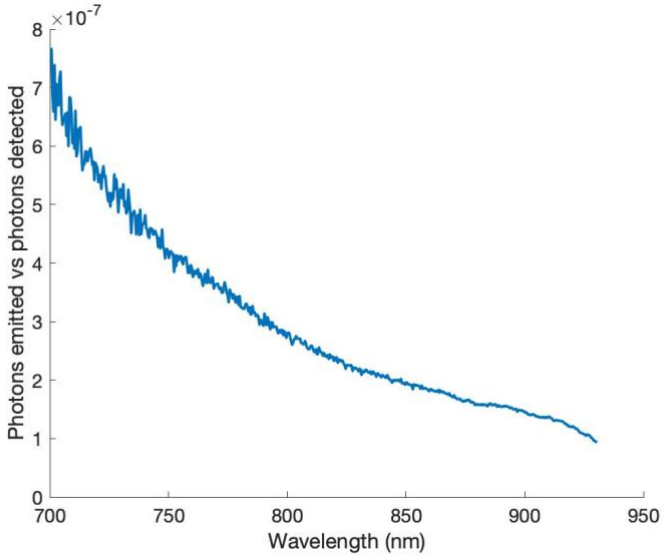

Figure 29: Ratio of detected counts on the visible spectrometer vs calculated blackbody emission of graphite at 450°C.

To check on the validity of the experiment, the experiments were repeated at 400 °C and 350 °C. In an ideal system the ratios would remain the same. For both the visible and the infrared spectrometers the ratios trended lower with lowered temperature—indicating that for lower

intensity emissions more photons must be present for a count to be detected. This may be due to nonlinearities in the system, or slight errors in background subtraction. At 350 °C very little emission is seen, so a small background error could lead to a large change in ratio.

For EMCCD data, the total photon counts over the range 400 nm to 745 nm was counted and compared to total emission over the area of the sample. The same area was integrated for each temperature. Each temperature gave a counts seen vs calculated emission ratio of around the same order of magnitude, as given in Table 4. This is equivalent to approximately one photon counted for every $5x10^4$ photons emitted.

Temperature (°C)	Detected counts	Calculated photons	Ratio
450	$2.3 \pm 0.002 \times 10^6$	$5.9 \pm 0.5 \times 10^{10}$	$3.9 \pm 0.3 \times 10^{-5}$
400	$2.1 \pm 0.005 \times 10^5$	$7.5 \pm 0.7 \times 10^9$	$2.8 \pm 0.3 \times 10^{-5}$
350	$2.1 \pm 0.01 \times 10^4$	$6.8 \pm 0.7 \times 10^8$	$3.1 \pm 0.3 \times 10^{-5}$

Table 4: EMCCD total detected blackbody radiation counts between 400-745 nm and calculated emission for each of the three temperatures used.

As expected from specifications, the EMCCD is the most sensitive detector in the system. The visible spectrometer is the next most sensitive, needing approximately an order of magnitude more photons to detect a signal. The infrared spectrometer is much less sensitive, needing approximately $1x10^9$ photons to detect a signal. This work allows approximate efficiencies of any emission to be calculated, allowing calculations of prototype specifications for any signal studied.

2.1.3. The sample stage

The sample stage is an Instek MCS622V heating/cooling stage that can be ramped and held at temperatures from 5 °C to 600 °C using water cooling, and down to -190 °C using liquid nitrogen cooling. Temperature dependent measurements on signals are important for two reasons:

1. To discover the temperature ranges at which the signals are present, and thus the temperature range of operation required of any sensor developed for commercial use, and,
2. To discover more about the kinetics and pathways of the signal.

Multi-photon upconversion luminescence can be both facilitated and quenched by phonons, depending on the upconversion pathway. Low-temperature analysis can help pinpoint the origins of the fluorescence by identifying the absorption bands and upconversion pathways used. This can be important in assessing the usefulness of the signal: for instance, if it occurs due to common ion inclusions and/or mineral lattice defects, it will likely be present in all or nearly all samples of that mineral. If the signal occurs due to uncommon inclusions or structures in the mineral, it will only be useful for identifying that mineral in specific circumstances.

The heating/cooling stage is mounted on an electronically controlled X-Y stage, for precise scanning of samples if this is needed in future. The stage is made of two Thorlabs MTS25-Z8 stages capable of 0.05 µm minimum distance movement and 25 mm total travel distance (see <www.thorlabs.com> for more details).

2.2. Sequences

In any full measurement on the Dual-Wavelength System, the following must be taken into account:
Inputs:

1. Excitation Wavelength 1
2. Excitation Energy 1
3. Excitation Wavelength 2
4. Excitation Energy 2
5. Delay between Excitation 1 and Excitation 2
6. Temperature of Sample

Outputs:

7. Emission Wavelength
8. Emission Intensity

Measurements in this thesis will be made at room temperature with no delay between the two laser pulses. All runs will have a pulse energy of 100%, unless specified otherwise. In this thesis then, we only have to take into account:
Inputs:

1. Excitation Wavelength 1
2. Excitation Wavelength 2

Outputs:

3. Emission Wavelength
4. Emission Intensity

The sequence used in this thesis is as follows:

1. Set excitation laser 1 to the first wavelength it will use.
2. Set excitation laser 2 to the first wavelength it will use.
3. Record EMCCD image at the highest gain settings that do not induce saturation.
4. Record Spectrometer measurement across the wavelength band of interest.
5. Set excitation laser 2 to the next wavelength in the sequence.
6. Repeat steps three to five until all wavelengths for laser 2 are used.
7. Set laser 1 to the next wavelength in the sequence.
8. Repeat steps two to six until all excitation wavelengths have been used.

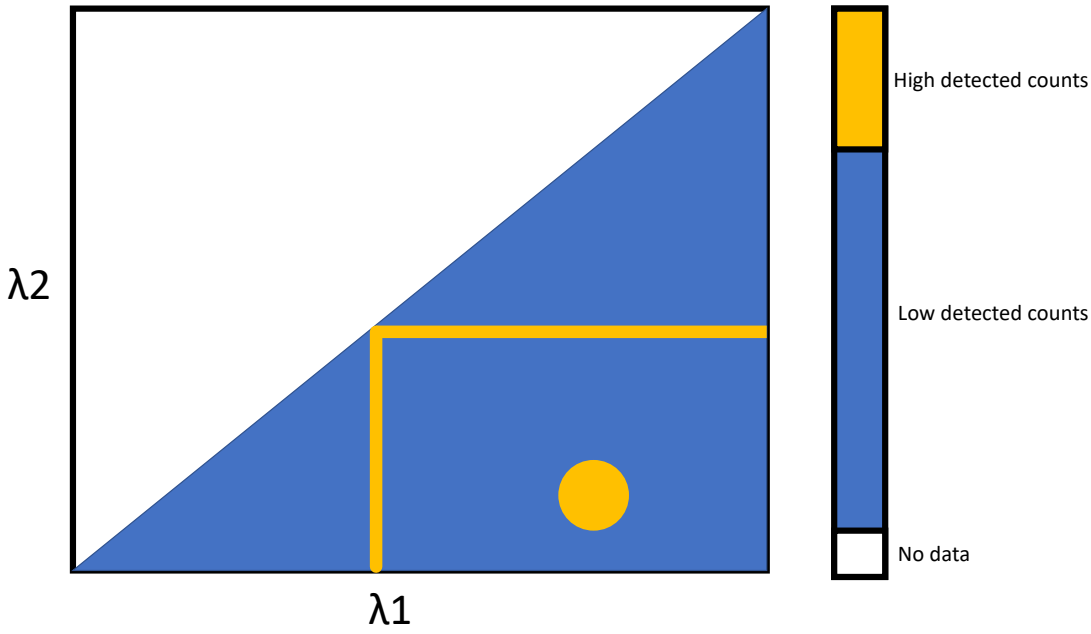

Figure 30: Diagram of features of the three-dimensional emission intensity vs wavelength 1 vs wavelength 2 graph used in this thesis. The yellow lines show the typical output of a one-wavelength excited upconversion emission ($\lambda_1 = \lambda_2$), and the yellow circle shows the typical output of an upconversion emission needing two different wavelengths ($\lambda_1 \neq \lambda_2$).

This sequence gives a four-dimensional data array consisting of excitation wavelength 1, excitation wavelength 2, emission wavelength, and emission intensity. In this thesis data is displayed as a three-dimensional plot of emission intensity vs excitation wavelength 1 vs excitation wavelength 2, with additional plots of emission wavelength vs emission intensity for areas of interest. The three-dimensional plot appears as a wedge of data as depicted as the blue area in Figure 30. Emission induced by one wavelength shows up as two straight lines on the graph (see yellow lines in Figure 30), and emission induced by two different wavelengths shows up as a circle asymmetrically placed on the graph (see yellow circle on the graph).

Information on sample type, excitation wavelengths, emission wavelengths, and emission data is collected for all experiments. This database of experimental data can be used to easily find gaps in past experiments, find data for re-analysis, and to inform future work.

Different excitation and emission wavelength ranges will require different filter combinations to clean the excitation wavelengths and prevent scattered light interfering with the emission measurements. Table 5 shows the filter combinations for the main sequences available with the OPOs, EMCCD, and visible spectrometer. Filters are stacked until their total optical density in the blocking range is greater than OD 9: at this level of rejection, the background component from scattered excitation photons is seen to become regligible, consistent with the detection efficiencies (section 2.1.2) measured.

Excitation range (nm)	Emission range (nm)	Excitation filters	Emission filter
OPO1: 1500-2500 nm OPO2: 1500-2500 nm	400-1100 nm*	715 nm LP	1100 nm SP*
OPO1: 1500-2500 nm OPO2: 750-1500 nm	250-700 nm	715 nm LP	700 nm SP
OPO1: 750-1500 nm OPO2: 750-1500 nm	250-700 nm	715 nm LP	700 nm SP
OPO1: 750-1500 nm OPO2: 530-750 nm	250-530 nm	OPO1: 715 nm LP OPO2: 715 nm SP	530 nm SP
OPO1: 530-750 nm OPO2: 530-750 nm	250-530 nm	715 nm SP	530 nm SP
OPO1: 1500-2500 nm OPO2: 530-750 nm	250-530 nm	OPO1: 715 nm LP OPO2: 715 nm SP	530 nm SP

*Table 5: Filters used for different upconversion fluorescence Dual-Wavelength System sequences. Filters are either long-pass (LP) or short-pass (SP) as indicated in the table. *While both the spectrometer and EMCCD in theory are only sensitive to 1100 nm, high intensity scatter can still be seen in some cases.*

2.3. Edinburgh Instruments FLS980 Spectrofluorimeter

Where specified, single-wavelength excitation experiments were conducted utilising an Edinburgh Instruments FLS980 Spectrofluorimeter <www.edinst.com>.

This spectrofluorimeter has three excitation sources:

- Fianium "Whitelase", a MHz picosecond pulsed source with a broad wavelength range from 420-2400 nm. Parts of this broadband source can be selected with a monochromator. While energy per pulse per wavelength is relatively low, the large pulse frequency and ability to excite over a broad range of wavelengths makes this source useful for looking at longer timeframe emission processes with broad absorption characteristics.
- Opotek "Opolette", a 20 Hz 5 nanosecond pulsed source with a tuneable wavelength range from 410-2400 nm. This source has a narrow linewidth and produces peak pulse powers high enough to be occasionally damage delicate samples and samples that easily saturate. It is the preferred laser of the three for exciting non-linear processes (e.g. upconversion), where a high photon flux is needed to induce detectable emissions.
- Edinburgh Instruments Picosecond Laser. This is a monochromatic 445 nm laser with a 99.9 ps pulse width. It is suitable for time-resolved scans of emissions excited at this wavelength.

Additional excitation sources used with the spectrofluorimeter include a set of UV diodes from QPhotonics <www.qphotonics.com>. Their specifications are in Table 6.

Peak wavelength (nm)	Peak power (µW)	Spectral width (nm)	Lens type
365	300	25	None
355	300	15	None
336.7	604	12.9	Hemisphere
320.1	637	10.1	Hemisphere
314.9	538	10.6	Hemisphere
298.3	451	10.4	Hemisphere
286.8	883	10.9	Hemisphere
282.3	856	10.8	Hemisphere
276.7	657	10.8	Hemisphere
267.4	662	10.5	Hemisphere
257.1	313	11.2	Hemisphere
247.4	248	10.7	Hemisphere

Table 6: Specifications of the UV diode set used in conjunction with the Edinburgh Instruments Spectrofluorimeter. Values are from QPhotonics test data.

The spectrofluorimeter has three different types of detectors:

- Hamamatsu air-cooled R928 photomultiplier (200-850 nm detection range).
- Hamamatsu liquid-nitrogen cooled R5509-72 photomultiplier (200-1,700 nm detection, though in this setup can only detect from 600-1,700 nm).
- InSb photodetectors (time resolved and solid state) (1,500-5,000 nm).

Each detector has a monochromator between it and the sample (the PMTs share one monochromator, and the InSb photodetectors share another). This allows the system to create wavelength-resolved emission scans.

The spectrometer's F90 software was used to control the lasers, detectors and monochromators, in order to produce the relevant emission, excitation, and time-resolved spectra. Energy measurements in experiments using the spectrofluorimeter used a Gentec-EO QE12LP-S-MB-DO pyroelectric energy meter <www.gentec-eo.com> with a minimum detectable energy of 0.7 µJ and a maximum pulse energy of 0.8 J.

2.4. Sample preparation

Upconversion fluorescence output can be dependent on specific ion inclusions, which may be located in some parts of a sample but not another. Upconversion fluorescence can also be dependent on the polarisation of light going through a crystalline structure (Yao et al., 2014). Unless otherwise specified, samples are crushed into powder form for analysis in the Dual-Wavelength System. This was done to eliminate polarisation as a variable requiring comprehensive investigation, and to enhance representivity when small portions of large samples were measured. The sample was crushed using either an agate mortar and pestle, or a Retsch PM100 Planetary Ball Mill, depending on the amount and hardness of the sample. The sample was crushed to a level (approximately between 0.1 and 1 mm in diameter) that is small enough to ensure samples that require mixing have no representivity issues, but the

macroscopic properties of the material (phonon presence, etc.) are still present. The powder is pressed into a pellet within a sample holder, in order to both provide a flat surface for illumination and prevent contamination of the sample stage. Unless otherwise stated, analysis using the Edinburgh Instruments FLS980 Spectrofluorimeter is done on bulk samples rather than pressed powder.

As the powder is pressed into a macroscopically 'flat' pellet, the surface area presented to the excitation laser beam is similar for all samples. Differences in transmission, reflection and absorption properties of different samples will have a large difference in the volume of sample excited for fluorescence sensing, with highly transmissive samples allowing the full volume to a depth of approximately 2 mm to be studied. Highly absorbing or reflective samples are expected to have lower fluorescence outputs, as a smaller volume of sample will be excited.

2.5. Error determination

The two main sources of error in a fluorescence measurement are due to fluctuations in excitation energy and random counting errors in emission detection. These errors are codependent, as changes in excitation energy will change the total emission detected and therefore the relative error. The dependency of emission to excitation energy differs depending on the type of fluorescence. At excitation energies far from fluorescence saturation, normal fluorescence emission has a linear dependency with excitation energy as in the following equation:

$$E_{out} = ME_{in}$$

Where E_{out} is the total energy of the isotropic emission, M is the efficiency of the fluorescence, and E_{in} is the energy of the incident light. Upconversion fluorescence has more complicated energy dependencies. At very small incident energies far from saturation, the emission is proportional to E_{in}^{N}, where N is the number of photons involved in the process. At medium-to-high incident energies, the following variables can influence energy dependence:

- The number of potential pathways of excitation or decay from each step of the upconversion fluorescence pathway. This can include further excitation steps (Pollnau et al., 2000), or energy transfer to defects or codopants.
- The relative probability of different potential pathways of excitation or decay. This can change at different energies: for example, in one-wavelength two-step upconversion, increasing the proportion of ion energy in the first excited state decreases total absorption of photons into this state, allowing proportionally more excitation light to be absorbed by the second excited state. In photon avalanche upconversion systems, the emission is initially proportional to the excitation energy; at high powers the first excited state becomes filled, depressing energy transfer up from the ground state and therefore proportionally enhancing emission (Chivian et al., 1979).
- The proportion of the ion population in the final excited state vs ground or intermediate states (saturation effects). When the proportion of the ion population in the final excited state is high, the efficiency of energy absorption is lowered and therefore so is the emission dependence on incident energy. The excitation energy at which these effects occur is dependent on three things: the population of ions being

excited, the absorption cross-section of the ions to the incident light, and the average time taken to complete upconversion fluorescence. The completion time is dependent on both the number and type of steps that occur in the upconversion pathway and the fluorescence lifetime of each excited state in the pathway.

As is evident from the above discussion, errors for upconversion emission are difficult to determine, especially for natural samples whose full defect and ion suite is not known. For most experimental work in this thesis, fluorescence emission was analysed without any need to quantify or compare different emission results as the principal goal was discovery of new fluorescence signals, and so comprehensive error analysis was not needed. More quantitative work conducted in chapters three and five involved creating trends in data for fitting purposes. In these measurements, emission was integrated over times long enough that the combined detection and excitation errors over all data points were much smaller than the errors of the fit, and so could be neglected.

While minimal error analysis was required by the nature of the work program reported in this thesis, to ensure reliability in measurements individual sources of error were researched and are discussed below:

Excitation source: Experiments in this thesis use Opotek "Radiant 355" <opotek.com/products/radiant-355-ld> lasers associated with the Dual-Wavelength System or an Opotek Opolette 355 OPO associated with the spectrofluorimeter. The pulse energy of these lasers was measured with the Dual-Wavelength System associated power meters for a number of pulses. In each case, the fluctuation in pulse energy was around 20 % of the total energy of the pulse.

Spectrofluorimeter detection: Experiments using the spectrofluorimeter used either the visible or near-infrared photomultiplier. Photomultiplier counting errors follow Poisson statistics, with a counting error equal to the square root of the detection counts (Bevington and Robinson, 2003).

Dual-Wavelength System detection: Both spectrometer and image detection from the Dual-Wavelength System utilise CCDs. The error in a CCD image is difficult to determine theoretically, as each pixel has a different relative error (Waterman and Evans, 2010). For spectrometer results, the width of the CCD array is binned, making this change in error small. The combined excitation and CCD error for the system can be determined by repeating an experiment multiple times under the same conditions.

A conventional fluorescence measurement was repeated 60 times in a row, ensuring minimal detector and excitation drift. Separate pixel bins were targeted from the bottom to the top of the emission peak in order to view the change in relative error at different emission intensities. As the pixel data is from the same measurement, any change in relative error occurs due to CCD behaviour rather than excitation error. The standard deviation of the 60 measurements changed from approximately 3.5 % of the mean for low emission intensities to 1.5 % of the mean for high emission intensities (Figure 31). While this is a definite trend, we can say that even for low emission intensities the relative error is low, far less than 5 %, and hence not of significance in the scope of this study.

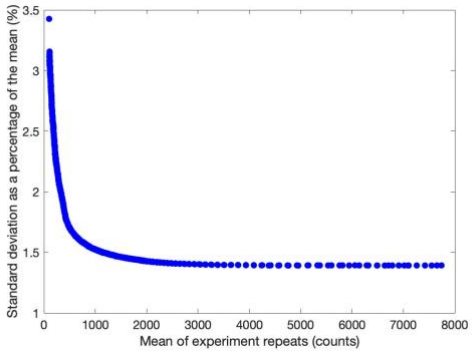

Figure 31: Changes in standard deviation of 60 identical experiments relative to the mean counts at different wavelengths. Emission was excited by the Radiant OPOs and detected using the near-infrared spectrometer.

3. — Erbium Doped ZBLAN glass—Novel Measurements of Upconversion Kinetics

3.1. Introduction

Er:ZBLAN is a glass that is a material of choice for the manufacture of mid-infrared fibre lasers due to its high transmission in this range and low phonon energy (Pollnau and Jackson, 2001). Quantifying the energy dynamics of the erbium ions is useful for improving the performance of Er:ZBLAN based fibre lasers (Golding et al., 2000). A discrepancy currently exists between the strength of the inter-ion energy transfer processes required to theoretically explain fibre laser results (Gorjan et al., 2011) and results directly measured in bulk ZBLAN (Pollnau et al., 2000b). It has been proposed that there are two different 'regimes' of energy transfer strength that can explain the difference in fibre laser and bulk glass results. These are called the 'strongly interacting' regime, associated with bulk glass measurements, and the 'weakly interacting' regime, associated with fibre models. Er:ZBLAN fibre may be in one or the other of these regimes, similar to or different to bulk glass. One of the strongest energy transfer process in Er:ZBLAN is the $^4I_{13/2} + {}^4I_{13/2} \rightarrow {}^4I_{15/2} + {}^4I_{9/2}$ transition. This process takes two ions in the first excited state and transfers one to a higher state ($^4I_{9/2}$) and drops the other to the ground state ($^4I_{15/2}$). It is problematic for erbium lasers operating around 1.5 μm and advantageous for those operating around 2.7 μm. The energy transfer parameter that describes the strength of this process has not been directly measured before in fibre. This chapter describes obtaining quantitative measurements of this parameter for the first time in fibre using the Edinburgh Instruments Spectrofluorimeter.

3.1.1. Erbium ZBLAN glass

Molecule	Percent (mol)
ZrF_4	53
BaF_2	20
LaF_3	4
AlF_3	3
NaF	20

Table 7: Typical proportions of the constituents of ZBLAN. ZBLAN glass may also contain InF3 and PbF2, which if present are in proportions between 1-3 mol % and 0.1-1 mol % respectively.

ZBLAN is a fluoride glass containing zirconium, barium, lanthanum, aluminium, and sodium (Table 7). The large variety of constituent ions allows the glass to be doped with other ions at high percentages—up to 4 mol% without glass deformation effects (Pollnau and Jackson, 2001), and up to 7 mol% while still maintaining most of the fibre properties. Rare earth dopants have similar atomic radii to zirconium and lanthanum, which allows for easy ion substitution. While in general ZBLAN is an ideal medium for fibre lasers, it is known to allow similar ions to clump together, and will undergo crystallisation if the conditions of its formation are not tightly controlled. In general, it has been found that more than 50% of erbium ions in Er:ZBLAN fibres are in clumps when the fibre is doped at greater than 1 mol% (Srinivasan et al., 2000).

Many energy levels in erbium doped ZBLAN have millisecond lifetimes (Table 8) which is long compared to many other processes and lifetimes in other ions and hosts. This increases the likelihood of energy transfer processes since there is an increased probability of nearby ions also being in excited states.

Typical lifetimes of erbium energy levels in ZBLAN at room temperature		
Reference Number	State Name	Lifetime (ms)
0	$^4I_{15/2}$	Infinite (ground)
1	$^4I_{13/2}$	9.9
2	$^4I_{11/2}$	7.9
3	$^4I_{9/2}$	0.008
4	$^4F_{9/2}$	0.177
5	$^4H_{11/2}$, $^4S_{3/2}$	0.530
5 (top)	$^4F_{7/2}$	0.005

Table 8: Typical erbium energy level lifetimes in ZBLAN for the states of interest. Values are taken from (Malouf et al., 2016).

The four energy transfer processes commonly known to affect erbium fibre lasers are as follows:

W11, or $^4I_{13/2} + {}^4I_{13/2} \rightarrow {}^4I_{15/2} + {}^4I_{9/2}$ (see Figure 32). This is the strongest energy transfer process known in Er:ZBLAN. It involves two erbium ions in the same state. This state is very long lived (9.9 ms), and so energy transfer has a greater chance of occurring. This chapter will focus on this process.

W22, or $^4I_{11/2} + {}^4I_{11/2} \rightarrow {}^4I_{13/2} + {}^4F_{7/2}$ (see Figure 32). Like W11, W22 involves two erbium ions in the same long-lived state.

W50, or $^4H_{11/2}/{}^4S_{3/2} + {}^4I_{13/2} \rightarrow {}^4I_{9/2} + {}^4I_{13/2}$ (see Figure 32) (Maes et al., 2019). This emission relies on two nearby ions being in different excited states at the same time, and so is less likely under simple excitation conditions. Since the $^4H_{11/2}$ and $^4S_{3/2}$ states are thermally coupled at room temperature the initial state of the first ion can be in either of these two states.

W42, or $^4F_{9/2} + {}^4I_{11/2} \rightarrow {}^4H_{11/2}/{}^4S_{3/2} + {}^4I_{13/2}$ (see Figure 32) (Henderson-Sapir et al., 2016). This process relies on an ion being in the $^4F_{9/2}$ state, which is comparatively short-lived compared with states in other energy transfer processes (see Table 8). However, for the pulsed excitation measurements described in this chapter this process is unlikely to occur.

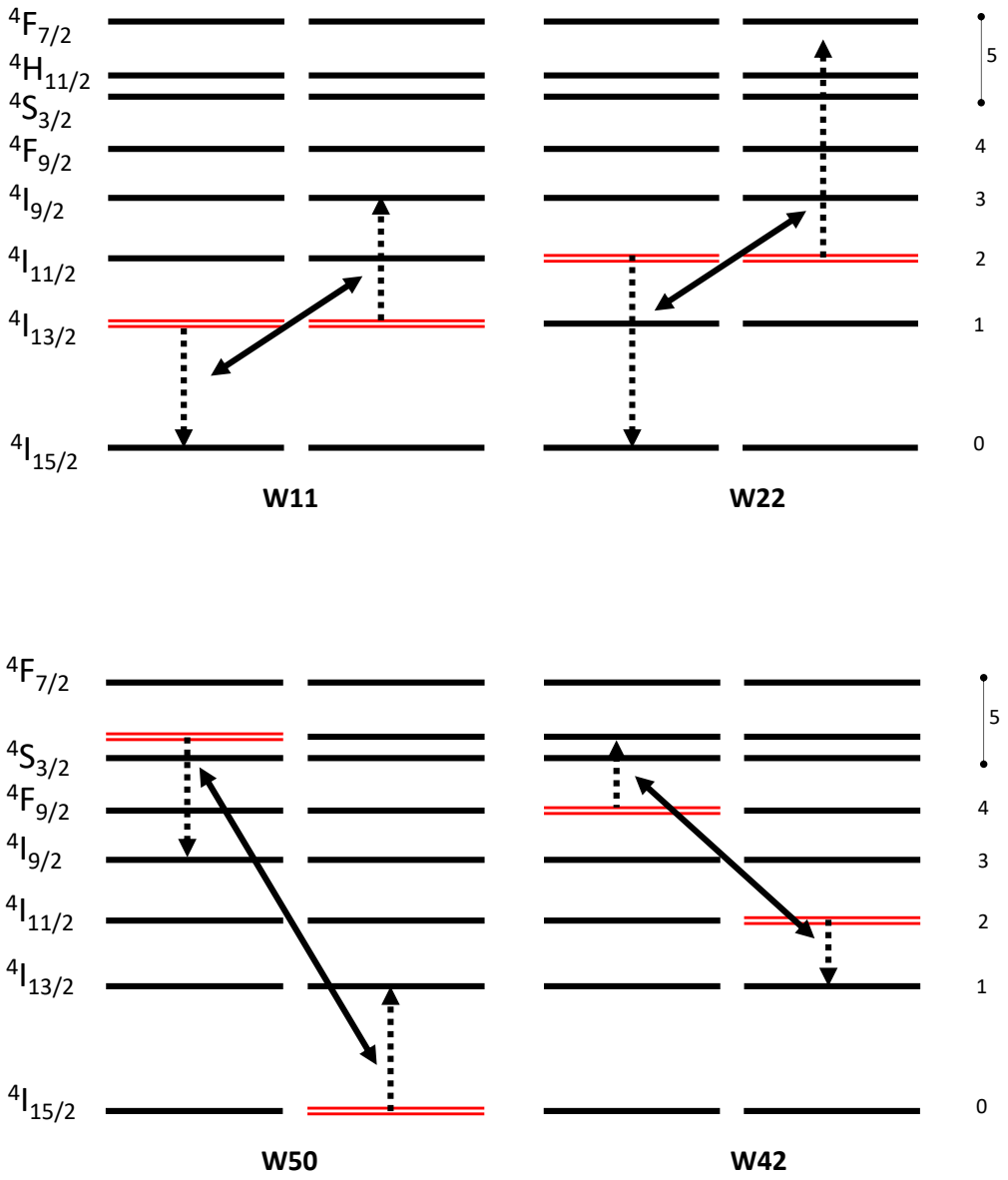

Figure 32: Energy transfer processes in Er:ZBLAN. Energy levels marked in red indicate initial states before energy transfer. Dashed arrows indicate the change in energy level due to energy transfer.

Erbium-doped ZBLAN fibre lasers

Er:ZBLAN is used in fibre form to generate many different wavelengths. The following are the most common:

1.5 µm laser: This laser wavelength is within the transmission range of silica, and so techniques to create high powered erbium 1.5 µm fibre lasers were first developed in doped silica fibres (Millar et al., 1987). These lasers use the erbium transition $^4I_{13/2} \rightarrow {}^4I_{15/2}$ (ground state) (Figure 33). Later work developed similar lasing transitions in fluorozirconate fibres (a family of fibres with composition including zirconium fluoride, of which ZBLAN is a member). Pumping wavelengths include 488 nm and 515 nm (Allain et al., 1989b), 514 nm (Smart et al., 1990), and 980 nm (Duling, 1991). ZBLAN-based 1.5 µm lasers are less common due to their duplication in silica. These lasers are negatively affected the most from W11 energy transfer, as the energy transfer process takes two ions directly out of the upper lasing state. Efficient operation therefore requires low erbium doping densities to be used.

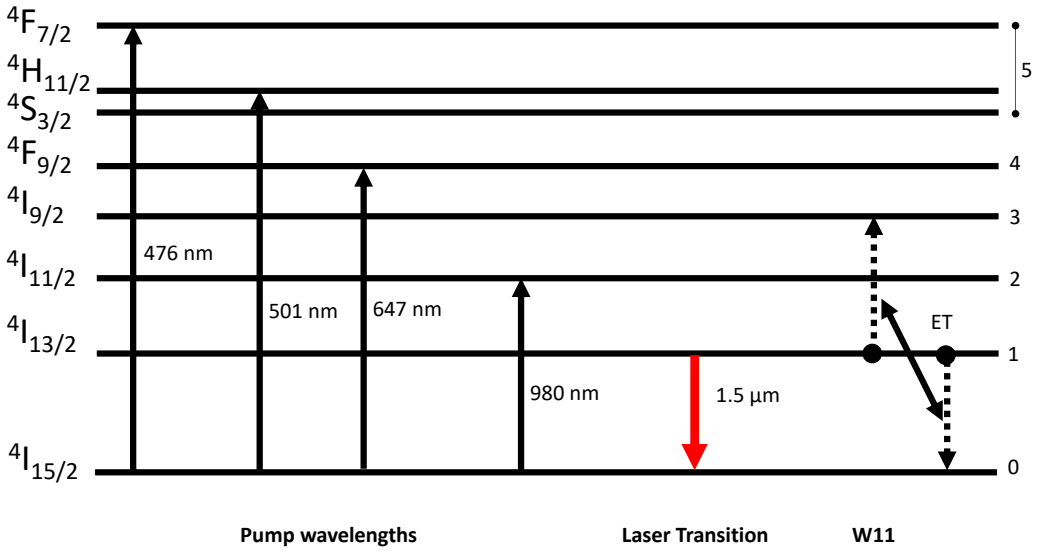

Figure 33: Band diagram depicting pump wavelengths (black arrows to the left) and laser energy transition of 1.5 µm laser (bold red arrow), and W11 energy transfer transitions (dashed black arrows to the right).

2.7 µm laser: Fluoride-based fibres become more important for laser applications at wavelengths longer than 2.5 µm. Silica fibre has a greater maximum phonon energy than fluorozirconate fibre, and transitions with smaller energy gaps (longer wavelengths) are more likely to be quenched by non-radiative effects. This occurs for the transition $^4I_{11/2} \rightarrow {}^4I_{13/2}$ (Figure 34) used for 2.7 µm emission. ZBLAN fibres do not have this problem, and so long-wavelength/small energy transitions are still radiative (Freichs, 1994). Laser pumping is possible at 476 nm (Brierley and France, 1988, Allain et al., 1989a), 501 nm, 647 nm (Allain et al., 1989a), 792 nm (Allen et al., 1990), and 980 nm (Freichs, 1994). There are a number of challenges involved in creating an efficient 2.7 µm laser, as outlined below:

- Pumping at visible wavelengths is inefficient, as multiple decays are needed to reach the upper lasing level and the quantum defect is large.

- Pumping at 800 nm (or 792 nm) and 980 nm creates excited state absorption (ESA), from $^4I_{13/2} \rightarrow {}^4H_{11/2}$ by 800 nm and from $^4I_{11/2} \rightarrow {}^4F_{7/2}$ by 980 nm (Freichs, 1994).
- W22 energy transfer occurs from the upper lasing level (Figure 32), and so is detrimental to lasing output.
- The lower lasing level ($^4I_{13/2}$) is not the ground state from which the laser is excited, and has a long lifetime. This can take erbium ions out of lasing photon production for long periods of time (almost 10 ms—see Table 8).

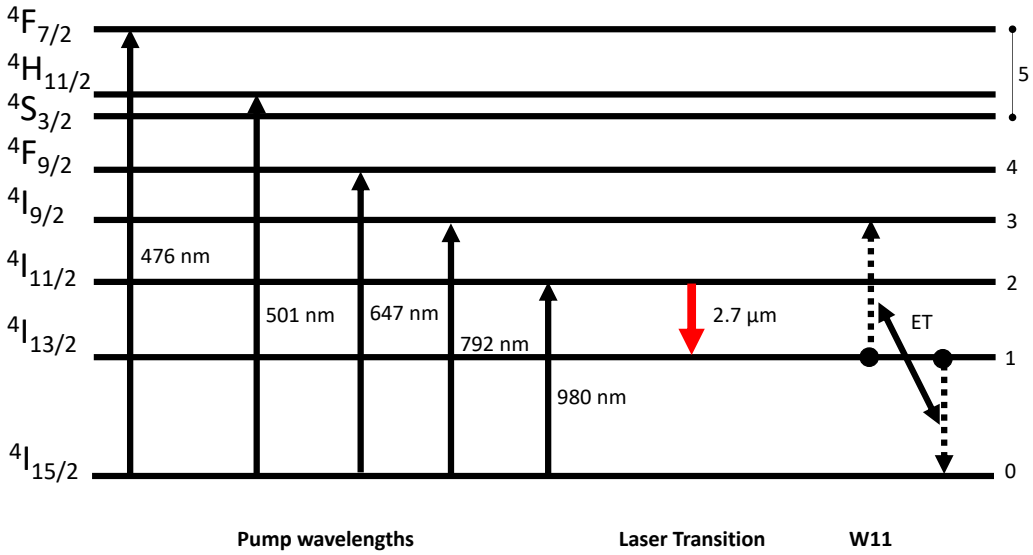

Figure 34: Band diagram depicting pump wavelengths (black arrows to the left) and laser energy transition of 2.7 µm laser (bold red arrow), and W11 energy transfer transitions (dashed black arrows to the right).

The long lifetime of the $^4I_{13/2}$ state limits the efficiency of 2.7 µm lasers, especially at high powers. Attempts have been made to decrease the lifetime of this state by co-doping with praseodymium (Ibrahim et al., 1993). Energy transfer occurs between the $^4I_{13/2}$ state in erbium and the $^4F_3$ and $^3F_4$ states in praseodymium, increasing the rate at which ions move from $^4I_{13/2} \rightarrow {}^4I_{15/2}$ states in erbium. When higher power erbium lasers were developed, however, codoping with praseodymium became a disadvantage as the erbium-praseodymium energy transfer competes with the W11 erbium-erbium energy transfer.

The W11 energy transfer is very advantageous to 2.7 µm fibre lasers, as it takes two ions in the lower lasing level and transfers one above the upper lasing level (able to undergo lasing), and the other at the ground state (ready to undergo excitation) (note Figure 34). Maximising W11 energy transfer while minimising negative effects is critical for optimising design of 2.7 µm erbium fibre lasers.

3.5 µm laser: These lasers use the $^4F_{9/2} \rightarrow {}^4I_{9/2}$ transition. They can be pumped directly to the $^4F_{9/2}$ state by excitation around 650-655 nm (Többen, 1991, Többen, 1992). In this method ions must then decay to the ground state before re-excitation, running into the same problems with bottlenecking in the $^4I_{13/2}$ state as 2.7 µm lasers. Another method is to use

dual-wavelength pumping (Henderson-Sapir et al., 2014) (see Figure 35). Pumping at 980 nm is designed to create a population in the $^4I_{11/2}$ state, while pumping at 1973 nm excites from $^4I_{11/2} \rightarrow {}^4F_{9/2}$. This creates efficient lasing with minimal 'trapping' of ions in the $^4I_{13/2}$ state. While W11 energy transfer becomes less relevant with dual-wavelength pumping, it is still important to consider when designing lasers with high doping levels. W22 energy transfer is more likely with large ion populations at $^4I_{11/2}$ and is advantageous in the 655 nm pumping regime as ions can otherwise stay in the $^4I_{11/2}$ state when decaying to the ground state for a long time, creating a bottleneck in the laser process. In the dual-pumping method 1973 nm pumping is much more efficient at transferring ions to the upper lasing state.

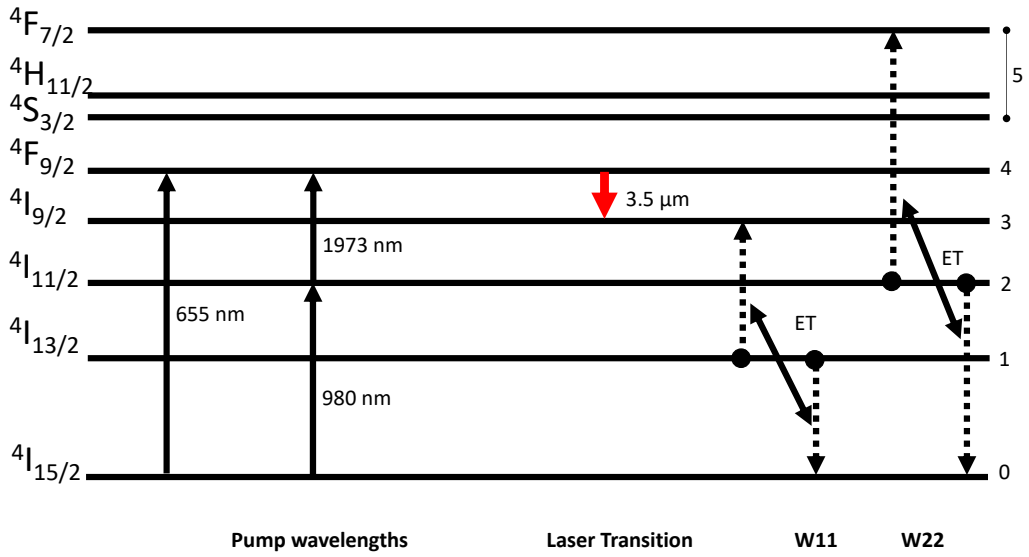

Figure 35: Figure 3: Band diagram depicting pump wavelengths (black arrows to the left) and laser energy transition of 3.5 µm laser (bold red arrow), and W11 and W22 energy transfer transitions (dashed arrows to the right).

3.1.2. Bulk glass predictions vs fibre laser behaviour

Optimising laser design depends on accurate models in order to assess laser excitation power, fibre dopant level, and core diameter. These models require accurate process parameters, usually gained from bulk glass measurements. Gorjan et al. (Gorjan et al., 2011) made a model of all decay and energy transfer processes, and fitted it to a 2.7 µm 6 mol% fibre laser output and emission data. They varied energy transfer parameters from zero to the highest bulk glass parameters measured. Three laser regimes were modelled. At zero or near zero energy transfer, excitation in the tens of Watts quickly created a 'bottleneck' of ions in the $^4I_{13/2}$ state, and efficiencies at high powers dropped. At energy transfer parameters over 0.5 10^{-17} cm^3s^{-1}, or the "strongly interacting" regime, the W11 energy transfer takes ions out of the $^4I_{13/2}$ state before a large population can accumulate there, and so the laser can still operate successfully at high powers. In the middle regime, or the "weakly interacting" regime, energy transfer allows laser operation to occur efficiently until excitation powers of hundreds of Watts, where bottlenecking at $^4I_{13/2}$ starts to occur.

The 2.7 µm fibre laser Gorjan et al. used followed the behaviour of the "weakly interacting" energy transfer regime (Gorjan et al., 2011). They theorised that in bulk glass erbium ions clumped, thereby increasing the energy transfer because clumping increases the probability that to ions are close enough to trade energies. There are indications, however, that significant clumping occurs in high-doped Er:ZBLAN fibres (Srinivasan et al., 2000). The energy transfer regime may depend on fibre dopant density (Srinivasan et al., 2000) and individual fibre construction and history (Gorjan et al., 2011).

3.1.3. Chapter synopsis and aim

The strength of the W11 parameter has previously been calculated from laser behaviour and the proportion of fluorescence emission from different erbium states (Gorjan et al., 2011). It has not previously been calculated in fibre from direct measurements of the states involved in the W11 process. This chapter describes the measurements undertaken and fits of the W11 parameter for fibres of different doping densities and differing manufacturers.

A model of erbium fibre behaviour will be created using rate equations, and the experimental parameters defined. This model will be fit to measurements from six fibres of varying doping density and supplier. The results of the fit and the reliability of the model will then be discussed.

3.2. Rate equation model

The effect of energy transfer on rate equations, from Chapter One, is described as:

$$\pm N_{donor} N_{acceptor} W_{da}$$

Where N_{donor} is the population of the donor excited state (i.e. how many ions are in a state able to transfer energy), $N_{acceptor}$ is the population of the acceptor ground state (i.e. how many ions are in a state able to accept transferred energy), and W_{da} is the strength of the energy transfer process, in units of volume per second. W_{da} is highly material-specific, depending on both the energy transfer probability in the host material, the ion doping level, and the amount of ion clumping in the material.

Assuming no three-photon upconversion, 1530 nm excitation, and that the three upper levels are thermally coupled, the following equations (3.1) show the change in population of the affected states:

$$\frac{dN_0}{dt} = -N_0 E_{ex}\sigma_{01} - N_5 N_0 W_{50} + N_1 A_{10} + N_2 A_{20} + N_3 A_{30} + N_4 A_{40} + N_5 A_{50}$$

$$\frac{dN_1}{dt} = +N_0 E_{ex}\sigma_{01} - N_1 E_{ex}\sigma_{13} - 2{N_1}^2 W_{11} + N_5 N_0 W_{50} + N_4 N_2 W_{42} - N_1 A_{10} + N_2 A_{21} + N_3 A_{31} + N_4 A_{41} + N_5 A_{51}$$

$$\frac{dN_2}{dt} = -2{N_2}^2 W_{22} - N_4 N_2 W_{42} - N_2 A_2 + N_3 A_{32} + N_4 A_{42} + N_5 A_{52}$$

$$\frac{dN_3}{dt} = +N_1 E_{ex}\sigma_{13} + {N_1}^2 W_{11} + N_5 N_0 W_{50} - N_3 A_3 + N_4 A_{43} + N_5 A_{53} \quad \textbf{(3.1)}$$

$$\frac{dN_4}{dt} = +N_1{}^2W_{11} - N_4N_2W_{42} - N_4A_4 + N_5A_{54}$$

$$\frac{dN_5}{dt} = +N_2{}^2W_{22} - N_5N_0W_{50} + N_4N_2W_{42} - N_5A_5$$

Where the suffix 0 denotes the ground $^4I_{15/2}$ level, 1 denotes $^4I_{13/2}$, 2 denotes $^4I_{11/2}$ and 3 the $^4I_{9/2}$ level, 4 the $^4F_{9/2}$ level, and 5 the thermally coupled levels between $^4F_{7/2}$ and $^4S_{3/2}$. A numbers are the inverse fundamental lifetimes of the decay of the state, N is the population density of a state, E is the excitation energy, and σ is the absorption cross-section of the ground state or excited state transition. Figure 36 shows the equations in 3.1 in band diagram form.

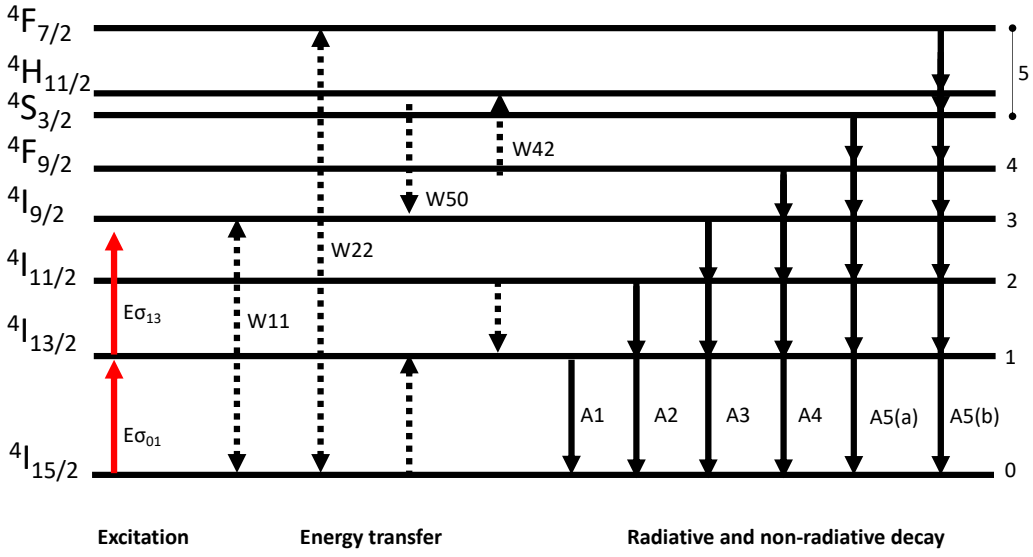

Figure 36: Band diagram of potential energy states of erbium in ZBLAN glass, depicting excitation absorption (left), excited state decay (right), and energy transfer (middle) that can occur under 1530 nm excitation.

Fitting variables to data is potentially less accurate the more variables are needed. To limit the number of variables in the equation, the excitation wavelength was moved to 1471 nm. Excited state absorption from the $^4I_{13/2}$ state to the $^4I_{9/2}$ state is minimised, while still allowing ground state excitation to the $^4I_{13/2}$ state. This limits the proportion of ions in the $^4I_{11/2}$ state (filled via A_{32} decay—see Figure 36), thereby minimising W22 energy transfer.

With a limited population in the $^4I_{11/2}$ state, we can neglect W22 energy transfer. This is the only mechanism by which the upper levels are populated, so W42 and W50 energy transfer processes are also suppressed. We are then left with a limited number of terms, shown in bold in Figure 37:

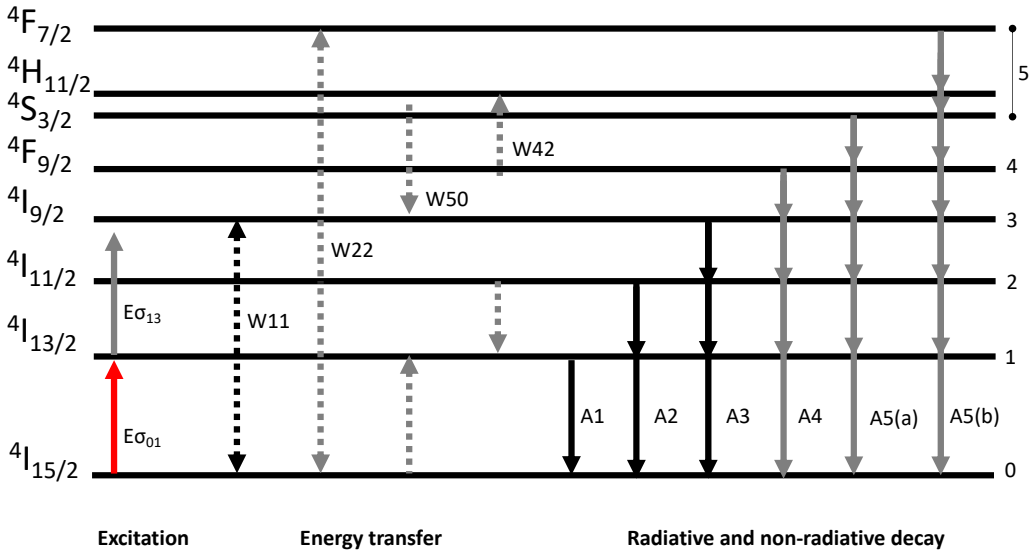

Figure 37: Band diagram of potential energy states of erbium in ZBLAN with excitation absorption (left), energy transfer (middle), and decay (right) that can occur under 1471 nm excitation. Negligible terms are in grey.

In this chapter we are measuring time resolved fluorescence using a 20 Hz 5 ns pulsed laser as an excitation source. 0.05 s is long enough for all excited state levels to depopulate to the ground state (see Table 8), and so the fluorescence from each pulse is independent of the one that came before. The 5 ns pulse is much shorter than the lifetimes of the states, and so the pulse can be assumed to be instantaneous for the time resolved measurements.

Without the W50 energy transfer, the N_0 state only affects the other states via ground state absorption to the $^4I_{13/2}$ state. This only occurs at time = 0, so the change in the N_0 population over time does not have to be accounted for in the model. From Table 8 we can see that the lifetime of the $^4I_{9/2}$ state is orders of magnitude smaller than the lifetime of the $^4I_{11/2}$ and $^4I_{13/2}$ states. The branching ratios of $^4I_{9/2}$ show that 99% of the time it decays to the $^4I_{11/2}$ state (Caspary, 2002). This means that the model can be simplified further, as the $^4I_{9/2}$ and $^4I_{11/2}$ states can be merged when looking at timescales longer than ~16 µs (2 lifetimes of the $^4I_{9/2}$ state). The simplified model then looks like:

$$\frac{dN_1}{dt} = -2{N_1}^2 W_{11} - N_1 A_{10} + N_2 A_{21}$$

$$\frac{dN_2}{dt} = +{N_1}^2 W_{11} - N_2 A_{21} - N_2 A_{20} \quad \textbf{(3.2)}$$

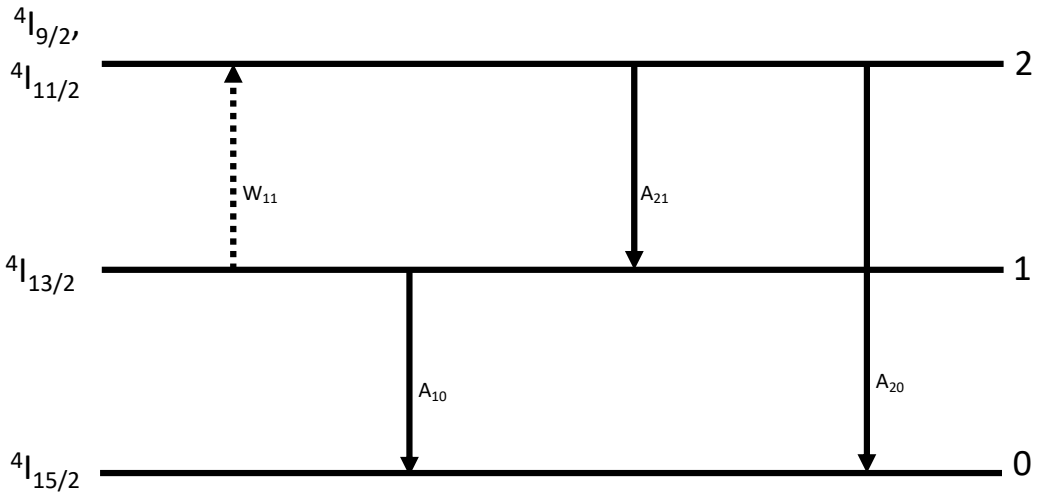

Figure 38: Band diagram depicting energy transitions taken into account in the model used for fitting to time resolved data. $^4I_{9/2}$ and $^4I_{11/2}$ states are condensed into one due to the comparatively fast (µs vs ms) non-radiative decay from $^4I_{9/2}$ to $^4I_{11/2}$.

Equation 3.2 and Figure 38 shows that there are now only four variables to take into account in the model (five including the initial value of the $^4I_{13/2}$ state). The following section will discuss in more detail the experimental parameters and how each variable is measured or calculated.

3.3. Experimental parameters and variables

The following describes how each variable for fitting to equation set 3.2 was collected or calculated:

3.3.1. Initial populations

The initial value of the population N_2 is considered to be 0, as there is minimal excited state absorption under 1471 nm excitation. This is verified by looking at time resolved emission at 980 nm, which starts at a background level and then rises over time.

The initial value of the population N_1 is defined as the number of ions excited to the $^4I_{13/2}$ state from the $^4I_{15/2}$ state by the laser pulse energy. This is equal to the number of ions available to be excited times the number of incident photons times the likelihood of a photon being absorbed by an ion. We assume that approximately all ions are in the ground state, and so we can use the ion density as the number of available ions. From the pulse energy we can derive the number of photons per pulse, and from the absorption cross-section we have the likelihood of ion absorption of a photon per area. N_1 is a population density, so everything is divided by the volume, V:

$$N_{1(initial)} = \frac{No.ions \times No.photons \times \frac{\sigma_{1471} L}{V}}{V}$$

Where σ_{1471} is the absorption cross-section of the $^4I_{15/2} \rightarrow {}^4I_{13/2}$ transition at 1471 nm, V is the volume of the core being examined, and L is the length of fibre examined. This can be rearranged to:

$$N_{1(initial)} = \frac{No.ions}{V} \times No.photons \times \frac{\sigma_{1471}}{a}$$

This gives us:

$$N_{1(initial)} = N_g \frac{E}{hv} \frac{\sigma_{1471}}{a} \qquad \textbf{(3.3)}$$

Where N_g is the ion density of the fibre core, E is the pulse energy, h is Planck's constant, a is the area of the fibre core, and v is the frequency of 1471 nm light. Equation 3.3 holds if we assume the following:

- Saturation effects, which result when N_g changes significantly over the course of the excitation pulse, are not present. This is ensured by making measurements for each fibre at different pulse energies (see Figure 39) and ensuring that the emission vs pulse energy has a linear relationship. Measurements not on the initial linear curve are not used.

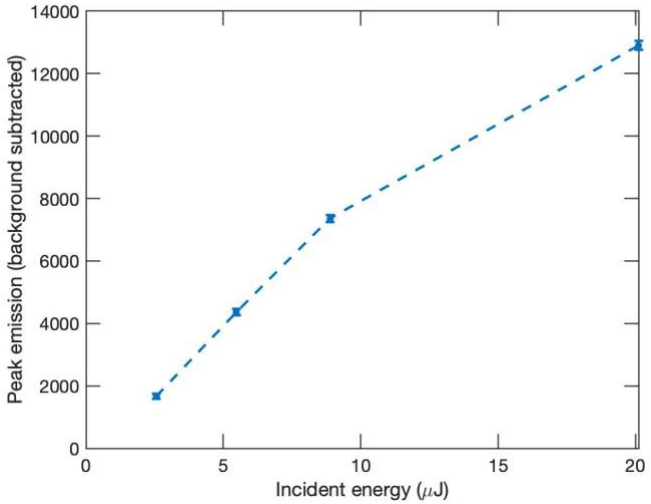

Figure 39: Peak emission vs incident energy graph for a 7 mol% erbium-doped ZBLAN fibre excited at 1471 nm. The last data point does not follow the linear trend shown by the other points and so the last experiment was discarded due to signs of saturation.

- The photon fluence is the same across the area of the fibre core. This is ensured by having the laser light not tightly focused at the fibre tip. Thus, although the beam is approximately Gaussian in profile, the change in energy density from the centre of the core to the edge of the core is small.
- The erbium ions are evenly distributed throughout the core area—i.e. the ions are not more likely to be in the centre of the core than the core edge, or vice-versa. While this

assumption is not experimentally verified, it is generally held to be true in the general Er:ZBLAN fibre laser literature.

- The number of available photons is approximately the same over the length of the fibre. While this may not be true over the entire length of the 3-5 cm length of fibre, the fluorescence is only measured over the first ~1 mm of fibre by using a collecting fibre with a 1 mm diameter.

The variables used in equation 3.3 are discussed in greater detail below.

3.3.2. Time-resolved population/emission data

A short length of fibre (typically 3-5 cm in length) was placed on an XYZ stage inside the Edinburgh Instruments Spectrometer and aligned with the focused beam of the Opolette OPO (Figure 40). The OPO was tuned to 1470 nm to excite ions to the $^4I_{13/2}$ state. Various neutral density filters were put into the path of the beam before focusing to vary the pulse energy.

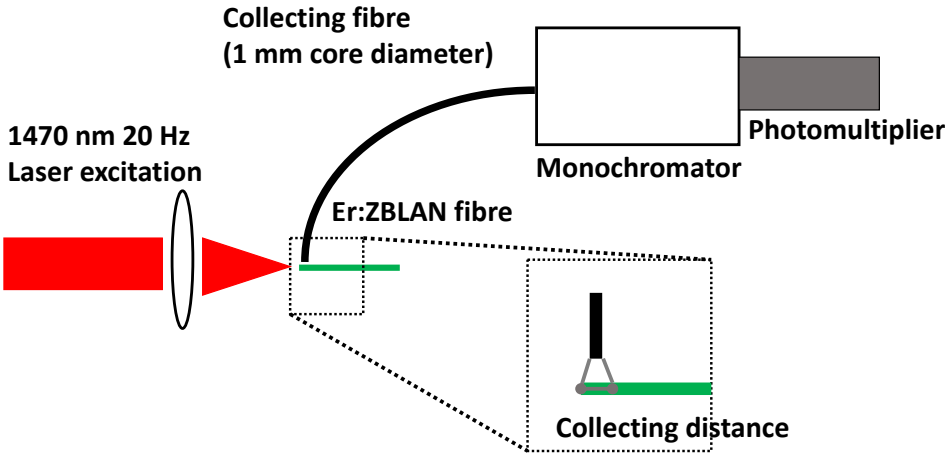

Figure 40: Experimental setup used in the Edinburgh Instruments Spectrofluorimeter to acquire time-resolved erbium-doped ZBLAN fibre emission measurements.

Each fibre was commercially bought, with varying core and inner ZBLAN cladding diameters (see Table 9). Outer polymer cladding and jacketing was removed from the tip of the fibre. The erbium content ranged from 1 to 7 mol %. Two 1 mol% and two 7 mol% fibres from different manufacturing batches were used in order to assess repeatability of experiments and fibre-to-fibre variability.

Specifications for Fibres Used		
Dopant Level (mol%)	Core diameter (μm)	Company of Production
1	16.5	Le Verre Fluoré
1 (from different reel)	16.5	Le Verre Fluoré
1.7	10	Fiber Labs
4	14	Fiber Labs
6	25	Fiber Labs
7	16.5	Le Verre Fluoré
7 (from different reel)	16.5	Le Verre Fluoré

Table 9: Specifications of erbium-doped ZBLAN fibres used to gain time-resolved data in the experiment.

Light from the tip of the fibre was collected via a 1 mm diameter core silica collecting fibre and passed to the slit of the monochromator associated with the Spectrofluorimeter. The monochromator was set to detect a centre wavelength of 1530 nm for emission to the ground state from the $^4I_{13/2}$ state, and a centre wavelength of 980 nm for $^4I_{11/2}$ state emission. The slit of the monochromator was set to allow a bandwidth between 0.5 nm and 10 nm through, depending on the intensity of fibre emission at the lowest power used. The minimum bandwidth allowable for the fibre was used, in order to minimise noise. Light was detected by the near-infrared photomultiplier.

The Edinburgh Instruments F980 Spectrofluorimeter software was used to record time dependent measurements of multiple pulses. Integration of subsequent pulses continued until signal was visible above the noise, taking between 15 minutes (for high doped fibres at 1530 nm) to 27 hours (for low doped fibres at 980 nm) depending on the intensity of emission. 40 ms of data was collected.

3.3.3. Energy per Pulse (E)

We assume negligible absorption over the measured length of the fibre, with E as the energy incident on the fibre core. A knife-edge measurement of the laser energy was taken at the yz position the fibre was placed. Assuming a Gaussian beam profile, the energy of the beam can be fitted to the knife edge measurement data with the following equation:

$$E(x) = \frac{A}{2}\left(1 - \mathrm{erf}(\sqrt{2}\frac{x - B}{C})\right) + m$$

Where E is the energy at displacement x, m is the minimum or background energy, A is the maximum energy, B is the mean displacement, and C is the full-width half maximum of the Gaussian beam. This matched well to the knife-edge data (see Figure 41).

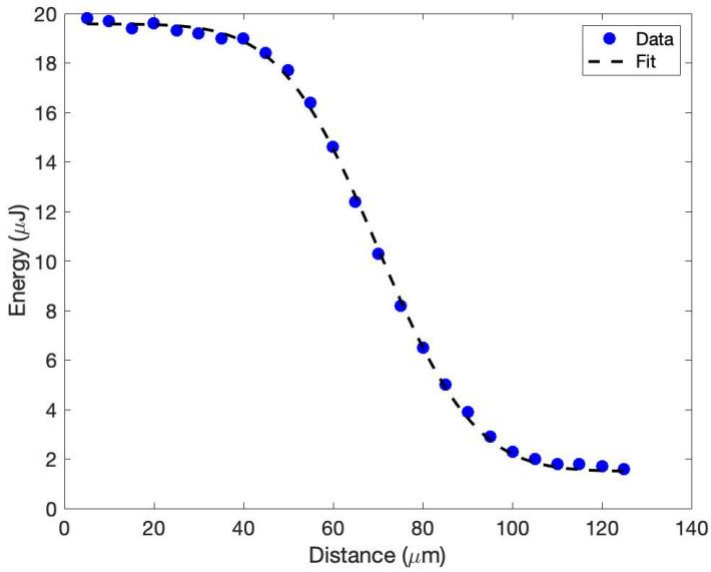

Figure 41: Knife edge measurement data and knife-edge Gaussian fit to the data. The 'knife-edge' is moved slowly in front of the beam, and the total energy of the beam after the knife edge measured using the Gentec energy meter detailed in section 2.3.

Using the full-width half maximum gained from the fit to the data, the proportion of the full beam incident on the fibre core was calculated, assuming that the fibre was accurately aligned to the beam. The beam was not tightly focused into the fibre, both to prevent fibre damage and to ensure small errors in alignment did not result in large errors of the calculation of E. The full energy of the beam was measured using a Gentec energy meter (see section 2.3) before focusing to prevent damage to the energy meter. An average of 500 pulses was used for energy measurements. Measurements were done after at least 1 hour of continuous firing of the laser, to ensure it was fully warmed up and stable. The full set of energies used in the experiments are detailed in Table 10.

Energies used in fibre experiments		
Fibre and experiment	Energy (J)	Error (J)
1 mol% (1530 nm)	1.49×10^{-6}	1.66×10^{-7}
	3.31×10^{-6}	1.66×10^{-7}
	5.46×10^{-6}	1.66×10^{-7}
	1.15×10^{-5}	1.66×10^{-7}
1 mol% (980 nm)	2.95×10^{-6}	2×10^{-7}
1 mol% (1530 nm)	1.56×10^{-6}	1.66×10^{-7}
	3.43×10^{-6}	1.66×10^{-7}
	5.52×10^{-6}	1.66×10^{-7}
	1.21×10^{-5}	1.66×10^{-7}
1 mol% (980 nm)	2.95×10^{-6}	2×10^{-7}
1.7 mol% (1530 nm)	4.31×10^{-6}	1.66×10^{-7}
	1.23×10^{-5}	1.66×10^{-7}
	1.60×10^{-5}	1.66×10^{-7}
	2.13×10^{-5}	1.66×10^{-7}
1.7 mol% (980 nm)	2.93×10^{-6}	2×10^{-7}
4 mol% (1530 nm)	2.12×10^{-6}	1.66×10^{-7}
	4.57×10^{-6}	1.66×10^{-7}
	7.37×10^{-6}	1.66×10^{-7}
	1.67×10^{-5}	1.66×10^{-7}
6 mol% (1530 nm)	6.11×10^{-6}	1.66×10^{-7}
	1.26×10^{-5}	1.66×10^{-7}
	2.22×10^{-5}	1.66×10^{-7}
	4.89×10^{-5}	1.66×10^{-7}
7 mol% (1530 nm)	2.57×10^{-6}	1.66×10^{-7}
	5.47×10^{-6}	1.66×10^{-7}
	8.89×10^{-6}	1.66×10^{-7}
7 mol% (1530 nm)	7.56×10^{-7}	7.56×10^{-8}
7 mol% (980 nm)	2.41×10^{-6}	2×10^{-7}

Table 10: Energies incident on fibre core for each time resolved measurement used in this chapter. Experiments marked "1530 nm" measured time-resolved emission at 1530 nm, and experiments marked "980 nm" measured emission at 980 nm.

3.3.4. Absorption cross section (σ_{ab})

Absorption cross-section data were taken from previous bulk glass measurements (Henderson-Sapir, 2015). In addition, individual absorption cross-section data was calculated for each fibre (Figure 43). These measurements will be more inaccurate than bulk glass measurements (McCumber, 1964), but will give an idea of systematic differences of absorption cross-section between fibres. This checks that the absorption cross-section does not change significantly between fibres that may have slightly different stoichiometry. The bulk glass absorption is therefore used in these measurements as the glass absorption properties are not expected to change from bulk glass to fibre, and the calculated fibre measurements are used to give an idea of the fibre-to-fibre error in the measurement.

To calculate the absorption cross-section for the $^4I_{15/2} \rightarrow {}^4I_{13/2}$ erbium transition, the emission between 1400 nm and 1600 nm was detected for each fibre via the Dual-Wavelength System Princeton Instruments PylonIR infrared spectrometer. 990 nm laser light was used to excite the $^4I_{11/2}$ state. 18% of the population of this state decays to $^4I_{13/2}$ (Malouf et al., 2016), and so exciting to this state gives reasonable $^4I_{13/2}$ to $^4I_{15/2}$ emission while minimising noise. The spectrometer data was converted to the emission cross-section via an arrangement of the Füchtbauer-Ladenburg equation:

$$\sigma_{em} = \frac{\lambda^4}{8\pi c n^2 \tau} \frac{N(\lambda)}{\int N(\lambda) d\lambda} \qquad \text{(Eichhorn, 2008b)}$$

Where N is the counts per wavelength, c is the speed of light, n is the refractive index of the glass, and τ is the radiative lifetime of the excited state. τ was taken to be the value for each fibre listed in Table 12. Both fibre suppliers state the refractive index of their glass is 1.5. In Er:ZBLAN, the radiative lifetime of the erbium $^4I_{13/2}$ state is approximately equal to the total lifetime. Figure 42 shows the emission cross-sections for all fibres. While there is a small amount of variation at the emission peak and at lower energy wavelengths, at 1471 nm the cross-sections are very similar.

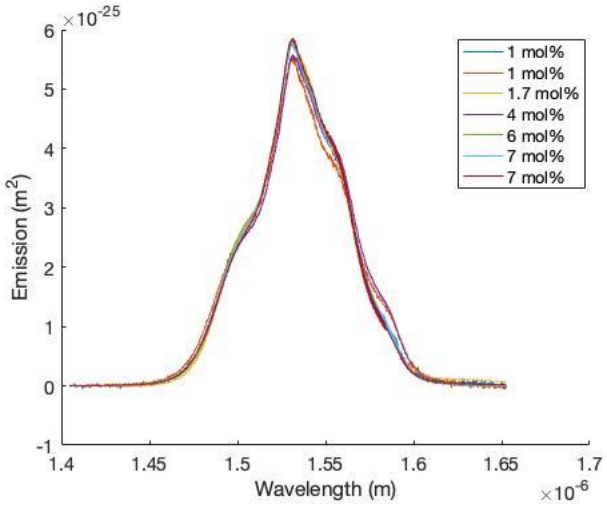

Figure 42: Emission cross-sections calculated from emission data using the near-infrared spectrometer for all Er:ZBLAN fibres used in this chapter.

Using the McCumber relationship (McCumber, 1964), we can acquire the absorption cross-section from the emission cross-section:

$$\sigma_{ab} = \sigma_{em} e^{\frac{(E-\epsilon)}{kT}} \qquad \text{(McCumber, 1964)}$$

Where k is Boltzmann's constant, T is the temperature, E is the photon energy at each wavelength (E = hc/λ), and ϵ is the zero phonon energy, or the lowest energy photon that can excite the erbium ion without the aid of a phonon. T was taken to be room temperature (21°C). The zero phonon energy was calculated by the following equation:

$$e^{\frac{\epsilon}{kT}} = \frac{1+\Sigma e^{\frac{-E_{1j}}{kT}}}{e^{-\frac{E_0}{kT}}(1+\Sigma e^{\frac{-E_{2j}}{kT}})} \qquad \text{(Miniscalo and Quimby, 1991)}$$

Where E_0 is the difference between the lowest energy levels of the two states, E_{1j} is the difference in energy between different Stark levels of the ground state ($^4I_{15/2}$), and E_{2j} is the difference in energy between different Stark levels of the excited state ($^4I_{13/2}$). The Stark levels are the different potential energy level changes that occur when an ion's potential electron energy levels are perturbed by the electromagnetic field of the surrounding medium. The Stark levels of each state can be estimated via peak fitting to emission measurements of erbium in ZBLAN at very low temperatures. The Stark level positions used here were calculated by Huang et al. (Huang et al., 2001).

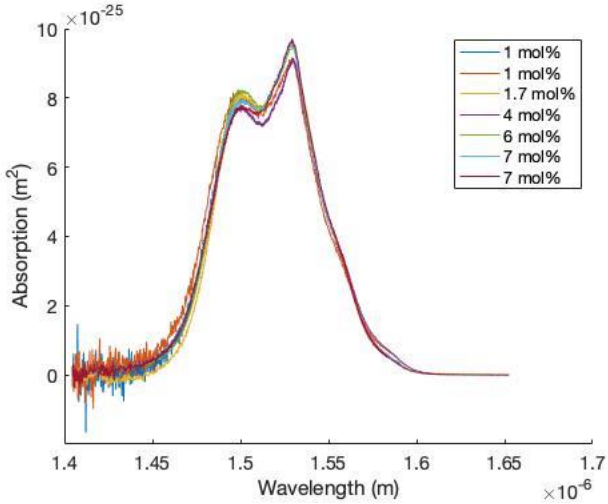

Figure 43: Absorption cross-sections calculated using emission data from the near-infrared spectrometer for all Er:ZBLAN fibres used in this chapter.

The absorption cross-sections gained by calculation were larger than the cross-sections in Henderson-Sapir and Caspary (Henderson-Sapir, 2015, Caspary, 2002) (see Table 11). This is likely due to a difference in calculated zero phonon energy, which the absorption cross-section equation is very sensitive to. Figure 43 shows fibre-to-fibre differences in absorption cross-sections were small, but were not all within errors. The errors calculated take into account random errors within the measurements, but not systematic errors between fibres. W11 results in this section were derived using the absorption cross-section values from

Henderson-Sapir (2015). While OPO software indicated that the laser was tuned to 1470 nm, spectrometer measurements showed a peak at 1471 nm. The absorption cross-section at 1471 nm was used for W11 calculations as the spectrometer is likely to be more accurate than the tuning software of the laser. The W11 calculations are very sensitive to the absorption cross-section value used, and so an error value of 0.4 x 10^{-25} m^2 calculated by the standard deviation of the different fibre results is used in section 3.4 in order to gain an approximate error for the W11 values.

Absorption cross-sections calculated from emission data	
Fibre used	Absorption cross-section (m^2)
Bulk Glass measurements	9.958 x 10^{-26}
1 mol%	2.7 ± 0.3 x 10^{-25}
1 mol%	1.9 ± 0.2 x 10^{-25}
1.7 mol%	1.4 ± 0.2 x 10^{-25}
4 mol%	1.8 ± 0.2 x 10^{-25}
6 mol%	1.7 ± 0.2 x 10^{-25}
7 mol%	2.1 ± 0.2 x 10^{-25}
7 mol%	2.0 ± 0.2 x 10^{-25}

Table 11: Absorption cross-section results at 1471 nm calculated from emission data using the method described above.

3.3.5. Number of ground state ions (N_g)

From Henderson-Sapir (Henderson-Sapir, 2015) the ion concentration (x 10^{20} cm^3) is approximately 1.6 times the mol% value. The mol% values were given by the fibre manufacturers.

3.3.6. Volume (V, aL)

The surface area of the fibre used was found from the diameter of the fibre core, given by manufacturer specifications (between 10 µm and 25 µm, depending on the fibre). In the equation for $N_{1initial}$, length L cancels out and is not used in the equation. Changes in L affects the total ion population but not the ion density. An assumption in the $N_{1initial}$ equation is that the total energy is approximately equal through the fibre length in which light is detected (~1 mm), which relies on the measurement of only a small length of fibre. The short segment measured is achieved by placing the tip of the collecting fibre as close as possible to the Er:ZBLAN fibre, making the length measured approximately 1 mm.

The highest doping rate of the fibres was 7 mol%, and the lowest energy used was approximately 1.5x10^{-6} Joules. Using the modal fibre core diameter of 16.5 µm, this gives a total number of erbium ions of 0.9x10^{13} and 1.1x10^{13} as the total number of photons. The absorption cross-section is of the order of 10^{-21} cm^2, and so the number of photons left unabsorbed after passing through this volume is a similar order of magnitude to the initial number of photons, and so the assumption holds.

3.3.7. Lifetime (1/A)

Three reciprocal lifetimes are used in the model, A1, A21, and A20. The total lifetime for N_1 (A1) and N_2 (A2) were found experimentally fitting to the tail of the 1530 nm time-resolved emission excited by 1471 nm and 980 nm time-resolved emission excited by 990 nm. Lifetimes

differed only slightly between fibres and the results agreed well with literature (Caspary, 2002). The branching ratio for A21 and A20 was taken to be 18% for A21 and 82% for A20 from Malouf et al. (Malouf et al., 2016).

Reciprocal Lifetimes used in the model		
Fibre	A1	A2
1 mol%	110	141
1 mol%	112	141
1.7 mol%	114	141
4 mol%	125	140
6 mol%	116	140
7 mol%	105	139
7 mol%	109	139

Table 12: Reciprocal lifetimes (s^{-1}) used in the differential equation model for fitting to data. Lifetimes are taken by fitting an exponential to the tail of low-energy excited time-resolved emission at 1530 nm and 980 nm.

The fit to obtain W11 values is very sensitive to the lifetime value. Values used in the model are shown in Table 12. An error in A2 of 1 and an error in A1 of 6 were used to gain an approximate error value of W11.

3.3.8. Calibration between 980 nm emission and 1530 nm emission

N_1 data can be normalised directly to the initial N_1 value, but the N_2 data can only be normalised if the difference in emission loss at 980 nm and 1530 nm in the experiment is known. The emission loss takes into account different transmission properties over the collecting fibre, different transmission characteristics in the monochromator gratings, and different sensitivities in the photomultiplier. The calibration value can be measured by experiment, by exciting 980 nm emission and 1530 nm emission directly with a known energy, but this value is sensitive to upconversion, changes in overall detector sensitivity over short time periods, errors in energy measurements, and errors in absorption cross-sections, making the errors in the measurement potentially very large. Instead for the results in this thesis the calibration value between 980 nm emission and 1530 nm emission was found by matching 7 mol% fibre 1530 nm W11 results with 980 nm W11 results for the same fibre.

3.4. Results and Discussion

Initial fitting to 1530 nm emission and results

Time-resolved emission at 1530 nm was normalised to the calculated $N_{1initial}$ value. Emission was fitted to N_1 in 3.2 using the Matlab® differential equation solver (see appendix A2 for code). The energy transfer parameter W_{11} was the only unknown variable.

Erbium percentage	W_{11} ($10^{-18}cm^3s^{-1}$) using 1530 nm decay	W_{11} (10^{-18} cm^3s^{-1}) using 980 nm decay
1 mol%	0.2 (0, 1.9)	1.3 (1.0, 2.1)
1 mol%	0.3 (0, 2.0)	-
1.7 mol%	0.3 (0.1, 0.8)	0.9 (0.6, 1.4)
4 mol%	2.5 (1.7, 4.4)	-
6 mol%	4.2 (2.5, 6.4)	-
7 mol%	11 (7.5, 18)	-
7 mol%	15 (9.1, 29)	Used for calibration

Table 13: W11 results using 1471 nm excitation, 1530 nm emission and 980 nm emission. Given confidence intervals are an indication of the variability using errors in lifetime and absorption cross-section measurements.

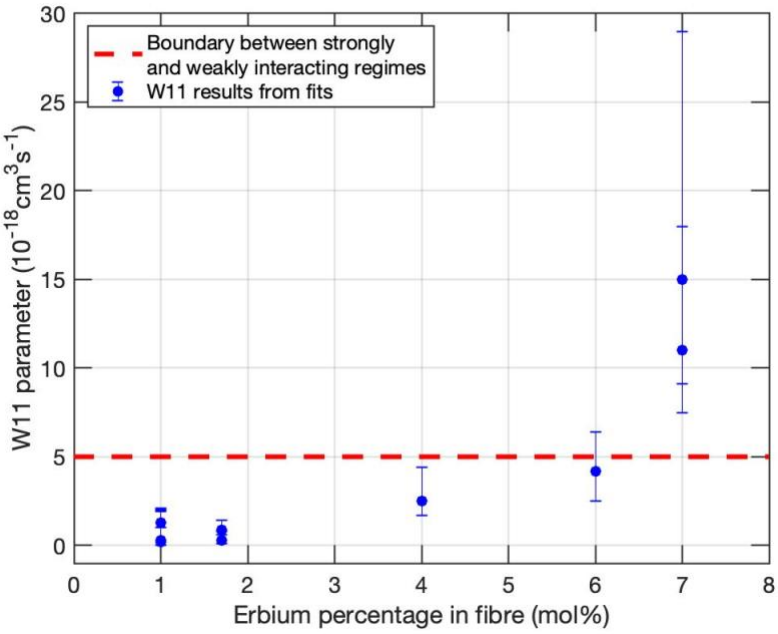

Figure 44: Erbium percentage in fibre vs measured W11 value for all fits. Confidence intervals are taken using the standard deviation of lifetime and absorption cross-section fibre-to-fibre variability. The red dashed line indicates the boundary between the weakly interacting regime and the strongly interacting regime (Gorjan et al., 2011).

The W11 level at which the strongly interacting regime comes into play is said to be 5 x10^{-18} cm^3s^{-1} (Gorjan et al., 2011). W11 results using the 1530 nm decay crossed this line: fibres with 1-4 mol% erbium were in the weakly interacting regime, 7 mol% erbium fibres were in the strongly interacting regime, and the 6 mol% fibre could be in either within errors (see Figure 44 and Table 13). The differential equation model fitted well to 1530 nm emission from ZBLAN fibres with 4, 6, and 7 mol% erbium (Figure 45—see appendix A3 for all fibre results). W11 results for data sets from the same fibre at different energy levels were similar, and the results in Table 13 are the average value. Fit errors were very small, but the fit was very sensitive to

changes in both lifetime values and absorption cross-section values. Confidence intervals in Table 13 are taken by varying these values in the model fit by the amount detailed in sections 3.3.4 and 3.3.7.

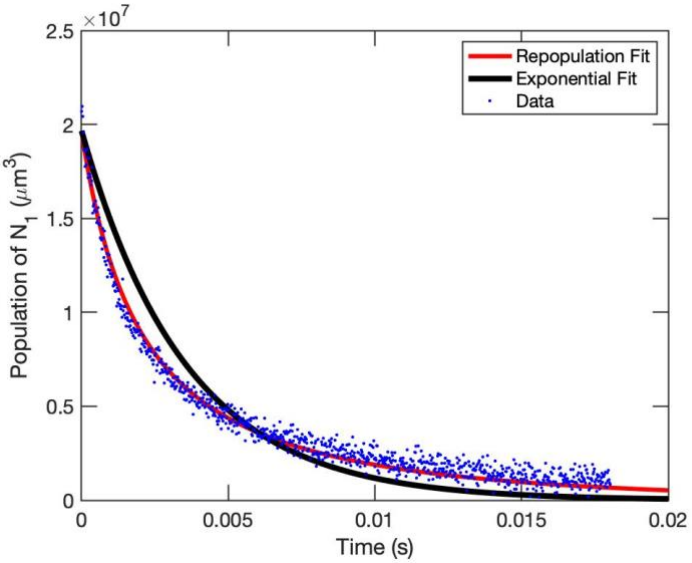

Figure 45: 7 mol% erbium-doped ZBLAN fibre time-resolved emission at 1530 nm fitted to N_1 in the rate equation model.

Fits to 1530 nm emission from 1 mol% and 1.7 mol% fibres were very close to fits to a simple exponential (Figure 46) and not all of the different energy data set series could be fitted for each fibre. Results given in Table 13 are for the fit with the smallest error. The difficulty in fitting the W11 parameter to the 1530 nm emission implies that for these fibres $A_1 >> 2*N_1*W11$, or that the depletion of the state is dominated by the fundamental lifetime of the state.

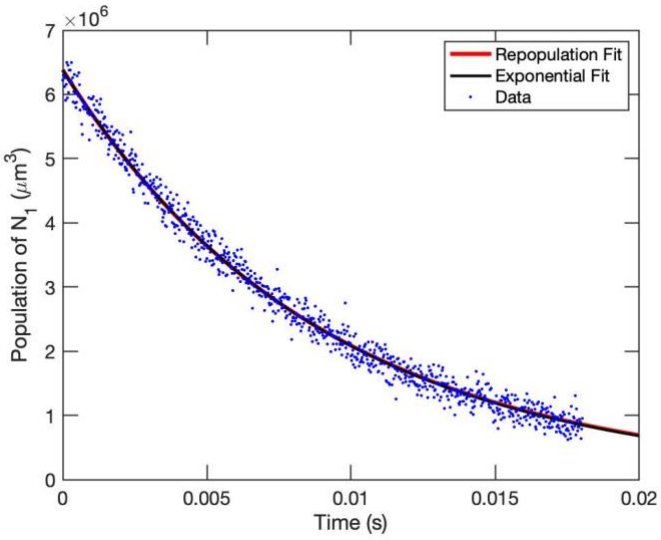

Figure 46: 1 mol% erbium-doped ZBLAN fibre time-resolved emission at 1530 nm fitted to N_1 in the rate equation model.

3.4.1. Fitting to 980 nm emission and results

The N_2 state is only populated by energy transfer, and so the energy transfer parameter has a much larger proportional effect on the total change of population at N_2. Time-resolved emission at 980 nm was measured for 1 mol%, 1.7 mol%, and 7 mol% fibres. For 1 mol% and 1.7 mol% fibres, approximately 27 hours of integrated signal time was necessary to gain a reasonable signal-to-noise level. For the 7 mol% fibre, one hour of integrated signal time was sufficient. The 7 mol% fibre was used to calibrate the sensitivity difference of the experimental system between 1530 nm and 980 nm, by changing the calibration constant so that the W11 value for 980 nm data matched that of 1530 nm data. This gave a reasonable fit to the data, with little-to-no trend in the fit residuals and an R^2 value of 0.98 (Figure 47).

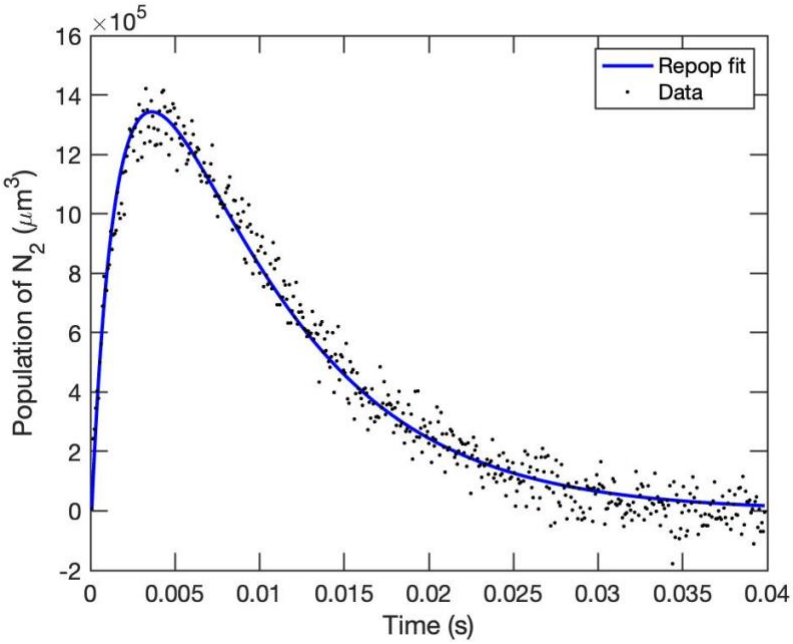

Figure 47: Fit to 7 mol% Er:ZBLAN fibre data of time-resolved 980 nm emission with the calibration constant used to normalise 980 nm data set so that W11 values match with 1530 nm data.

It should be noted that the normalisation of 980 nm data using 1530 nm measurements relies on the sensitivity of the detector remaining the same between 980 nm measurements and 1530 nm measurements. The photomultiplier is cooled with a liquid nitrogen pump, and drifts in temperature may change the sensitivity of the detector. The sensitivity change between a 980 nm measurement and a 1530 nm measurement can be estimated using the background counts of the emission, as the background count rate changes with changing sensitivity. Dividing the emission by the background before normalisation did not affect the W11 fit result, indicating that the sensitivity difference between 980 nm emission and 1530 nm emission data is small. It should be noted however that W11 values gained from 980 nm will have larger errors than 1530 nm emission fits due to this variable.

1 mol% and 1.7 mol% fibre data gave W11 results of 1.4 $x10^{-18}$ cm^3s^{-1} and 0.9 $x10^{-18}$ cm^3s^{-1} respectively (see Table 13). The equations fitted well to the data (see Figure 48), though the large scatter in the data means that a wide range of values allowed a good fit; more integration than the 27 hours used will be needed for more clarity in this fit. The W11 results

were larger than the results found for 1530 nm emission, but were within the large relative errors of the 1530 nm results and are still smaller than the results for the 4 mol% fibre.

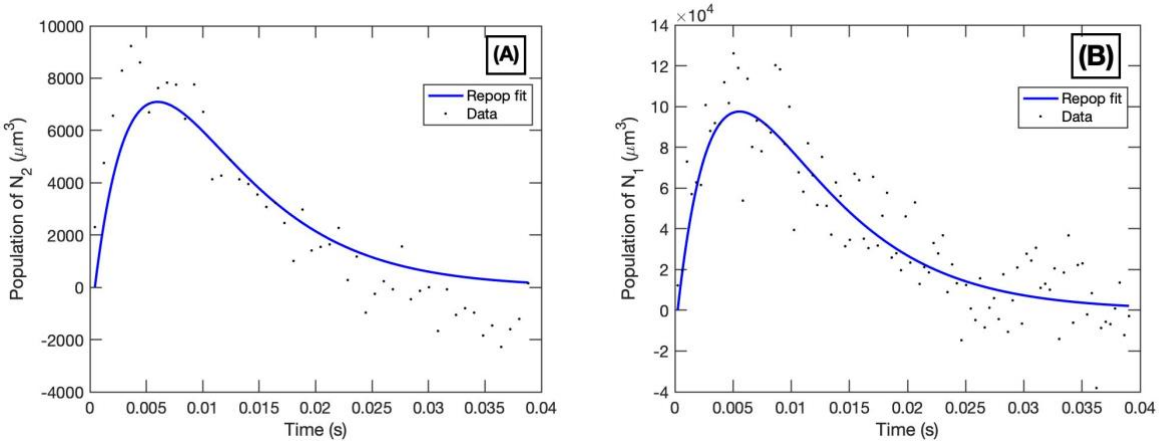

Figure 48: Fit to time-resolved emission at 980 nm for A) the 1 mol% Er:ZBLAN fibre data; B) the 1.7 mol% Er:ZBLAN fibre data. Each data point represents 5 binned data points to increase clarity.

3.5. Summary and conclusions

For the first time, energy transfer parameters have been calculated directly from emission in Er:ZBLAN fibre. W11 values calculated via 1530 nm emission were on the order of 10^{-18} cm^3s^{-1} and crossed from the weakly interacting regime for low-doped fibres to the strongly interacting regime for high-doped fibres (6 mol% and 7 mol%). Values calculated for 1 mol% and 1.7 mol% fibres via 980 nm emission were higher than those calculated by 1530 nm, but are still within the range expected considering the other fibre results (see Figure 44). The W11 values gained using 980 nm emission have tighter errors than 1 and 1.7 mol% W11 values gained using the 1530 nm emission, but longer integration times for 980 nm measurements are needed for greater precision of W11 results for these lower-doped fibres.

The calculated 1.7 mol% W11 value using the 980 nm emission was lower than the 1 mol% W11 value, which may be indicate the presence of unaccounted errors, but is likely an indication of the level of fibre-to-fibre variability within erbium-doped ZBLAN fibres. This variability will need to be taken into account in future fibre laser models.

4. — Potential for Fluorescence in Some Commercially Significant Minerals

4.1. Introduction

While mines by definition are at deposits of higher-than-crustal average levels of commercially exploitable minerals, the concentration of those minerals typically varies throughout the deposit. Real-time detection of economically significant minerals can aid in rock sorting, "selective mining" or "grade engineering", allowing mine feed with low or no concentration of the mineral of interest to be discarded. This creates increased efficiency, as these discarded rocks would otherwise go through further cost-incurring mineral processing. In addition, different minerals with the same end product (e.g. the copper sulphides) may behave differently under the same mining processes, and so knowing the proportions of these minerals present can aid in processing decisions. There is therefore great economic need for a real-time detection method capable of identifying mineral species, such as fluorescence sensing, to be useful in detecting these minerals in a mining context.

Novel measurements from the Dual-Wavelength System are presented in this chapter; minerals of interest are reviewed below. It must be emphasised that the Dual-Wavelength System measurements were used to test the reliability and output of the System, and were conducted before the Princeton Instruments near-infrared spectrometer was integrated. This meant that excitation and emission scans in the most likely infrared bands of these minerals were not conducted in this study; excitation and emission areas to focus on in further studies are highlighted and discussed.

Minerals selected for the study reported in this chapter were chosen as they are minerals of historical and continued commercial significance for Australia (Britt et al., 2019). Their historical importance ensures accessible museum-grade samples for measurement, and their continued significance ensures their relevance. The samples selected are:

- Copper and iron sulphides. Pyrite (iron sulphide) is a commercially significant iron mineral, and is also found in copper porphyry deposits. Distinguishing between copper-iron and iron sulphides is important for grade determination. The different copper sulphides can react differently in ore processing, and so it is valuable to be able to distinguish between them.
- Zinc iron sulphides. Zinc production in Australia is generally through sphalerite (Zn, Fe)S. The presence of sphalerite and the zinc content of the sphalerite are valuable variables for mine production and processing.
- Uranium oxide. In commercially significant concentrations, uranium can be a valuable mined resource; below commercially significant concentrations uranium can be a significant penalty element when mining other resources. Knowing the concentration of uranium and the mineral it resides in can determine the commercial viability of an ore and the processing it must undergo before an end-product is made.

4.2. Experimental parameters

All experiments shown in this chapter were conducted on crushed and pelletised samples with the Dual-Wavelength System equipment (see chapter two). Ultra-violet excited emission was measured using one Radiant OPO with the UV module installed, and the visible-range spectrometer. Emission was observed whilst exciting from 220 nm to 400 nm in 20 nm steps. The filters used are shown in Table 14:

Excitation range	Filters in laser path	Filters in detector path
220 nm	-	325 nm longpass
240-300 nm	311 nm shortpass	325 nm longpass
320-360 nm	390 nm shortpass	400 nm longpass
380-400 nm	430 nm shortpass	440 nm longpass

Table 14: Filters used in ultraviolet excitation experiments shown in this chapter.

Dual-excitation scans used the Resonate Systems Labview software to automatically create and collect experimental data. Minerals mentioned in this chapter underwent 750 nm-1500 nm dual-excitation scan, which used 715 nm longpass filters to prevent leaked higher-energy OPO excitation light reaching the sample, and 700 shortpass filters on the EMCCD and visible spectrometer. The infrared spectrometer was not used as it was a later addition to the system and not available at the time of measurements. Where mentioned, some minerals were put under the 540 nm-700 nm dual-excitation scan, which used 715 nm shortpass filters to prevent leaked lower-energy excitation light from reaching the sample, and 530 nm shortpass filters on the detection equipment. Unless stated otherwise, OPOs were used at full power.

Samples were prepared as described in chapter two. Samples were originally in a bulk crystal or matrix form, and obtained from offcuts of museum-grade samples. Samples obtained from the Tate Museum have been previously identified by mineralogists. Only traditional mineral identification methods were used for all samples except the pyrite and chalcocite samples, which had additional identity confirmation via X-ray diffraction (XRD) analysis. Subsamples were taken and crushed by hand. The resulting powder was pelletised for use in the Dual-Wavelength System. The amount of sample required for a pellet is approximately 1 gram, and pellet size was approximately 1 cm^2. Table 15 lists samples used in this chapter.

Sample appearance before crushing	Sample description and notes
Copper and iron sulphides	
	Pyrite (FeS_2), Gumeracha Talc Mine, South Australia, Australia (Tate Museum # 18395) This sample is one of multiple single-crystal octahedral or dodecahedral pyrite samples collected. The mineral structure has previously been confirmed by the Tate Museum via XRD analysis.

	Covellite (CuS), Anaconda, Mt. Malcolm, Western Australia, Australia (Tate Museum # 2054) Covellite in this sample appears as bright spindle growths in a dark earthy matrix.
	Chalcocite (Cu_2S), Burra Mine, South Australia, Australia (Tate Museum # 19763) While this sample is weathered on the surface, it has a relatively solid crystal structure throughout, though includes pyrite. Previous studies from the Tate Museum have confirmed the mineralogy of this sample via XRD.
	Chalcopyrite ($CuFeS_2$), Mt. Lyell, Tasmania, Australia (Tate Museum # 4265) This is a large mineral specimen that includes both chalcopyrite and pyrite.
	Bornite (Cu_5FeS_4), Moonta, South Australia, Australia (Tate Museum # 3751) This mineral has minimal visible weathering on the outside, and is a single mineral sample.
Zinc/iron sulphides	
	Ruby Sphalerite (ZnS), Ballard Mine, Baxter Springs, Kansas, USA (Tate Museum # 19525) This sphalerite when crushed is a pale white/pink colour, which generally indicates a low iron content. The intact crystal is translucent, unlike sphalerite samples with higher iron contents. While most sphalerites in the field would not be this iron-poor, fluorescence results from this sample would be a good starting point for further work.

	Sphalerite ((Zn,Fe)S), Broken Hill Mine, Broken Hill, New South Wales, Australia (Tate Museum # 2511) This sphalerite grew adjacent to manganocalcite (as well as galena), which may mean that it has incorporated a reasonable amount of manganese into its structure. This sample was chosen as manganese is the main fluorescence centre currently known in natural sphalerite (Baramin, 2010).
Uranium oxide	
	Uraninite (UO_2), South Alligator Gorge, Northern Territory, Australia (South Australian Museum # G30201) Upon visible inspection this sample looks like one mineral type internally, but has yellow weathering components on the external face. Due to the small size of the sample (<1 cm^3) when processing for analysis some of this yellow material was incorporated into the sample pellet.

Table 15: List of samples used in this chapter with descriptions and photographs of intact sample appearance.

4.3. Copper and iron sulphides

4.3.1. Introduction

Copper sulphides are the largest source of mined copper in the world (2020a, King, 2005). Large deposits are found in Australia, especially in the copper-gold deposits of the Gawler Craton in South Australia. Copper and iron sulphides tend to have small band gaps and have previously been researched for their semiconductor properties (Zhou et al., 2014, Hwang et al., 1982). Table 16 lists the copper and iron sulphides used in this chapter and their band gaps:

Name	Molecular Formula	Band Gap energy (eV)	Minimum wavelength to bridge the Band Gap (nm)
Pyrite	FeS_2	0.9	1377
Chalcopyrite	$CuFeS_2$	0.6	2066
Chalcocite	Cu_2S	1.8	688
Covellite	CuS	2	619
Bornite	Cu_5FeS_4	1	1240

Table 16: Name and band gap energies of various sulphide minerals. Energies are from (Crundwell, 1988).

Unfortunately there are few known fluorescence signatures associated with copper sulphides, and none recorded in natural materials. Chalcocite nanoparticles have been seen to fluoresce between 900 and 1200 nm (Kriegel et al., 2012, van der Stam et al., 2017). Cathodoluminescence in powder pellets and thin films appear in the same region (Hwang et al., 1982, Loferski et al., 1979). The cathodoluminescence peak shifts with different phases of

chalcocite trending towards covellite (Cu_2S to $Cu_{1.75}S$), associated with the shifting band gap. Two-photon absorption emission has been seen in covellite nanodisks, emitting broadly around 400-550 nm when exciting around 800-1400 nm (Marin et al., 2016). This emission was enhanced by surface plasmon resonance and would be unlikely to be seen in bulk material.

The literature on pyrite emission is sparse, but natural pyrite has been seen to have OSL and TL characteristics (Tan et al., 2003), implying a potential for fluorescence via ion inclusions and the band gap. Both copper and gold-associated pyrite showed OSL and TL from different emission centres.

4.3.2. UV excited spectra

Of the copper and iron sulphides studied in this chapter (see Table 15), in the limited wavelength range analysed only chalcocite showed emission (Figure 49). Emission in the near-infrared was seen when excited at 400 nm, but not for any other excitation wavelength. A repeat with 400 nm excitation the day after showed no emission, which is thought to be due to the freshly-ground chalcocite oxidising to covellite (a known phenomena under normal temperature and atmospheric conditions (Kriegel et al., 2012)).

The emission peaks at 925 nm and 1025 nm are likely chalcocite peaks—chalcocite nanoparticles and thin films are known to fluoresce between 900-1100 nm using different excitations. (Kriegel et al., 2012) observed luminescence at around 900 nm when exciting at 400 nm, but the luminescence was quenched as the sample was exposed to oxygen, which creates copper vacancies. Usually chalcocite fluorescence is seen as only one peak, but different copper to sulphur ratios (i.e. trending towards covellite) have different optical properties. Partial oxidation, therefore, would create the multiple peaks seen in our sample.

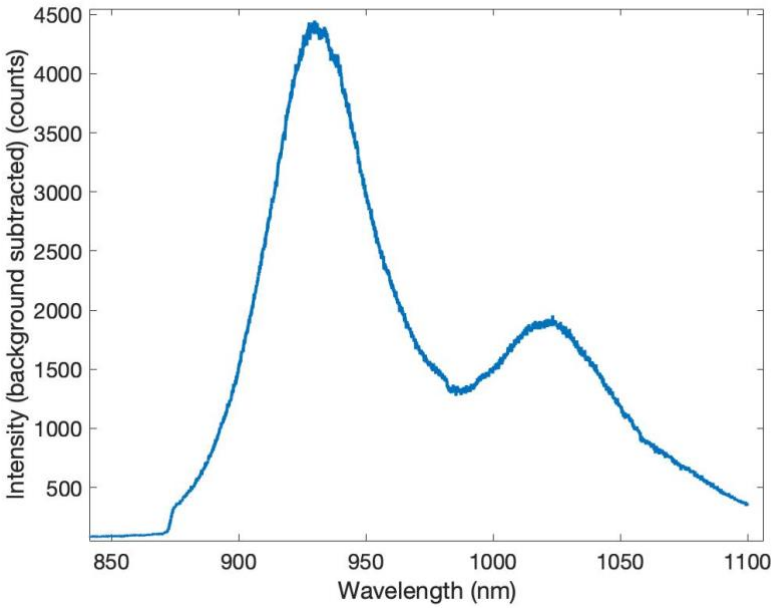

Figure 49: Chalcocite emission detected using 400 nm excitation and the visible spectrometer.

4.3.3. Dual-wavelength excitation scans

Copper sulphides have large optical absorption cross-sections and low thermal conductivity; it was found in initial tests on copper sulphides and pyrite that using the OPOs at 100% power (up to 20 mJ in the wavelength range scanned) damaged the samples (Figure 50). New samples excited at approximately half laser power (up to 10 mJ) were not damaged and did not show any upconversion fluorescence.

Figure 50: Crushed and pelletised bornite samples. Left: undamaged; right: damaged by laser light. The yellow circle marks the approximate position of the damage (seen visually by dull vs lustrous appearance). The outer sample holder dimensions are 12 mm by 12 mm.

4.4. Zinc sulphides (sphalerite)

4.4.1. Introduction

Sphalerite (Zn,Fe)S is the main ore used for zinc production. The proportion of iron to zinc is variable, with zinc-rich sphalerite called 'ruby sphalerite' and iron-rich sphalerite called 'marmatite'. The fluorescence of sphalerite can change significantly depending on the proportion of zinc to iron present in its structure. Studies of intrinsic 490 nm luminescence in artificially created sphalerite microcrystals indicate that iron acts to quench luminescence present in pure ZnS (Sambasivam et al., 2009), potentially due to the broad absorption of iron ions and the increased phonon energy of iron-containing sphalerite. Natural bulk samples are not known for luminescence via lattice defects, but emission via inclusion of ions such as Mn^{2+} or Cu^{+} is well known (Baramin, 2010). Experiments with artificially grown Mn-doped ZnS microcrystals reproduce the Mn emission at 590 nm seen in natural samples, and also find defect-related violet emission at 390 nm (Ab-Rahman et al., 2010). The below sections show UV-excited results for our natural samples, and discussion on upconversion fluorescence studies.

4.4.2. UV excited spectra

The Broken Hill sphalerite showed the expected manganese emission peak (
Figure 51) at every excitation wavelength besides 380 nm, which would fall between two absorption peaks. The ruby sphalerite showed a broad emission structure comprising many peaks (Figure 52 and Figure 53): peaks near 900 nm and 700 nm were seen at all excitation wavelengths, while multiple peaks from 600 to 1000 nm began to emit at lower energy excitation.

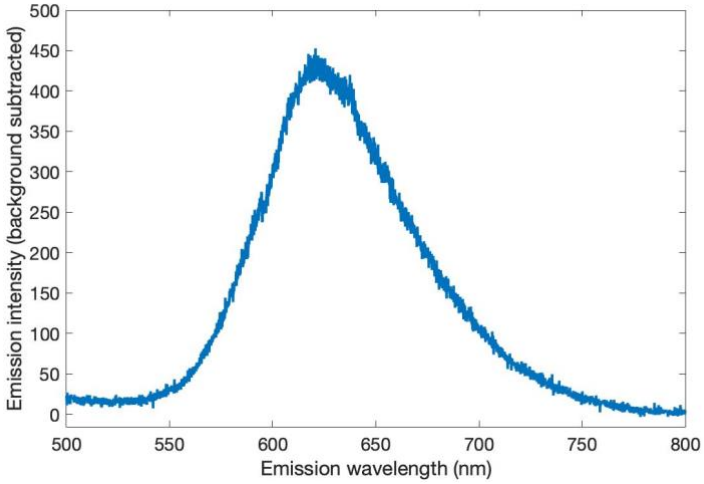

Figure 51: Manganese 2+ peak in Broken Hill Sphalerite, excited at 220 nm using the Radiant 2608 OPO and detected by the Princeton Instruments visible spectrometer.

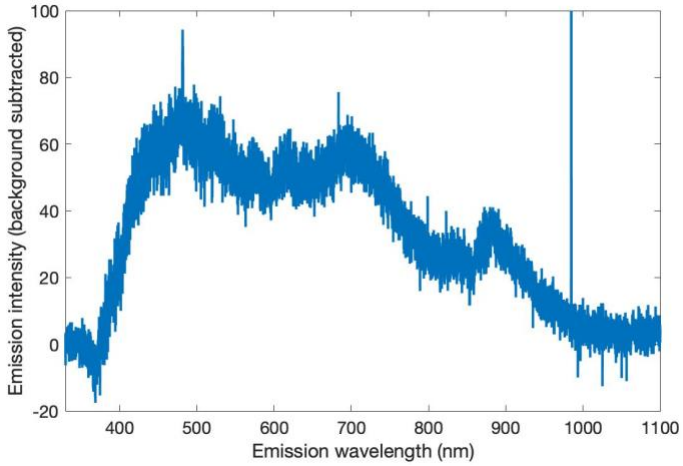

Figure 52: Ruby Sphalerite emission excited at 240 nm and detected using the Princeton Instruments visible spectrometer.

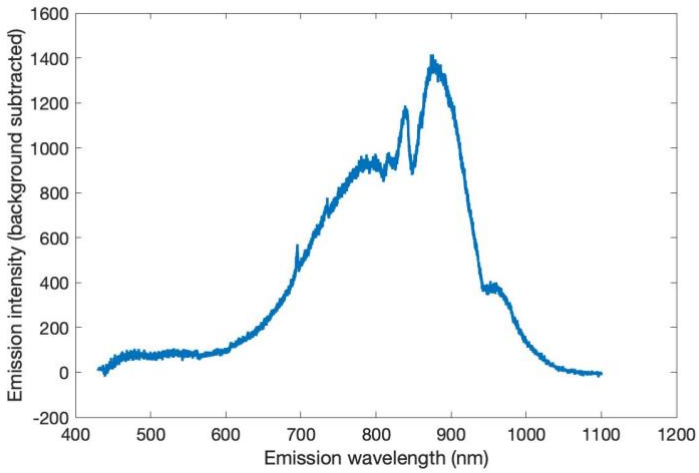

Figure 53: Ruby Sphalerite emission excited at 400 nm and detected by the Princeton Instruments visible spectrometer.

4.4.3. Dual-wavelength excitation signal/noise issues

Dual wavelength scans proved complex to analyse, due to increased excitation leakage at octaves of the excitation wavelength. Current filters, up to three stacked together, were not enough to lower this to insignificant levels. While this may be due to the large reflection coefficient of sphalerite in the near-infrared range (20-60% as compared to at or below 10% for the copper sulphides), this problem was not observed for fluorapatite, which has a comparable reflection coefficient (Kokaly et al., 2017). A potential explanation is that the large rare earth element and transition metal incorporation in fluorapatite, which increases absorption. Sphalerite may also have a different response to crushing, producing powdered grains with shapes more favourable for scattering. While small, broad features would have been hidden by this highly reflective behaviour, we can say that no large, distinct upconversion fluorescence features were seen in sphalerite.

4.5. Uraninite

4.5.1. Introduction

Uranium is a radioactive element from the actinide series, commonly used for power generation and military purposes, and formerly used as a phosphor for green glass. Due to its toxicity and radioactivity, it can be a hazard in mine sites, and is typically carefully monitored even when present in commercially insignificant amounts. Uranium ores of economic significance include uraninite (UO_2), pitchblende (U_3O_8), and brannerite ($UTiO_6$) (2018b). Uraninite, the most common of these minerals, was chosen for the below analysis.

Uranium fluorescence occurs due to the excitation of electrons within the uranium ion's inner 5f electron energy shell, analogous to the 4f optically active shell in rare earths. Which areas of the inner shell of the ion are optically active depends on the oxidative state of the ion. Uranium comes in many oxidative states, though most natural samples have uranium in 4+ or 6+ form. U^{2+} emits fluorescence at around 2600 nm, while U^{3+} emits fluorescence around 450 nm (Hargreaves, 1970). U^{4+} is known to emit fluorescence at 350 nm (Mandal et al., 2007). The uranyl ion, or UO_2^{2+} (U^{6+} combined with 2 oxygen ions), emits between 500-600 nm (Nichols and Merritt, 1911), and is the origin of the characteristic "green glass" colour imparted by uranium in glass.

Fluorescence in natural uranium minerals is most commonly seen via intrinsic uranyl ion fluorescence, around 550 nm (Baramin, 2010). The uranyl ion is a component of various uranium silicate and carbonate structures, often including rare earths, phosphate compounds, or transition metals. While many of these fluoresce, the uranyl ion is not commonly associated with the more commercially significant uranium minerals, such as uraninite, which have uranium occurring in a 4+ oxidative state.

There have been previous upconversion fluorescence studies on uranium compounds (Hubert et al., 1984, Mandal et al., 2007). Hubert et al. analysed upconversion in U^{4+}:$ThBr_4$, and reported red luminescence from 950 nm excitation, 1170 nm excitation, and a mixture of both wavelengths. Mandal et al. observed fluorescence at 366 nm and between 400 and 420 nm after excitation at 498 nm in U^{4+} phosphite crystals. Power dependence studies indicate a two-photon process. The Mandal et al. predicted excitation path involves a large non-

radiative decay step, and so this particular upconversion pathway would be more efficiently excited by two wavelengths.

Most commercially significant uranium ores have uranium in a 4+ state, such as uraninite (UO_2). U^{4+} typically has broad absorption lines compared with 2+ or 3+ ions (Hargreaves, 1970), and is known to fluoresce in artificial compounds (Mandal et al., 2007, Hubert et al., 1984). While some rare earths are able to fluoresce and upconvert as constituents of the intrinsic structure of a host material (such as erbium in erbium oxide), it is unknown whether uranium is able to do this, as it requires a very well shielded optically active area. The broad absorption lines in U^{4+} seen by Hargraves in their uranium-doped CaF_2 implies that there may be significant host perturbation in U^{4+} even within a low-phonon energy material like fluorite.

4.5.2. UV excited emission

All excitation wavelengths showed an emission peak at 550 nm (Figure 54). This is typical of the uranyl (UO_2^{2+}) ion (Nichols and Merritt, 1911), and so is likely from the yellow weathering material on the edge of the solid sample rather than the uraninite itself.

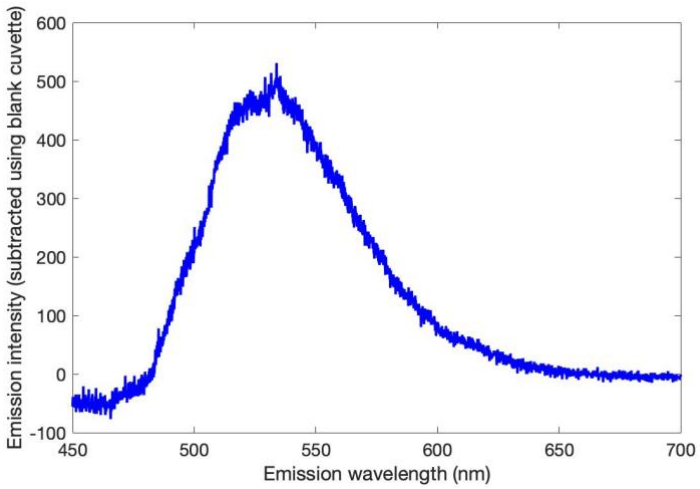

Figure 54: Emission from uraninite sample exciting at 340 nm and detecting emission using the Princeton Instruments visible spectrometer..

4.5.3. Dual-wavelength excitation scans

Dual-wavelength scans were performed in the relatively limited wavelength range between 750 nm and 1500 nm did not show any signal between 400-700 nm for the uraninite in this range, but future work includes excitation of these wavelength ranges is intended when the Dual-Wavelength System capability is in place. Visible dual-wavelength scans exciting between 540 nm and 700 nm could have showed the 550 nm uranyl ion emission when exciting at 540 nm to 560 nm (Figure 55), but the signal seen is more likely to be the tail of the laser excitation, as the excitation range is much narrower than the UV-excited signal.

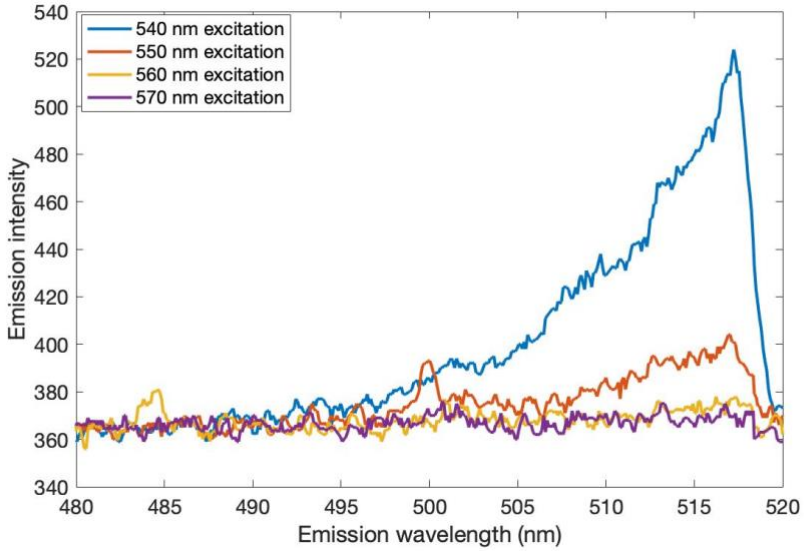

Figure 55: Signal-signal dual-wavelength excitation spectral response of the uraninite sample at excitation wavelengths near emission range and edge of filter. Data are the emission where the wavelengths are 'doubled' in the matrix—540 nm on OPO 1 (3603) with 540 nm on OPO 2 (3608), for example. The sharp drop of emission at 517 nm shows the shortpass filter cutoff.

4.6. Discussion and future work

Upconversion scans using the Dual-Wavelength System were successfully trialled on multiple samples. Although no upconversion fluorescence was seen in this section, only a small range of wavelength combinations were tested, crucially, the choice was limited by the available wavelengths. Wavelength ranges more suited to these minerals will be tested in future work, and are identified and discussed below.

Chalcocite fluorescence was observed but only persisted for a short period of time, leading to the belief that the pressed powder oxidised to covellite in air, as previously reported (Kriegel et al., 2012). Copper sulphides have low transmission across most wavelengths, and so it would not be feasible even for larger pieces of chalcocite to show chalcocite emission through the opaque outer oxidised layer. Chalcocite/covellite determination, then, is not feasible in the field using real-time fluorescence detection unless the ore is measured immediately after fracture. There is some scope for chalcocite fluorescence measurements for application in core analysis and laboratory-based methods.

Upconversion fluorescence has been shown to occur in semiconductors by using the band gap as a second excited state (Wang et al., 2007, Johnson et al., 1982). The step involving the band gap allows travel across the material, linking excitation and emission processes that may be physically far apart. In this process, the fluorescence emission is of a lower energy than the band gap of the material. The Dual-Wavelength System scans completed in this initial study used detection ranges of 400-700 nm, whereas the sulphide band gaps are in the 600-2,000 nm range, and so band gap-associated emission was outside the detection range. Future scans will be able to take advantage of the spectral range of the infrared spectrometer (900-1700 nm) while exciting with OPO wavelengths between 1,500 nm and 2,500 nm.

Future sphalerite upconversion studies will have to take into account sphalerite's high reflectivity. A solution suitable for randomly-orientated mineral such as powders or cross-belt sensing is to simply add further filters in front of the detection optics. However, this will need careful optimising to avoid negating the ability to detect fluorescence emission with a low fluorescence efficiency, as while the filters have windows of low optical density in the detection areas of interest the optical density is not zero.

A potential way to minimise reflections in detector optics from a sample is to direct the main specular reflections to a particular area. To this end we could trial replacing pressed powder pellets with polished sections. The crystal structure of the sphalerite sample will have an effect on how light is scattered, but the bulk of scattered light will scatter off the flat surface at an incident angle to the surface. The sample can be angled so that reflections impact a light absorber and so do not strike detectors or mirrors in the sample chamber.

Upconversion fluorescence in U^{4+} ions had previously been seen when uranium ions were doped into a sample host; the excitation wavelengths 950 nm and 1117 nm (Hubert et al., 1984) were replicated in the 750 nm to 1500 nm dual-wavelength scan, but did not show upconversion emission in the Alligator Gorge uraninite sample. The 498 nm excitation (Mandal et al., 2007) was not replicated in our experiments but will be tested in future programs.

U^{4+} ions are easily perturbed by host lattice structures compared with rare earth elements due to a decrease in electron shielding of the optically active energy bands. This increases the likelihood of ion-lattice interaction and non-radiative de-excitation pathways; it is therefore unlikely that they will give fluorescence in a relatively simple structure such as uraninite. It is more likely that upconversion fluorescence would be found in more complex uranium-bearing minerals where the ion is further removed from the lattice, such as brannerite ($UTiO_6$), coffinite ($U(SiO_4)$-nH_2O), and uranium phosphates such as torbernite ($Cu(UO_2)_2(PO_4)_2$-$12H_2O$). The complex structure of the lattices of these minerals gives uranium ions a greater chance to be isolated from non-radiative energy transition states. Complex uranium structures that contain the uranyl ion, such as torbernite, are known to have fluorescence pathways, and so are more likely to undergo upconversion fluorescence. These complex minerals are also known to incorporate large amounts of rare earths in their structures, paving the way for inclusion-based upconversion fluorescence.

In summary, more promising upconversion excitation and emission ranges have been identified for future sulphide mineral scans including wavelengths deeper into the infrared then it was possible to study with this apparatus as-available during this work. Simple-structure uranium-bearing minerals may not have the potential for intrinsic mineral upconversion fluorescence, but complex uranium minerals and ion inclusion-related upconversion occur in synthetic samples and will be investigated for natural samples in future studies.

5. — Upconversion Fluorescence and the Potential for Concentration Determination of Natural Fluorine-Bearing Minerals

5.1. Introduction

Fluorine is a highly reactive element which can either help or hinder mineral processing, hence knowledge of the concentration of fluorine in mineral processing is an important control parameter. In this chapter:

- Upconversion fluorescence is reported in a natural mineral for the first time.
- Two naturally occurring minerals that contain fluorine—fluorite and fluorapatite—are analysed for "novel" fluorescence signatures. Selected signatures are then tested for use as mineral concentration proxies.
- A previously unreported conventionally excited fluorescence signature was discovered for fluorite, associated with lattice defects.
- A known conventional fluorescence signal in fluorapatite is successfully used to determine fluorine grade in a natural ore series.

5.1.1. Fluorescence of fluorine minerals

Fluorine is predominantly held in two naturally occurring minerals, fluorite (calcium fluoride, CaF_2); and fluorapatite (calcium fluorophosphate, $Ca_5(PO_4)_3F$). It can also be found in biotite (a type of mica) and other minerals in significant amounts depending on geology of the area.

Fluorite is a natural mineral most famous for its luminescence properties (the word 'fluorescence' comes from 'fluorite' (Stokes, 1852)). Fluorite is known to strongly uptake rare earth elements that are in the environment at formation. Fluorite has a low maximum phonon energy, which leads to limited non-radiative pathways, longer excited state lifetimes, and subsequent enhancement of fluorescence. Rare earth elements can be easily identified in fluorite by their distinctive emission lines (Czaja et al., 2012). An interesting property of fluorite is its tendency to 'clump' 3+ ion-state rare earth elements together, in either pairs for light rare earths or groups of six for heavy rare earth elements (Catlow et al., 1984) in order to balance out lattice charge and structural deformation. This clumping allows ion inclusions in fluorite to be in close proximity to each other to enable energy transfer processes, despite natural inclusion concentrations generally being far below the typical doping percentages of synthetic upconversion materials.

Fluorapatite is also a known fluorescent mineral (Baramin, 2010). Compared with other minerals it is a low phonon energy material (Duminis et al., 2017) and so fluorescence is more likely to occur. Synthetic fluorapatite has been previously studied as a laser material (Faure et al., 1996) and as a host lattice for upconversion nanoparticles (Li et al., 2014, Syamchand and Sony, 2016). Like fluorite, it is known to strongly uptake rare earth elements. These substitute for calcium in the lattice, and 3+ ion-state rare earth ions balance lattice charge in two ways (Karbowiak and Hubert, 2000). One is by substituting in nearby calcium lattice sites with an adjacent calcium vacancy to balance charge ($3Ca^{2+} \rightarrow 2RE^{3+}$ + Vacancy). Another is by

the substitution of a F^- ion adjacent to the calcium site with an O^{2-} ion. This means that fluorapatite is unlikely to produce the large clumping sites that fluorite does.

5.1.2. Mineral Sensing

Samples of these fluorine minerals were chosen as test minerals of fluorescence-based ore grade determination because of their known abundance in mineral deposits and fluorescent nature. For a mineral signature to be useful for identifying a specific mineral for use in mineral mining and processing, a number of conditions need to be met:

1) Signals must be strong enough to be detected at mineral concentration levels at or below the threshold at which the mineral begins to interfere with processes or becomes commercially significant.
2) Signals must be present in all occurrences of a mineral at a particular mine site (to prevent false negatives).
3) The surrounding ore must have a low or subtractable background that does not interfere with the mineral signal (to allow analysis and prevent false positives).
4) Resolution of the signal must take less time than the minimum readout speed required by the mineral processing procedure (near real-time).

The desired spectral properties will be different for each mineral signal, surrounding ore, and process. Tests with bright signals typical of fluorine minerals in laboratory settings will confirm if fluorescence has the potential to be used in the field, or whether there are fundamental issues with fluorescence signals that preclude this application.

5.1.3. Chapter synopsis and aims

Fluorite is an ideal test mineral for upconversion studies in a natural sample, combining good likelihood of success with clear economic applications. It may provide bright upconversion due to its clumping of rare earths and low phonon energies. The rare earth ion erbium studied in chapter three is useful for initial upconversion studies, as it has multiple upconversion fluorescence pathways that can be excited with one wavelength.

This chapter reports the following:

- The identification of fluorescent signatures in fluorite and fluorapatite samples using Stokes' (conventional) fluorescence techniques.
- Signatures that are common to all mineral samples of the same type are chosen and analysed in synthetic and natural ore concentration series.
- Upconversion fluorescence properties of fluorites are analysed from known erbium excitation levels, and other upconversion signatures are searched for using the Dual-Wavelength System in a highly fluorescent fluorite sample.
- Erbium upconversion is used to analyse the potential for upconversion fluorescence in grade determination on a synthetic concentration series.

5.2. Rare-earth and transition metal conventional fluorescence from fluorite and fluorapatite

5.2.1. Rare-earth conventional fluorescence in fluorites

Much of the fluorescence emission in fluorite and fluorapatite occurs from rare earth ion inclusions in the lattice despite their often low concentrations. This is because in rare earth

elements (REE) the optically active potential energy levels are far more shielded than transition metal ions from electromagnetic interference from the lattice. This means that energy levels are not overly perturbed by the lattice and remain narrow, which decreases the likelihood of non-radiative pathways of de-excitation and increases the likelihood of fluorescence.

Conventional fluorescence has been analysed as a way to non-destructively identify the presence of rare earth ions in fluorite by Czaja et al (2012), who identified the best excitation wavelengths to use for production of identifiable rare earth signatures in natural fluorite samples. Table 17 below shows excitation and emission wavelengths identified as suitable for rare earth identification (Czaja et al., 2013, Rodnyĭ et al., 2007). While rare earth ions have relatively narrow absorption features, careful selection of excitation wavelengths by Czaja et al. (2013) have allowed comprehensive rare earth identification via a limited number of wavelengths.

Element	**Excitation wavelength (nm)**	**Visible and near-infrared emission wavelengths (nm)**
Ce^{3+}	302	336 (broad)
Pr^{3+}	442	641
Nd^{3+}	521	864, 1065
Sm^{2+}	485	683, 699, 730, 761, 793
Sm^{3+}	442; 485	598, 607, 614; 594, 604, 650
Eu^{2+}	415	420 (broad)
Eu^{3+}	415	420, 594
Gd^{3+}	260	310
Tb^{3+}	485	495, 546, 582, 623
Dy^{3+}	300	574
Ho^{3+}	415	553
Er^{3+}	485; 521	520, 535, 542, 547, 550, 666; 1529
Yb^{3+}	521	978

Table 17: Fluorescence excitation and emission wavelengths identified as suitable for rare earth identification for fluorite using data from (Czaja et al., 2013, Rodnyĭ et al., 2007).

Nine fluorite samples were obtained from the South Australian Museum (Table 18). The samples were analysed using the Edinburgh Instruments Spectrofluorimeter (see section 2.3). Each fluorite was excited by visible laser lines from the Opotek "Opolette" OPO, and UV diodes discussed in section 2.3. The excitation wavelengths used were chosen to match those in Table 17: 298, 257, 415, 442, 485, and 521 nm. Visible and NIR emission spectra were collected (representative results are shown in Figure 56, Figure 57 and Figure 58). Table 18 shows the identified emission centres for each sample. The peaks used for identification and the emission results for all samples are found in appendix A4.

Colour	Provenance	Identified emission centres
Green	Torrington, New South Wales South Australian Museum # G992	Ce^{3+}, Nd^{3+}, Sm^{3+}, Pr^{3+}, Ho^{3+}, Er^{3+}, Gd^{3+}, and possibly $Eu^{3+ \text{ and/or } 2+}$ Dy^{3+}, and Yb^{3+}
Green	Olympic Dam, South Australia South Australian Museum # G19352	Eu^{2+}, Ho^{3+}, and Er^{3+}, and possibly Tb^{3+} and Dy^{3+}
White/green	Stolberg, Germany South Australian Museum # G4407	Ce^{3+}, Nd^{3+}, Sm^{3+}, Eu^{3+}, Ho^{3+}, Er^{3+}, Gd^{3+}, and possibly Yb^{3+} and Dy^{3+}
Colourless	Pernatty Lagoon, South Australia South Australian Museum Mines Dept. Collection # 843	Eu^{2+}, Ho^{3+}, Er^{3+}, and possibly Dy^{3+}
Yellow	Edith River, Northern Territory South Australian Museum # G19599	Ce^{3+}, Nd^{3+}, Sm^{3+}, Tb^{3+}, Er^{3+}, and possibly Pr^{3+}, Dy^{3+} and Ho^{3+}
Brown	Broken Hill, New South Wales South Australian Museum # G10118	Pr^{3+}, Nd^{3+}, Sm^{3+}, $Eu^{3+ \text{ and/or } 2+}$, Er^{3+}, Gd^{3+}, and possibly Dy^{3+}
Blue	Elmwood Mine, USA South Australian Museum # G14114	Eu^{2+}, Er^{3+}, and possibly Dy^{3+}
Purple	Jinka Station, Northern Territory South Australian Museum # G10042	Tb^{3+}, Dy^{3+}, Ho^{3+}, and Er^{3+} (only seen using 257 nm diode)
Black	Marienschacht, Germany South Australian Museum # G34520	no emission seen

Table 18: Fluorite samples used, their colour, provenance, and the rare earth emission centres which have been identified via their fluorescence peaks in this study.

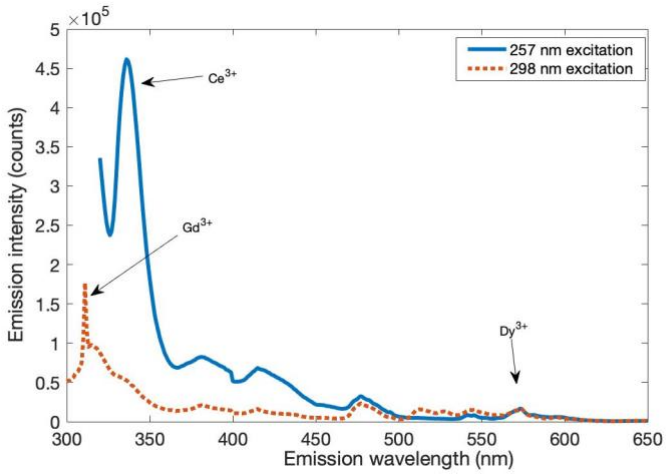

Figure 56: Visible fluorescence emission scans of Torrington fluorite using 257 nm and 298 nm excitation by UV diodes. Rare earth emission peaks are identified. Unlabelled peaks are from either spurious background signal or unidentified signatures.

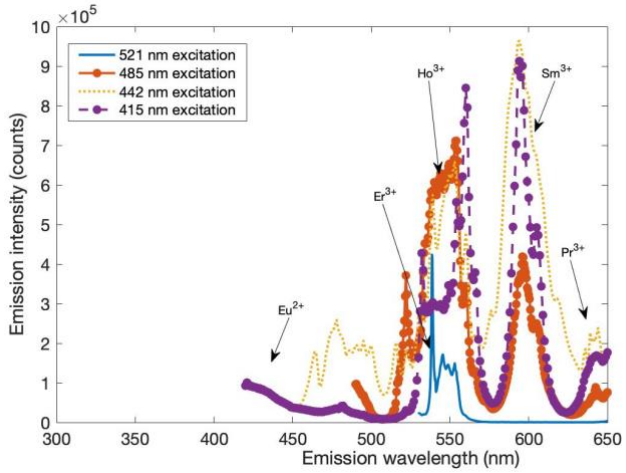

Figure 57: Visible fluorescence emission scans of Torrington fluorite using 415 nm, 442 nm, 485 nm, and 521 nm excitation by the "Opolette" OPO. Rare earth emission peaks are identified.

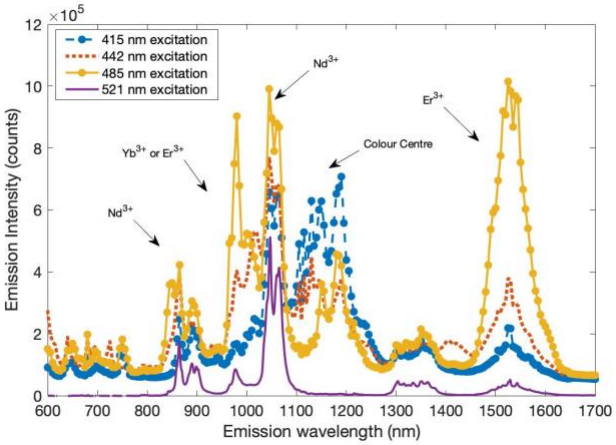

Figure 58: Near-infrared fluorescence emission scans of Torrington fluorite using 415 nm, 442 nm, 485 nm, and 521 nm excitation. Rare earth emission peaks are identified.

5.2.1.1. Purple and black fluorites

The purple and black colours in fluorite are associated with radiation damage (Bill and Calas, 1978). No emission was seen from the purple and black fluorite samples using excitation from the Opolette OPO laser system. Ionising radiation can result in the displacement of fluorine ions out of their place in the lattice, producing fluorine vacancy defects (F-centres). The crystal structure cannot maintain itself when many of these defect centres form in the same area: the lattice collapses, and nanoparticles of calcium ions form. The optical absorption of the calcium nanoparticles is dependent on their size, which varies with radiation damage but is usually around 30-40 nm in diameter (Bill and Calas, 1978). In purple coloured fluorites the absorption covers most of the blue-to-yellow part of the spectrum and peaks near 570 nm. In black coloured fluorites the calcium nanoparticles are larger and absorb most of the visible spectrum. During the 257 nm excitation, Tb^{3+}, Dy^{3+}, and Er^{3+} peaks were seen that weren't detected using visible light excitation. This may be because the calcium nanoparticles absorb excitation light in the visible, making it unavailable for rare earth element absorption, but do not absorb the ultraviolet.

Calcium nanoparticles have also not been reported to absorb in the near-infrared; therefore it is assumed that infrared excitation should not be affected by lattice degradation. Additional experiments were conducted on the Jinka Station (purple) fluorite. The sample was excited at 700 nm, 864 nm, and 980 nm to attempt to observe near-infrared peaks associated with Sm^{2+}, Nd^{3+}, and Er^{3+} respectively; however, no emission was seen from this small set of excitation wavelengths.

Studies of fluorites with bands of different colours show that purple sections of the fluorites can have lower concentrations of rare earth inclusions than sections of different colours formed at the same time (Bill and Calas, 1978). The "Opolette" OPO laser source is of lower pulse energy than the "Radiant" sources, and the concentration of rare earth inclusions in the purple fluorite could be too low to detect. Other defect-associated absorption may be interfering with excitation around this wavelength range: M-centres are created by two fluorine vacancies adjacent to one another and absorb broadly between 700 nm and 800 nm.

5.2.1.1. Clear and coloured fluorites

The other samples analysed produced bright emissions: all samples had erbium and europium peaks, and some had a range of other rare earth inclusions. While erbium and holmium peaks overlap in the visible wavelength range, the holmium signal can be identified by a brighter signal when exciting at 485 nm and the erbium signal can be identified by a sharp 538 nm peak brightest when exciting at 521 nm. The Broken Hill and Elmwood Mine samples contained a broad unidentified peak around 1000 nm (see Figure 59). Broken Hill, Edith River, Stolberg and Torrington fluorites showed emission peaks between 1300 nm and 1400 nm (see Figure 58) which have been associated with samarium ions. Bright near-infrared peaks between 1100 nm and 1200 nm (see Figure 58) were seen in the fluorites without visible calcium nanoparticle-related discolouration. This emission is discussed in more detail later in this chapter.

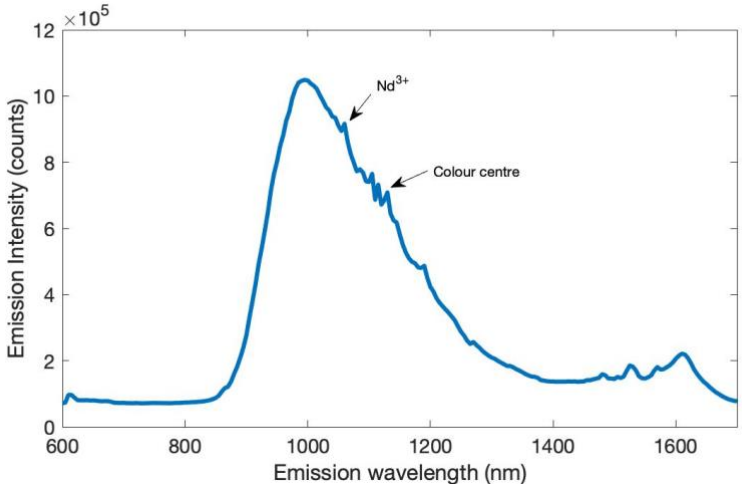

Figure 59: Broken Hill fluorite sample near-infrared fluorescence emission excited at 415 nm, showing the broad 1000 nm peak. The sharp emission peaks of Nd^{3+} and the colour centre can be seen partially obscured by the longer-wavelength edge of the broad emission peak.

5.2.2. Rare earth and transition metal emission in apatite samples

Rare earth inclusions were identified in apatite samples using the same experimental procedure as in fluorite. Experiments were conducted on five fluorapatites and one hydroxyapatite sample. Rare earth absorption lines are not predicted to change drastically between fluorite and fluorapatite, and so the fluorite excitation lines advised by Czaja et al. (2013) were used. Excitation was from the Opolette OPO laser at 415 nm, 442 nm, 485 nm, and 521 nm.

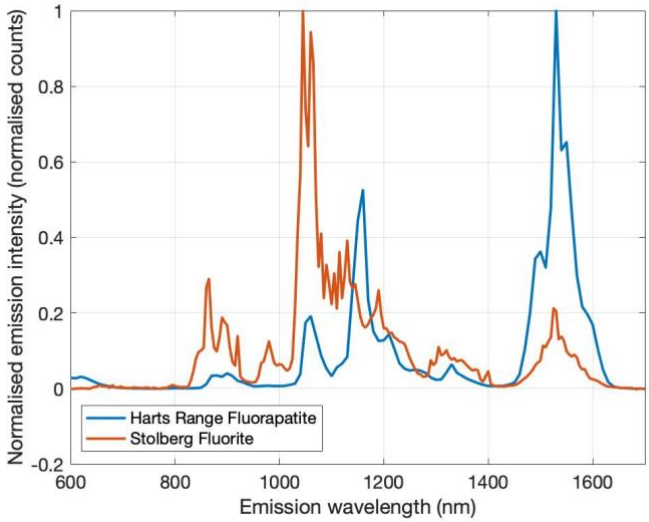

Figure 60: Fluorapatite and fluorite comparison of normalised emission from the Harts Range fluorapatite sample and the Stolberg fluorite sample. Emission from neodymium at 1064 nm and erbium at 1530 nm have different shapes but the peaks are in approximately the same position, allowing ease of identification.

Emission peak positions shift between minerals as the host lattice perturbs the potential energy states of the ion inclusions. This effect between fluorite and fluorapatite is low in these

measurements, and emission seen from fluorapatite was similar to rare earth peaks targeted in fluorite (see Figure 60 for an emission comparison). This is likely due to the well-shielded nature of the optical transitions in the rare earth ions. A number of rare earth inclusions were identified (Table 19). Samples also contained a prominent 1100-1250 nm Mn^{5+}-related peak (Figure 61), as seen by previous authors (Baramin, 2010).

Colour	Provenance	Identified emission centres
Grey/green	Rosetta Head, South Australia Tate Museum # 20446	Dy^{3+}, Mn^{5+}
White/clear	Williamstown, South Australia Tate Museum # 21036	Nd^{3+}, Dy^{3+}, Er^{3+}, possibly Sm^{3+} and Pr^{3+}, Mn^{5+}
Olive yellow	Alice Springs, Northern Territory Tate Museum # 25359	Pr^{3+}, Nd^{3+}, Sm^{3+}, Tb^{3+}, Dy^{3+}, possibly Eu^{3+}, Er^{3+}, and Yb^{3+}, Mn^{5+}
Green	Hart's Range, Central Australia Tate Museum # 19589	Nd^{3+}, Dy^{3+}, Er^{3+}, possibly Tb^{3+}, Mn^{5+}
Green	Lake Baikal, Russia South Australian Museum # G19557	Nd^{3+}, Er^{3+}, Dy^{3+}, Tb^{3+}, possibly Sm^{3+}, Yb^{3+}, Mn^{5+}
Hydroxyapatite (grey, opaque)	Podelien, Russia South Australian Museum # G4781	Nd^{3+}, Sm^{3+}, Eu^{3+}, Dy^{3+}, possibly Yb^{3+}

Table 19: Fluorapatites and their identified emission signatures. All Australian fluorapatites were donated by the Tate Museum, The University of Adelaide; the Russian apatite samples were donated by the South Australian Museum.

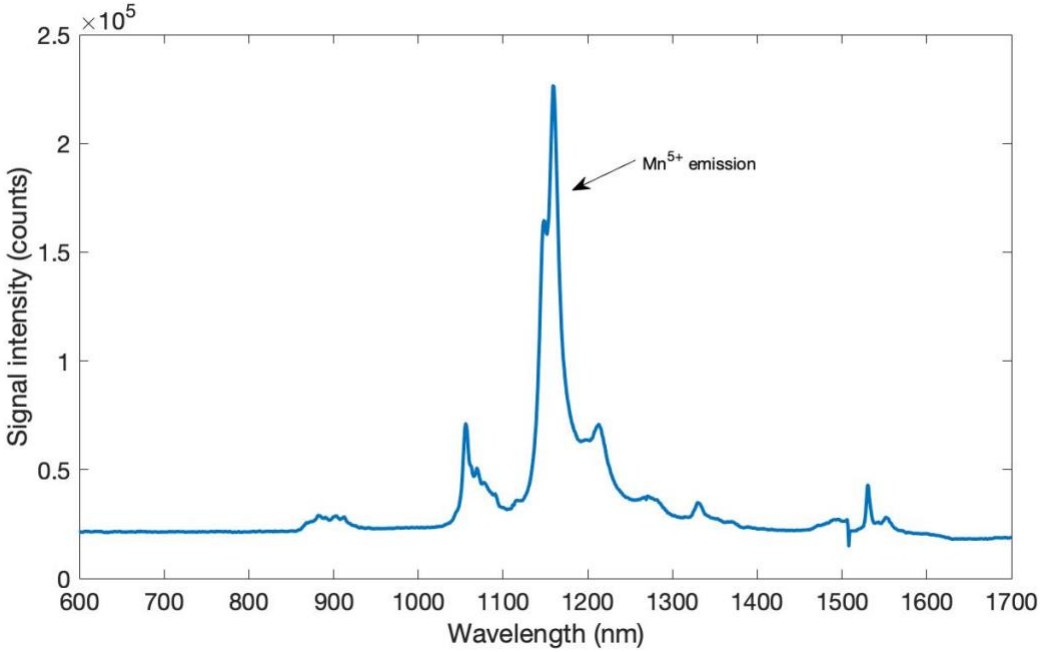

Figure 61: 521 nm excited fluorapatite emission at 1130-1250 nm from the Lake Baikal sample, Russia showing near-infrared manganese emission.

5.3. Colour centre emission from fluorite

5.3.1. M-centre

The M-centre defect in fluorite is caused by two adjacent fluorine vacancies (Letz and Parthier, 2006). It emits a broad peak at 720 nm when excited by 400-450 nm or 600-750 nm light. In pure calcium fluoride fluorine ions can migrate to other defect sites, allowing concentrations of defects to disperse over time. In natural fluorite M-centres are stabilised by the introduction of a sodium ion into the lattice (Mühlig et al., 2010). Fluorite samples were excited with a 92 mW 402 nm continuous wave laser in order to detect M-centre emission.

The three green fluorites (Olympic Dam, Torrington, Stolberg) showed broad peaks around 700-750 nm (Figure 62). The Olympic Dam sample emission peaked at 720 nm; Torrington and Stolberg samples appeared to have multiple overlapping peaks. The bluer of the overlapping peaks could be due to europium ion emission (at 700 nm), or cerium-F-centre emission (715 nm). Cerium-F-centre emission is associated with the green colour of fluorites (Bill and Calas, 1978). Cerium was identified by other emission peaks in Torrington and Stolberg samples, but not in the Olympic Dam fluorite.

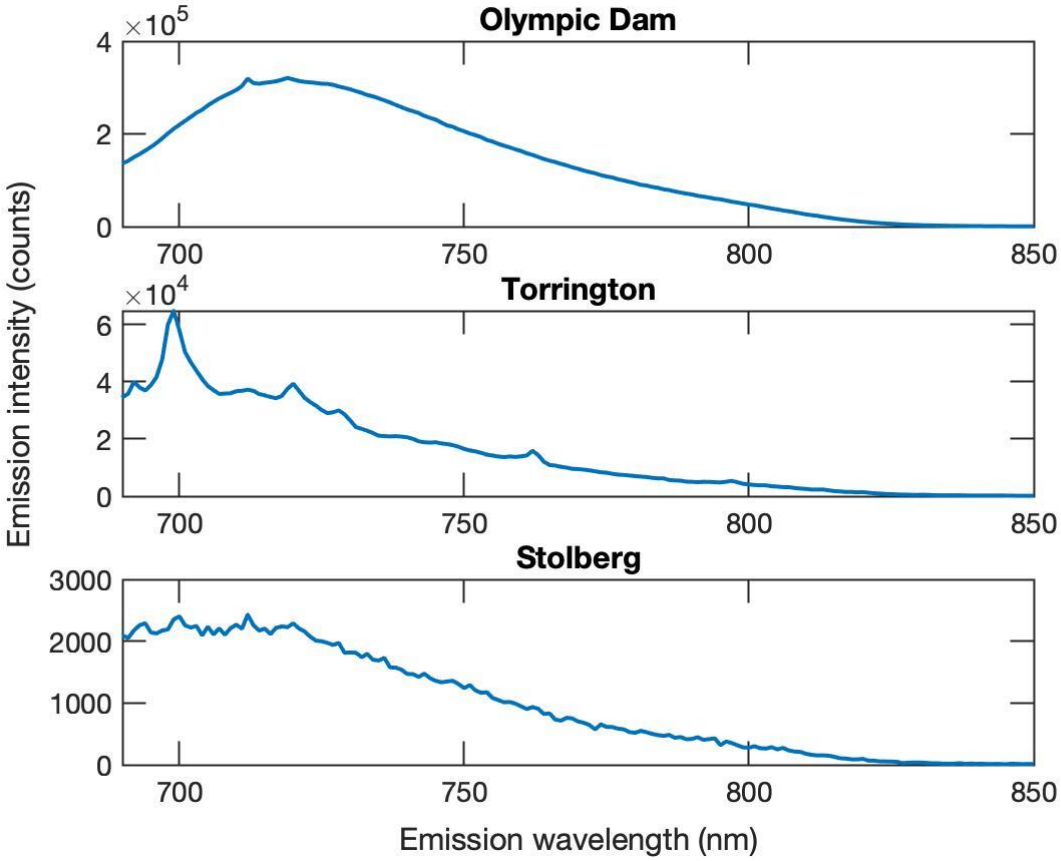

Figure 62: Emission of the green fluorites (Torrington, Olympic Dam, Stolberg) when excited by a 402 nm CW source. Emission was depleted when exposed over an extended duration to the excitation light, but no shift in peak position was seen.

It is unknown why only the green fluorite samples showed M-centre emission, as it is likely that other fluorites would also contain significant number of M-centre defects. It should be noted that the Olympic Dam sample is known to come from a site with a high background radiation rate. This would give it a higher concentration of F-centre and M-centre defects than other samples, and it does have a higher intensity M-centre peak than Torrington and Stolberg samples. Purple fluorites would likely have even more defect centres than the green Olympic Dam sample. It is possible however that the breakdown in lattice structure in purple fluorites prevents the absorption and emission of M-centres.

Under 402 nm continuous wave excitation the M-centre defect emission intensity was not constant, and the emission was observed to deplete rapidly over time. However, signal regeneration was also observed, and a day of low exposure to light (placed in a cupboard in a near-light-tight box) was sufficient to repopulate the M-centre to original levels. Pulsed excitation depletes the defect slower than continuous wave excitation due to less total energy being deposited on the sample, and so the depletion can be measured with the OPO laser systems. Figure 63 shows M-centre depletion after repeated measurements using the Dual-Wavelength System OPO at 600 nm.

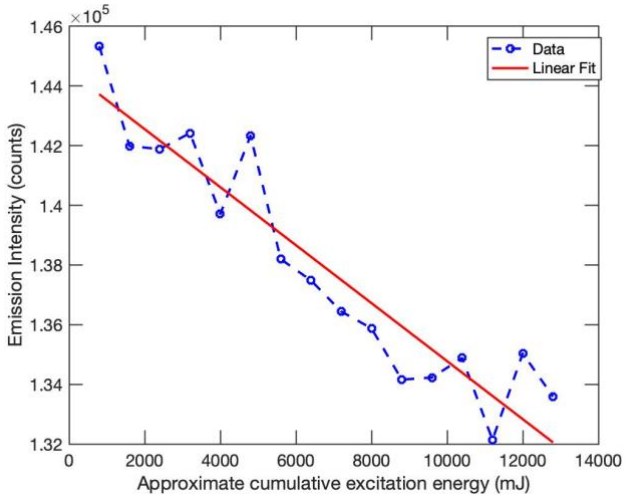

Figure 63: Depletion of the M-centre emission from the Olympic Dam fluorite sample after repeated measurements exciting at 600 nm. The excitation beam is approximately Gaussian and approximately 1 cm in diameter at the sample.

5.3.2. Colour centre

All fluorite samples apart from the purple and black samples showed emission between 1100 nm and 1200 nm. This emission was not found in fluorescence literature, and so further experiments were conducted in order to investigate the fluorescence origin. The experiment was repeated using the Dual-Wavelength System and the Princeton Instruments PylonIR spectrometer, which provide greater signal to noise and resolution. The emission was resolved into three main peaks at 1107 nm, 1118 nm, and 1131 nm, with lower intensity peaks at 1146 nm and 1192 nm (see Figure 64). While in the same range as Mn^{5+} and Ho^{3+} emissions, the spectral peaks did not match (Lyapin et al., 2014), ruling out these known fluorescence origins.

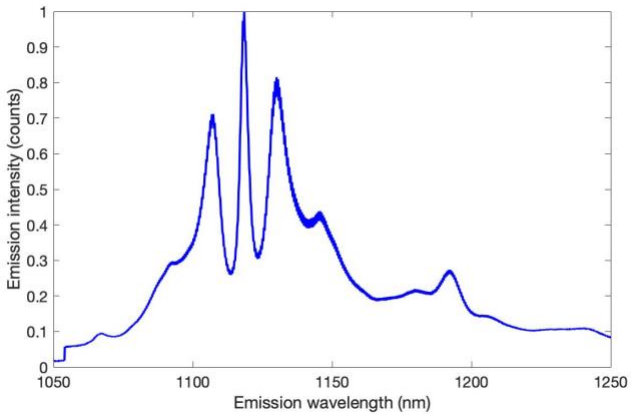

Figure 64: Fluorite emission from the colour centre when excited by 600 nm. Fluorite sample shown here is Torrington fluorite.

This near-infrared emission, like the M-centre, 'bleached' with extended exposure to excitation light at 600 nm, indicating a similar defect origin. In contrast, shorter wavelengths such as 450 nm laser light, or fluorescent and LED lighting served to re-sensitise the sample. Figure 65 shows the emission intensity of multiple experiments following one another when exciting at 600 nm. The intensity is plotted as a function of experiment number—each experiment exposed the sample to approximately 1,200 mJ of 600 nm light (from an approximately Gaussian beam with a diameter of 1 cm), but this was not tightly controlled. Further studies on emission bleaching and re-sensitising should use exact pulse numbers per experiment in order to lower errors.

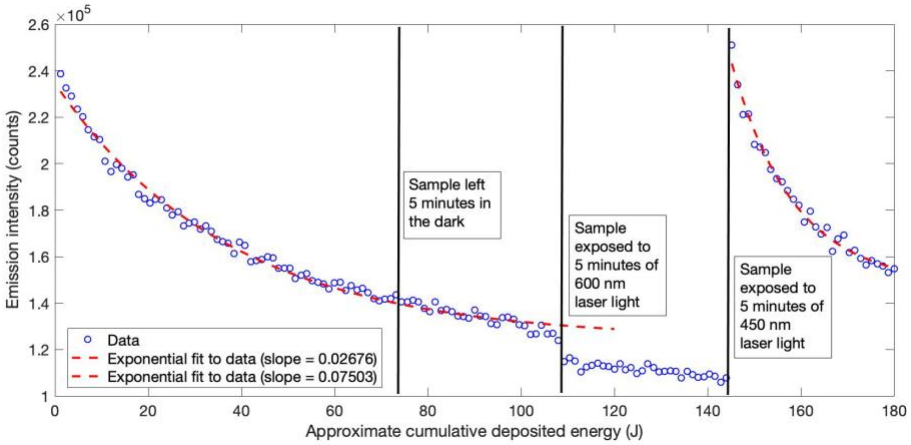

Figure 65: Multiple identical Torrington fluorite colour centre emission experiments exciting at 600 nm, showing a trend of decreasing emission intensity over time/experiment. Vertical lines show different procedures in the runs. Exponential fits to data have slopes that are different within errors, potentially implying changes in process. Accurate fluence numbers cannot be given due to the non-uniformity of the beam, but the beam diameter at the sample stage is approximately 1 cm. More kinetic information could be gained by repeating this experiment with a uniform beam.

A check was conducted to ensure the decrease in signal was real—the emission was measured using the Princeton Instruments PylonIR spectrometer, which may slowly drift in sensitivity over time due to changes in detector temperature. A break in experiments for five minutes

did not show a step decrease in emission, which rules out spectrometer sensitivity drift as the reason for the decrease in emission. Five minutes of 450 nm excitation (approximately 15 J) then re-sensitised the sample to previous emission intensity levels, presumably be re-populating the colour centre.

Excitation measurements can reveal information about absorption and emission interactions. Excitation measurements were conducted between 450 nm and 675 nm and used one "Radiant" OPO of the Dual-Wavelength System. Emission intensity was calculated using the 1118 nm peak observed with the NIR spectrometer. The Olympic Dam sample was used as it had intense 1118 nm emission and no overlapping rare earth peaks, which would minimise counting errors in the measurements. Two variables were accounted for:

- OPO power changes with wavelength: the pulse energy at each wavelength was measured with a power meter. The emission was assumed to be conventional Stokes' fluorescence, with a linear relationship to excitation energy. It was also assumed that for all excitation powers used, the sample was far from saturation. The emission intensity was divided by the excitation pulse energy to reveal the wavelength-dependent excitation efficiency.
- Depletion and/or sensitisation of the emission with excitation exposure: excitation wavelengths near 450 nm sensitise the signal, while wavelengths near 600 nm deplete the signal. After each measurement a repeat measurement exciting at 450 nm was taken. The difference in 1118 nm emission intensity was used as an indication of the sensitivity of the sample. The 1118 nm emission from different wavelengths was normalised by dividing by the 450 nm excited emission intensity.

Accounting for these variables gives us an excitation curve of 1118 nm emission normalised to both sensitisation drift and excitation pulse energy. The emission at 1118 nm peaked when the excitation wavelength was between 575 nm and 625 nm. A further increase in fluorescence was seen when exciting in the blue/violet part of the spectrum (Figure 66). The shape of the excitation curve follows the shape of fluorine vacancy absorption in pure CaF_2 (Cramer, 2004).

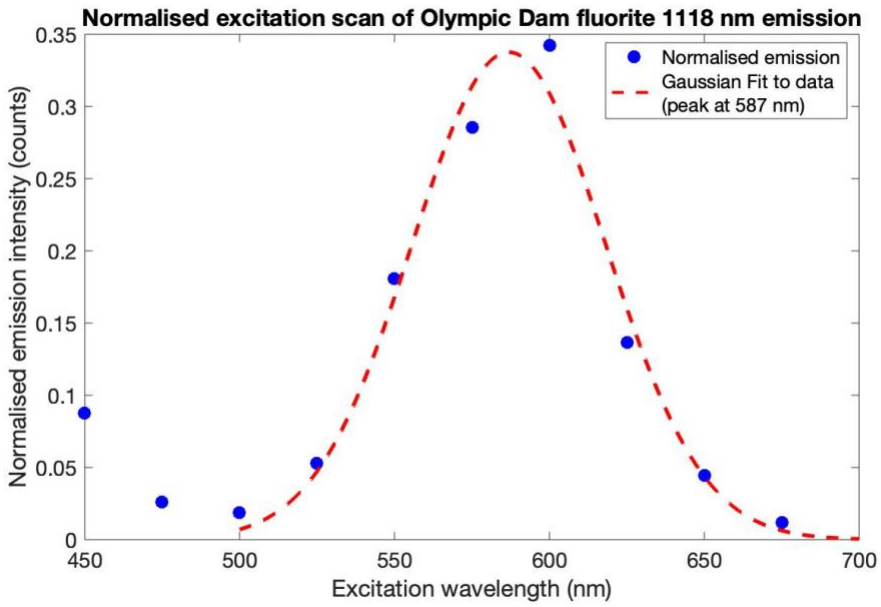

Figure 66: Colour centre-derived 1118 nm emission intensity as a function of excitation wavelength in the Olympic Dam sample. After each excitation wavelength an additional measurement was made at 450 nm for normalisation purposes, in order to account for depletion and sensitisation during the measurement.

Fluorine vacancies have been created in pure fluorite using high-powered ultra-violet excitation at 157 nm and 193 nm, with fluences of 10 mJ/cm^2 and 50 mJ/cm^2 respectively (Cramer, 2004, Rix, 2011). To test if the 1118 nm signal is associated with fluorine vacancies, a clean uncoated calcium fluoride lens was crushed and pelletised. Initial excitation of the pure sample at 600 nm did not give fluorescence. The sample was then exposed to 260 nm light from the Radiant OPO for half an hour (approximately a total deposited energy of 7.2 J. Accurate fluence measurements cannot be given for this excitation as the beam differs in intensity over the sample surface; however it is approximately Gaussian and has a diameter of approximately 1 cm at the sample). This excitation served to sensitise the sample, and after this ultra-violet excitation, emission was seen when exciting at 600 nm. The emission matched the peaks seen in natural samples (Figure 67), and similarly decayed after repeated measurements (Figure 68). Room lights and 450 nm excitation were not sufficient to re-sensitise the synthetic calcium fluoride sample, however, emission intensity was recovered after approximately a further five minutes of 260 nm excitation (1.2 J). It was concluded from this experiment that the emission peaks seen are associated with the calcium fluoride lattice defects rather than any potential inclusions in the natural samples, but the lack of sensitivity to 450 nm light in the synthetic sample may indicate that in the natural samples inclusions play a part in stabilising the emission centre.

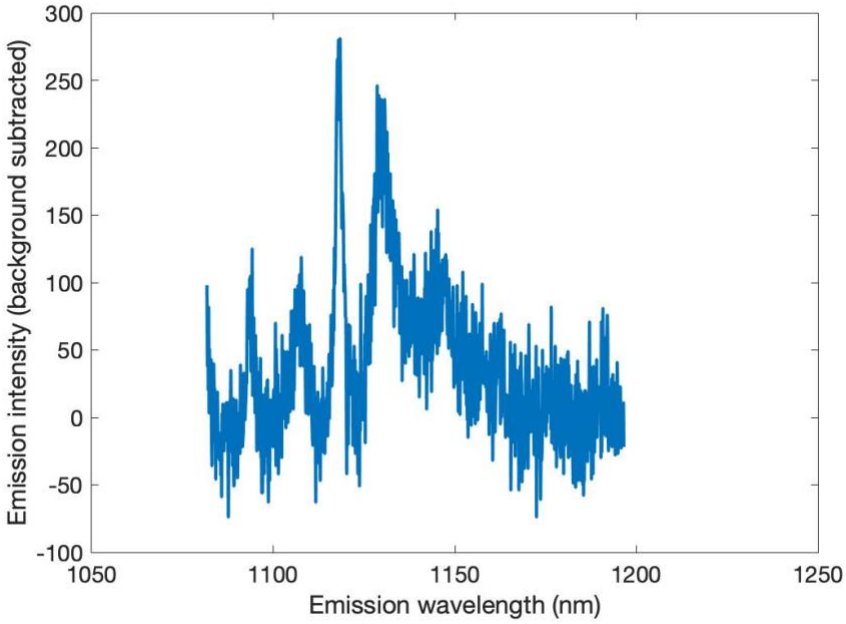

Figure 67: Calcium fluoride emission peaks (averaged) after sensitisation with 1.2 J of 260 nm. Emission was about two orders of magnitude lower than that in natural samples and acquiring reasonable signal/noise used multiple measurements after repeated re-sensitisation using 1.2 J of 260 nm excitation using a Gaussian-like beam with a diameter of approximately 1 cm.

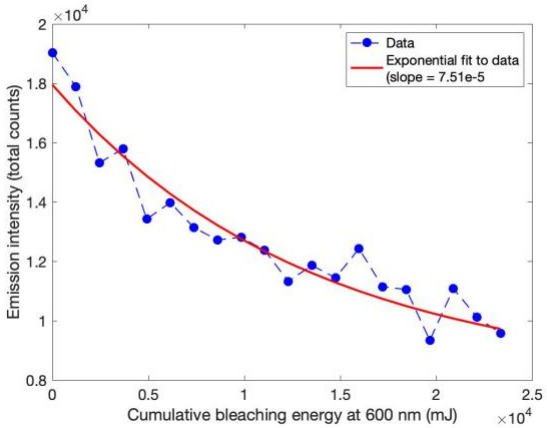

Figure 68: Depletion of 1118-1130 nm colour centre emission from pure calcium fluoride after repeated measurements exciting at 600 nm.

Fluorine vacancies have also been induced in fluorite by irradiation from a beta source (Cramer, 2004, Chinkov and Shtan'ko, 1998). Crushed optics-grade synthetic calcium fluoride was subjected to approximately 500 Gy of beta radiation from a strontium source, but no emission was detected. This may be because fluorine vacancies are inherently unstable in low-impurity calcium fluoride, and their concentration is limited at room temperature barring permanent lattice damage (Rix, 2011, Ryskin et al., 2017).

The 1118 nm emission was not seen in the Jinka Station purple fluorite sample using visible excitation and the Edinburgh Instruments Spectrofluorimeter. However when crushed and

excited at 600 nm in the Dual-Wavelength System the signal was seen (Figure 69). This could be due to a combination of four separate issues:

1. The excitation intensity is much greater in the Dual-Wavelength System;
2. The collection efficiency is greater in the Dual-Wavelength System;
3. The sample was crushed and pelletised before measurement in the Dual-Wavelength System rather than being excited in its natural crystal form. This process exposes inner parts of the fluorite that are less exposed to external sources of radiation, and therefore less damaged.
4. Lattice-damage defects may also be created by the crushing process.

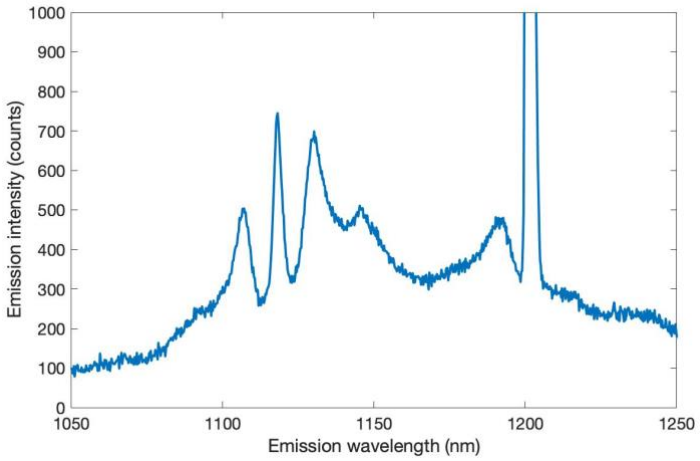

Figure 69: Colour centre emission from crushed and pelletised Jinka Station purple fluorite when exciting at 600 nm in the Dual-Wavelength System.

Lattice breakdown may suppress the 1118 nm signal: radiation damage in fluorite occurs due to internal radiation sources and/or external sources. If external radiation sources are more prevalent, lattice breakdown would occur at the edges of a large crystal more than the interior. The crystal sizes at which this effect would occur are determined by the limited ranges (approximately > 5 µm and 2-3 mm respectively) of α- and β-radiation from naturally occurring radionuclides, leaving only ɣ-radiation to irradiate further into larger crystals. Crushing and pelletising a sample would expose the interior of large crystal at the surface of the pellet. If the interior of the crystal is less damaged crushing would show fluorescence that would not be seen in pristine samples.

This has implications for real-time mineral identification procedures. On-belt analysis would access exposed freshly fractured new surfaces. Museum-grade samples are however larger than the crushing size (larger than ~1 mm diameter), and fluorite in an ore would generally be in much smaller crystals. The centre of smaller crystals would have less shielding mass from exterior radiation sources, and so the source of radiation damage and the reason for enhanced signal when crushed needs to be known before judgement on the F-centre associated 1118 nm emission's use for fluorite sensing in high radiation environments. More study on purple fluorites is needed before development of this signal for use with real-time sensors in high-radiation level deposits.

5.4. Fluorine concentration determination using conventional fluorescence

5.4.1. Ubiquitous signatures in fluorite and fluorapatite

A fluorescence signature must be present in all or almost all specimens of the target mineral in order to be useful for mineral sensing. Apart from the Marienchacht (black) fluorite, all fluorite and fluorapatite samples showed fluorescence from rare earth inclusions, but these inclusions were not the same for all samples. Rare earth signatures in fluorite are likely to be useful for mineral sensing, but more work is needed to study the variation of rare earth signatures across a single site before sensor development. Furthermore, and importantly, rare earth element signatures from fluorapatite and hydroxyapatite were very similar, and so rare earth elements are less likely be able to be used to distinguish between different apatite species in the field.

In contrast, lattice-based and transition metal-based signatures are more likely to be particular to a particular mineral species, and two different fluorescence signatures in the near-infrared appeared consistent across samples of the same mineral (Figure 70):

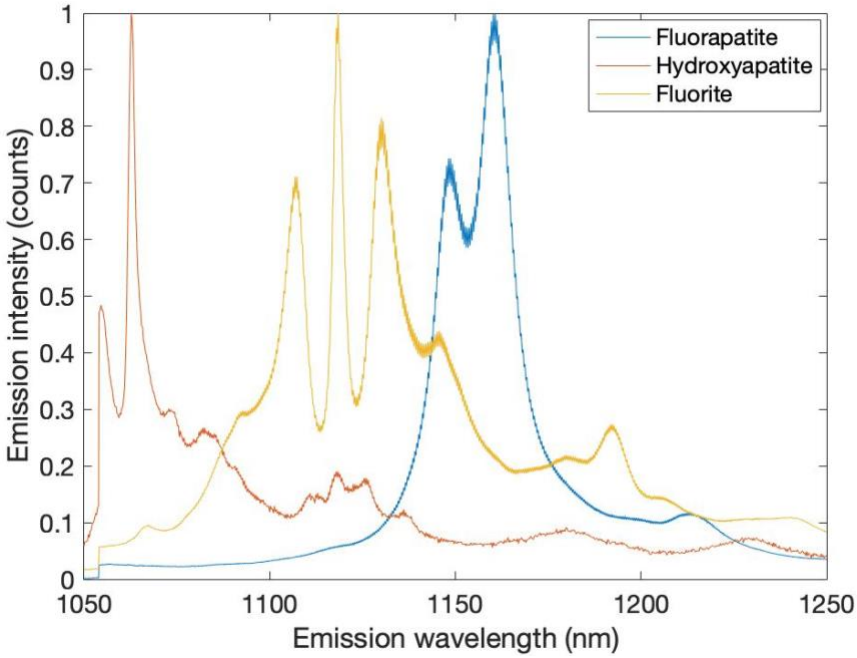

Figure 70: Normalised fluorite, fluorapatite, and hydroxyapatite emission under 600 nm excitation using the IR spectrometer extension to the Dual-Wavelength System.

The 1107, 1118, and 1131 nm peaks associated with the F-centre appeared in all fluorite samples apart from the Marienshacht (black) fluorite. In Figure 70 these are depicted by the yellow curve.

The 1150 and 1160 nm peaks associated with Mn^{5+} in fluorapatite appeared in all fluorapatite samples (the blue curve in Figure 70) and not in the hydroxyapatite sample (red curve in Figure 70) or in fluorite samples.

Hence it is apparent that the F-centre and the Mn^{5+} centre emission peaks can then be suitably mineral-specific to be useful for fluorine detection in complex ores where fluorite and fluorapatite are common fluorine-bearing minerals. The signatures have an advantage for sensor design in that they have similar excitation and emission ranges. This conveniently means the same sensor can be optimised for both fluorine-bearing minerals.

5.4.2. Ore sample fluorine and fluorescence characterisation

Six ore samples were provided by CRC ORE, all with known fluorine levels (see Table 20). The zero percent ore was used to create a concentration series by blending with crushed Torrington fluorite. The other samples were used to see if signals from museum-grade samples were present in ore samples.

Sample Name	Percentage of fluorine (by assay)
G5	5
S1	2.1
S2	0.6
S3	0.12
S4	0.44
S5	2.3
CPO	0

Table 20: Ore samples used in this chapter and their fluorine percentages.

G5 and S-series samples were excited by ultra-violet light to view any visible spectra. Both ore types had a large peak at 420 nm and a small, broad peak at 865 nm (see Figure 71). The S-series showed an additional peak at 570 nm, and G5 a broad set of peaks around 650 nm, similar to that of Ag^{1+} in barite (MacRae et al., 2016).

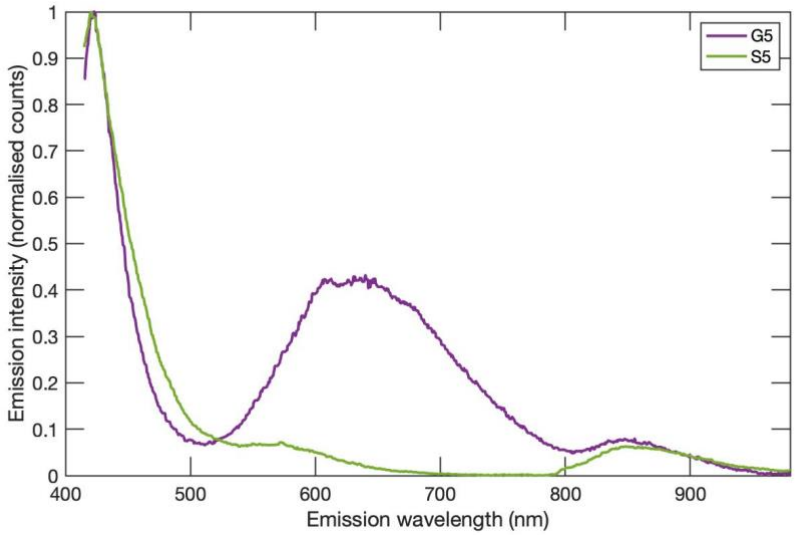

Figure 71: Normalised G5 and S5 ore sample emission excited by 340 nm laser light.

Museum-grade fluorite samples analysed earlier in this chapter showed emission peaks at 420 nm associated with europium emission, and 865 nm associated with neodymium emission. This does not mean that similar peaks in the ore samples come from fluorite. Rare earth element absorption and emission properties do not change significantly in hosts with similar properties. Assay measurements provided with the samples indicated that they included a large range of minerals, including minerals that are known for their optically active properties such as quartz, garnet, fluorite, and fluorapatite.

In the crushed sample a number of grains could be identified as potentially being quartz (clear, colourless), and garnet (red, translucent). 'Garnet-like' grains (red, translucent grains) from the G5 < 2 mm unprepared sample were manually picked out and analysed at 340 nm in order to check for optical signatures from non-fluorine-bearing minerals. Garnet-like grains were chosen as they are easy to identify. While 'garnet' is a mineral family rather than a specific mineral, garnets are known to fluoresce via a number of different ionic inclusions (Baramin, 2010). The grains showed peaks reasonably identical to the 420 nm and 865 nm peaks seen in fluorite and the ores (Figure 72). A low intensity 570 nm peak was also seen. The garnet sample also showed near-infrared emission, but these signatures were very different to emission seen from fluorite, fluorapatite, and the ores when excited at 600 nm (Figure 73). No garnet near-infrared fluorescence was seen when exciting in the visible. It was therefore concluded that the emission seen in the samples that matched those of museum-grade fluorapatite is likely to come from fluorapatite in the sample, and unlikely to come from other optically suitable mineral hosts.

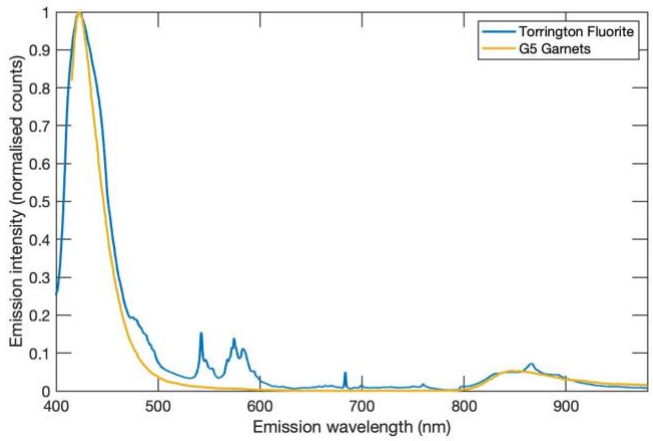

Figure 72: Emission from G5 ore garnet-like grains and Torrington fluorite, excited with 340 nm laser light.

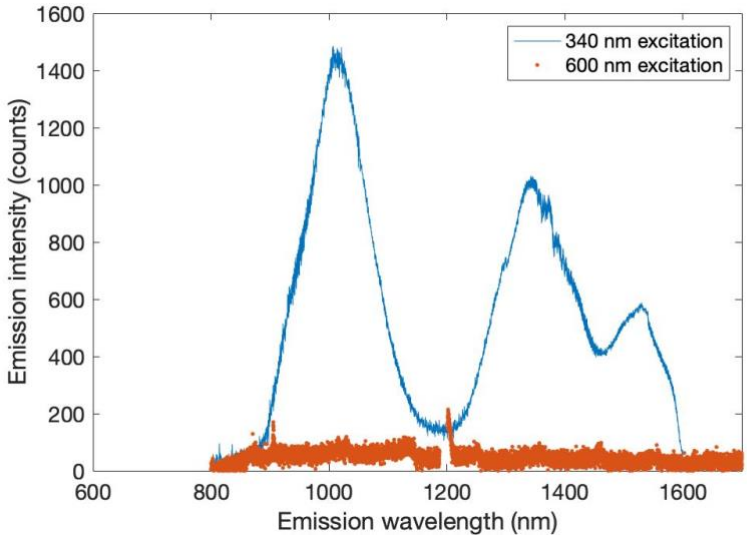

Figure 73: Near-infrared emission of the garnet-like grains from the G5 ore, excited at 340 nm and 600 nm. Gaps at 870 nm and 1199 nm in the 600 nm excited data correspond to OPO Idler leakage and grating octave detection of the excitation line respectively.

Both G5 and S-series ore showed Mn^{5+}-like emission when exciting at 600 nm (Figure 74). Fluorite peaks at 1118 nm were not seen. In Figure 74 the G5 data has increased luminescence in the shoulder of the emission between 1100 nm and 1157 nm. This may be due to a very small fluorite signal swamped by the fluorapatite signal. It may also be due to other ore-specific signals.

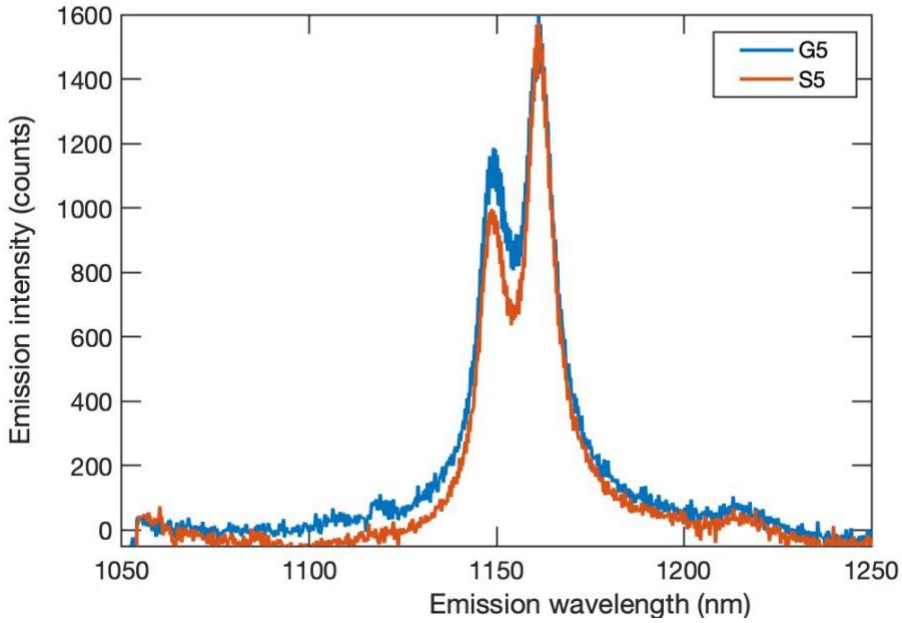

Figure 74: G5 (blue) and S5 (red) ore sample emission using 600 nm laser light.

The assay data for the ores provided by CRC ORE suggest that fluorite is the most significant fluorine-bearing mineral present in both samples. The lack of signal may be due to lattice collapse—a survey of a private collection from the site of the G5 sample indicates that most of the fluorite present is purple in colour (Lilly, 2019). Previous studies of S-series fluorite have indicated that much of it is intergrown with silicates, which may also subdue emission in the wavelength range studied.

5.4.3. Fluorine concentration determination

The fluorapatite manganese signal and the fluorite colour centre signal were tested for their ability to distinguish between different concentrations of each of these minerals. The fluorapatite signal was seen in the S-series ore samples, and so concentration measurements were conducted on the S-series ore. The fluorite signal was not seen in these ore samples, and so an artificial concentration series was made using crushed Torrington fluorite and the zero-percent fluorine (CPO) sample (see Table 20). Pelletised samples of the S-series and the Torrington fluorite/CPO concentration series were excited at 600 nm. Emission between 1100 nm and 1200 nm was integrated. Emission intensity correlated well with fluorine concentration for both the manganese signal in ore (
Figure 75) and the colour centre signal in the artificial series (Figure 76).

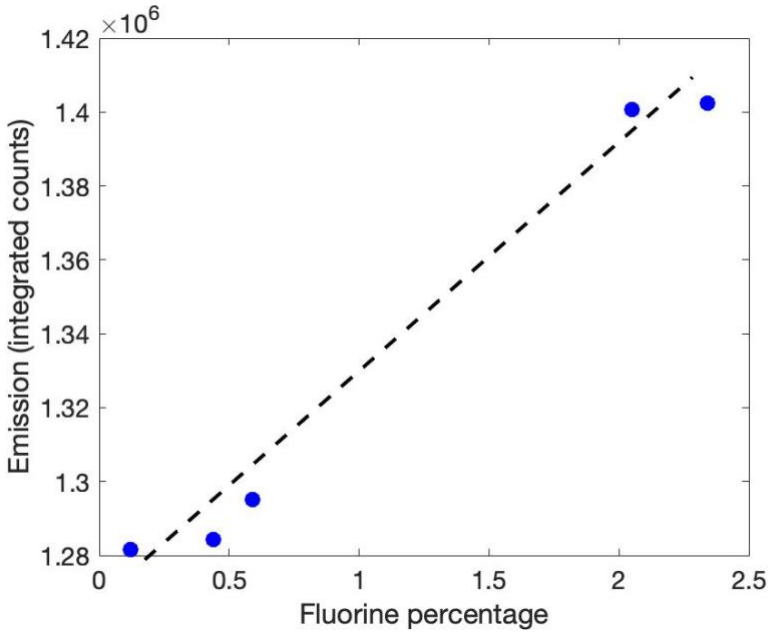

Figure 75: S-series ore 1100-1200 nm emission data using 600 nm excitation. The linear dashed fit line is presented as an aid to the eye.

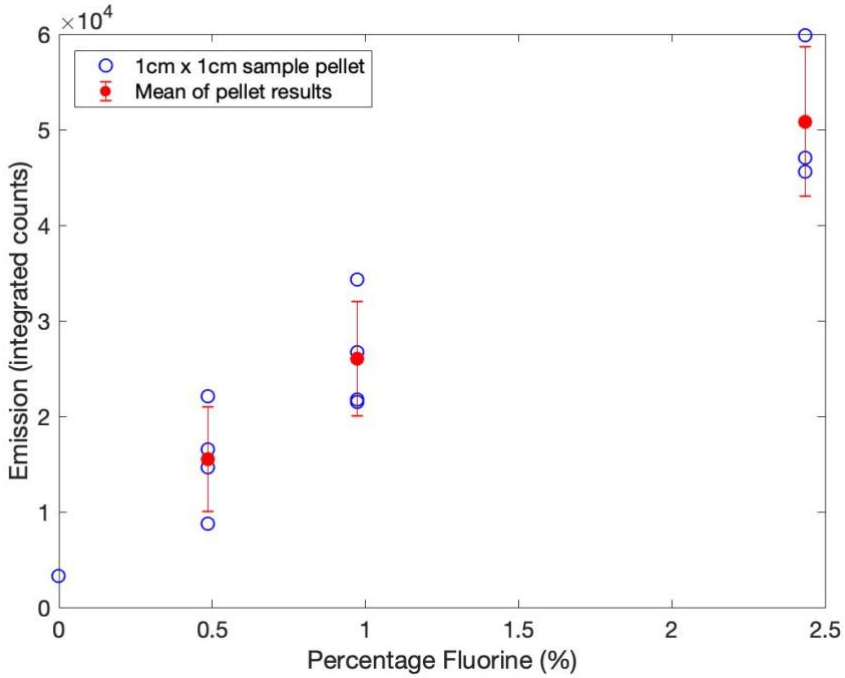

Figure 76. Near-infrared emission vs fluorine concentration in the synthetic mass series at low fluorite concentrations. Emission peaks between 1100 nm and 1200 nm were excited by 600 nm laser light. Multiple samples were prepared and analysed to show the variability of signals using the same ore and fluorite sample.

The fluorite concentration series samples were not re-sensitised before emission with 450 nm laser light. Sensitisation was only due to incidental exposure to fluorescent and LED room lights. This indicates that it is possible to determine fluorite grade using the F-centre related emission without a deliberate re-sensitisation step before excitation. In both concentration series results the emission was not background subtracted, and so the concentration emission

trend does not pass through zero at zero percent fluorine. For a fixed sensor with a known background environment such as a belt sensor, the background can be measured as a calibration step and subtracted from each measurement, and therefore reduce and further the minimum detectable concentration level. For a mobile sensor, the background must be measured for subtraction before each analytical measurement for quantitative measurements to be possible.

5.5. Upconversion fluorescence

Conventional single-photon-excited fluorescence appears suitable for fluorine concentration measurements using previously studied fluorapatite-based manganese emission in the ore samples analysed, and newly-discovered near-infrared signals in fluorite from a synthetic concentration series. In certain circumstances, upconversion fluorescence can have the following advantages:

1. In some mine sites ores contain complex mixtures of minerals. In these cases, upconversion fluorescence excitation wavelengths are less likely to excite other minerals, as upconversion fluorescence is far less likely to occur coincidentally as a parasite signal than is conventional fluorescence, due to upconversion requiring two photons of the correct energies for excitation. This allows detection of the mineral signature without the interference of other signals.
2. Minerals at some sites may have a large proportion of ion inclusions. Multiple signals from the same mineral can make analysis more complex, especially if some overlapping signals are only present in only some areas of the site. Upconversion fluorescence excitation wavelengths are more likely to excite only one emission centre at a time, simplifying analysis greatly by not exciting most or all potentially confounding signals.

Upconversion fluorescence does have potential disadvantages. It needs a higher photon flux than conventional fluorescence. The fact that upconversion fluorescence is less likely to occur in any one sample results in a reduced chance of finding a useful signal. Synthetic samples are artificially doped with rare earth ions at 0.5-15% levels, while natural rare earth ion impurities are generally at ppm levels, lowering maximum emission intensities. Natural samples are also more likely to have a range of different impurities, increasing the chance of quenching ions being present. In the following section some practicalities of using upconversion fluorescence were studied in a series of experiments:

1. Fluorite samples containing erbium are analysed for a common erbium upconversion signal.
2. The Dual-Wavelength System is tested using a fluorite with multiple rare earth inclusions.
3. Erbium upconversion signals are tested for use in determining fluorite grade using the fluorite concentration series described in the previous section.

5.5.1. Upconversion from 980 nm excitation of natural fluorites

Initial tests were designed to test whether upconversion fluorescence feasible for detection from natural minerals. Erbium is widely used in upconversion materials (see chapter three) and therefore erbium-containing natural fluorite samples are ideal candidates for natural

mineral upconversion fluorescence. Each sample was excited at 980 nm using the Opolette OPO to identify visible upconversion signals in erbium-containing fluorites.

Figure 77 shows the energy levels involved in erbium upconversion fluorescence using 980 nm excitation. The ion first undergoes ground state absorption to the $^4I_{11/2}$ state, and then either excited state absorption or energy transfer (W22, see chapter three) to the $^4F_{7/2}$ state. From this state excited ions non-radiatively decay to the $^4H_{11/2}$, $^4S_{3/2}$, and $^4F_{9/2}$ states, emitting 530 nm 550 nm, and 670 nm fluorescence respectively.

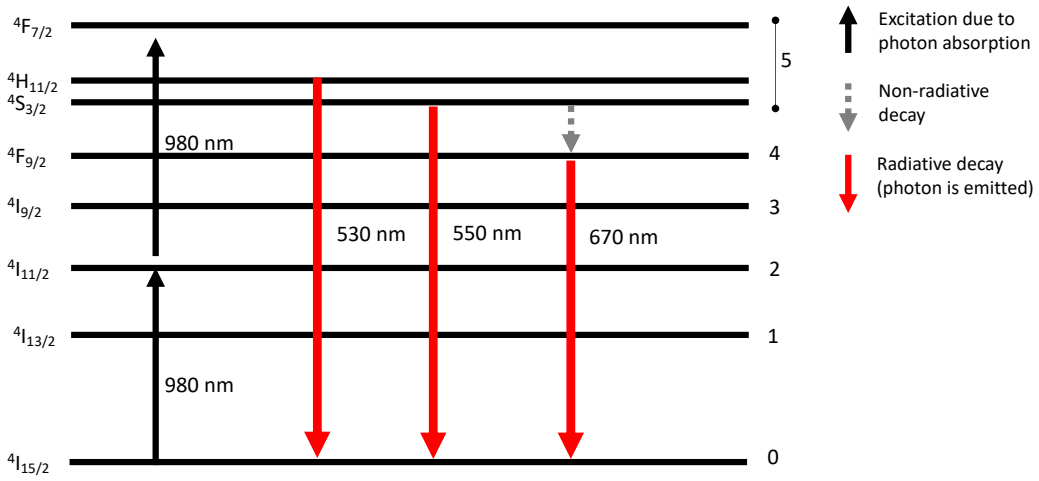

Figure 77: Band diagram of potential energy levels involved in erbium-associated upconversion and visible emission in fluorite exciting at 980 nm.

The emission range observed was between 400 nm and 680 nm. Only four of the fluorites in Table 18 showed detectable upconversion emission. These were the Broken Hill fluorite (brown-yellow), Torrington (green), Olympic Dam (green), and Stolberg (green) samples. The other samples may have much lower erbium concentrations, making upconversion harder to detect. They may also contain inclusions that absorb wavelengths at the excitation or emission steps, preventing emission by creating non-radiative pathways.

Power dependence (emission intensity vs excitation energy) graphs provide information about the processes involved in upconversion fluorescence. Linear dependences indicate that one photon is involved in the emission process, quadratic dependences indicate that two photons are involved in the emission process, and so on. Changes in power dependence indicate a change in process or kinetics. Power dependence is usually interpreted by measuring the slope of the emission intensity vs excitation beam energy data in log-log form. This allows the presence of complex mixes of processes to be identified.

Power dependence graphs were constructed for the four fluorite samples that produced upconversion fluorescence. Emission was measured for different excitation beam energies (25 µJ to 1 mJ), between 400 nm and 680 nm. Each sample had different emission characteristics, so for each sample the area that provided 90 % of a peak at the highest power

excitation was summed for analysis. Erbium 530 nm and 550 nm peaks were summed together. The Opolette laser power at the sample was varied over two orders of magnitude using different combinations of neutral density filters. The excitation pulse energy was measured using a Gentec power meter (see section 2.3) in the beam line after all filters and mirrors.

Erbium upconversion fluorescence emission from 980 nm excitation can occur via sequential absorption or energy transfer (see chapter one and chapter three). Both pathways to emission require two photons, a log-log plot of power dependence at low excitation powers will provide a slope of two for both processes (Pollnau et al., 2000a). At high powers, the first excited state ($^4I_{13/2}$) will start to saturate, and the slope will change from 2 to 1. In simple energy transfer upconversion environments, this slope change can be fairly rapid (Suyver et al., 2005). However, the complex environment in natural CaF_2 samples can provide different slopes, as detailed below.

If we assume all erbium ions are in rare earth element clumps as detailed by Catlow et al. (Catlow et al., 1984), there are three different scenarios any single erbium ion could be in:

- The ion is in a clump of different rare earths that do not affect 980 nm excited upconversion fluorescence. In this scenario, the erbium ion is isolated from other erbium ions, and is likely to undergo excited state absorption rather than energy transfer.
- The ion is in a clump of different rare earths that do affect 980 nm excited upconversion fluorescence. This could be by absorbing excitation or fluorescence, or providing resonant energy transfer from excitation or fluorescence states. In this scenario the emission efficiency will be affected by the behaviour of the other ions.
- The ion is in a clump of rare earths which includes another erbium ion. This creates a scenario where W22 energy transfer upconversion is very likely due to the close proximity of the ions.

Each ion scenario provides a different sub-population affected differently by the excitation light. Each sub-population is independent of the others, and will saturate at a different excitation power level. In continuous-wave excitation, at higher powers individual ion emission pathways can saturate and secondary pathways start to emerge. In nanosecond pulsed systems such as ours this is unlikely, and different processes will be the product of different sub-population behaviours. The point of saturation will depend on the efficiency of the process, and the amount of erbium ions in the sub-population. In a log-log slope analysis, the following slopes indicate:

- Slope of one: no sub-populations are saturated
- Slope of two: all sub-populations are saturated
- Slope between one and two: some but not all sub-populations are saturated.

The slope will change over different excitation energies as different sub-populations come into different regimes. Regions of stable slopes between one and two can give information about the ratio of erbium ions giving fluorescence from saturated and unsaturated sub-populations. When the slope in log-log form is not stable it indicates at least one sub-population is undergoing a change in regime.

Below are discussions on the emission and power dependence for each of the four samples that showed upconversion emission under 980 nm excitation.

5.5.1.1. Upconversion fluorescence from Broken Hill sample

Despite targeting erbium upconversion transitions, the upconversion seen in the Broken Hill sample when exciting at 980 nm was not characteristic of erbium emission. While erbium peaks in fluorite occur at 530 nm, 550 nm, and 660 nm, Broken Hill emission peaked at 490 nm (
Figure 78).

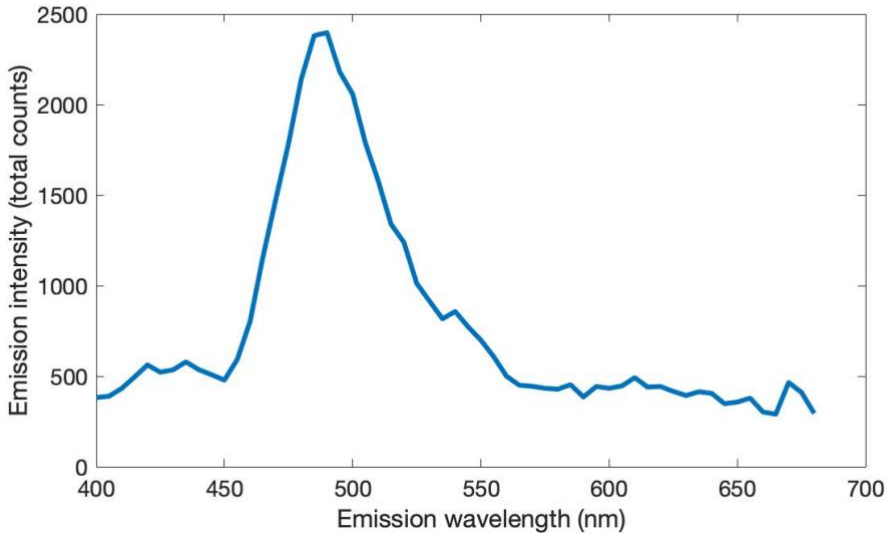

Figure 78: Broken Hill fluorite upconversion fluorescence spectra, 5 nm resolution, 980 nm excitation.

Emission at 490 nm is typical of both Tb^{3+} (Czaja et al., 2012) and Cu^{+} (Fleischauer and Fleischauer, 1970). It is more likely in this sample that the emission comes from Cu^{+} ions. Tb^{3+} ions generally also emit at 545 nm, 585 nm, and 682 nm, which are not seen here. The ion

that is absorbing the excitation light may still be erbium, with energy transfer to the Cu^{+} 490

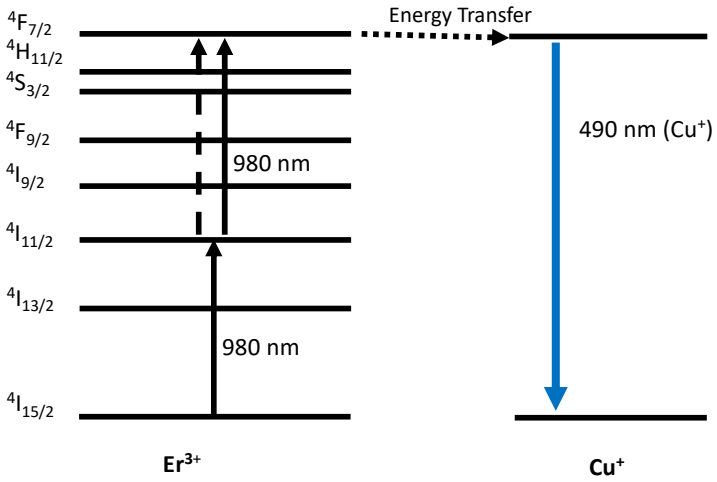

nm peak (see
Figure 79). There is also a broad 1000 emission nm peak (see Figure 59) of unknown origin in the conventional fluorescence scans of Broken Hill, which may also absorb 980 nm light.

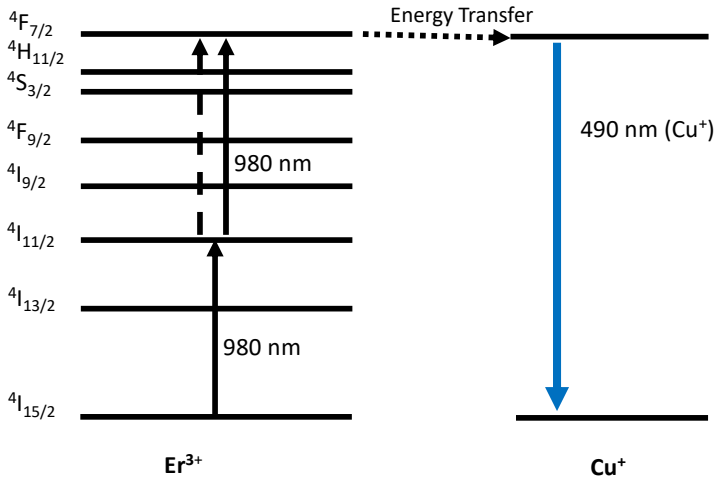

Figure 79: Band diagram of the proposed pathway for 490 nm emission in Broken Hill fluorite.

If erbium is part of the Broken Hill upconversion process, it is likely that we do not see erbium emission due to efficient energy transfer from the $^4F_{7/2}$ state. Transition metals are known for their strong and broad absorption (Wenger et al., 2002), and so transfer to Cu^{+} ions would likely be efficient.

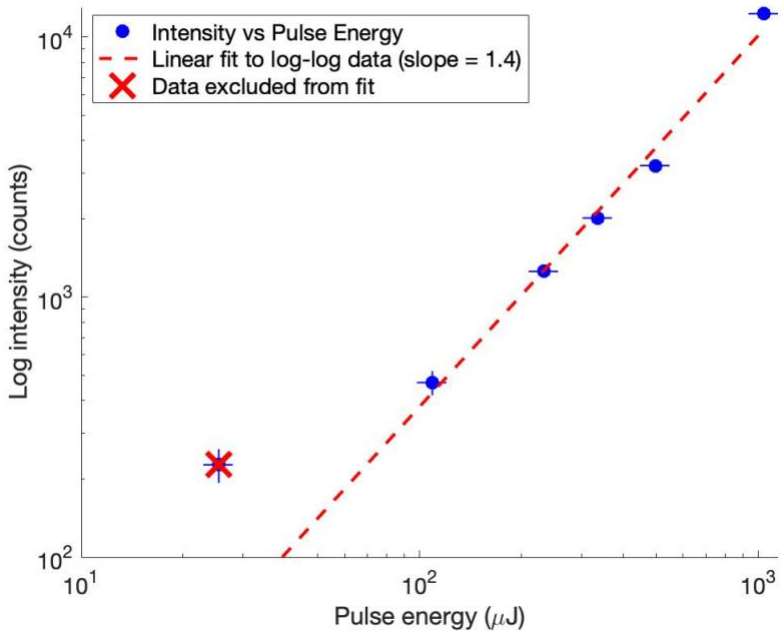

Figure 80: Broken Hill fluorite upconversion fluorescence dependence on excitation power, log-log plot, 980 nm excitation.

The first data point of the Broken Hill power dependence scan (Figure 80) does not fit on a linear slope with the other data points. This suggests that there is a regime change between 25 µJ and 109 µJ. The rest of the data points fit on a slope of 1.4, with 95% confidence bounds of 1.2-1.7. This indicates that there are at least two sub-populations that are contributing to the upconversion fluorescence, one which is saturated and one which is unsaturated between 109 µJ and 1029 µJ. If the 980 nm excitation light is absorbed by erbium ions, these sub-populations may include neighbouring erbium ions undergoing W22 energy transfer, and isolated erbium ions undergoing excited state absorption.

5.5.1.2. Upconversion fluorescence from Olympic Dam sample

Emission from the Olympic Dam sample included 550 nm and 670 nm peaks (Figure 81). These are typical of erbium upconversion. The emission appeared to be concentrated in isolated spots on the mineral (Figure 84). This behaviour indicates clumping of ions in a generally lower ion concentration mineral.

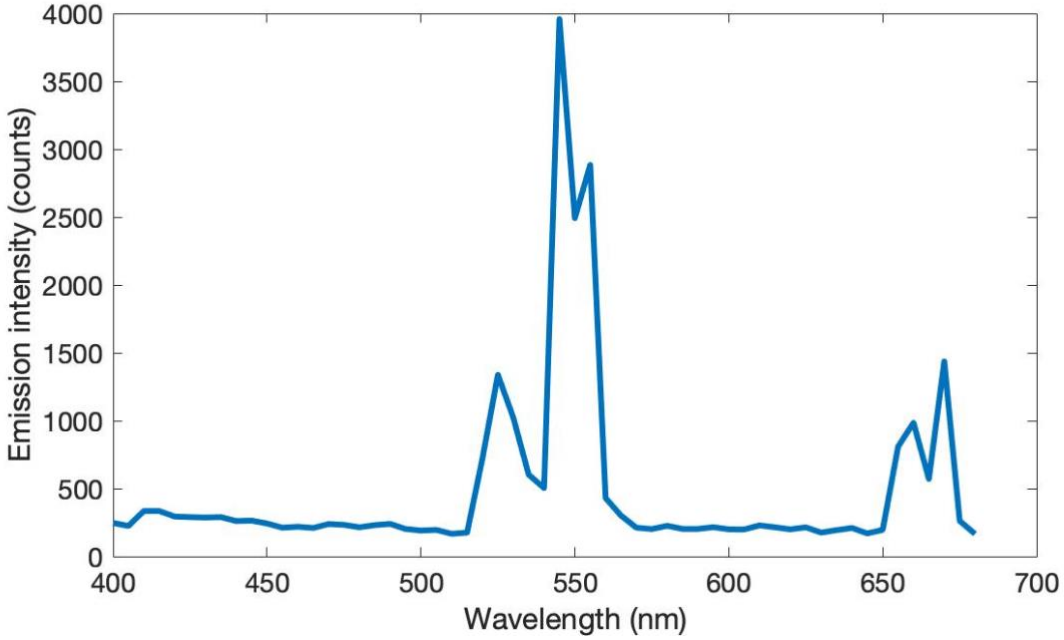

Figure 81: Olympic Dam fluorite upconversion fluorescence spectra, 5 nm resolution, 980 nm excitation.

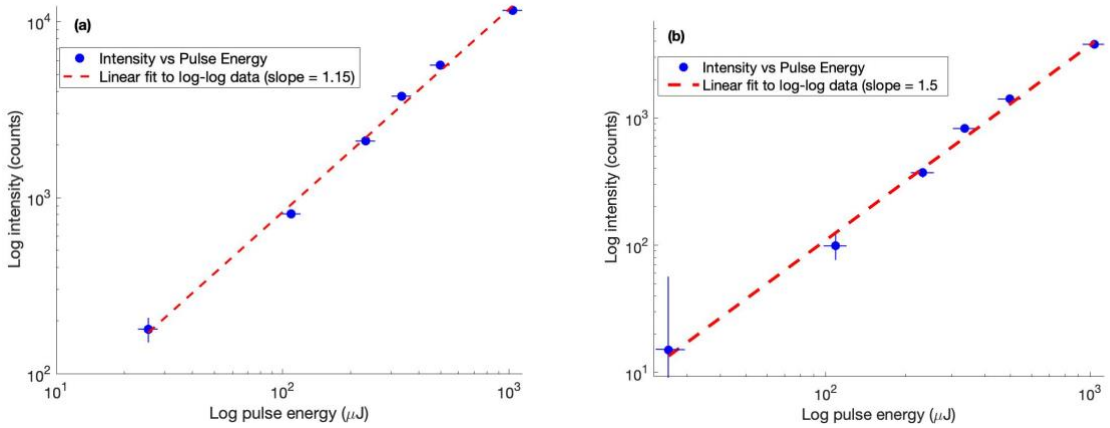

Figure 82: Log power dependence plots of Olympic Dam fluorite fluorescence at a) 550 nm emission and b) 670 nm emission.

The power dependence of the erbium emission from 550 nm and 670 nm appear similar to each other (Figure 82), but with different slopes of 1.15 and 1.5. In an erbium-only environment, these slopes would be identical, as both emission peaks occur via upconversion to the $^4F_{7/2}$ state and decay to the emission states (see Figure 21). The 550 nm emission is at slope 1 within errors, and may be completely saturated. The 670 nm emission slope shows approximately half the ions at saturation and half unsaturated. An explanation for this difference is that the unsaturated subpopulation of ions contributing to 670 nm emission are clumped near ions that induce energy transfer at the $^4S_{3/2}$ state or reabsorb the 550 nm emission but not the 670 nm emission (see Figure 83). Ions in the Olympic Dam sample that can do this are Ho^{3+}, Dy^{3+}, and Tb^{3+}. The proportion of 670 nm emission to 550 nm emission

is larger in the Olympic Dam sample than it is in the Torrington sample (compare Figure 81 and
Figure 88), lending weight to the idea that sub-populations of erbium ions can have suppressed emission.

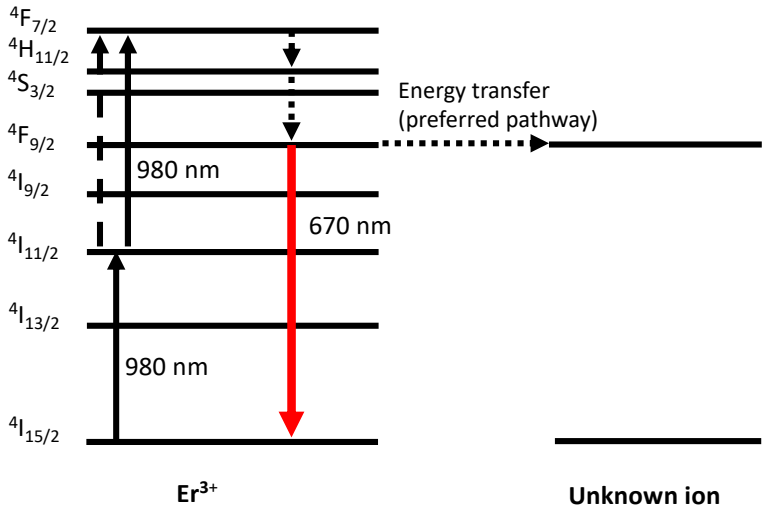

Figure 83: Band diagram of proposed pathway for suppression of 550 nm emission.

Figure 84: Olympic Dam (left) and Torrington (right) fluorites emitting upconversion due to CW 980 nm excitation. Photos courtesy of Georgios Tsiminis.

5.5.1.3. Upconversion fluorescence from Stolberg sample

Emission from the Stolberg fluorite showed the 550 nm peak from erbium but not the 670 nm peak. It also showed a large 420 nm peak (

Figure *85*), which is associated with europium rather than erbium. This is likely due to energy transfer from the $^4F_{7/2}$ state of erbium to the excited europium state (see

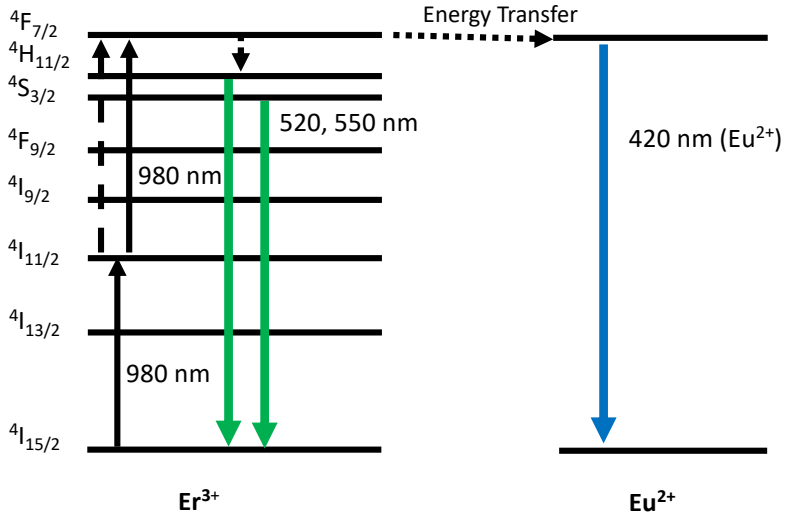

Figure *86*). The 670 nm emission in erbium is not seen. This may be due to energy transfer to a neighbouring ion that has energy levels near to the $^4F_{9/2}$ state but not the $^4S_{3/2}$ state (see Figure 90). Rare earth ions that can produce this effect are Sm^{3+} and Pr^{3+}, and it is noted that Sm^{3+} conventional fluorescence was identified in the Stolberg sample.

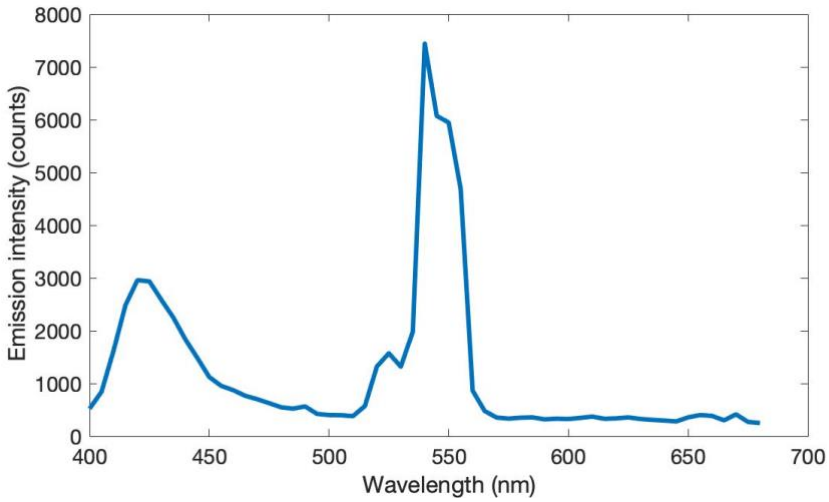

Figure 85: Stolberg fluorite sample, upconversion fluorescence spectra, 5 nm resolution, 980 nm excitation.

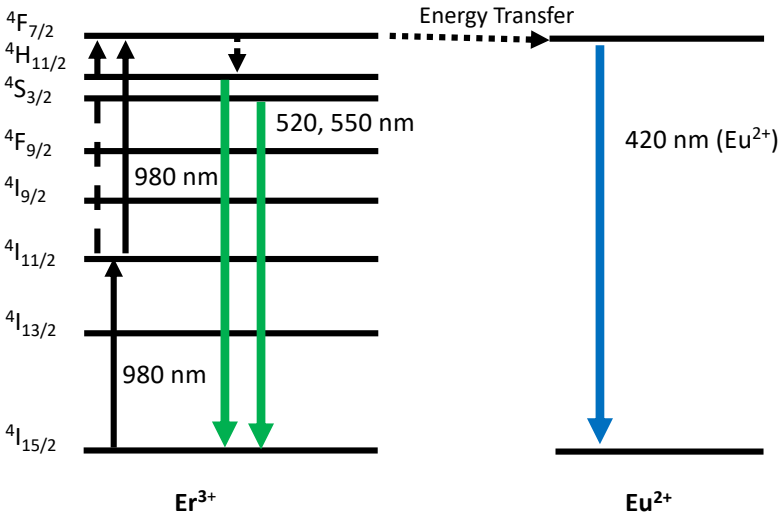

Figure 86: Band diagram of the proposed process for upconversion emission in Stolberg fluorite sample exciting at 980 nm.

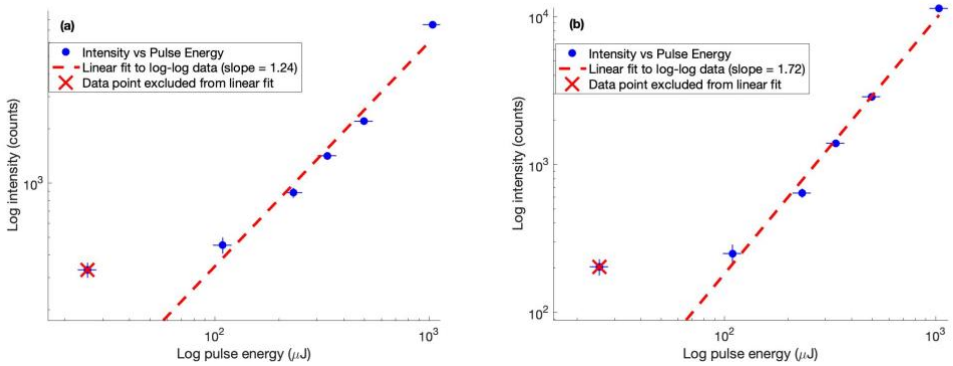

Figure 87: Stolberg fluorite emission intensity dependence on excitation power at a) 420 nm emission, and b) 550 nm emission.

The first data point (25 μJ) in the Stolberg emission was not on the linear slope in power dependence plots of both the 420 nm and 550 nm emission (Figure 87), similar to the power dependence plot in the Broken Hill fluorite sample (Figure 80). In both cases, the emission counts were large enough to rule out counting errors for this discrepancy, and the excitation energy is well above the minimum detectable power of the power meter (0.7 μJ). A likely scenario to explain both results is that at very low powers other non-emissive pathways such as energy transfer to different ions are suppressed, leading to higher-than-expected emission counts.

While the slope fits were different (1.2 and 1.7 respectively) the slope errors were large and the 95 % confidence intervals overlap. Both 420 nm emission and 550 nm emission occur after upconversion to the $^4F_{7/2}$ state in erbium, but 420 nm emission, however, only occurs via the sub-population of erbium ions with europium ion neighbours.

5.5.1.4. Upconversion fluorescence from Torrington sample

Torrington fluorite emission was similar to that of Olympic Dam. Emission at 550 nm and 670 nm was seen (

Figure 88). Inspection visually shows the emission to be evenly dispersed throughout the material (Figure 84).

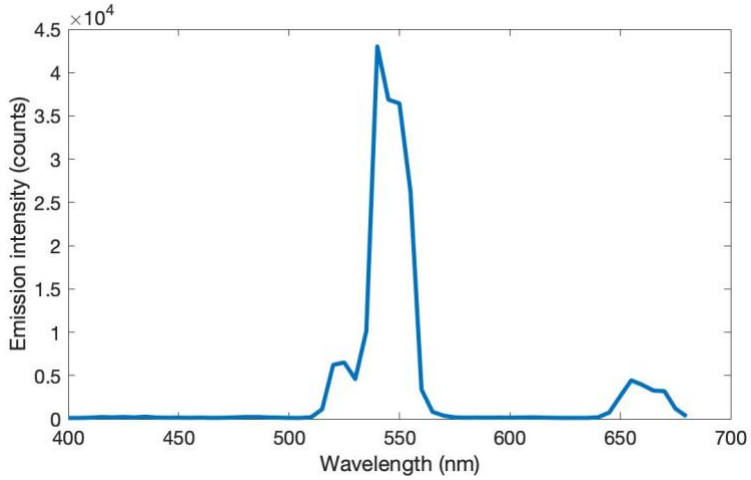

Figure 88: Torrington fluorite sample, upconversion emission spectra, 5 nm resolution, 980 nm excitation.

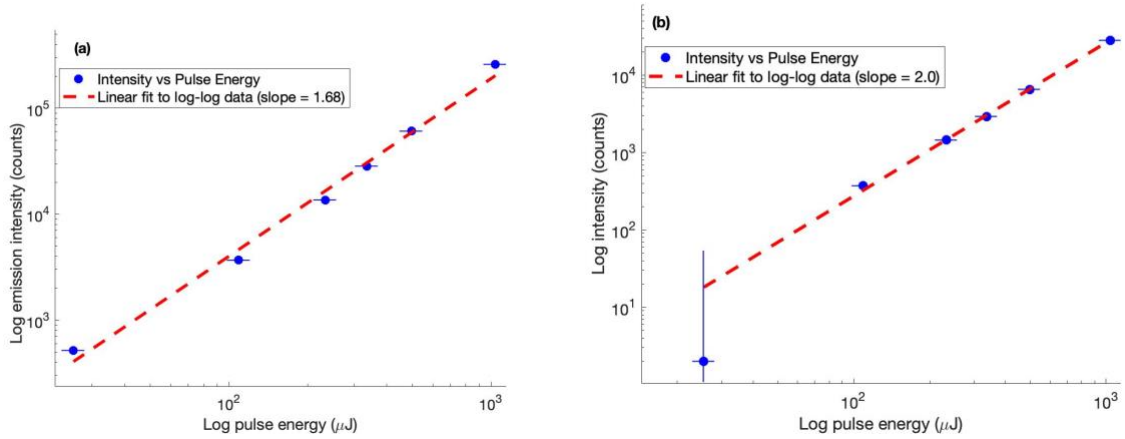

Figure 89: Torrington fluorite sample, log-log emission dependence on excitation energy for a) 550 nm emission and b) 670 nm emission.

The power dependence plots of Torrington 550 nm and 670 nm emission (Figure 89) have different slopes. It is likely that the 670 nm suppression process hypothesised for the Stolberg sample is occurring in this sample (see Figure 90). The fact that 670 nm emission has an unsaturated slope of 2 and the 550 nm emission slope has a slope indicating at least one saturated sub-population supports the hypothesis that the 550 nm emission is occurring in more sub-populations than the 670 nm emission, which in some sub-populations is suppressed.

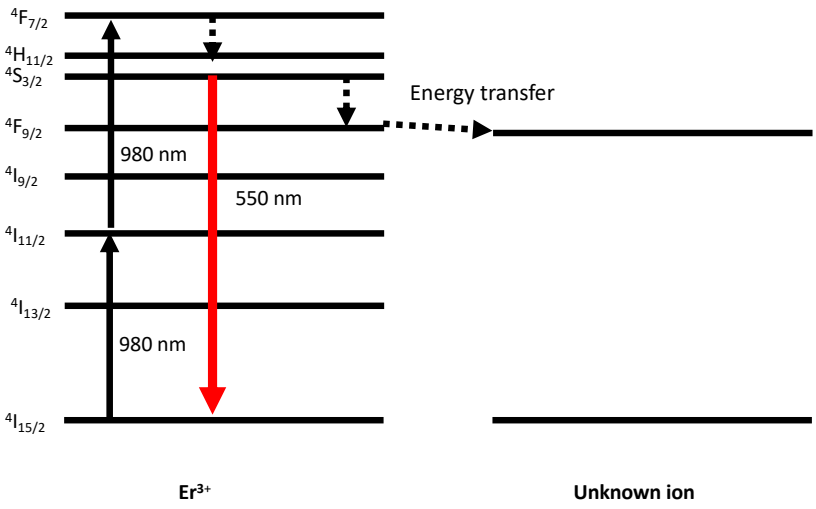

Figure 90: Band diagram of the proposed process for quenching of 670 nm emission.

5.5.2. Dual-wavelength scans of Torrington fluorite emission

The Dual-Wavelength System two-wavelength scan functionality was set up in order to find and identify upconversion from an unknown or complex sample. The Torrington fluorite sample, with some known upconversion properties and multiple identified rare earth ion inclusions, was deemed a suitable test of the scan capabilities of the Dual-Wavelength System. A crushed and pelletised subsample (prepared as in chapter two) was placed in the Dual-Wavelength System chamber. Excitation ranged over all wavelengths between 750 nm and 1500 nm in 10 nm steps, and emission detection was between 375 nm and 710 nm using both the EMCCD and the spectrometer. Initial data analysis indicated that emissions detected by the EMCCD were bright enough to be also detected by the spectrometer. The analysis in this section uses the spectrometer results, which contains the relevant spectral information.

Figure 91 shows a false colour "wavelength 1" vs "wavelength 2" 3D map of emission, using a log scale for emission intensity. Two bright bands corresponding to wavelength 1 and wavelength 2 at 980 nm can clearly be seen. Faint emission near 750 nm can also be seen, but other emission features are difficult to see due to very low counts compared to the very high counts of the erbium 980 nm excited emission.

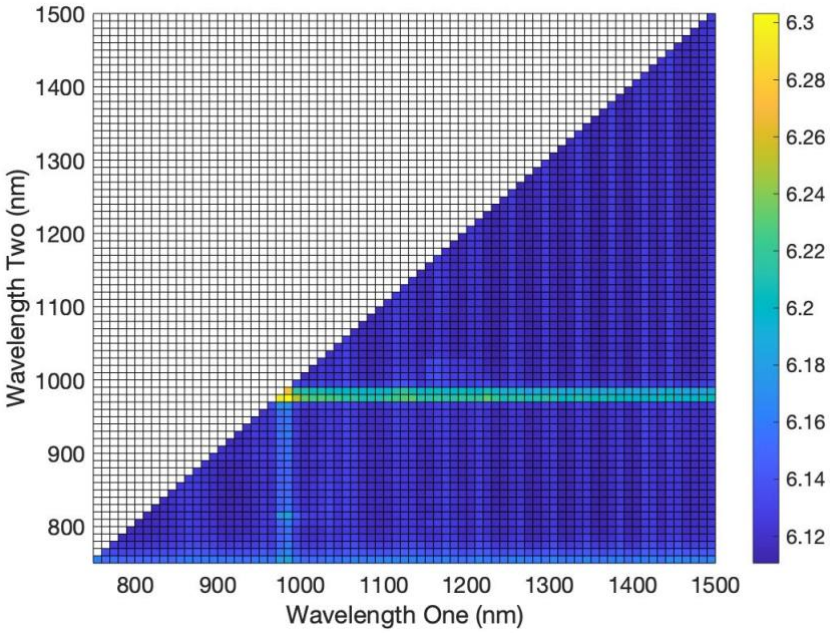

Figure 91: Dual-Wavelength System logarithmic false colour emission intensity map for Torrington fluorite crushed and pelletised sample excited by two OPOs from 750 nm to 1500 nm. The map shows intensity of emission vs wavelength 1 vs wavelength 2.

To allow both strong and weak emissions to be easily seen on the one map, a "yes/no" binary map of emission was created (see Figure 92, see appendix A5 for code for creating the map). If more than 10 bins in the spectrometer data (approximately a width of 5 nm) were twice the mean value, that wavelength combination was considered to have signal. This method allows low count data to be shown alongside high count data, and shows additional features near 900 nm, 1000 nm, and 1160 nm.

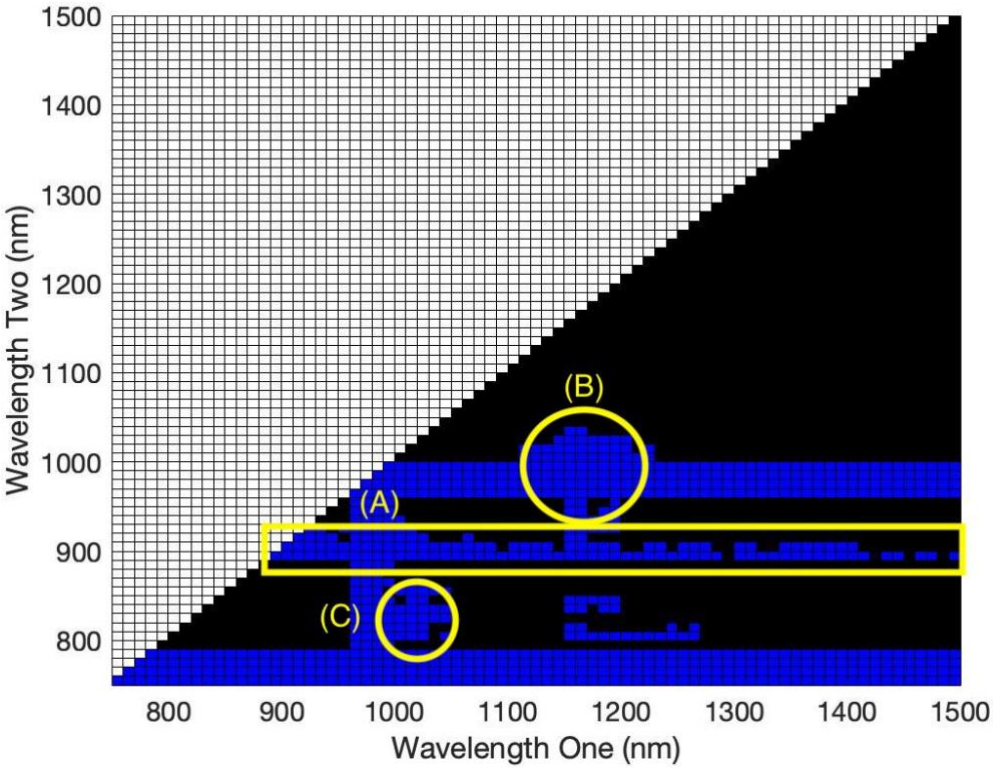

Figure 92: Dual-Wavelength System emission presence map of Torrington fluorite crushed pelletised sample excited by two OPOs from 750 nm to 1500 nm. The map shows presence of emission vs wavelength 1 vs wavelength 2. Emission highlighted by yellow boundaries are discussed in more detail below.

The brightest feature, the 980 nm excited emission, is the erbium upconversion emission described for this sample in the previous subsection. The 750 nm excited emission is at the edge of the filter range, and is likely phonon-assisted fluorescence from either samarium or neodymium fluorescence centres between 700 nm and 800 nm. The other main features are described below:

5.5.2.1. Emission under 900 nm excitation

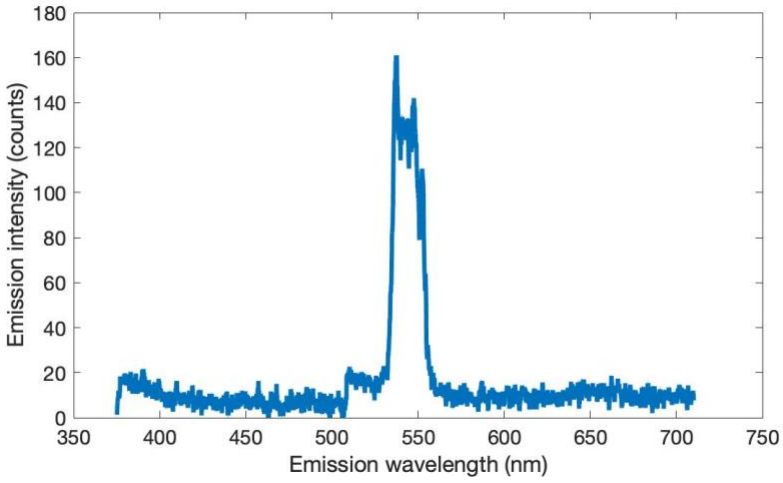

Figure 93: Torrington fluorite sample dual-wavelength upconversion emission at excitation wavelengths 900 nm (wavelength 1) and 900 nm (wavelength 2).

The 900 nm excited upconversion emission highlighted in Figure 92 (A), only occurs at one wavelength, but was not been previously seen in natural fluorite. This shows the value of even one-wavelength scans for finding new fluorescence signatures. Emission occurs at 540 nm, where one would expect erbium or holmium peaks (Figure 93). The $^5I_5$ energy level in holmium can be accessed by this photon energy, from which the ion can undergo excited state absorption to the close-together $^5F_1$ to $^3K_8$ states (Figure 94). Another explanation for this emission is two-photon absorption into the erbium ion. The emission structure is different from conventional 980 nm-excited erbium emission and so holmium is the most likely source. The intensity of the emission excited by 900 nm is an order of magnitude weaker than the 750 nm or 980 nm excited peaks. It is not known whether this is because the holmium ion density in the sample is much less than erbium or samarium ion densities, or because the upconversion process is much less efficient.

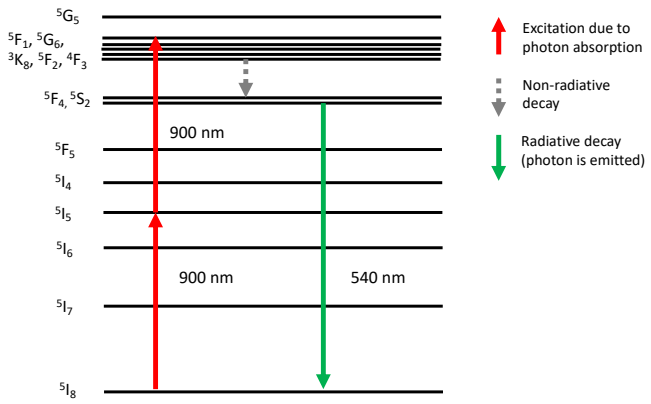

Figure 94: Band diagram of holmium upconversion using 890 nm excitation to excite the $^5I_5$ and $^5F_1$ levels. This process is the most likely process to produce the upconversion emission detected.

5.5.2.2. Emission under 1160 nm and 1010 nm excitation

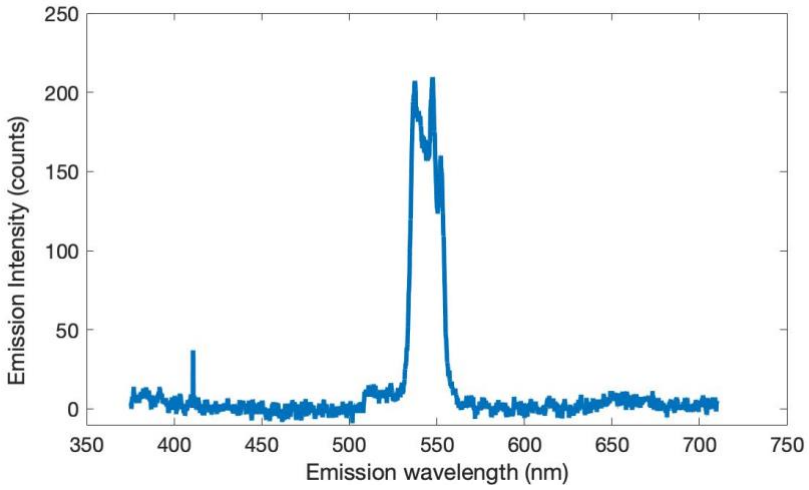

Figure 95: Torrington fluorite sample dual-wavelength upconversion emission at excitation wavelengths 1160 nm (wavelength 1) and 1010 nm (wavelength 2).

The emission highlighted in Figure 92 (B) is the strongest emission excited by two wavelengths found in this sample, and would not have been found without a dual-wavelength scan. Absorption of wavelengths around 1160 nm give rise to emission, but the strongest emission appears when a second wavelength is also applied, set at 980-1020 nm. This gives rise to the holmium-like emission seen with 900 nm excitation (Compare Figure 93 and Figure 95). Photons at 1160 nm can reach the $^5I_6$ holmium energy level. Excited state absorption of an additional 1010 nm photon can reach the $^5S_2$ level, which gives rise to holmium emission in the 500 nm to 600 nm range (Figure 96).

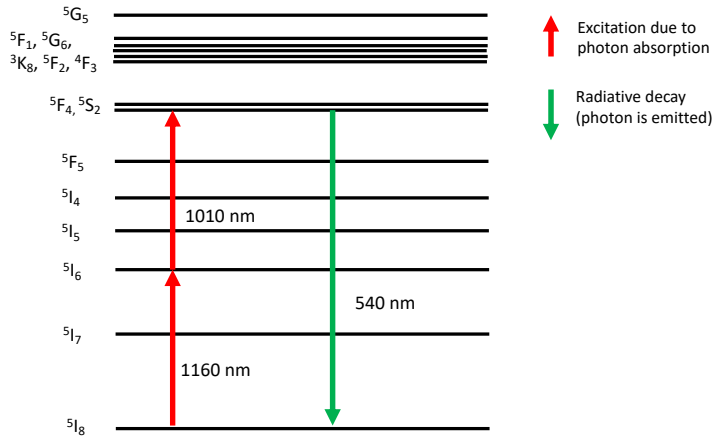

Figure 96: Band diagram of potential holmium upconversion using 1160 nm to excite the $^5I_6$ level and 1010 nm to excite the $^5S_2$ level.

5.5.2.3. Emission under 1020 nm and 830 nm excitation

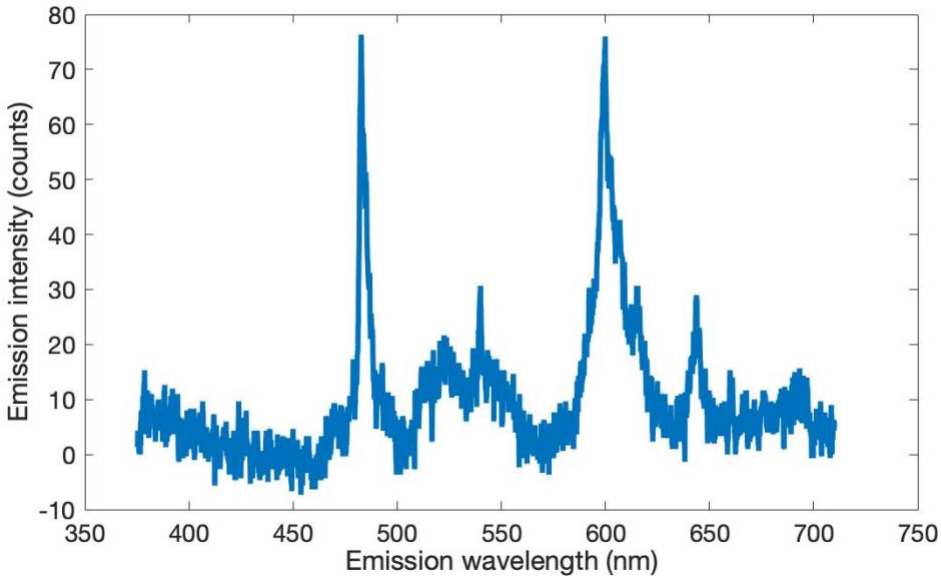

Figure 97: Torrington fluorite sample dual-wavelength upconversion emission at excitation wavelengths 1020 nm (wavelength 1) and 830 nm (wavelength 2).

Upconversion from 1020 nm and 830 nm excitation is highlighted in Figure 92 (C). The spectrometer data show three sharp emission peaks at 482 nm (~ 5 nm FWHM), 600 nm (~10 nm FWHM), and 643 nm (~5 nm FWHM) (Figure 97). (What appears to be a feature at 525 nm in Figure 97 is a grating stitching error that is present in every measurement). 482 nm and 600 nm emission is associated with samarium (Czaja et al., 2012). While strong 643 nm emission is associated with praseodymium it can also be emitted from samarium ions (Herrera et al., 2016). Upconversion emission is likely due to sequential absorption in samarium ions, either to the $^6F_{9/2}$ state via 1020 nm excitation or the $^6F_{11/2}$ state via 830 nm excitation, and then excited state absorption to the $^4G_{5/2}$ state (Figure 98).

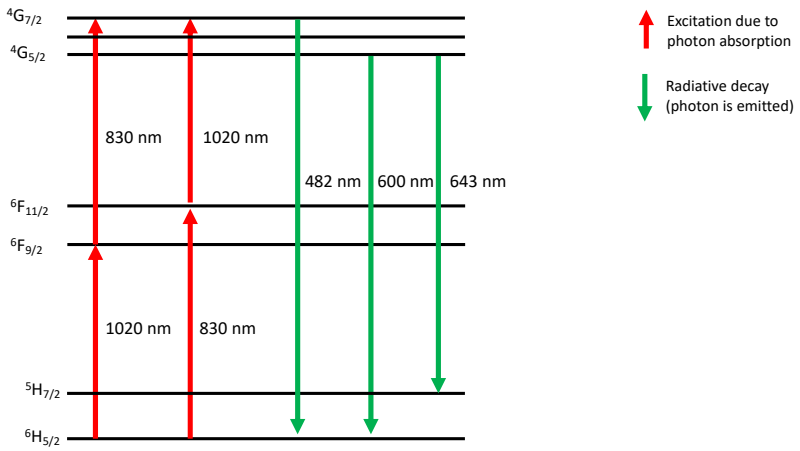

Figure 98: Band diagram of potential upconversion and emission pathways in samarium 3+. Only energy levels that are involved in the process are labelled for clarity.

The dual-wavelength scan shows that upconversion can be seen from multiple rare earths residing as ion inclusions in fluorite. The initial one-wavelength test showed that erbium upconversion was not seen in all erbium-containing samples, but may still be a useful marker in some sites for the presence of fluorite. A complication to this is the fact that erbium will be present as inclusions in other minerals. The following section investigates whether erbium upconversion in different hosts can be distinguished from one another. Erbium upconversion is then tested on the fluorite concentration series.

5.6. Erbium upconversion fluorescence for mineral identification

5.6.1. Identifying host minerals from erbium inclusions

There are three potential types of upconversion fluorescence pathways in natural minerals:

1. intrinsic, where the fluorescence depends on the intrinsic structure of the material (e.g. vacancy defects)
2. extrinsic, where the fluorescence depends on something other than the host mineral (e.g. ion inclusions), and
3. hybrid pathways (for example using an ion inclusion first-step to get to the conduction band).

Intrinsic pathways are mineral-specific by nature, as minerals are defined by their atomic composition and lattice structures. Extrinsic pathways can be present in multiple minerals, though behave differently in different lattice structures. Hybrid pathways can be mineral-specific, but may be similar for similar classes of materials.

In the case of ion inclusions, the host lattice has a unique crystal field. This perturbs the potential energy states of the ion, which changes the ion emission wavelength. This perturbation may be enough to identify the host even when the hosts are similar. This would allow ion inclusion emission to be used as a proxy for mineral identification.

To test this hypothesis we studied the upconversion fluorescence of erbium in three different hosts: an oxide, ZBLAN glass, and a natural fluoride sample. Erbium is a rare earth ion and thus the host has a minimal impact on the optically active energy levels of the ion. This means that the ability to easily distinguish between the three 'hosts' in the test above would indicate that the technique should also work well for other rare earth ion inclusions.

5.6.2. Emission scans of upconversion pathways

Initial studies were done using the Edinburgh Instruments Spectrofluorimeter (section 2.3), and the following specific samples were investigated:

1) Erbium Oxide (Er_2O_3) in powder form
2) Erbium-doped ZBLAN (Er:ZBLAN) 6 mol% doped glass fibre
3) Bulk crystal fluorite sample from Torrington, NSW.

The samples were excited by the Opolette OPO tuned to 975 nm and 1530 nm. The maximum pulse energy of the laser was used (1 mJ per pulse and 200 μJ per pulse respectively). The samples were at room temperature (21°C). For the fibre, the laser pulse was focused to a spot size of approximately 1 mm to ensure enough excitation was focused into the erbium-doped core while not damaging the fibre. For the oxide powder and the fluorite sample, emission was only lightly focused to a spot size of approximately 1 cm diameter. Emission collection

times varied depending on the emission intensity of the sample, and results were normalised to the maximum emission peak.

When Er:ZBLAN is excited with 975 nm it emits at 521 nm, 550 nm, and 650 nm as shown in Figure 99. In the erbium-containing fluorite, these peaks are at the same positions but the intensity of the peaks is different, with the 521 nm peak suppressed compared with the Er:ZBLAN peak (Figure 99). The peak shape of the 550 nm emission is different, possibly due to differences in Stark splitting of the transition in different hosts. In erbium oxide, the peaks are shifted, most likely due to the increased phonon energy of the host, which increases the non-radiative quenching of certain states.

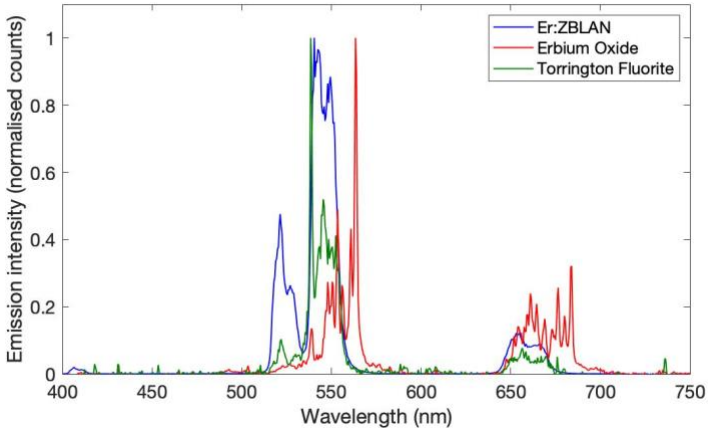

Figure 99: Normalised upconversion emission spectra from Er:ZBLAN, erbium oxide, and Torrington fluorite, when excited by 975 nm.

Similar effects can be seen when exciting at 1530 nm. Er:ZBLAN shows all peaks seen under 975 nm excitation, and erbium oxide peaks are shifted compared with the peaks of the fluoride materials. The 800 nm peak in erbium oxide is enhanced compared to the other peaks (Figure 100). While the 800 nm peak is seen in Er:ZBLAN (see semilog plot in Figure 101 below) it is unusual to see a bright 800 nm peak of comparable size to the 550 nm and 670 nm peaks. The lifetime of the $^4I_{9/2}$ state is very fast and most of the ions in this state decay to the $^4I_{11/2}$ state rather than the ground state. An explanation as to why we see enhanced 800 nm emission from erbium oxide excited at 1530 nm compared with the visible emission is that in erbium oxide the three-photon upconversion necessary for emission at 520 nm, 550 nm and 670 nm is very unlikely. A large integration time was needed to see any visible emission from the erbium oxide, and so the normalisation factor is much larger than that of the Er:ZBLAN emission. This means that, in comparison, the very small amount of 800 nm emission is enhanced in our normalised plot.

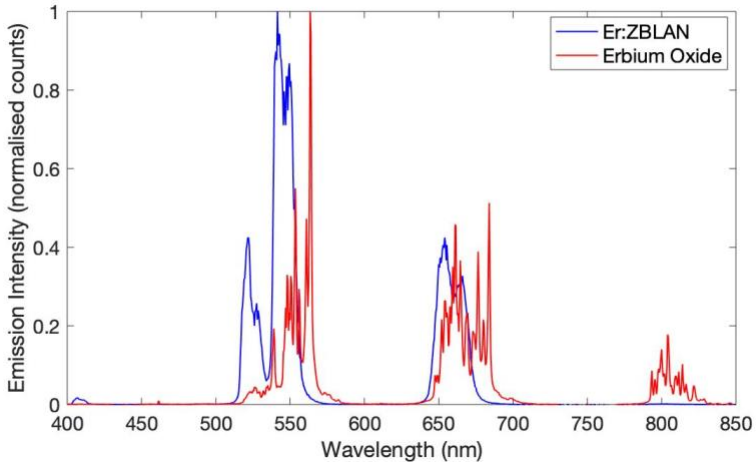

Figure 100: Erbium upconversion emission from erbium oxide and erbium-doped ZBLAN fibre excited by 1530 nm. The fluorite sample did not show emission above background counts, and so the results are not shown here.

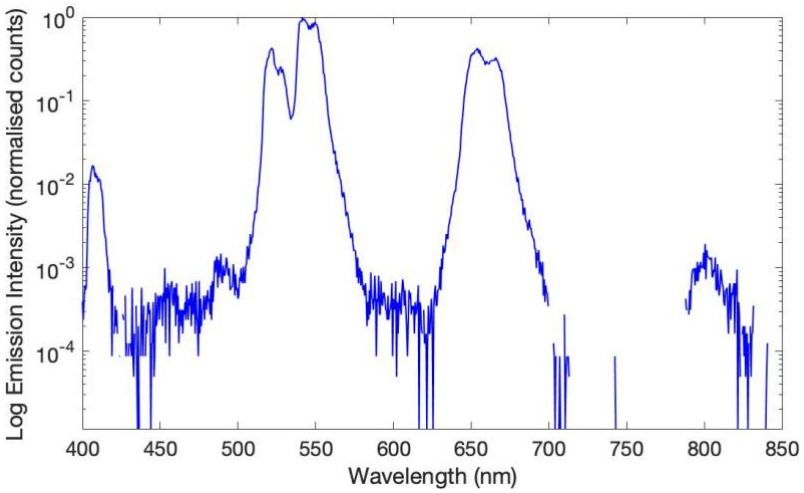

Figure 101: Semilog plot of erbium-doped ZBLAN emission excited at 1530 nm. The semilog plot shows the very small peaks at 420 nm and 800 nm that are not visible on the linear plot.

No emission was seen in the erbium-containing fluorite when exciting at 1530 nm, which may be for a number of reasons:

- The erbium population in the fluorite sample is much lower than in the artificial samples. For three-photon upconversion in particular, it is much less likely that the energy transitions will match perfectly in any one material to gain efficient excited-state absorption upconversion, with energy transfer upconversion playing a larger role in the total emission seen. The low levels of erbium may be preventing energy transfer upconversion between erbium ions, decreasing the total likelihood of upconversion. However, in fluorite crystals heavy rare earths such as erbium tend to clump in groups of six (Catlow et al., 1984). This would make energy transfer more likely despite the small erbium population.
- Other ion inclusions or defects within the sample are absorbing the 1530 nm excitation light. There may also be strong energy transfer pathways between the erbium $^{4}I_{13/2}$ and $^{4}I_{9/2}$ states and other rare earth ions.

The distinctive shape of the fluorite-hosted erbium was found with conventional fluorescence exciting at 521 nm in almost all natural fluorites with emission above background in this area (Figure 102). The exception was the Edith River sample. As the emission was larger in magnitude than the Pernatty Lagoon sample, which followed the erbium shape, this is not due to lack of signal. The yellow colouration of the Edith River sample is due to O_3^- molecules in the fluorite lattice, substituting for two adjacent fluorine ions (Bill and Calas, 1978). If this lattice substitution is in large enough concentrations it can change lattice behaviour, and shift the erbium peaks (as seen in Figure 99 with Er_2O_3 compared with Er:ZBLAN and the Torrington fluorite). This highlights the need for mine-specific calibration of detection criteria if fluorescence is to be used for real-time sensing in the field.

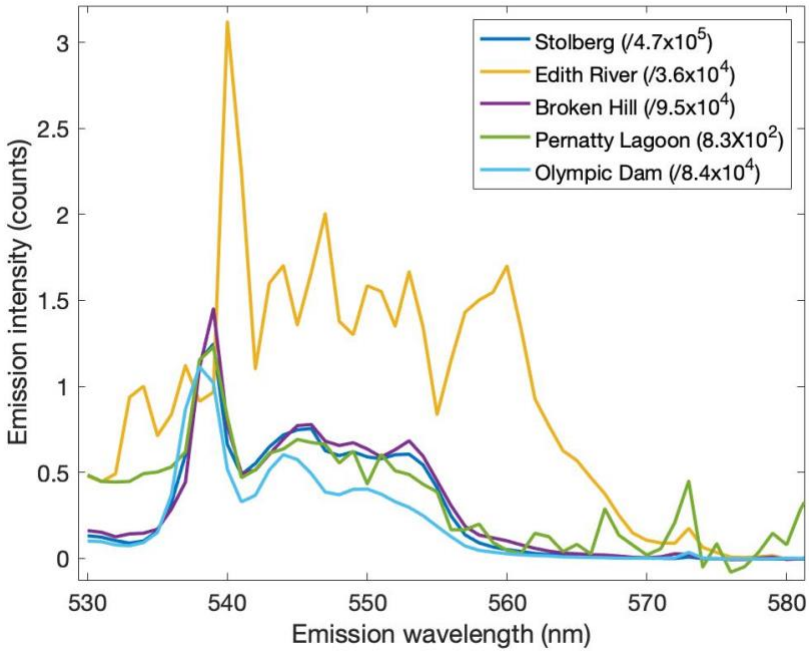

Figure 102: Normalised comparison of other fluorite sample conventional fluorescence emission at 530-580 nm when exciting at 521 nm. Most show the typical very high 538 nm peak and the lower intensity peaks between 540 and 560 nm.

It is concluded that erbium emission from different hosts is similar but can be differentiated from one another. In an erbium-rich environment, identifying the host mineral would be possible. The ease of identification would depend on the host minerals present.

Three possible ways to use erbium to identify host minerals are:

1. Presence of emission: some minerals, such as fluorite and haematite, easily allow rare earth inclusions into their crystal structure. Others, such as copper sulphides, do not. In addition, some minerals have intrinsic properties that prevent emission from particular excitation or emission wavelengths.
2. Position of peaks: as seen above with between fluorides and the oxide, rare earth emissions can be shifted to a longer wavelength due to properties of the host mineral. Noting where the emission peak occurs can therefore distinguish between two mineral types.

3. Ratio of peaks/emission position: Er:ZBLAN and Er:CaF_2 did not have a discernible difference in peak position, however the intensity of the emission at different wavelength did change. The Torrington fluorite can be easily differentiated from Er:ZBLAN and erbium oxide by analysing the ratio between the emission at 538 nm and the emission at 522 nm (for Er:ZBLAN: around 1:1; for erbium oxide: around 6:1; for fluorite, around 10:1).

5.6.3. Concentration determination using erbium upconversion fluorescence

Upconversion from ion inclusions has potential use in mineral sensing. A test was conducted on a known sample set in order to test for the ability to determine fluorine concentration. The known Torrington fluorite sample was mixed in various concentrations by weight into a copper-porphyry ore obtained by CRC ORE, chosen because assay work indicates it does not contain fluorine. A mixture series was created with fluorite percentages of 0, 1, 2, 5, 10, 25, 50, 75, and 100%. The erbium upconversion signal was detected using 980 nm excitation in the Dual-Wavelength System. It is noted that one fluorite sample was used for the concentration series, which gives each series a similar erbium-to-fluorite ratio. This may not be the case even in ores that grew close together, and future work will be needed on samples from the same mine site to map emission variability before use in the field.

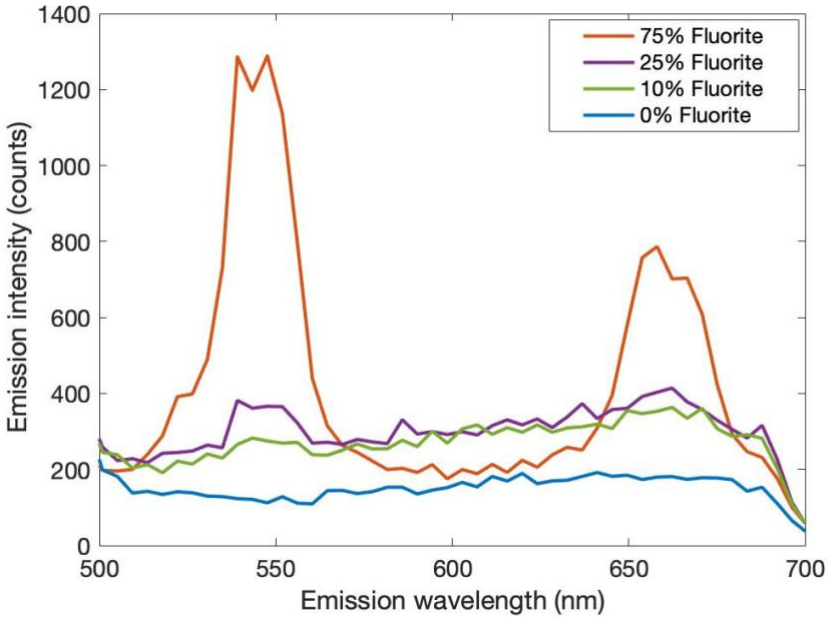

Figure 103: Upconversion emission for mixture series samples containing 0, 10, 25, and 75% Torrington fluorite excited at 980 nm. Fluorescence signal was integrated for the same amount of time for each sample.

Figure 103 above shows the emission spectra at the same integration time from samples of differing weight percentages of fluorite. In Figure 103 the 0 % fluorite sample still has a large background signal. While it is cut off by a filter in the figure above 700 nm, investigations using a 950 nm SP filter showed that this background signal is a very broad emission peaking at 900 nm. The origins of this emission is unknown, but as it is seen in every sample of the synthetic fluorite concentration series apart from the 100 % fluorite sample, it follows that it comes from a component of the zero-fluorine sample (CPO, see Table 20). This sample

contains a small amount of copper ore and other minerals in a fine, clay-like matrix. More work is needed to define which part of this sample is responsible for the broad background upconversion emission.

In the 75% fluorite sample, the fluorite emission peaks at 540 nm and 660 nm are clearly visible, and the 25% fluorite sample shows the 540 nm peak above the background signal. It is possible to subtract the background signal because of its predictable shape. Subtraction used the 0% fluorite sample as the background signal shape and normalised the height of the background to the emission between the erbium peaks at 594-619 nm. The emission of the 540 nm peak and 660 nm peak were integrated. This subtraction method worked very well, allowing differentiation between 1% and 2% fluorite ore (Figure 104, the first two data points). This indicates that the background shape remains constant throughout the sample.

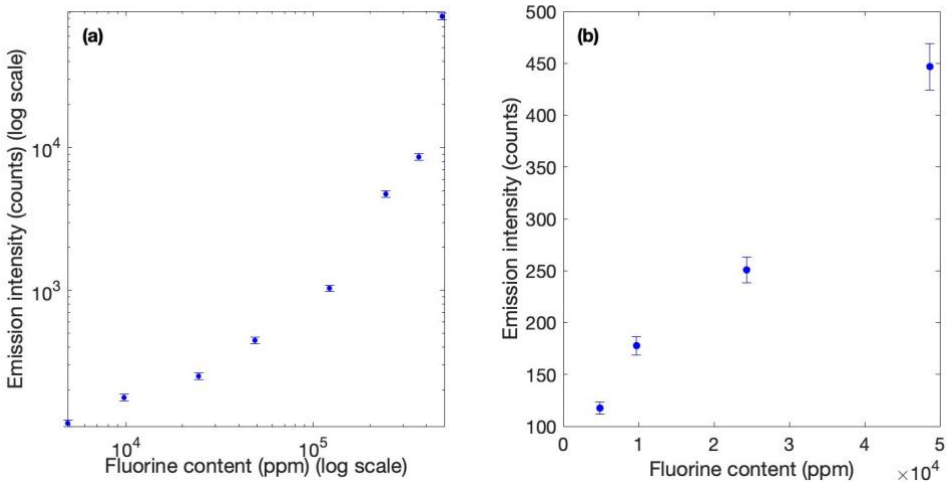

Figure 104. A) Log-log plot of background subtracted fluorite emission vs fluorine concentration using the sum of the 530 nm and 660 nm erbium upconversion emission peaks. Fluorine content corresponds to 1, 2, 5, 10, 25, 50, 75, and 100% Torrington fluorite by weight. B) Linear plot of the 1-10 % fluorite emission. The emission was excited by 980 nm laser light.

In Figure 104 it is shown that the increase in fluorescence with an increase of fluorite is not linear. This is due to two main reasons:

1) Fluorine content is a volumetric number, and fluorescence depends on the surface area;
2) Fluorite in this case is more transparent than the ore sample, and so a larger fluorite content increases the overall transparency of the sample. This allows more fluorite to be excited and fluoresce at deeper levels of the sample, compounding the increase in fluorescence.

These two variables will change at different mine sites and different places in a processing stream, depending on surface roughness (size of material) and overall sample transparency. Calibration curves will have to be made for sensors when they are in place for real-time sensing applications.

5.1. Emission efficiency and prototype specifications

Future work in assessing the viability of fluorescence for real-time sensing on mining sites requires building and testing prototype sensors. This requires the general efficiency of the fluorescence process to be known in order to calculate minimum detector efficiencies and excitation powers needed for the specific use-case for the testing environment. Using the Dual-Wavelength System calibration found in section 2.1.2.9, the number of photons per millijoule of excitation energy for samples used in this thesis can be calculated. Table 21 shows the photons emitted per millijoule of excitation energy (or the sample fluorescence efficiency) for selected samples used in Chapter Five. Large variability in fluorescence efficiency from the same mineral types can be seen, indicating that mine-specific testing must be done before prototype specifications can be calculated, with the aim being for the prototype to be capable of detection to the concentration threshold of significance at that mine.

Calculated Photon Emission		
Sample	Emission (counts) detected per mJ of excitation	Photons emitted per mJ per hemisphere
S1 (2.1% F)	3E+01	3E+10
G5 (5% F)	1E+02	1E+11
Fluorite (Torrington)	1E+04	1E+13
Fluorite (Jinka Station)	1E+02	1E+11
Fluorite (Olympic Dam)	1E+04	1E+13
Fluorite (Upconversion)	9E+02	1E+09
Fluorapatite (Alice Springs)	2E+02	2E+11
Fluorapatite (Harts Range)	3E+05	3E+14

Table 21: Calculated total photon emission derived from counts detected, excitation power, and system detection efficiency for various samples shown in Chapter Five.

The samples in Table 21 can provide a general guide as to what specifications a prototype would likely need for minimum fluorescence output in different scenarios. Using the Matlab® code listed in appendix A6, the minimum excitation density at a fluorapatite-bearing ore was calculated for a 2 cm^2 detector one metre away from the ore sample. Two detector scenarios were considered: a photodetector integrating over all wavelengths allowed by a filter, and a spectrometer. While the photodetector would have a greater detection efficiency, the spectrometer would be able to distinguish between the peaks of interest and 'noise' peaks from other minerals or equipment. A spectrometer would also be the most efficient way to distinguish between fluorite and fluorapatite emission.

Two detection scenarios were also considered. One was detecting 5000 ppm fluorapatite diffusely spread in the ore sample, and one was detecting one 1 cm^3 block of fluorapatite in an ore sample on a conveyor belt moving at 5 m/s. For each scenario, the detector was integrating over 1 s of data.

Minimum excitation power at the ore to detect a signal from fluorapatite (mW/cm^2)		
Detection Type	Diffuse	1 cm^3 block
Photodetector	0.1 mW	0.2 mW
Spectrometer	1 mW	2.5 mW

Table 22: Minimum excitation power in mW needed to detect 5000 ppm fluorapatite diffused in ore or a 1 cm^3 block of fluorapatite on a 5 m/s conveyor belt in order to detect a signal. This assumes a detector area of 2 cm^2 and a distance from the sample of 1 m.

Table 22 shows the minimum excitation power needed for the two scenarios above. In a real system, the minimum power needed would be slightly higher as the power calculations assume a flat surface, which is not reasonable for pre-crushed ore on a conveyor belt. The calculations also assume the emission from the ore is directly below the detector, which is reasonable for an array of detectors across a conveyor belt but not one detector over the entire belt width. The numbers do indicate the approximate order of magnitude of excitation needed for a prototype, and indicate that potentially cheaper sources of illumination such as LEDs can used rather than more expensive laser systems.

Particular mine-site specifications can change the results of the calculations significantly. Three of the most significant variables are discussed below:

- *Distance from the conveyor belt to the detection source*: this changes the proportion of emission below the detector reaching it by 1/distance^2, and so the minimum distance to the detector is important to find and test before illumination requirements are set.
- Background signal present: if the detector setup is shielded from background sources of light such as natural sunlight and room lighting, the power requirements to see a signal above background is much lower. Spurious signal from the sample can also change the power requirements, as spectrometers rather than photodetectors may have to be used if there are variable illumination sources present, increasing the power requirements by an order of magnitude.
- *Proportion of the belt that needs to be illuminated and the type of illumination*: this changes the specifications of both power and focusing apparatus. For full belt coverage, assuming a belt width of 60 cm, to spot each small block of fluorite as it passes a minimum total power of 12 mW (per 1 cm x 60 cm illumination line) at the sample will be needed, and the ease of providing this needed power will depend on the divergence of the excitation light and the distance of the excitation source from the sample.

5.2. Discussion and future work

To the best of our knowledge this is the first time upconversion has been reported in a natural mineral. This first investigation of upconversion fluorescence in natural minerals has shown that upconversion fluorescence has the potential to be a new and viable detection method for natural fluorite.

Upconversion experiments revealed bright signatures from erbium in fluorite, from both pulsed laser systems and from continuous-wave portable lasers. Further upconversion signatures were observed from europium, holmium, samarium and praseodymium inclusions.

It was shown that erbium in fluorite can be distinguished from erbium in other hosts using its upconversion emission signature. Not all fluorites with erbium Stokes' emission produced erbium upconversion emission detectable with the Edinburgh Instruments Spectrofluorimeter.

Future work recommended in this space would involve scanning each sample using the Dual-Wavelength System. This would repeat experiments with higher powered excitation and greater detection efficiency, and it would be aimed to additionally show any two-wavelength excitation upconversion, and explore the two-wavelength space into the as-yet unresearched mid-infrared.

The purple Jinka Station fluorite did not show emission using the Opolette OPO with the Spectrofluorimeter, but showed emission using excitation from the 257 nm UV LED. This indicates that UV excitation may be a useful detection method for the purple lattice-damaged fluorites, while noting that UV excitation has the disadvantage of being non-specific in its excitation properties. It can produce large background signatures, especially in high-organic environments.

Future work would involve two-wavelength excitation on purple fluorites. This may induce upconversion emission that bypasses the broad visible absorption peak from calcium nanoparticles in these damaged fluorites. The investigation reported in this thesis was limited to using only a small part of the 210-4400 nm excitation range now available with the Dual-Wavelength System. Further work should search for upconversion peaks in this extended range.

Conventional fluorescence scans found two lattice defect-related emissions in fluorite. One was the known M-centre emission at 720 nm, which was only seen in the green fluorite samples of this study. The second was an emission at 1118 nm, reported here for the first time, which appears to be related to the fluorite fluorine vacancy. This emission can be induced in pure calcium fluoride by ultra-violet light exposure. It was seen in all intact samples apart from the Jinka Station and Marienshacht fluorites. The Jinka Station fluorite showed the emission when crushed. Further research on this emission would attempt to identify what levels of lattice damage cause and suppress the signal. Additional work would be to quantify the signal's desensitisation and rejuvenation qualities. Application-focused work would assess the usefulness of the signal as a marker for fluorite in real-world, out-of-laboratory conditions.

Three fluorescence signatures were tested for their suitability in determining mineral concentration:

1) conventional fluorescence from fluorite;
2) conventional fluorescence from fluorapatite, and
3) upconversion fluorescence from fluorite.

Fluorapatite emission came from manganese inclusions. Bright signals were seen in the fluorine-containing ore from both erbium inclusion-related upconversion and defect-related conventional fluorescence.

Previous work by CRC ORE on the mineralogy and composition of the ore showed that fluorapatite was not the largest host of fluorine in the ore studied, but the emission was still a good proxy for fluorine grade, able to distinguish between ores with sub-percent and greater than two percent fluorine levels from the same mine site.

Fluorite conventional near-infrared fluorescence originating from a lattice defect signature was not seen in the ore samples, even though fluorite was the largest host of fluorine in the ore calculated from assay ratiometrics. In the synthetic concentration series, this signature was able to distinguish between one and two percent fluorine concentration samples. While the lattice defect signal depleted under extended 600 nm excitation, the concentration series results were fluorite dependent without deliberate rejuvenation of the signal prior to measurement. The high resolution of the results show that the signal is useful without prior processing, potentially for real-time on-belt sensing.

Upconversion fluorescence from erbium inclusions in fluorite was also tested for grade determination using the concentration series. It was able to distinguish between one and two percent fluorine concentration. The zero-fluorine ore used in the fluorite concentration series appeared to have broad upconversion emission, but simple background subtraction methods were found to be suitable to identify the fluorine signals, indicating that minimal signal processing would be needed to use near real-time fluorescence sensing techniques in the field.

6. Chapter Six: Discussion and Conclusions

6.1. Discussion of aims

Three aims were outlined in chapter one of this thesis. The following discusses the results in relation to these aims.

6.1.1. Develop and characterise a dual-wavelength upconversion fluorescence facility.

The Dual-Wavelength System described in chapter two fully physically and optically integrates the apparatus consisting of two tuneable laser systems, two spectrometers, an EMCCD, and a temperature stage into a novel facility controlled by an overarching software control and data-recording package. Detection efficiency was characterised for all three detectors as detailed in section 2.1.2.9. This characterisation process also showed the success of the automation of the temperature stage.

6.1.2. Apply the facility to explore and identify upconversion fluorescence previously unknown in minerals.

Initial upconversion 750 nm-1500 nm excitation and 400-700 nm emission detection scans were conducted on uraninite, commercially significant sulphide minerals, and fluorite. A fluorite sample showed upconversion fluorescence from a number of rare earth inclusions, and to our knowledge, this is the first time upconversion fluorescence has been shown in a natural mineral.

The uraninite and sulphide minerals did not show any detectable upconversion emission in the relatively limited ranges of the excitation and emission detection used. Different excitation and detection ranges may prove to have better results, as detailed in the future work section below.

A zero-fluorine ore used for a concentration series proved to have a broad upconversion fluorescence signal, which indicates potential for future work on clays and other fine matrix minerals.

6.1.3. Assess the viability of these newly-discovered fluorescences—both upconversion and "conventional" single-photon fluorescence—as real-time, non-contact mineral detection, identification and quantification techniques.

Fluorescence for mineral grade identification was tested using three separate signals: the erbium upconversion emission from fluorite, the conventional fluorescence emission from fluorite, and the conventional fluorescence manganese emission from fluorapatite. In a synthetic concentration series, both conventional fluorescence and upconversion fluorescence were capable of distinguishing between one and two percent fluorite by weight. For the ore sample provided by CRC-ORE, conventional fluorescence was capable of distinguishing between sub-percent and two percent fluorine mixtures.

Calculations of the fluorapatite manganese fluorescence efficiency shows that on a conveyor belt fluorescence detection of fluorine-bearing minerals should be feasible even when using

low powers, allowing both scalability and for the use of cheap components. The success of concentration series tests and the affordability of prototype and field deployment makes fluorescence highly viable as a mineral detection technique.

6.2. Conclusions

There were five main outcomes to this thesis:

1) The Dual-Wavelength System was produced and characterised. The system is designed for automatically exciting a sample with two independently tuneable lasers and scanning through different wavelength ranges. For each set of wavelengths it can simultaneously use three detectors to both record spectra of emission between 250 nm to 1700 nm, and to image between 250 nm to 1050 nm. This has allowed the two-wavelength excitation scans in this thesis to take place.

2) A process has been devised and tested to quantitatively measure energy transfer parameters directly in doped fibres. This allowed the first quantitative measurements of the W11 Er:ZBLAN energy transfer parameter in a number of fibres, and can be used in future to measure other energy transfer parameters and other fibre types.

3) A new colour centre emission in the near-infrared was discovered in fluorite. This appears to be associated with the F-centre or fluorine vacancy defect in fluorite. It was seen both in natural and synthetic samples.

4) Upconversion fluorescence was discovered in natural fluorite. While synthetic fluorite is known to upconvert, this is the first time upconversion has been reported from a natural mineral sample. Multiple fluorites showed upconversion fluorescence from erbium inclusions, and two-wavelength excitation scans revealed emission from multiple other rare earth element inclusions.

5) Stokes' near-infrared fluorescence and upconversion fluorescence from fluorine-bearing minerals were tested successfully on fluorine mineral concentration series, indicating the viability of fluorescence for real-time mineral identification down to sub-percentage levels and grade detection for concentration changes of approximately a percent.

6.3. Future work

A number of further experiments and projects can lead from the initial studies carried out in this thesis. The most significant are highlighted below:

6.3.1. Expanding the Dual-Wavelength System capabilities

Towards the end of this research the Dual-Wavelength System was expanded using additional support from the Defence Next Generation Technology Fund Grand Challenge "Counter Improvised Threat", (Project CIT-186), incorporating new additions. These include the 800-1700 nm infrared spectrometer used in this thesis and a mid-IR OPO laser capable of emitting laser light at 2500 nm to 4400 nm. These additions greatly increase the range capabilities for future work and will be advantageous when scanning for fluorescence in sulphide minerals,

particularly those of copper, which have band gaps between 600 nm and 1500 nm and absorption features in the 2000-4000 nm range. Many transition metals also have optically active areas in the detection range accessible using the near-infrared spectrometer. It is feasible that transition metal inclusion-based emission would have less sample-to-sample variability as many transition metals are more abundant than rare earth elements (percentage rather than sub-percentage levels of crustal abundance). Future work would involve fully integrating these parts into the Dual-Wavelength System and testing them on suitable materials.

6.3.1. Expanding the range of two-wavelength excitation scans

All the two-wavelength excitation scans reported in this thesis were performed between the wavelengths 750-1500 nm, or the visible 530-700 nm. While suitable for detection of upconversion emission from rare earth elements, these ranges are not suitable for detecting potential intrinsic emission from sulphide minerals with band gaps in the near-infrared. Future work will expand the excitation into the mid-infrared, using the Ekspla mid-IR OPO and the near-infrared spectrometer.

6.3.2. Quantifying the energy transfer parameters of doped fibres

A successful process was identified to experimentally determine the strength of the energy transfer parameters in erbium-doped fibres. Future work will include using this technique to quantify other energy transfer parameters in the Er:ZBLAN fibre, and using the technique on other fibre types, such as erbium-praseodymium codoped fibres, important for creation of new fibre lasers.

6.3.3. Near-infrared fluorescence scans

A significant knowledge gap in the literature, on emission wavelengths in the near-infrared, was noted when studying known emissions from minerals. Older literature reports used bialkali and S20 photomultiplier tubes, then in more recent decades silicon detectors with sensitivity from 200-1000 nm, and infrared detectors such as InSb detectors with sensitivity between 1500-5000 nm. This leaves a gap in infrared emission detection between 1000 nm and 1500 nm, bridged by InGaAs detectors in the past thirty years. Very bright natural signals have been detected in the 1000-1500 nm range in the past such as the Mn^{5+} fluorapatite signal studied in chapter six (MacRae et al., 2016) and the 1530 nm erbium signal studied in chapter three (Allain et al., 1989b). In general however experimental coverage of this range is much less comprehensive, virtually non-existent compared to that of the visible or mid-IR ranges.

Future work in this range would concentrate on filling knowledge gaps in the near-infrared. This includes conducting "conventional" fluorescence scans of minerals of interest with ultraviolet or visible excitation while observing emission with the near-infrared spectrometer between 800 nm and 1700 nm.

6.3.4. Fully characterising the fluorite colour centre

Conventional fluorescence analysis in chapter five discovered a new 1118 nm fluorescence emission that appears to originate from lattice defects in fluorite. To our knowledge this emission has not been previously reported. This may be both because it is in the historic near-infrared detector range gap, and because the emission depletes rapidly under continuous

wave excitation. Future work on this emission would target characterising its origins and quantifying its depletion and re-sensitisation characteristics, such as whether radiation, exposure to light, crushing, or heating deplete and/or re-induce the signal.

6.3.5. Investigating the variability of mineral emission intensity from the same location

The tests of fluorescence for use in determining mineral grade reported in this thesis used either a man-made concentration series or an ore series where fluorine concentration is modified by mineral processing, and all members of the series came from the same starting ore. These tests do not take into account variability of fluorescence centres from sample-to-sample in the same location, which needs to be tested in order to determine the limits of fluorescence techniques for grade determination beyond "yes/no" mineral sensing.

6.3.6. Producing and testing prototype mineral sensors

Before fluorescence techniques can be used for mineral detection in the field a prototype module must be built and tested in out-of-lab pilot-plant controlled trials to demonstrate scalability, and performance under near-mine site conditions. Specifications must be calculated for the development of prototypes for a specific use-case. The prototypes can then be refined and committed for field trials.

Appendices

Appendix A1

The below Matlab® code was used to calculate blackbody radiation rates for absolute efficiency measurements in chapter two.

```
function nophotonsblackbody

%A function to figure out how many photons you'll see at a particular
%temperature in a particular wavelength band.

%We use Planck's radiative equation:
% I(T,wl) = 2*pi*h*c^2*wl^-5/(e^(h*c/wl*k*T) - 1)
%Which gives you the emission per steradian per area of emissive object for
%a perfect black body.
%We then times this by delta wl, emissivity of the sample, area of emissive
%object, and steradians over a hemisphere (2pi).
%We then convert this energy (J) into photons by using E = hc/wl


wl1 = 400; %starting wavelength in nm
wl2 = 700; %ending wavelength in nm

x=linspace(wl1,wl2,(wl2-wl1)+1); %x for plotting purposes
wl=x.*1e-9; %Translating x into SI units for y value

h=6.626e-34; %Planck constant (SI units)
k=1.38e-23; %Boltzmann's constant (SI units)
T=500+273.15; % 0 degrees C in K
c=3e8; %Speed of light (SI units)
A = pi*((6e-3)^2); %Area of emissive body (m^2)
em=0.98; %Emissivity of pressed graphite
sigma = 5.67e-8; %Stefan-Boltzmann constant

%Planck's radiative equation:
y=(2*pi*h*(c^2)).*(wl.^-5)./(exp((h*c)./(wl.*k.*(T)))-1);
%How much energy possible to see:
yy=y*A*em*(wl(2)-wl(1)); %area x emissivity x steradians
%How many photons:
photon = (h*c)./wl;
yy=yy./photon;

disp('Total number of photons in range is:')
sum(yy)

plot(x,yy)
```

Appendix A2

The below Matlab® code was used to solve the differential equation set 3.2 and fit to the time-resolved data.

Using functions defined below to fit the differential equations to the data:

```
% A function to model the population levels in Er:ZBLAN including
% upconversion. This will be used to check a function
% N2_Er_Pop_model_V2 that uses the ode solvers to solve the population
% model and use this output to fit to data obtained from the fluorescence
% measurement
%Author: D. Ottaway
%Modified by J. Moffatt

close all
clear all
clc

targetfile = input('Input experiment code '); %Inputs data specific to exp.
%The input code is the file name of the data you want to use. I will add a
%text file explaining each data file.
endfile='.csv'; %For loading 1530 nm and 980 nm values from filename.
filename=sprintf('%s%s',targetfile,endfile); %Needed to extract y data.

propdat=1; %Proportion of data we are going to be using for fitting.

%The number of bins we want to sum together. This is mainly for aesthetic
%purposes to get rid of noise in the plots, as the fit doesn't care about
%random noise.
nobins=1;

%Default Graphic Settings to make plots better
set(0,'DefaultAxesFontSize',14);
set(0,'DefaultAxesFontWeight','normal');
set(0,'DefaultTextFontSize',14);
set(0,'DefaultTextFontWeight','normal');
set(0,'DefaultUicontrolFontSize',16);
set(0,'DefaultUicontrolFontWeight','normal');
set(0,'DefaultAxesTickLength',[0.025 0.015]);
set(0,'DefaultAxesLineWidth', 1.0);
set(0,'DefaultLineLineWidth', 2.0);

% load the Erbium Parameters
ExpParam = Initial_Population(targetfile);
a.Ninitial = ExpParam(1);
%Ninitial uses data specific to the experiment.
rates
%Rates are the different rates of decay/ET for the populations involved. It
%also includes the calibration constant.

save 'a_file' a %This allows N2_Er_Pop_model_V2 et al to see these values.

options = [];

%This is the x value for y.
load('xvalue.mat');
```

```
xa=x;

%% Reshaping
%This is here in case we are changing the bin size (getting rid of noise by
%summing data points). To x, 1530, and 980 data it cuts off the amount
%of data from the end of the data to make the number of points a multiple
%of the number of bins to be summed together, and then average (for x) and
%sum (for y) the bins. Note that nobins is defined at the top of Er_Model.

%Changing x value:
if nobins > 1
lengthx=length(x);
recut=floor(lengthx/nobins);
xa((recut*nobins+1):lengthx)=[];
resh=reshape(xa,nobins,recut);
xa=mean(resh)';
end

%Loading y data for experiment:
%Experimental data
Exdat=csvread(filename);
ya=Exdat(:,2);
y1530=Exdat(:,1);

%Reshaping 980 nm emission data:
if nobins > 1
ya((recut*nobins+1):lengthx)=[];
resh=reshape(ya,nobins,recut);
ya=sum(resh)';
end

%Reshaping 1530 nm emission data:
if nobins > 1
y1530((recut*nobins+1):lengthx)=[];
resh=reshape(y1530,nobins,recut);
y1530=sum(resh)';
end

%% Normalising
disp(a.Ninitial)
%Normalise y data:
%First finding the value to normalise 1530 data

ynorm=y1530(1);

normalisation = (a.Ninitial/ynorm)*a.calibration;
%This is the normalisation factor that takes into account the difference
%between the expected and measured N1 initial (from the 1530 nm data) and
%the difference between expected and measured data at 1530 nm and 980 nm
%(a.calibration--see rates.m for more information).

%Changing ypeak to calculated values rather than gathered values.
N2 = ya.*normalisation';
N1 = y1530.*(a.Ninitial/ynorm);
%Changing the name of the x variable again, because why not.
time_v = xa;

save 'a_file' a
```

```
%% Fitting

ee = round(propdat*length(time_v));
eed = length(time_v);
time_v(ee:eed)=[];
N1(ee:eed)=[];
N2(ee:eed)=[];

% Set Up the fitting routine
%myfittype3 = fittype('N2_Er_Pop_model_V2_repop(x,W11,Ninitialv)',...
%    'dependent',{'y'},'independent',{'x'},...
%    'coefficients',{'W11', 'Ninitialv'} );

myfittype3 = fittype('N2_Er_Pop_model_V2_repop(x,W11)',...
    'dependent',{'y'},'independent',{'x'},...
    'coefficients',{'W11'} );

 %Perform the fit
%     [myfit3,gof3,ab3]     =     fit(time_v,N2,myfittype3,'StartPoint',[2e-
4,a.Ninitial],...
%     'Lower', [0,(0.01*a.Ninitial)], 'Upper', [2e-3,(2*a.Ninitial)],...
%     'Robust', 'LAR');

  [myfit3,gof3,ab3] = fit(time_v,N2,myfittype3,'StartPoint',[2e-4],...
     'Lower', [0], 'Upper', [2e-3],...
     'Robust', 'LAR');

 %% Outputting results

%Extracting fitted value and confidence intervals
%disp(myfit3.Ninitialv)

disp('***')
disp('Repopulation W11 results')
disp('***')
disp('W11 result:')
aW11=1e-12.*myfit3.W11 %Translating from um to cm
%disp('W22 result:')
%aW22=1e-12.*myfit3.W22 %Translating from um to cm
disp('Confidence intervals:')
cofit = confint(myfit3);
W11conf=1e-12*cofit(:,1)%Translating from um to cm
disp('Goodness of fit')
disp(gof3)

% Plot the fitted function against the data
plot(myfit3,'b')
hold on
plot(time_v,N2,'k.','MarkerSize',5)
legend('Repop fit','Data')
```

Calculating the initial population using equation 3.4:

```
function Ninitial = Initial_Population(targetfile)
%This function calculates the initial population density of Er:ZBLAN fibre
%from an input of experimental data values.
%Authors: D. Ottaway and J. Moffatt.


formatspec='%C%f%f%f'; %Format of input data from Var_per_file, which is
%the look-up table for values used in each data run.
LookUpTable=readtable('Var_per_file.csv','Delimiter',',','Format',...
    formatspec); %loading LookUpTable
FN=LookUpTable(:,'FileName'); %Looking up variable list from first column.
LookUpTable(:,'FileName')=[];
Aa=table2array(FN);
AA=cellstr(Aa);
LookUpTable.Properties.RowNames=AA; %Creating table list of properties.

% doping in mol% of the fibre.
doping=table2array(LookUpTable(targetfile,'Doping'));

%Diameter of the fibre core.
Diam=table2array(LookUpTable(targetfile,'Diam'));
Diam=Diam*1e4; %Changing from cm to um

%Energy incident on the core.
E=table2array(LookUpTable(targetfile,'E'));

%Error of energy incident on the core (I don't think I use this anymore).
%erE=table2array(LookUpTable(targetfile,'erE'));

%Constants:
%r=0.9e-13; %The absorption cross-section of erbium at 1470 nm (um^2).
%r = 2.683e-13;
r = 0.9958e-13;
Ng=(1.601*doping)*1e8; %The approx. number of ground state ions per um^3.
A=pi*(Diam^2)/4; %The area of the core of the fibre (um^2).
h=6.63e-34; %Plank in m^2kg/s
v=2.039e14; %2.039e14; %Frequency of light being absorbed (Hz).

%Finding N. This is an estimate of the number of electrons raised to the
%4I13/2 state from the ground state, given a particular wavelength,
%incident energy, and ion density.

Ninitial=(E*Ng*r)/(h*v*A); %Note that this is a density value (/A*L)
```

Defining the differential equation set 3.3:

```
function Ndot = Er_Pop_Model_repop(N,a)
% A function that contains the ODEs that solve the energy transfer
% parameter W11 for Er:ZBLAN. This is the repopulation ODE.
%4I9/2 has a really short lifetime (shorter than the bin length of my
%data) and almost all of the population of this state (99%) goes to 4I11/2,
%so repopulation is assumed to come from the lower state rather than 4I9/2.

% Unpack the structure a
A1 = a.A1; %This is the fundamental lifetime of 4I13/2 state (1530 nm)
A2 = a.A2; %This is the fundamental lifetime of 4I11/2 state (980 nm)
A21 = a.A21; %Fundamental lifetime of 4I11/2 to 4I13/2 (980 nm to 1530 nm)
W11 = a.W11; %The energy transfer parameter (dummy parameter).
%W22 = a.W22; %Another energy transfer parameter.

% The ODEs set
Ndot(1) = N(2)*A21 - 2*W11*(N(1).^2) - N(1)*A1; %From 1530 peak
Ndot(2) = W11*(N(1).^2) - A2*N(2); %Combined 980, 800 nm
%Ndot(2) = W11*(N(1).^2) - A2*N(2) - W22*(N(2).^2); %Combined 980, 800 nm%

%_____________________________________________Combined 4I9/2, 4I11/2 energy state
%    ^W11      |
%    |         |Repopulation (A21)
%    |         \/
%_____________________________________________4I13/2 energy state
%    ^Ninitial |
%    |         |
%    |         |What we are measuring(A1)
%    |         \/
%_____________________________________________4I15/2 energy state

Ndot = transpose(Ndot);
end
```

Solving the differential equation set:

```
function N = N2_Er_Pop_model_V2_repop(tdata,W11)
%function N = N2_Er_Pop_model_V2_repop(tdata,W11,Ninitialv)
%A function by DJO to solve the ODEs in Er_Pop_Model_V2.

% Load the initial parameter file
%Er_Parameters
load('a_file')
A2 = a.A2;
A1 = a.A1;
A21 = a.A21;
Ninitial = a.Ninitial;

% Now overwrite the upconversion parameter
a.W11 =  W11; % What we are attempting to solve
%a.W22 = W22;

% Set up the function used to numerically solve the erbium population model
Er_Pop = @(t,N) Er_Pop_Model_repop(N,a);

% Unfortunately the fitting routine starts by putting a ridiculous starting
% vector to test the function. This first part of the if statement counters
%this nonsense
if min(tdata)>0.1;
tout = tdata;
N = zeros(size(tdata));
else
[tout,Nout] = ode45(Er_Pop,tdata,[Ninitial;0]);
N = Nout(:,2); %Spitting out solution to 4I11/2 (980 nm)
end
```

Appendix A3

The following figures are the results of fitting the differential equation set in Chapter Three to all fibres.

Using 1530 nm emission:

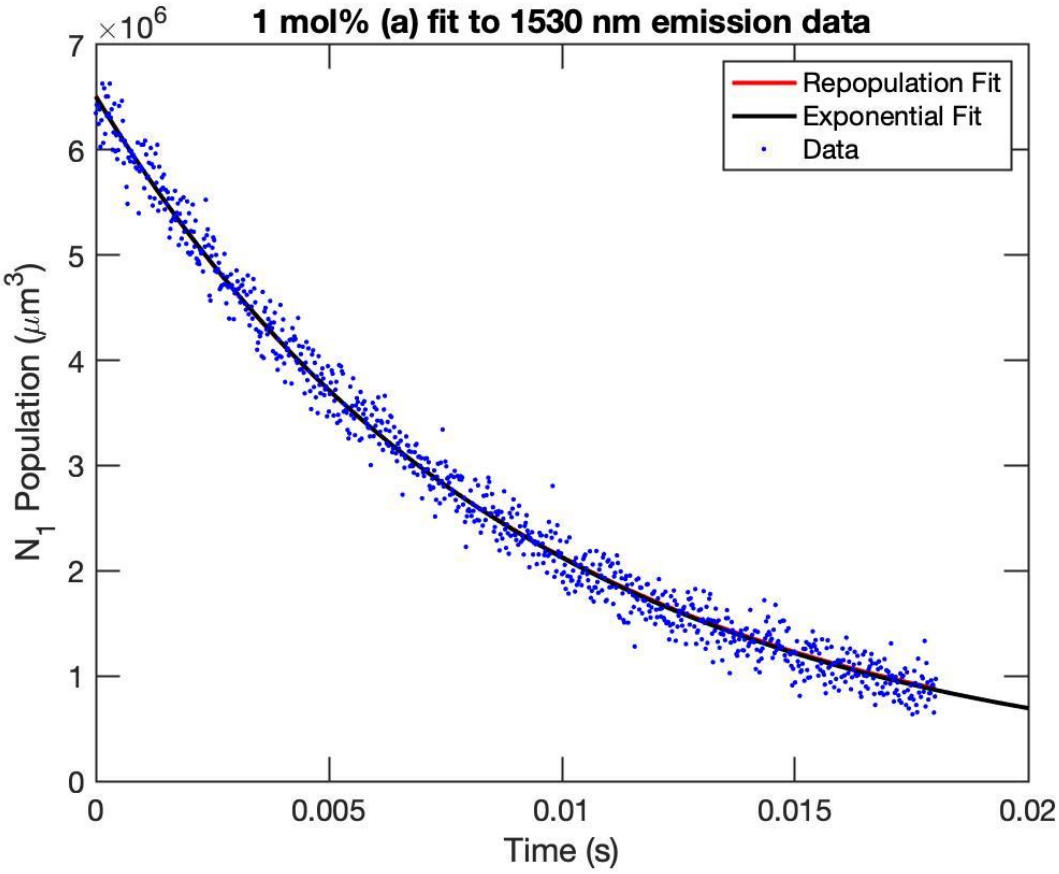

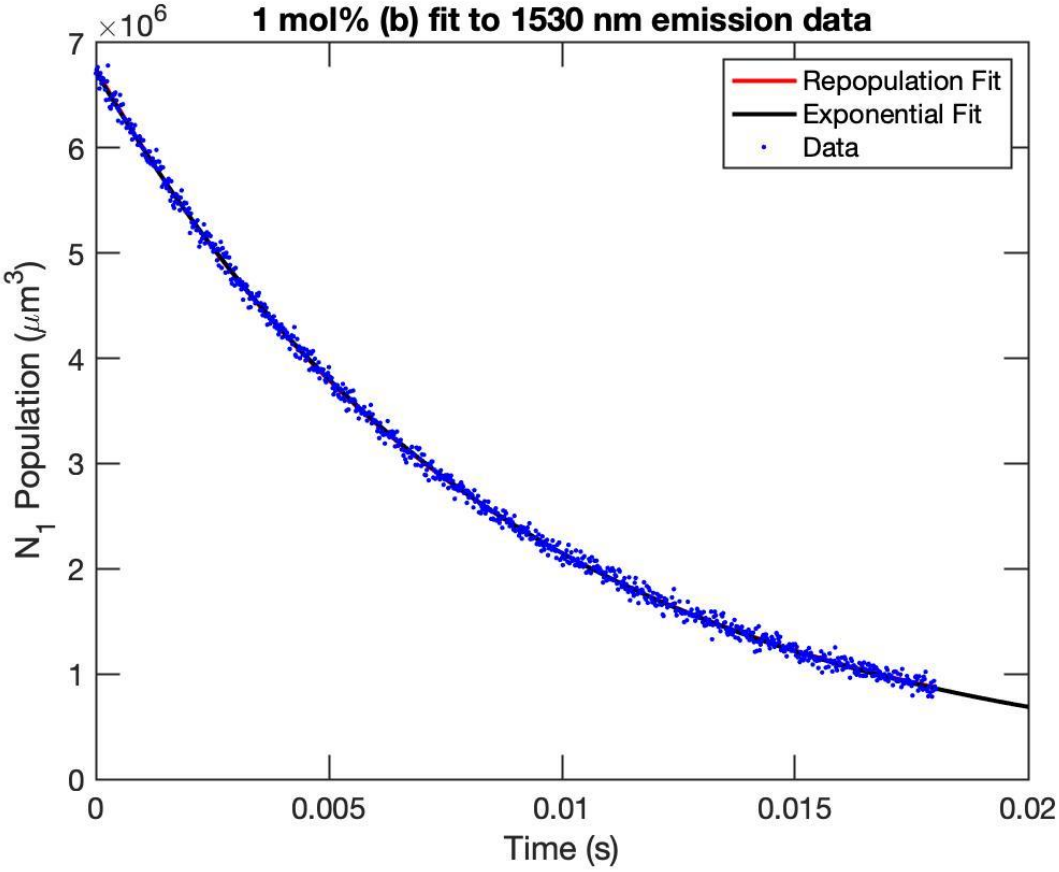
1 mol% (b) fit to 1530 nm emission data
×10^6
Repopulation Fit
Exponential Fit
Data
N1 Population (μm3)
Time (s)
0
1
2
3
4
5
6
7
0
0.005
0.01
0.015
0.02

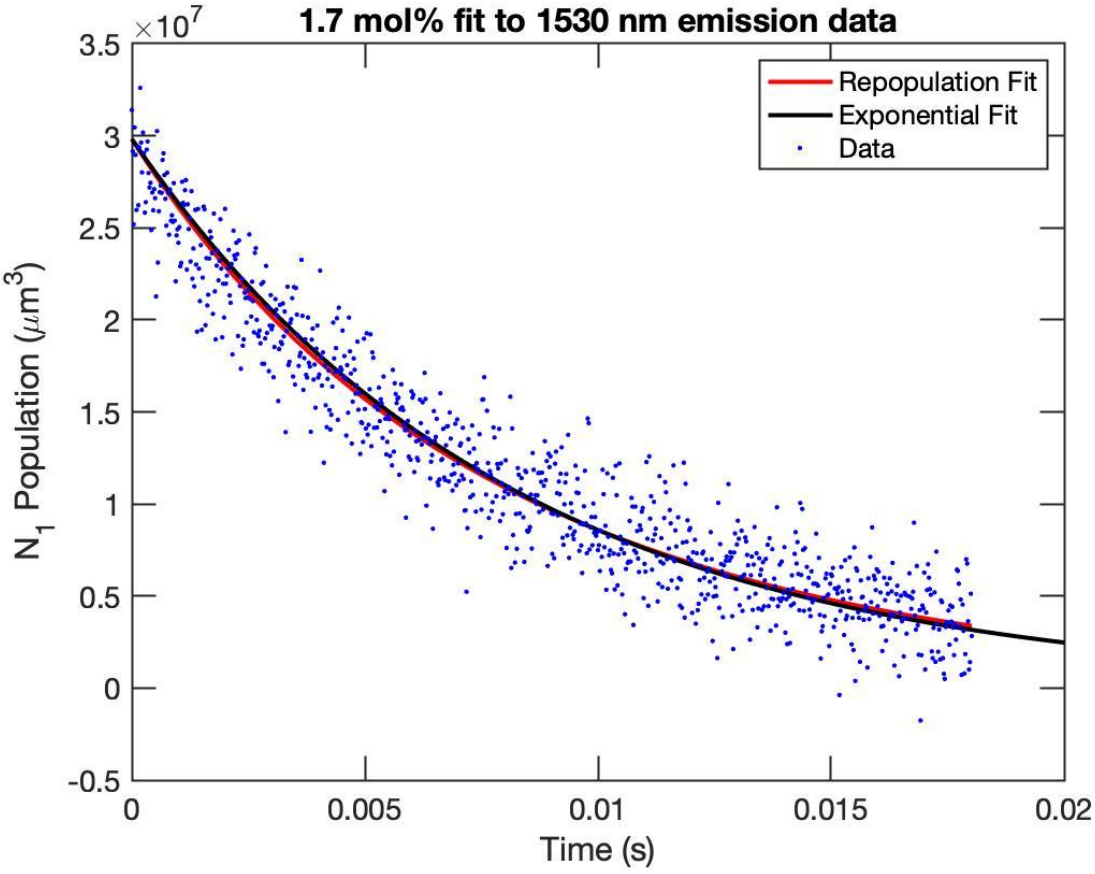
1.7 mol% fit to 1530 nm emission data
×10^7
Repopulation Fit
Exponential Fit
Data
N1 Population (μm3)
Time (s)
-0.5
0
0.5
1
1.5
2
2.5
3
3.5
0
0.005
0.01
0.015
0.02

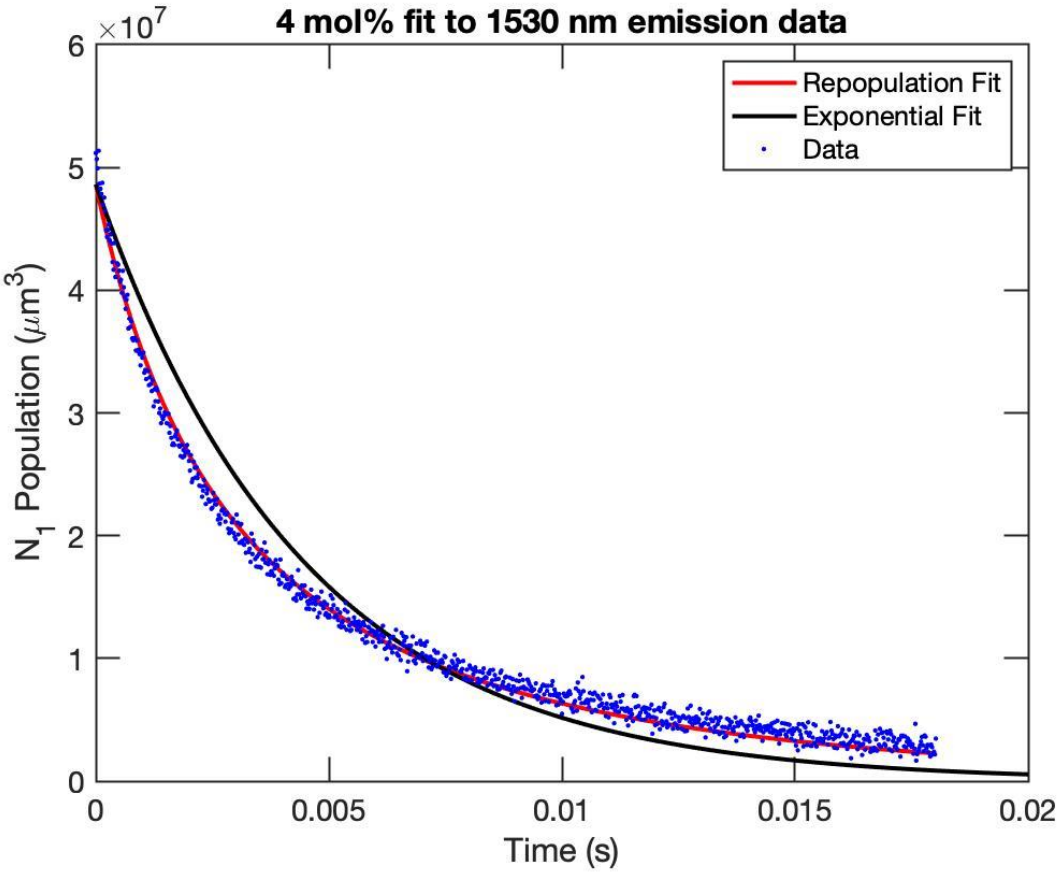
4 mol% fit to 1530 nm emission data
×10^7
Repopulation Fit
Exponential Fit
Data
N1 Population (μm3)
Time (s)
0
1
2
3
4
5
6
0
0.005
0.01
0.015
0.02

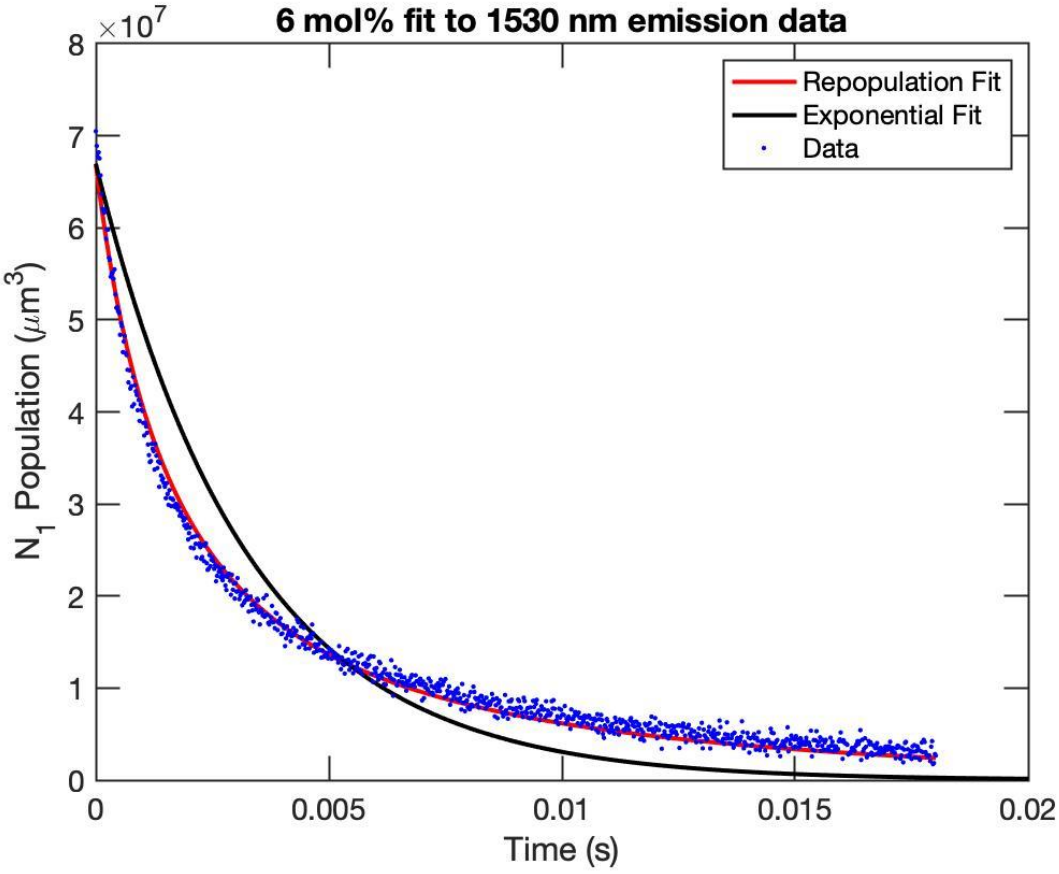
6 mol% fit to 1530 nm emission data
×10^7
Repopulation Fit
Exponential Fit
Data
N1 Population (μm3)
Time (s)
0
1
2
3
4
5
6
7
8
0
0.005
0.01
0.015
0.02

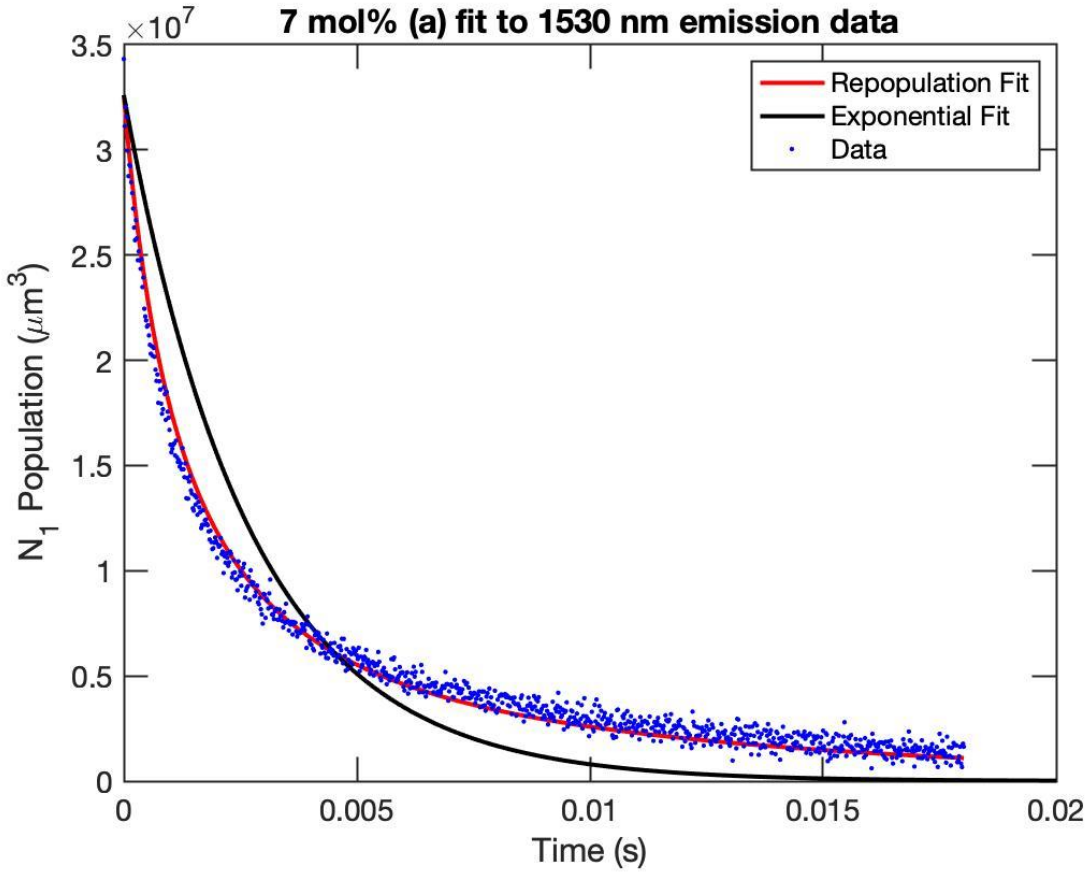
7 mol% (a) fit to 1530 nm emission data
×10^7
Repopulation Fit
Exponential Fit
Data
N1 Population (μm3)
Time (s)
0
0.5
1
1.5
2
2.5
3
3.5
0.005
0.01
0.015
0.02

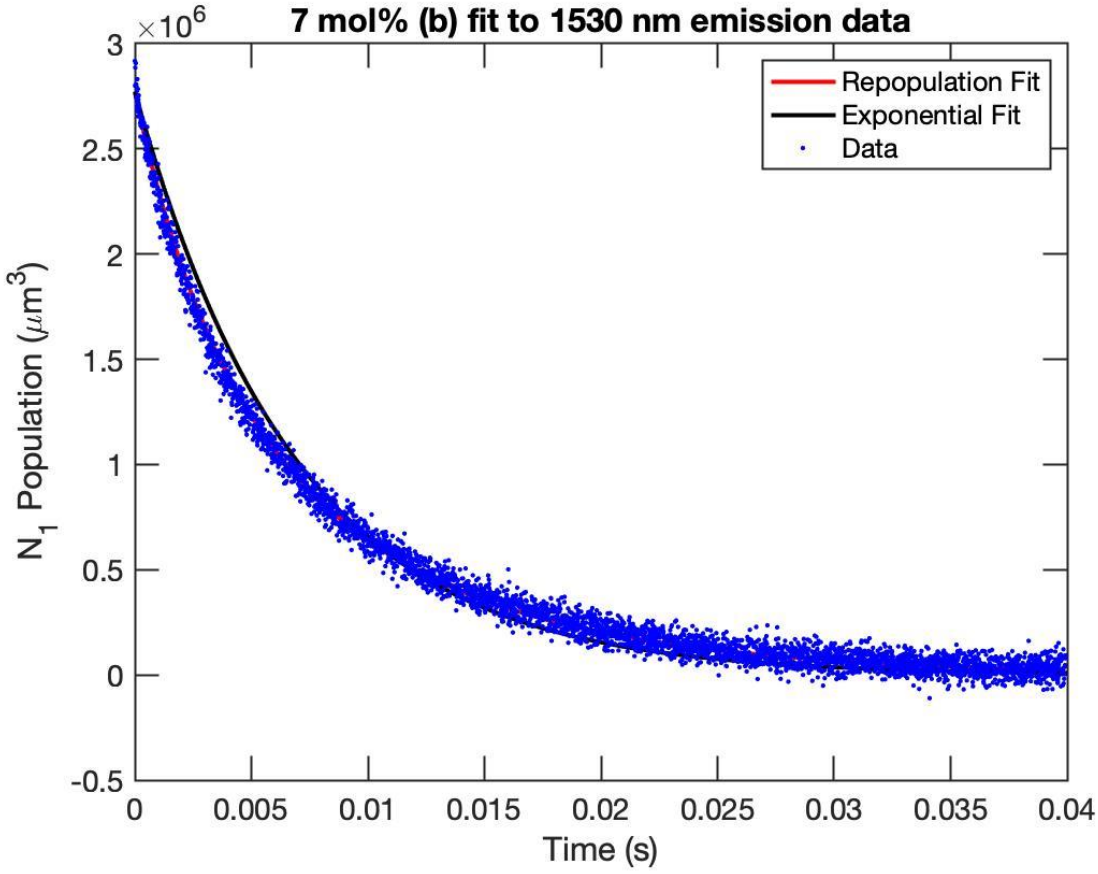
7 mol% (b) fit to 1530 nm emission data
×10^6
Repopulation Fit
Exponential Fit
Data
N1 Population (μm3)
Time (s)
-0.5
0
0.5
1
1.5
2
2.5
3
0.005
0.01
0.015
0.02
0.025
0.03
0.035
0.04

For 980 nm emission:

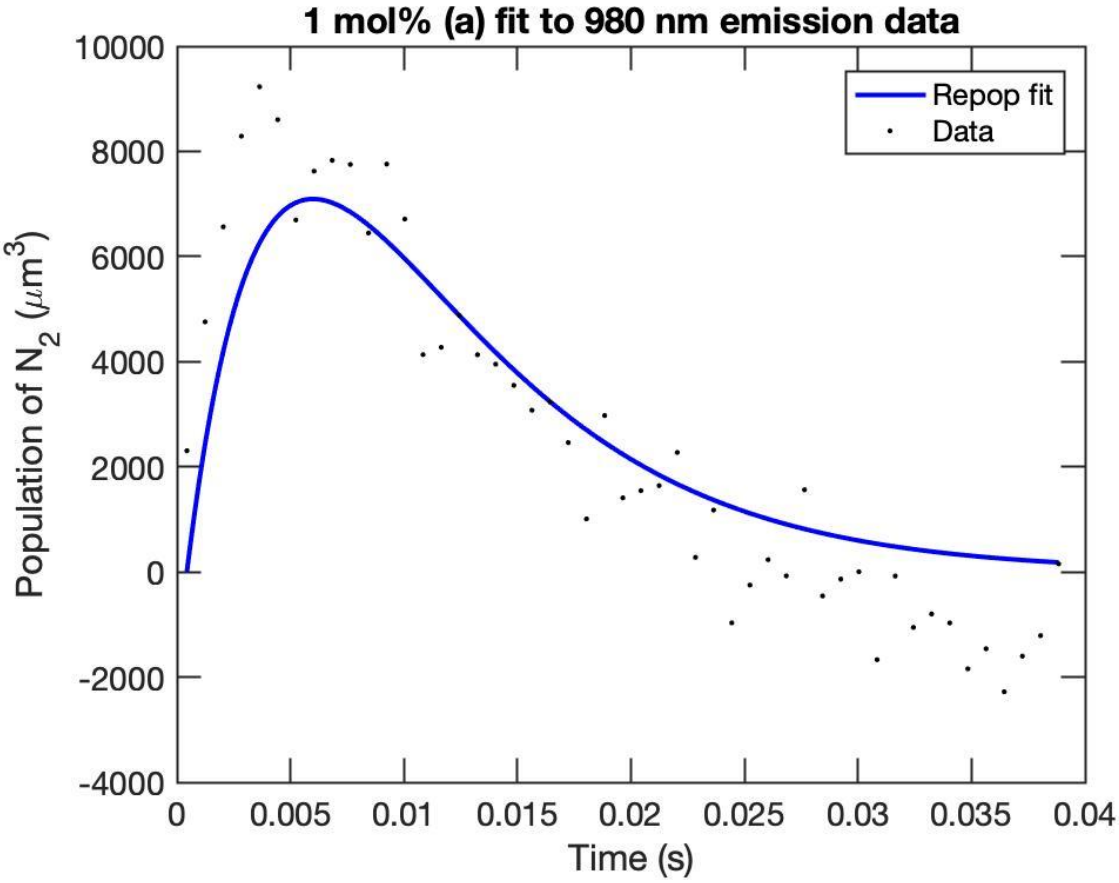

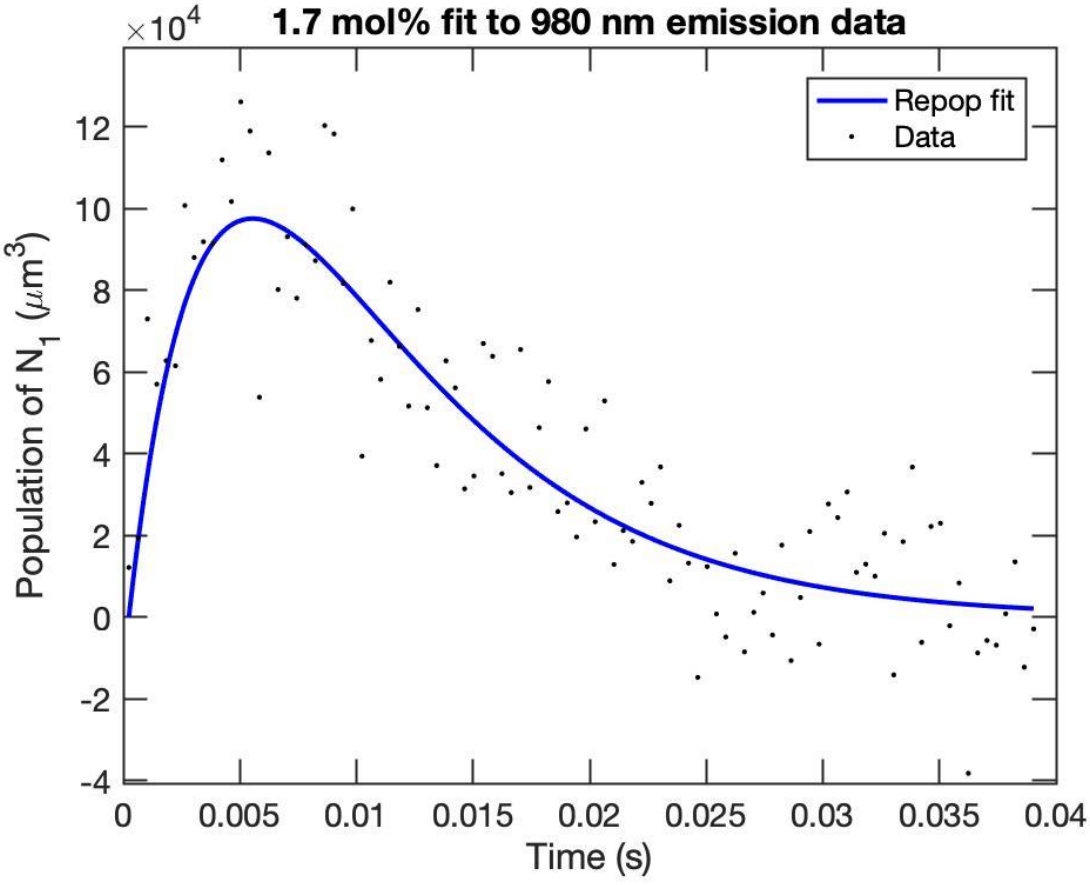

Appendix A4

This appendix shows the conventional fluorescence peaks used to identify rare earth elements in fluorite and fluorapatite in chapter five. First the particular peaks used for identification are identified, then the emission detected for each sample are shown.

Peak identification

Cerium

Cerium is identified by the 336 nm emission peak seen via the 298 nm excitation. The 298 nm diode has broad shoulders that are shown in Figure 105. The cerium peak is still distinguishable from this background, as seen in Figure 106.

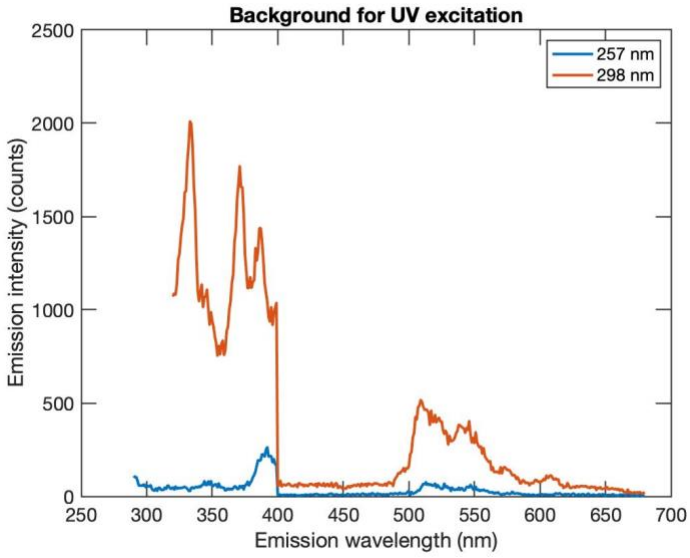

Figure 105: Background detected from diode signal shoulders and spurious signal.

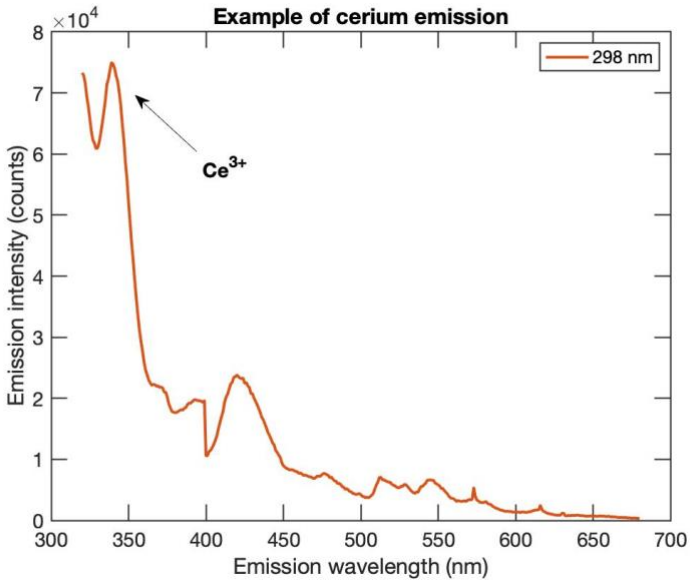

Figure 106: Example of cerium emission from the Stolberg sample using 298 nm excitation.

Neodymium

Neodymium is most easily identified by the 1065 nm emission, shown in Figure 107. 521 nm excitation shows this emission the clearest, though the peak is still visible under 415 nm, 442 nm, and 485 nm excitation.

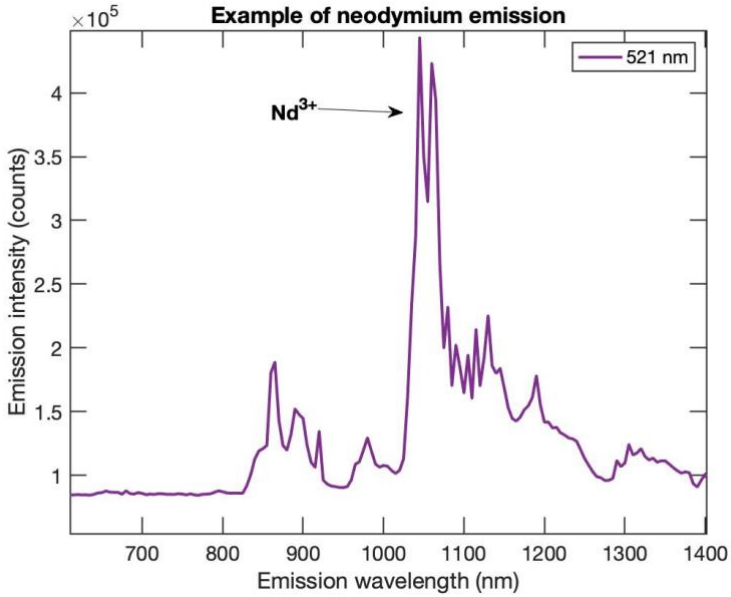

Figure 107: Example of neodymium emission from the Stolberg sample using 521 nm excitation.

Samarium

Samarium is most easily identified via the emission near 600 nm, shown in Figure 108.

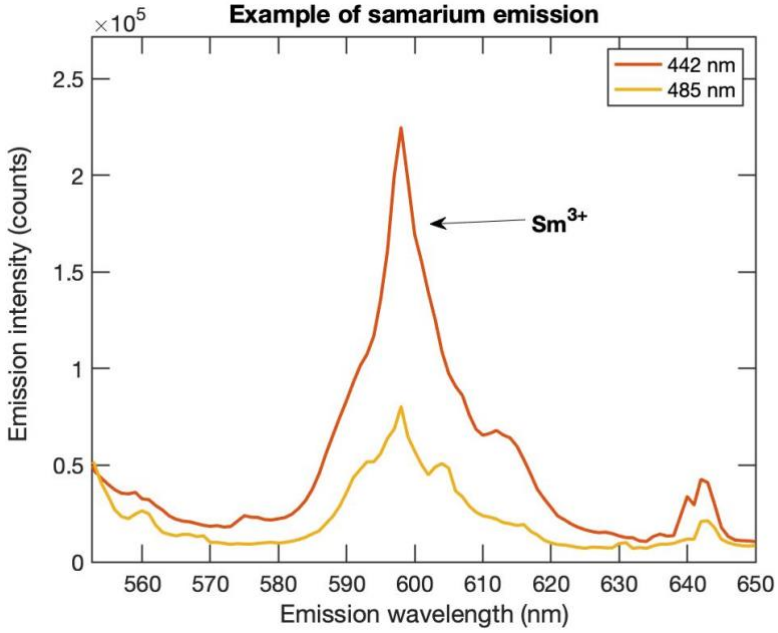

Figure 108: Example of samarium emission from the Broken Hill sample using 442 nm and 485 nm excitation.

Praseodymium

The 641 nm emission from praseodymium is easily obscured by holmium, erbium and samarium emissions near 650 nm. Praseodymium is identified by ensuring the emission peaks at 640 nm, and is brightest when excited by 442 nm (see Figure 109).

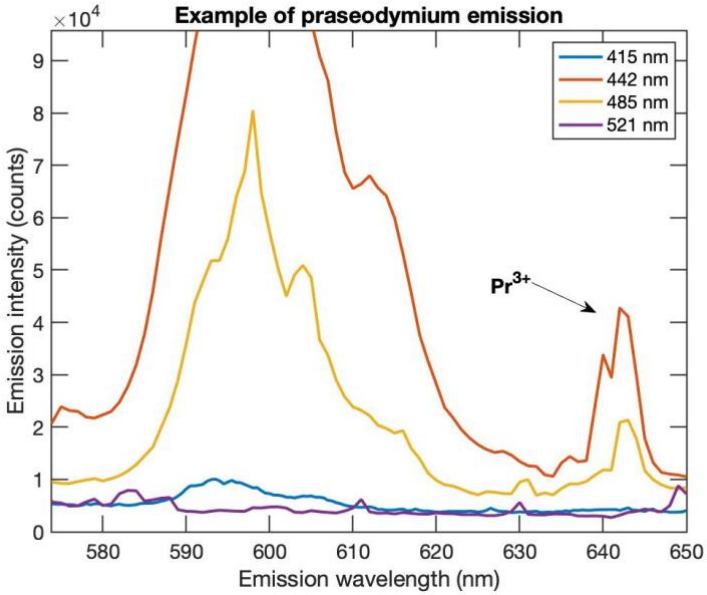

Figure 109: Example of praseodymium emission from the Broken Hill sample using 442 nm excitation.

Holmium

The holmium emission between 530 nm and 560 nm is the most distinctive holmium peak seen. It is present in the same area as the erbium peak and can be hard to identify in samples with small holmium concentrations and large erbium concentrations. Holmium presence in the fluorite samples was identified from erbium by a bright signal when excited at 415 nm, and a lack of the sharp erbium 538 nm peak. In Figure 110 the erbium signal is brighter than the holmium signal, but the holmium can still be distinguished using these points.

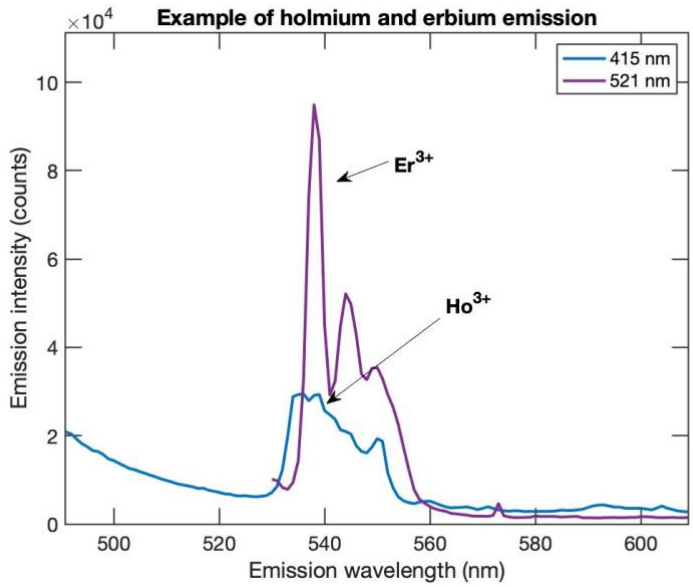

Figure 110: Example of holmium and erbium emission from the Olympic Dam sample using visible excitation.

Erbium

Erbium can be distinguished by the sharp peak at 538 nm that is brightest when excited at 521 nm (Figure 110). There is also a distinctive erbium peak at 1530 nm (Figure 111).

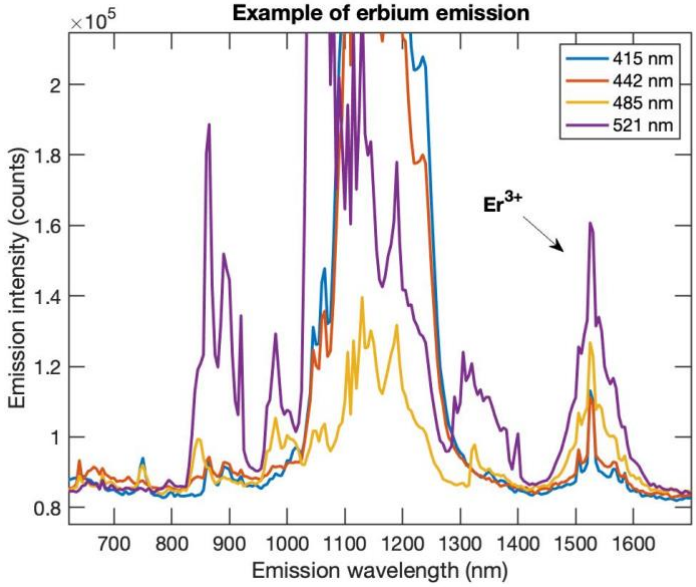

Figure 111: Example of erbium emission from the Stolberg sample using visible excitation.

Gadolinium

Gadolinium can be distinguished using the sharp 310 nm emission when excited by the 257 nm diode (Figure 112).

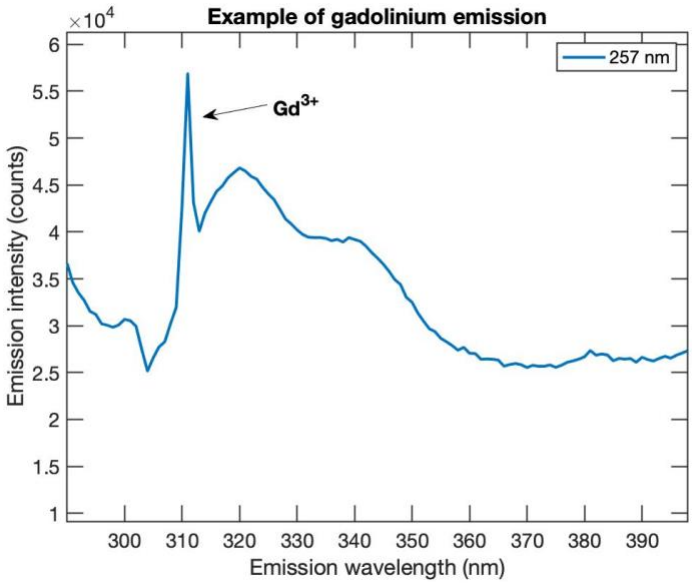

Figure 112: Example of gadolinium emission from the Stolberg sample using 257 nm excitation.

Europium

Europium is distinguished by 420 nm emission using 415 nm excitation. The 420 nm emission is also sometimes visible under 257 nm excitation (see Figure 113). The much dimmer 594 nm emission that is only present in Eu^{3+} is not easily identifiable when the large 600 nm samarium emission is present, and so the charge state of the europium ion is sometimes not identifiable.

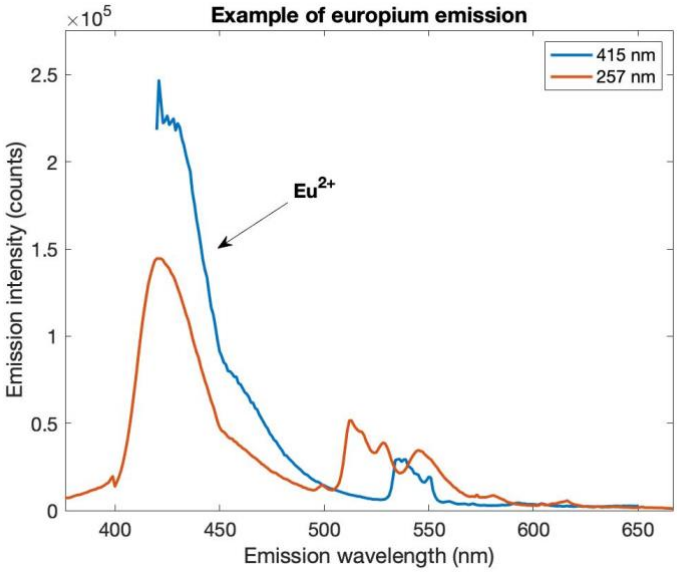

Figure 113: Example of europium emission from the Olympic Dam sample using 257 nm and 415 nm excitation.

Dysprosium

In the fluorite samples in chapter five, dysprosium emission is generally dimmer than other rare earth emission, and so is more difficult to identify. The 574 nm emission exciting with the 298 nm diode is used for identification (Figure 114).

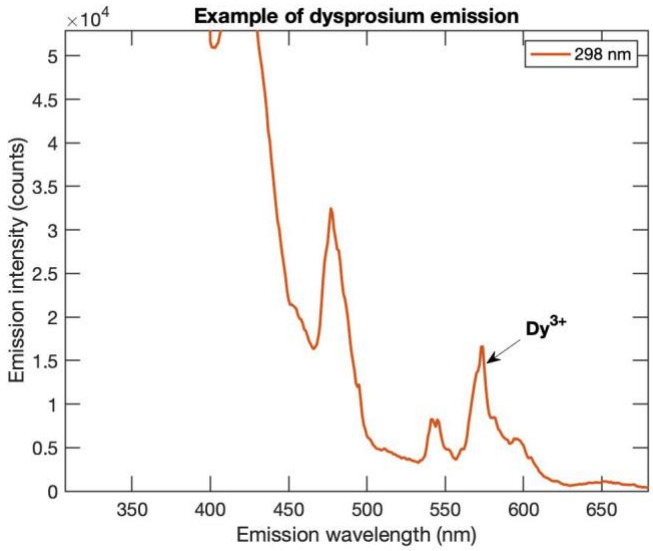

Figure 114: Example of dysprosium emission from the Torrington sample using 298 nm excitation.

Ytterbium

Ytterbium is distinguished by a reasonably broad emission at 980 nm when exciting at 521 nm. 980 nm emission is often emitted by erbium ions in other hosts. While all other fluorite samples showed 530 nm emission and 1530 nm erbium-associated emission, only a few showed 980 nm emission, and thus this emission is attributed to ytterbium.

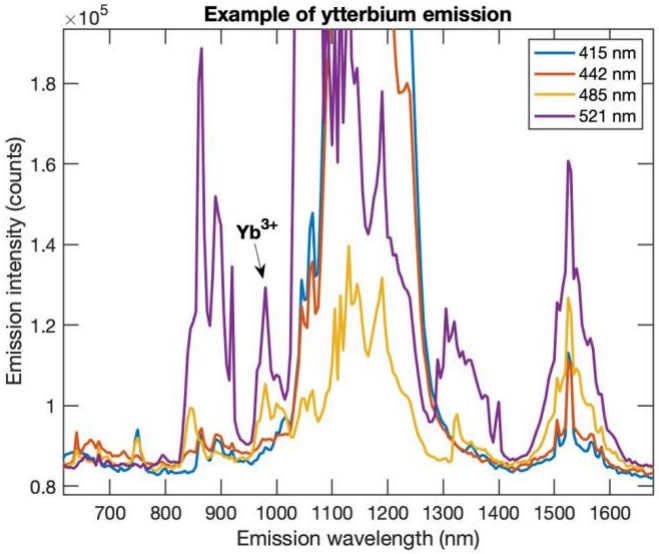

Figure 115: Example of ytterbium emission from the Stolberg sample using visible excitation.

Sample emission

In this section the emission obtained for each sample are shown. UV, visible, and near-infrared excitation was used to obtain fluorite sample emission; only visible and near-infrared excitation was used to obtain apatite sample emission, and so gadolinium and cerium were not observed. In chapter five, dysprosium was specifically targeted by the 298 nm diode, but could be seen using visible excitation.

Fluorites

Torrington

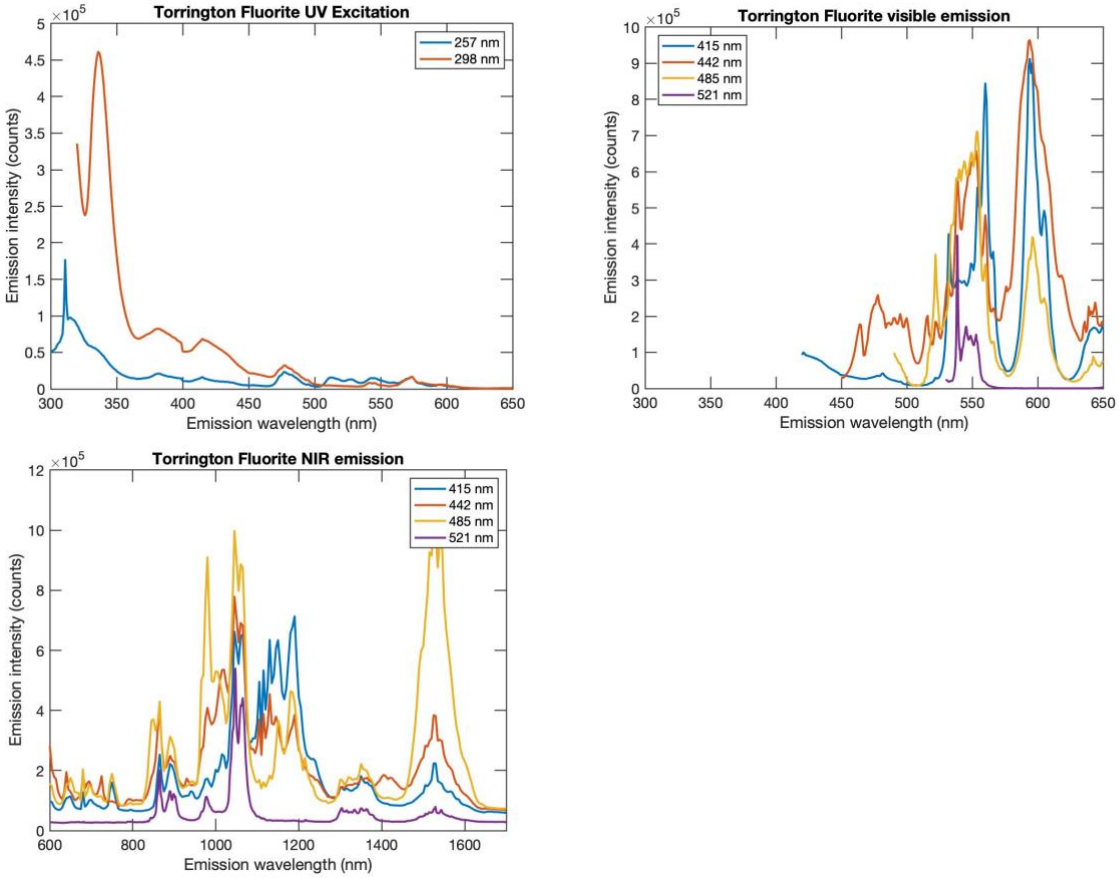

Figure 116: Emission using the Edinburgh Instruments Spectrofluorimeter using the Torrington fluorite sample.

Olympic Dam

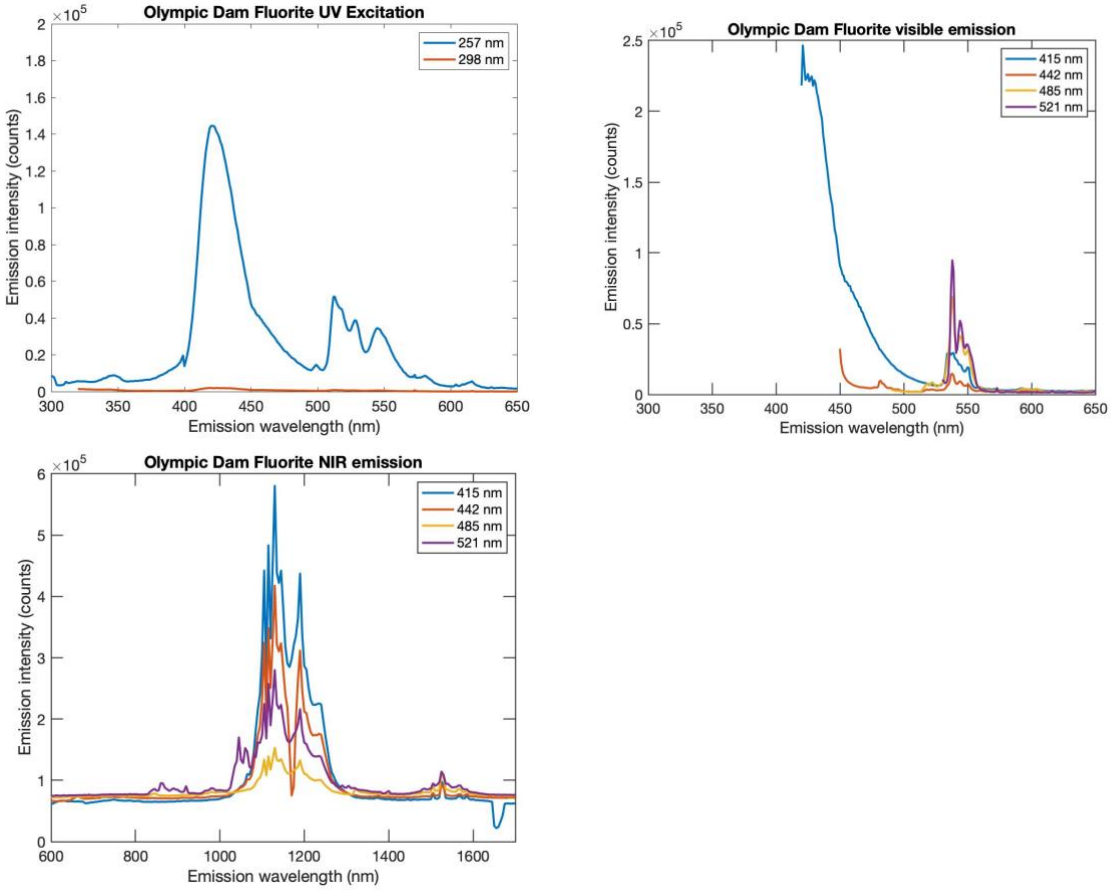

Figure 117: Emission using the Edinburgh Instruments Spectrofluorimeter using the Olympic Dam fluorite sample.

Stolberg

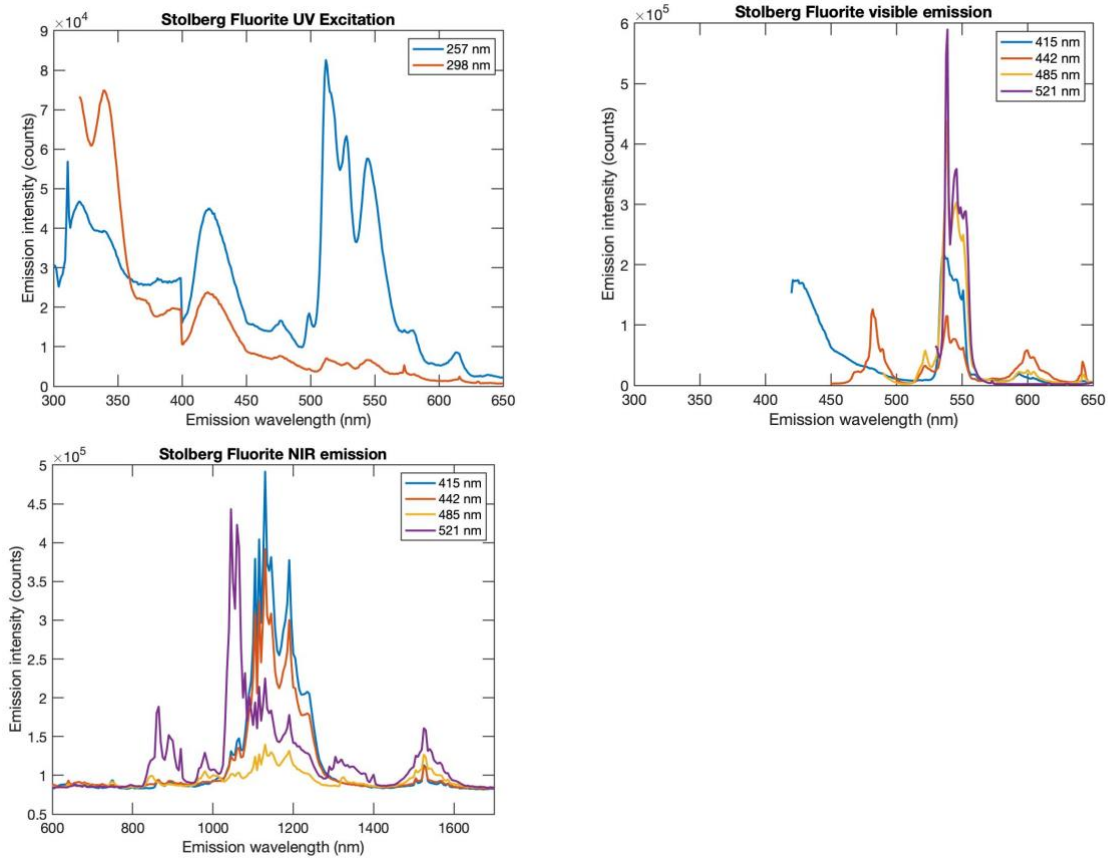

Figure 118: Emission using the Edinburgh Instruments Spectrofluorimeter using the Stolberg fluorite sample.

Pernatty Lagoon

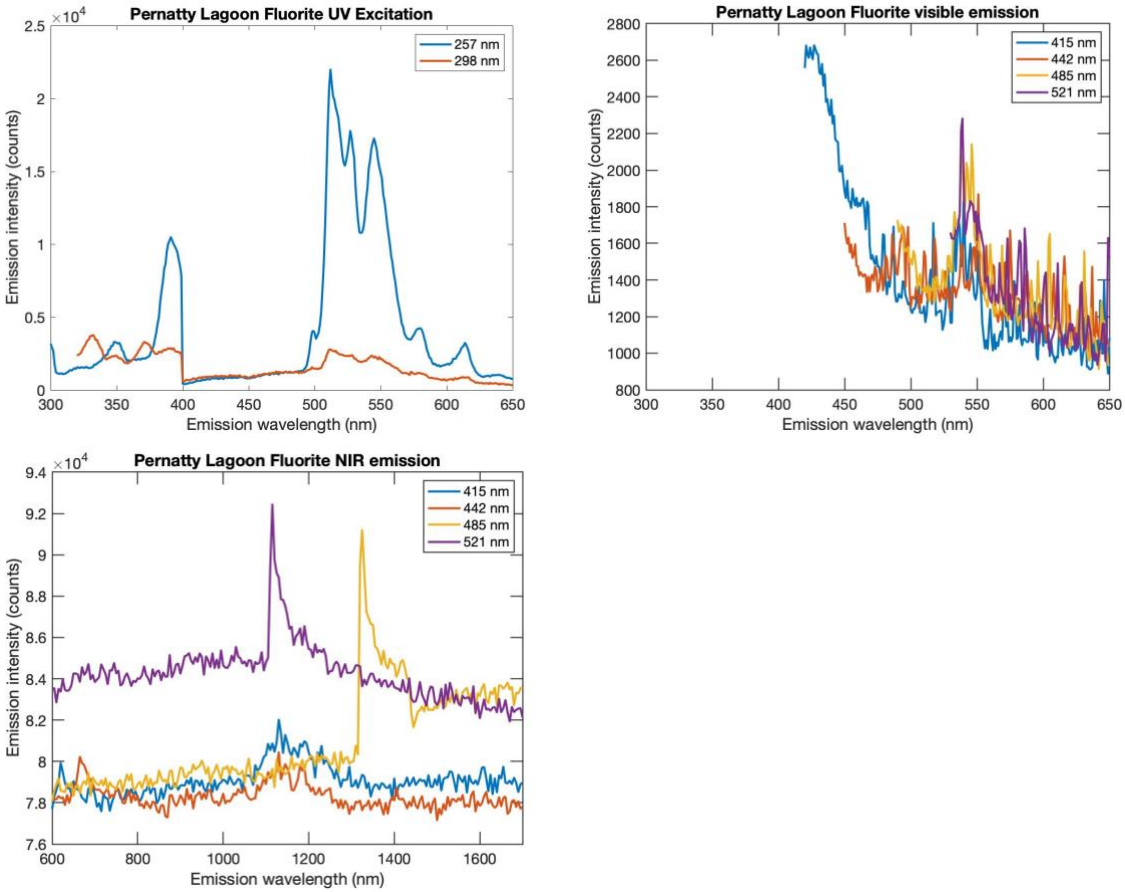

Figure 119: Emission using the Edinburgh Instruments Spectrofluorimeter using the Pernatty Lagoon fluorite sample.

Edith River

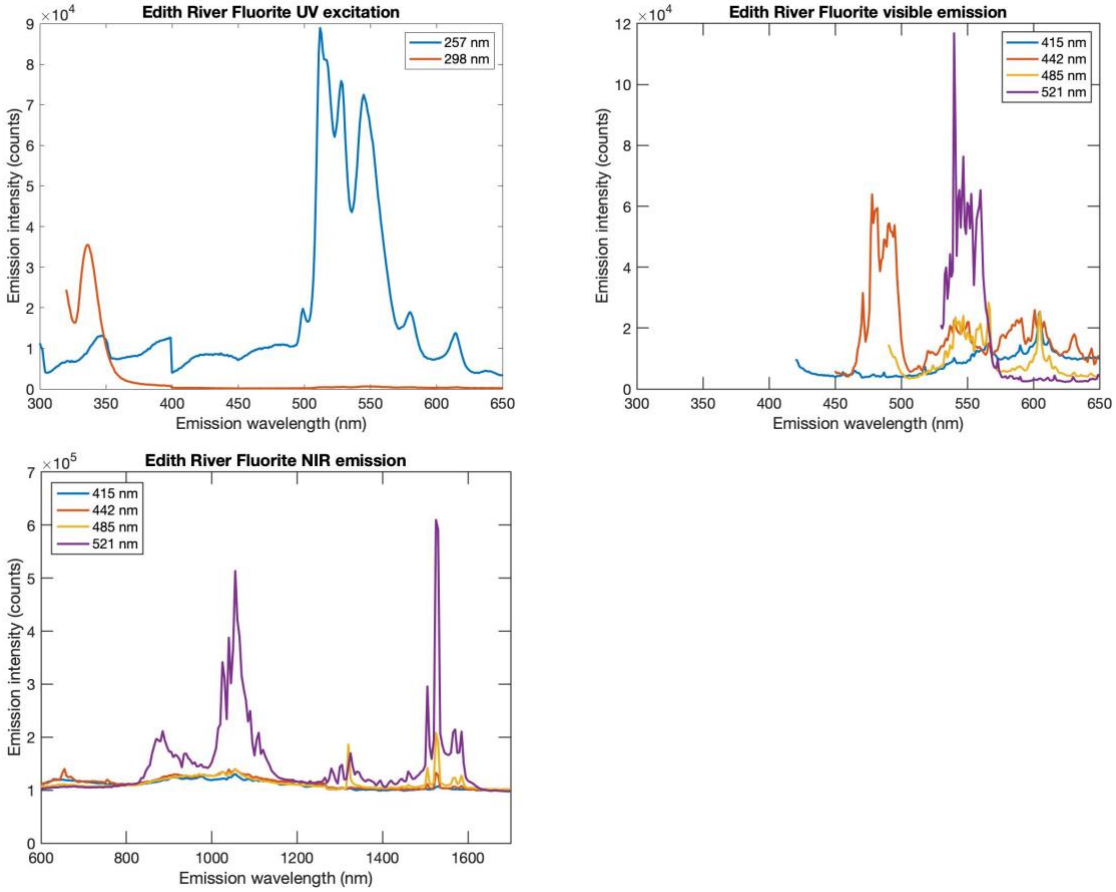

Figure 120: Emission using the Edinburgh Instruments Spectrofluorimeter using the Edith River fluorite sample.

Broken Hill

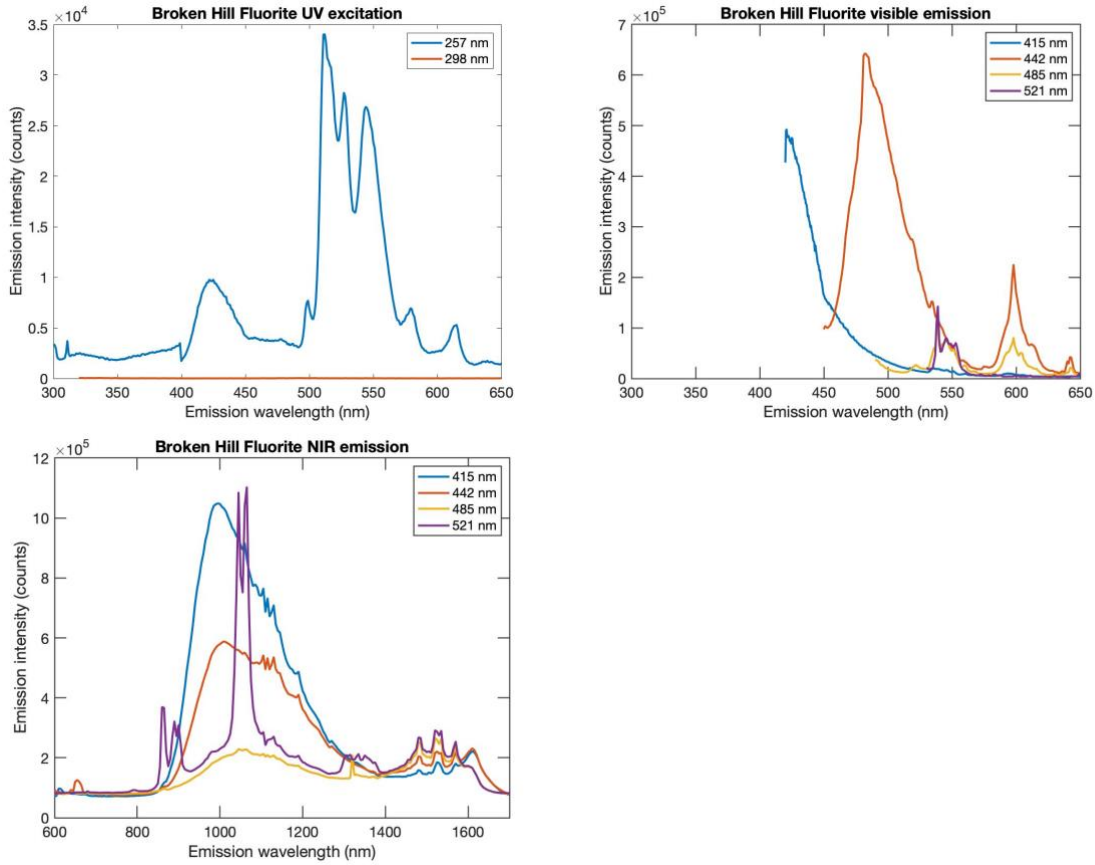

Figure 121: Emission using the Edinburgh Instruments Spectrofluorimeter using the Broken Hill fluorite sample.

Elmwood Mine

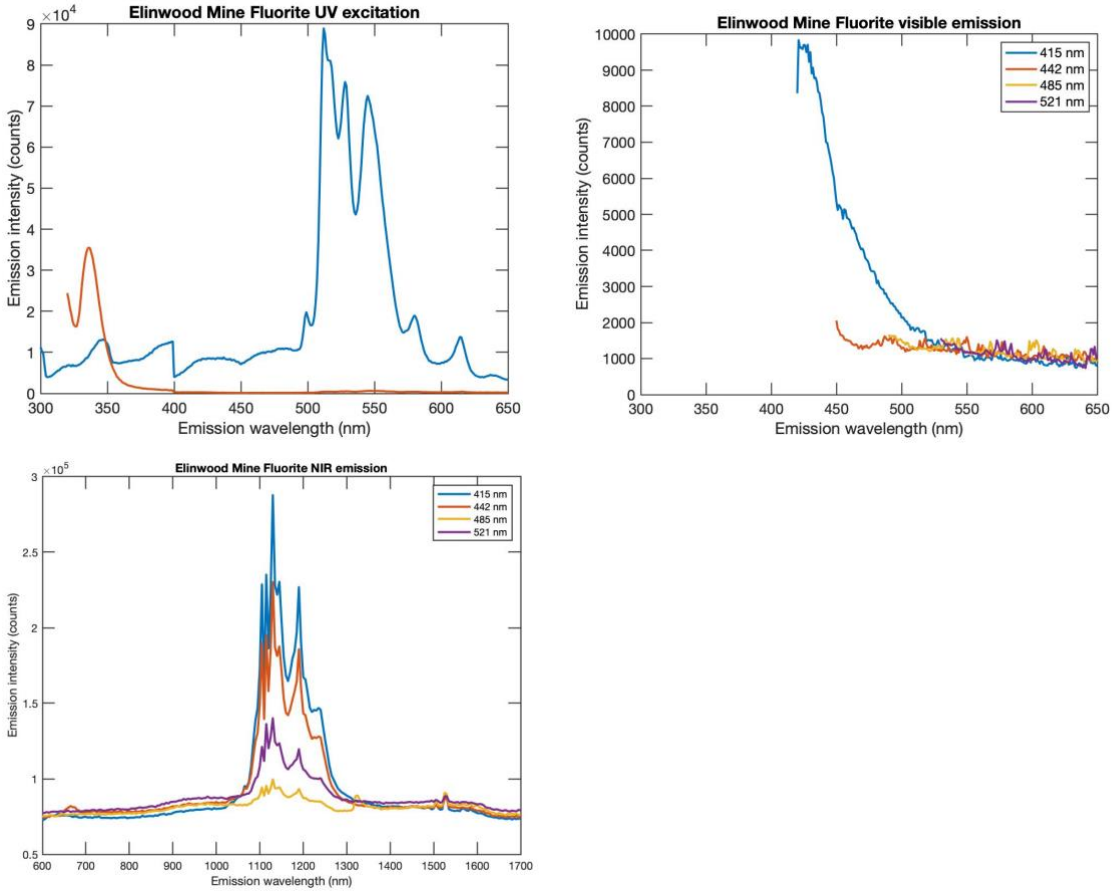

Figure 122: Emission using the Edinburgh Instruments Spectrofluorimeter using the Elmwood Mine fluorite sample.

Jinka Station

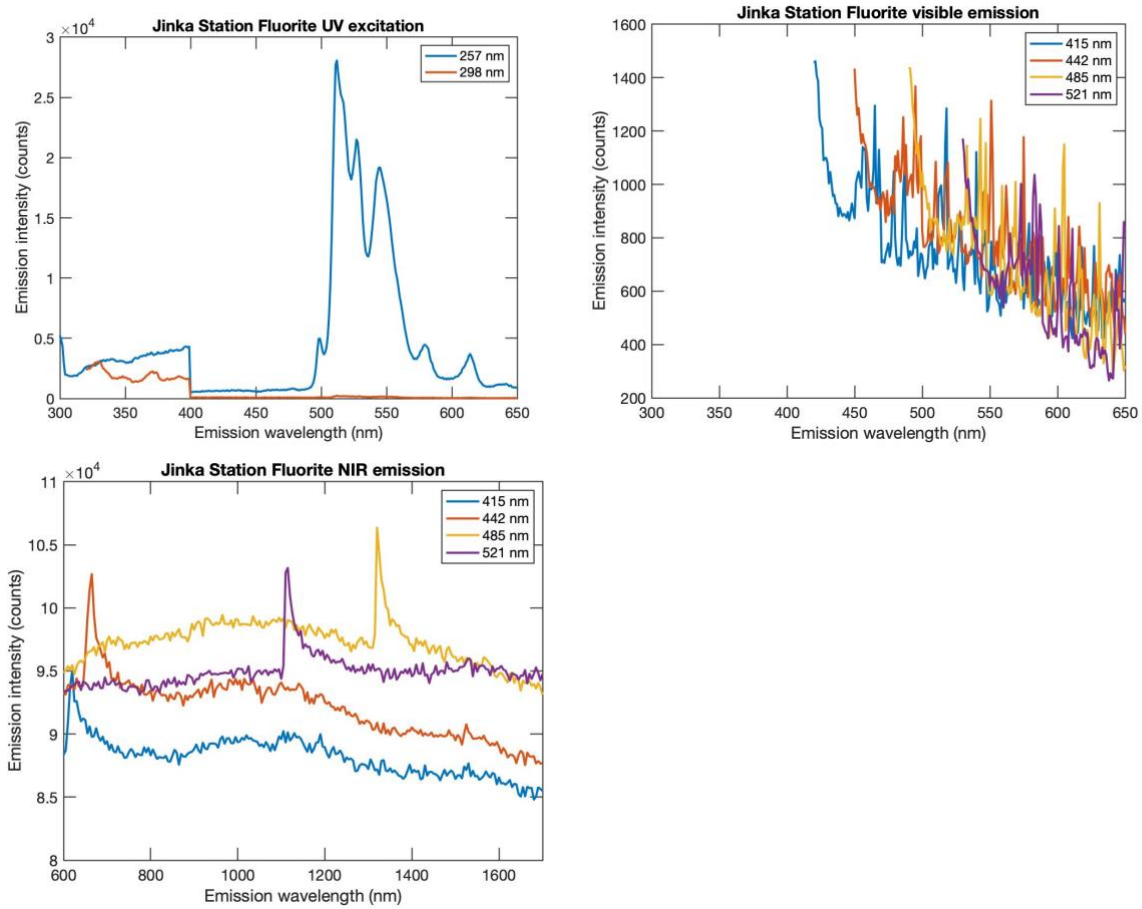

Figure 123: Emission using the Edinburgh Instruments Spectrofluorimeter using the Jinka Station fluorite sample.

Marienschacht

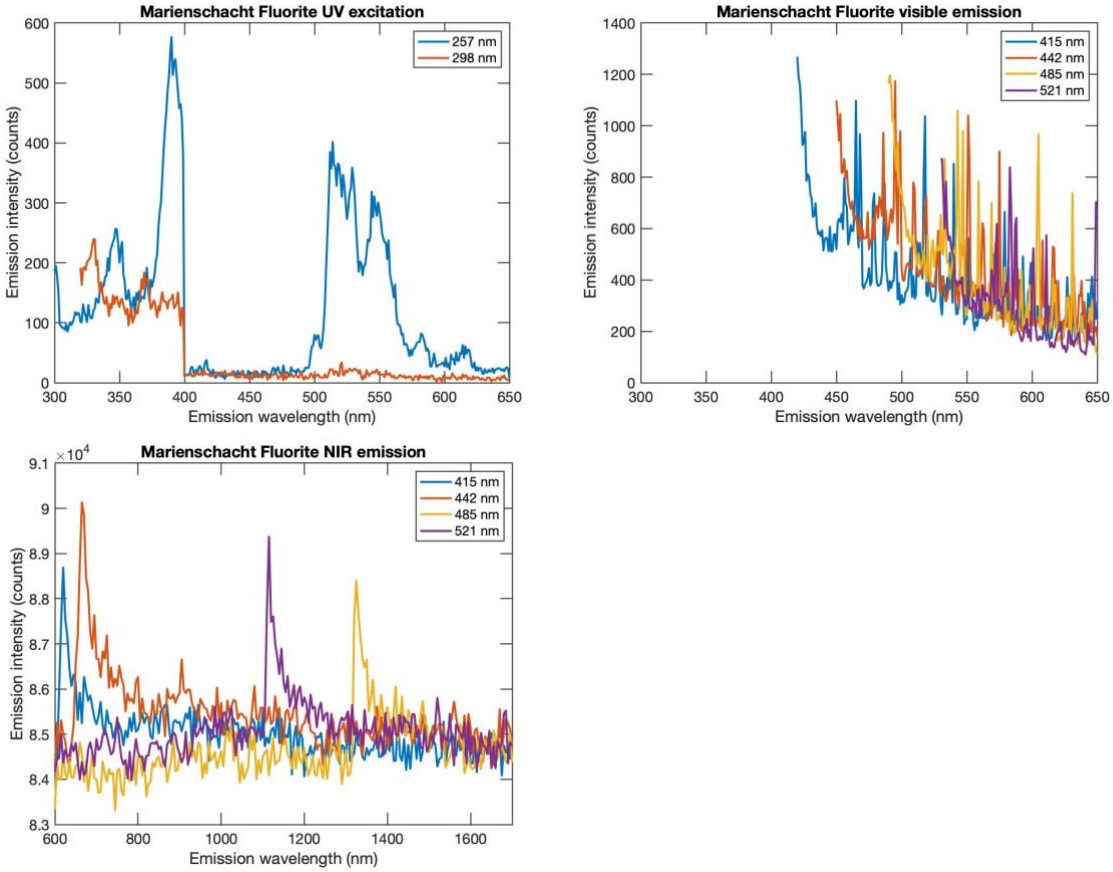

Figure 124: Emission using the Edinburgh Instruments Spectrofluorimeter using the Marienschacht fluorite sample.

Apatites

Rosetta Head

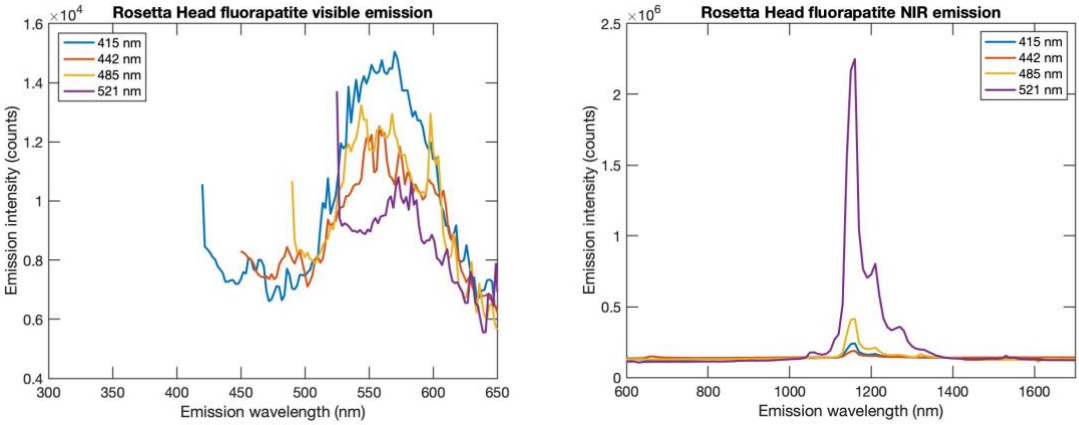

Figure 125: Emission using the Edinburgh Instruments Spectrofluorimeter using the Rosetta Head fluorapatite sample.

Williamstown

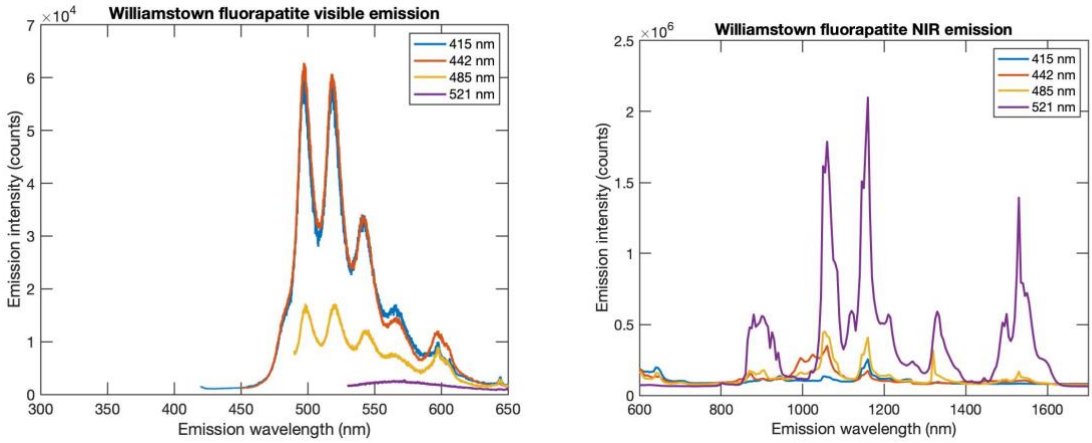

Figure 126: Emission using the Edinburgh Instruments Spectrofluorimeter using the Williamstown fluorapatite sample.

Alice Springs

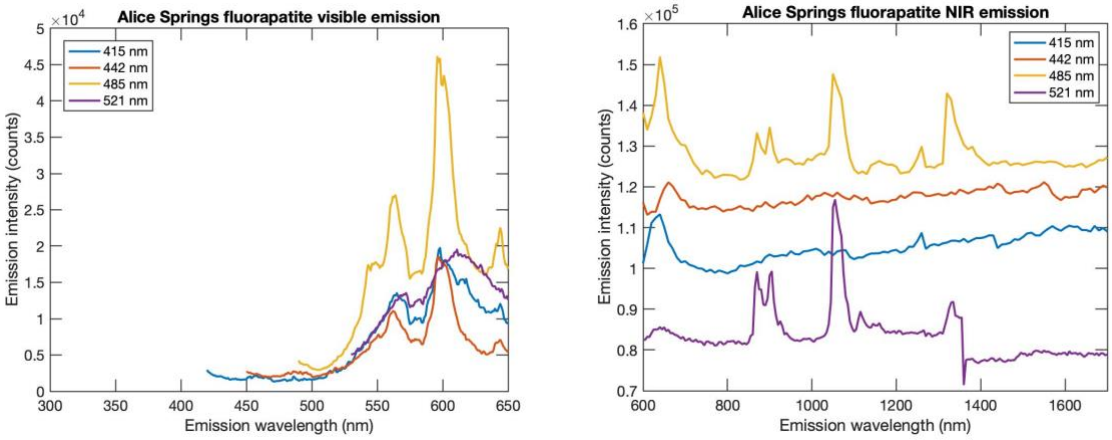

Figure 127: Emission using the Edinburgh Instruments Spectrofluorimeter using the Alice Springs fluorapatite sample.

Hart's Range

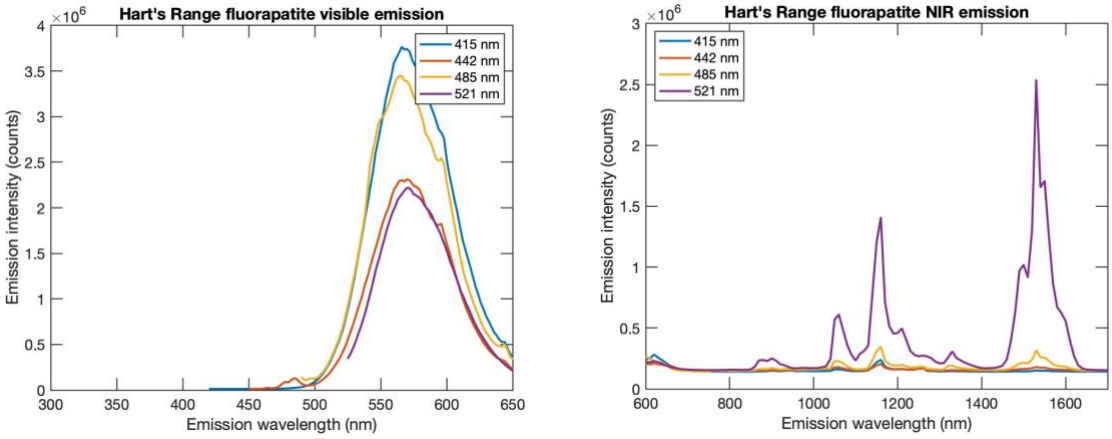

Figure 128: Emission using the Edinburgh Instruments Spectrofluorimeter using the Hart's Range fluorapatite sample.

Lake Baikal

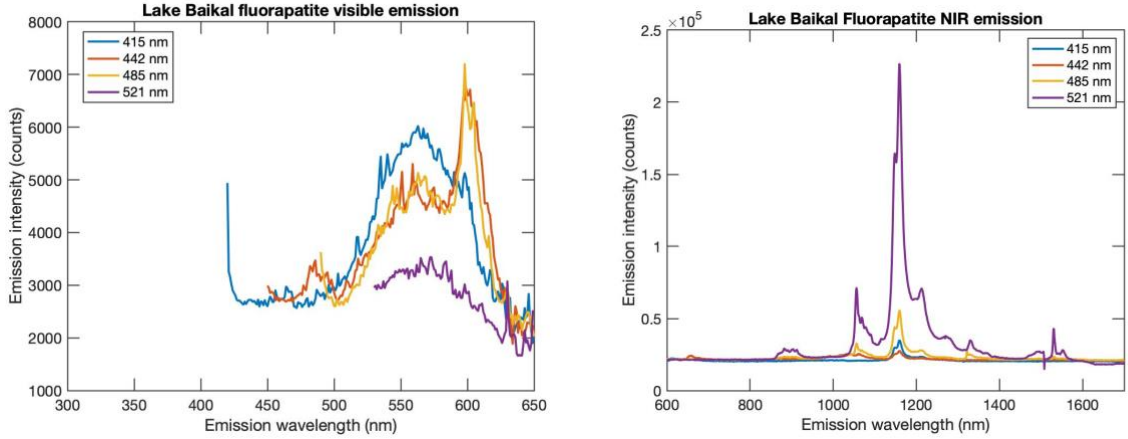

Figure 129: Emission using the Edinburgh Instruments Spectrofluorimeter using the Lake Baikal fluorapatite sample.

Podelien (hydroxyapatite)

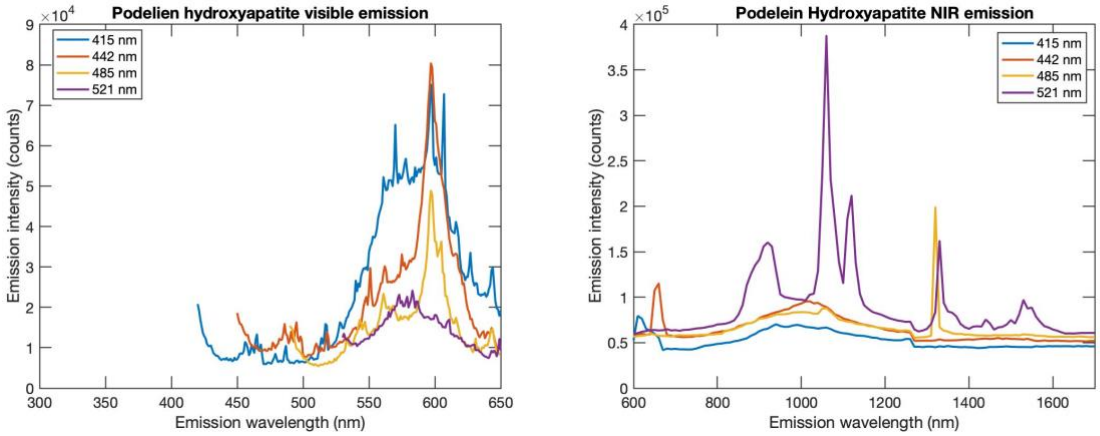

Figure 130: Emission using the Edinburgh Instruments Spectrofluorimeter using the Podelien hydroxyapatite sample.

Appendix A5

The below Matlab® code was used to identify areas of higher than background signal in a dual-wavelength scan and plot them.

```
function spectrobinasys

%A function to analyse the output of the spectrometer data from the dual
%wavelength system. It outputs a binary yes/no map as to where emission is,
%so that we can identify low and high emission areas on the same map. Note
%that this is is for square ranges where wavelength combinations are not
%repeated.

%First of all, we need to create the file names we are looking at.

close all
clear all

%% Change these variables if necessary

%This is the lowest wavelength scanned.
first = 750;

%This is the highest wavelength scanned.
last = 1500;

%This is the step size used.
step = 10;

filerange = [1 1 3336 1];

%%

difference = (last-first)./step;

ff = first./step;

string1 = '*wl1-';
string2 = '*wl2-';

%Finding the wavelengths: note that this is for square ranges where
%wavelength combinations are not repeated.
for nn = 1:difference+1;
    wl1 = ((nn-1)+ff)*step; %Defining wavelength 1.

    wl2s = linspace(first,wl1,nn); %Defining all second wavelengths.

    for n2 = 1:length(wl2s);
        wl2 = wl2s(n2); %Defining wavelength 2.

        fname = sprintf('%s%d%s%d%s',string1,wl1,string2,wl2,'*');

        finding_name = dir(fname);
        full_name = {finding_name.name}; %Finding full file name.
```

```
        full_name = char(full_name);


        A = dlmread(full_name,',',filerange); %Reading in data.

        %This part is if the bin width is very small over spectrometer data

        %Averaging over a resh amount of bins.
        %resh=50;
        %cut=floor(length(A)/resh);
        %if cut*resh == length(A);
        %    A=A;
        %else
        %    A(cut*resh+1:length(A))=[];
        %end
        %
        %aa=reshape(A,resh,length(A)/resh);
        %A=mean(aa);

        %This bit is defining a 'noise' level above which is a signal.

        highstep = median(A) + 0.2*sqrt(median(A));
        %'highstep' is the upper end of the expected noise.

        count = 0;

        %If the data is 2x higher than the expected upper noise level, we
        %count it as signal.
        for ii = 1:length(A)
            if A(ii) > highstep
                count = count+1;
            end
        end

        %Fluorescence signals have a width of usually more than 5-10 nm
        %If there is more than 10 data points considered signal (to get rid
        %of outlier noise, cosmic ray hits, etc.) then we count the
        %wavelength combination to have created emission.
        if count >10
            zspace = 1;
        else
            zspace = 0;
        end
        zspace=sum(A);

        Result = [wl1,wl2,zspace];

        %Writing results into csv file.
        dlmwrite('BinaryEmission.csv',Result,'-append','delimiter',',','...
            ,'newline','pc');

    end
end

%Reading out results
AA = csvread('BinaryEmission.csv');
x = AA(:,1);
y = AA(:,2);
z = AA(:,3);
```

```
%Plotting results
xx=linspace(750,1500,(difference+1));

[X,Y] = meshgrid(xx,xx);

%colormap
map = [0 0 0
    0 0 0.4
    0 0 0.5
    0 0 0.6
    0 0 0.8
    0 0 1.0];
colormap(map);

pcolor(xx,xx,griddata(x,y,z,X,Y));
title('Places of emission in dual wavelength scan')
xlabel('Wavelength One (nm)')
ylabel('Wavelength Two (nm)')


end
```

Appendix A6

The below Matlab® code was used to calculate the minimum total power at the sample needed for detection of a sample over a conveyor belt.

```
function mWneeded

%A function to explore variables used for designing a prototype.

%First the Photons per mJ per hemisphere:
eff = 1e11; %Approximate efficiency of fluorapatite.

%Next the amount of photons needed to see above background.

background = 4000*50; %The background used for photodetectors.
%background = 4000; %The background used for spectrometers.
%This is the background per second for a shielded detector.

time = 1; %How many seconds we are integrating over.

%Minimum counts needed to see above the background counts.
counts = (2.*time.*sqrt(background)); %(photodetector).
%counts = (2.*time.*sqrt(background))*50; %(spectrometer).

%Next the detector specifications and position

detsee = 2; %This is area the detector or detector/lens combination takes
%up (cm^2)
distance = 100; %Distance of the detector/lens from the source (cm)

QE = 0.5*0.85*(2*0.93); % for photodetector.
%QE = 0.5*0.5*0.85*(2*0.93); % for spectrometer.

%Efficiency of the detector, assuming:
%Coupling efficiency of 0.5 for the spectrometer fibre
%QE of 0.5 for the detector.
%Transmission of 93% for the filter (using 2 filters).
%Transmission of 85% for the lens.

photons = counts.*(1./QE); %How many photons need to hit the detector to
%see the amount of counts.

%Assuming Lambertian emission change is not required as the detector is
%directly above the sample.
%The amount of photons needed from the sample to see counts at the detector
%is fullcounts = counts/detector_area * surface area hemisphere of emission

%Photons coming emitted from the sample.
fullcounts = (photons./detsee).*(2.*pi.*(distance.^2));

%For 500 ppm fluorite (assuming 5000 ppm fluorapatite)
DiffusedmW = (fullcounts./(eff*(5000e-6)))/time; %For diffused
disp(DiffusedmW)
%For 1 cm chunk of fluorite moving at 5 m/s
BlockmW = ((fullcounts./eff)/(1e-2/5))/time; %for 1 cm chunk
disp(BlockmW)
```

```
end
```

Bibliography

2018a. *ASD TerraSpec Halo Mineral Identifier* [Online]. Surrey, England: Malvern Panalytical. Available: https://www.malvernpanalytical.com/en/products/product-range/asd-range/terraspec-range/terraspec-halo-mineral-identifier?creative=325180323359&keyword=%2Bmineral%20%2Bdetector&matchtype=b&network=g&device=c&gclid=CjwKCAiAyeTxBRBvEiwAuM8dncBmjPAspKRZDIUVPVDoF4s_i1tjapMUwk2N4Kz0yhzkYeREeClzmxoCdbkQAvD_BwE [Accessed 5/2/2020 2020].

2018b. *Geology of Uranium Deposits* [Online]. United Kingdom: World Nuclear Association. Available: https://www.world-nuclear.org/information-library/nuclear-fuel-cycle/uranium-resources/geology-of-uranium-deposits.aspx#ECSArticleLink1 [Accessed 07/02/2020 2020].

2018c. *Opals - The Gem of the Outback* [Online]. Coober Pedy, Australia: Coober Pedy Retail, Business and Tourism Association. Available: cooberpedy.com/opals-2 [Accessed 09/07/2020 2020].

2020a. *Copper* [Online]. Australia: Commonwealth of Australia (Geoscience Australia). Available: https://www.ga.gov.au/education/classroom-resources/minerals-energy/australian-mineral-facts/copper [Accessed 07/02/2020 2020].

2020b. *Opal Mining* [Online]. Coober Pedy, Australia: Opalios. Available: opalios.com.au/pages/opal-mining [Accessed 09/07/2020 2020].

2020c. *Spectral Geology* [Online]. ACT, Australia: Commonwealth of Australia (Geosciences Australia). Available: https://www.ga.gov.au/scientific-topics/disciplines/spectral-geology [Accessed 4/2/2020 2020].

AB-RAHMAN, M. S., ARIF, N. A. M. & EHSAN, A. A. 2010. Conductivity studies of variable ZnS:Mn nanocrystals. *International Conference on Photonics.* United State of America.

ALLAIN, J. Y., MONERIE, M. & POIGNANT, H. 1989a. Erbium-doped fluorozirconate single-mode fibre lasing at 2.71µm. *Electronics Letters,* 25**,** 28-29.

ALLAIN, J. Y., MONERIE, M. & POIGNANT, H. 1989b. Lasing at 1.00 micron in erbium-doped fluorozirconate fibres. *Electronics Letters,* 25**,** 318-319.

ALLEN, R., ESTEROWITZ, L. & GINTHER, R. J. 1990. Diode-pumped single-mode fluorozirconate fiber laser from the4I11/2→4I13/2transition in erbium. *Applied Physics Letters,* 56**,** 1635-1637.

AUZEL, F. 1966a. Compteur quantique par transfert d'energie de Yb3+ à Tm3+ dans un tungstate mixte et dans un verre germanate. *Comptes rendus hebdomadaires des séances de l'Academie des sciences. Séries A et B, Sciences mathématiques et Sciences physiques,* 263**,** 819-821.

AUZEL, F. 1966b. Compteur quantique par transfert d'energie entre deux ions de terres rares dans un tungstate mixte et dans un verre. *Comptes rendus hebdomadaires des séances de l'Academie des sciences. Séries A et B, Sciences mathématiques et Sciences physiques,* 262**,** 1016-1019.

BAIRA, M., BEKHTI-SIAD, A., HEBALI, K., BOUHANI-BENZIANE, H. & SAHNOUN, M. 2018. Charge compensation mechanisms in favor of the incorporation of the Eu 3+ ion into the ZnO host lattice. *Physica B: Condensed Matter,* 537**,** 296-300.

BAKUMENKO, V. L., VLASOV, A. N., KOVARSKAYA, E. S., KOZINA, G. S. & FAVORIN, V. N. 1965. Stepwise excitation of fluorescence of CaWO4 activated with Er3+. *Journal of Experimental and Theoretical Physics Letters,* 2**,** 16-18.

BARAMIN, G. 2010. *Complete List of Luminescent Minerals* [Online]. Available: http://www.fluomin.org/uk/list.php?liste=1 [Accessed 29/05/2019 2019].

BARKLA, C. G. 1915. X-Ray Fluorescence and the Quantum Theory. *Nature,* 95**,** 7-7.

BENNETT, D., MILJAK, D. & KHACHAN, J. 2009. The measurement of chalcopyrite content in rocks and slurries using magnetic resonance. *Minerals Engineering,* 22**,** 821-825.

BERTHOU, H. & JÖRGENSEN, C. K. 1990. Optical-fiber temperature sensor based on upconversion-excited fluorescence. *Optics Letters,* 15**,** 1100-1102.

BILL, H. & CALAS, G. 1978. Color centers, associated rare-earth ions and the origin of coloration in natural fluorites. *Physics and Chemistry of Minerals,* 3**,** 117-131.

BLOEMBERGEN, N. 1959. Solid State Infrared Quantum Counters. *Physical Review Letters,* 2**,** 84-85.

BRIERLEY, M. C. & FRANCE, P. W. 1988. Continuous wave lasing at 2.7 micron in an erbium-doped fluorozirconate fibre. *Electronics Letters,* 24**,** 935-936.

BRITT, A., SENIOR, A., SUMMERFIELD, D., HUGHES, A., HITCHMAN, A., CHAMPION, D., HUSTON, D., SIMPSON, R., KAY, P., SEXTON, M. & SCHOFIELD, A. 2019. Australia's Identified Mineral Resources 2018. Canberra, Australia.

BROICHER, H. F. 2000. Bulk sorting by LIF: Quality control of ores for bulk sorting and blending by laser induced fluorescence analysis. *Mining Engineering,* 52**,** 24-28.

BROICHER, H. F. 2005. Dilution control - online and real-time recognition of ore and waste by LIF. *Proceedings of the SME Annual Meeting, Salt Lake City, UT, USA, 28 February-02 March 2005,* 05-66**,** 1-5.

BROWN, M. R. & SHAND, W. A. 1963. Infrared Quantum Counter Action in Pr-Doped Fluoride Lattices. *Physical Review Letters,* 11**,** 366-368.

BROWN, M. R. & SHAND, W. A. 1964a. Infra-red quantum counter action in Dy doped CaF2 and SrF2. *Physics Letters,* 6**,** 19.

BROWN, M. R. & SHAND, W. A. 1964b. Infra-red quantum counter action in Ho doped fluoride lattices. *Physics Letters,* 11**,** 219-220.

BROWN, M. R. & SHAND, W. A. 1964c. Infrared quantum counter action in Er-doped fluoride lattices. *Physical Review Letters,* 12**,** 367-369.

CAMPBELL, M., BUMBS, W., STRASSER, J., YERSIN, H. & FLINT, C. D. 1997. Energy migration and up-conversion in Cs2NaErxY1-xCl6 at 1.2 K. *Proceedings of SPIE,* 3176**,** 103-107.

CASPARY, R. 2002. *Applied rare-earth spectroscopy for fiber laser optimization.* Doctor of Philosophy, Technischen Universität Carolo-Wilhelmina zu Braunschweig.

CATLOW, C. R. A., CHADWICK, A. V., GREAVES, G. N. & MORONEY, L. M. 1984. Direct observations of the dopant environment in fluorites using EXAFS. *Nature,* 312**,** 601-604.

CHATTERJEE, D. K. & YONG, Z. 2008. Upconverting nanoparticles as nanotransducers for photodynamic therapy in cancer cells. *Nanomedicine,* 3**,** 73-82.

CHEN, S. L., STEHR, J., REDDY, N. K., TU, C. W., CHEN, W. M. & BUYANOVA, I. A. 2012. Efficient upconversion of photoluminescence via two-photon absorption in bulk and nanorod ZnO. *Applied Physics B,* 108**,** 919-924.

CHEN, Z., JIA, H., ZHANG, X., LIU, J., ZENG, S., LI, Y., MA, Z., DONG, G. & QIU, J. 2015. BaCl2:Er3+--A high efficient upconversion phosphor for broadband near-infrared photoresponsive devices. *Journal of the American Ceramics Society***,** 1-6.

CHINKOV, E. P. & SHTAN'KO, V. F. 1998. Luminescence of self-trapped excitons in calcium fluoride under pulsed electron radiation. *Physics of the Solid State,* 40**,** 1226-1227.
CHIVIAN, J. S., CASE, W. E. & EDEN, D. D. 1979. The photon avalanche: A new phenomenon in Pr3+-based infrared quantum counters. *Applied Physics Letters,* 35**,** 124-125.
CRAMER, L. P. 2004. *Defects in calcium fluoride generated by 157 nm laser and low-energy electrons.* Doctor of Philosophy, Washington State University.
CRESSWELL, P. J., ROBBINS, D. J. & THOMSON, A. J. 1978. Rhenium(IV) as a sensitiser for two-step blue up-converters. *Journal of Luminescence,* 17**,** 311-324.
CYR, P. S. & MORITZ, H. 2016. *Ultraviolet Odyssey: Sterling Hill and Franklin, New Jersey* [Online]. Mindat.org. Available: mindat.org/a/ultravioletodyssey [Accessed 08/07/2020 2020].
CZAJA, M., BODYŁ-GAJOWSKA, S., LISIECKI, R., MEIJERINK, A. & MAZURAK, Z. 2012. The luminescence properties of rare-earth ions in natural fluorite. *Physics and Chemistry of Minerals,* 39**,** 639-648.
CZAJA, M. B., BODYL-GAJOWSKA, S. & MAZURAK, Z. 2013. Steady-state luminescence measurement for qualitative identification of rare earth ions in minerals. *Journal of Mineralogical and Petrological Sciences***,** 47-54.
DENG, R., QIN, F., CHEN, R., HUANG, W., HONG, M. & LIU, X. 2015. Temporal full-color tuning through non-steady-state upconversion. *Nature Nanotechnology,* 10**,** 237-242.
DENK, W., STRICKLER, J. H. & WEBB, W. W. 1990. Two-photon laser scanning fluorescence microscopy. *Science,* 248**,** 73-76.
DIAMOND, I., GRANELLI, S. G., MCDONAGH, A. F., NIELSEN, S., WILSON, C. B. & JAENICKE, R. 1972. Photodynamic therapy of malignant tumours. *The Lancet,* 300**,** 1175-1177.
DOWNING, E., HESSELINK, L., RALSTON, J. & MACFARLANE, R. 1996. A three-color, solid-state, three-dimensional display. *Science,* 273**,** 1185-1189.
DULING, I. N. I. 1991. Subpicosecond all-fibre erbium laser. *Electronics Letters,* 27**,** 544-545.
DUMINIS, T., SHAHID, S. & HILL, R. G. 2017. Apatite Glass-Ceramics: A Review. *Frontiers in Materials,* 3.
EICHHORN, M. 2008a. Quasi-three-level solid-state lasers in the near and mid infrared based on trivalent rare earth ions. *Applied Physics B,* 93**,** 269-316.
EICHHORN, M. 2008b. Quasi-three-level solid-state lasers in the near and mid infrared based on trivalent rare earth ions. *Applied Physics B,* 93**,** 269-316.
EL HADDAD, J., DE LIMA FILHO, E. S., VANIER, F., HARHIRA, A., PADIOLEAU, C., SABSABI, M., WILKIE, G. & BLOUIN, A. 2019. Multiphase mineral identification and quantification by laser-induced breakdown spectroscopy. *Minerals Engineering,* 134**,** 281-290.
FAURE, N., BOREL, C., TEMPLIER, R., COUCHAUD, M., CALVAT, C. & WYON, C. 1996. Optical properties and laser performance of neodymoium doped fluoroapatites SrxCa5-x(PO4)3)F (x=0,1,2,3,4,and 5). *Optical Materials,* 6**,** 293-303.
FEOFILOV, P. P. & OVSYANKIN, V. V. 1967. Cooperative luminescence of solids. *Applied Optics,* 6**,** 1828-1833.
FLEISCHAUER, P. D. & FLEISCHAUER, P. 1970. Photoluminescence of transition metal coordination compounds. *Chemical Reviews,* 70**,** 199-230.
FREED, S. 1931. Electronic Transitions Between an Inner Shell and the Virtual Outer Shells of the Ions of the Rare Earths in Crystals. *Physical Review,* 38**,** 2122-2130.

FREICHS, C. 1994. Efficient Er3+-doped CW fluorozirconate fiber laser operating at 2.7 micron pumped at 980 nm. *International Journal of Infrared and Millimeter Waves,* 15**,** 635-649.

GAMELIN, D. R. & GÜDEL, H. U. 1998. Two-photon spectroscopy of d3 transition metals: near-IR-to-visible upconversion luminescence by Re4+ and Mo3+. *Journal of the American Chemistry Society,* 120**,** 12143-12144.

GAMELIN, D. R. & GÜDEL, H. U. 2001. Upconversion processes in transition metal and rare earth metal systems. *Topics in Current Chemistry,* 214**,** 1-56.

GIBART, P., AUZEL, F., GUILLAUME, J.-C. & ZAHRAMAN, K. 1996. Below band-gap IR response of substrate-free GaAs solar cells using two-photon up-conversion. *Japan Journal of Applied Physics,* 35**,** 4401-4402.

GLEESON, D. 2019. XRF ore sorting shows potential at Yukon zinc project. *International Mining* [Online]. Available: https://im-mining.com/2019/08/01/xrf-ore-sorting-shows-potential-yukon-zinc-project/ [Accessed 5/2/2020].

GOLDING, P. S., JACKSON, S. D., KING, T. A. & POLLNAU, M. 2000. Energy transfer processes in Er3+-doped and Er3+, Pr3+-codoped ZBLAN glasses. *Physical Review B,* 62**,** 856-864.

GORJAN, M., MARINCEK, M. & COPIC, M. 2011. Role of Interionic Processes in the Efficiency and Operation of Erbium-Doped Fluoride Fiber Lasers. *IEEE Journal of Quantum Electronics,* 47**,** 262-273.

HARGREAVES, W. A. 1970. Energy Levels of Uranium Ions in Calcium Fluoride Crystals. *Physical Review B,* 2**,** 2273-2284.

HEBERT, T., WANNEMACHER, R., MACFARLANE, R. M. & LENTH, W. 1992. Blue continuously pumped upconversion lasing in Tm:YLiF4. *Applied Physics Letters,* 60**,** 2592-2594.

HENDERSON-SAPIR, O. 2015. *Development of dual-wavelength pumped mid-infrared fibre laser.* Doctor of Philosophy, The University of Adelaide.

HENDERSON-SAPIR, O., MUNCH, J. & OTTAWAY, D. J. 2014. Mid-infrared fiber lasers at and beyond 3.5 mum using dual-wavelength pumping. *Opt Lett,* 39**,** 493-6.

HENDERSON-SAPIR, O., MUNCH, J. & OTTAWAY, D. J. 2016. New energy-transfer upconversion process in Er³⁺:ZBLAN mid-infrared fiber lasers. *Opt Express,* 24**,** 6869-83.

HERRERA, A., FERNANDES, R. G., DE CAMARGO, A. S. S., HERNANDES, A. C., BUCHNER, S., JACINTO, C. & BALZARETTI, N. M. 2016. Visible–NIR emission and structural properties of Sm3+ doped heavy-metal oxide glass with composition B2O3–PbO–Bi2O3–GeO2. *Journal of Luminescence,* 171**,** 106-111.

HUANG, Y. D., MORTIER, M. & AUZEL, F. 2001. Stark level analysis for Er3+-doped ZBLAN glass. *Optical Materials,* 17**,** 501-511.

HUBERT, S., SONG, C. L. & GENET, M. 1984. Up-conversion of U4+ in ThBr4. *Journal of Luminescence,* 31 & 32**,** 219-221.

HUNTLEY, D. J., GODFREY-SMITH, D. I. & THEWALT, M. L. W. 1985. Optical dating of sediments. *Nature,* 313**,** 105-107.

HWANG, H. L., LOFERSKY, J. J., DEMEO, E. A. & BEAULIEU, R. 1982. Application of luminescence in studies of photovoltaic properties of Cu-Cd-S solar cells. *Journal of Crystal Growth,* 59**,** 425-531.

IBRAHIM, H., RONARC'H, M., GUILBERT, M., POIGNANT, H. & ALLAIN, J. Y. 1993. Erbium-praesodymium co-doped 2.7 micron fluoride amplifier. *Journal of Non-Crystalline Solids,* 161**,** 290-293.

JACOBSEN, S. M. & GÜDEL, H. U. 1989. Higher excited state luminescence in Ti2+:MgCl2 dynamics of radiative and nonradiative processes. *Journal of Luminescence,* 43**,** 125-137.

JEAN WEIGLE, G. 1945. Quelques problèmes actuels de la Physique des cristaux. *Experientia,* 1**,** 99-126.

JIANG, C., ZHAO, T., YUAN, P., GAO, N., PAN, Y., GUAN, Z., ZHOU, N. & XU, Q. H. 2013. Two-photon induced photoluminescence and singlet oxygen generation from aggregated gold nanoparticles. *ACS Appl Mater Interfaces,* 5**,** 4972-7.

JOHNSON, E. J., KAFALAS, J., DAVIES, R. W. & DYES, W. A. 1982. Deep center EL2 and anti-Stokes luminescence in semi-insulating GaAs. *Applied Physics Letters,* 40**,** 993-995.

JOHNSON, L. F. & GUGGENHEIM, H. J. 1971. Infrared-Pumped Visible Laser. *Applied Physics Letters,* 19**,** 44-47.

JOSHI, C., KUMAR, K. & RAI, S. B. 2010. Intense white luminescence from combustion synthesized Ca12Al14O33:Yb3+/Yb2+ single phase phosphor. *Journal of Fluorescence,* 20**,** 935-959.

JOUBERT, M.-F. 1999. Photon avalanche upconversion in rare earth laser materials. *Optical Materials,* 11**,** 181-203.

JUDD, B. R. 1962. Optical absorption intensities of rare-earth ions. *Physical Review,* 127**,** 750-761.

KAISER, W. & GARRETT, C. G. B. 1961. Two-Photon Excitation in CaF2:Eu2+. *Physical Review Letters,* 7**,** 229-231.

KARBOWIAK, M. & HUBERT, S. 2000. Site-selective emission spectra of Eu3_:Ca5(PO4)3F. *Journal of Alloys and Compounds,* 302**,** 87-93.

KASHA, M. 1950. Characterization of electronic transitions in complex molecules. *Discussions of the Faraday Society,* 9**,** 14-19.

KING, H. M. 2005. *Copper: Mineral Properties and Uses* [Online]. Geology.com: Geology.com. Available: https://geology.com/minerals/copper.shtml [Accessed 07/02/2020 2020].

KLEINMAN, D. A. 1962. Theory of Second Harmonic Generation of Light. *Physical Review,* 128**,** 1761-1775.

KNAPP, H., NEUBERT, K., SCHROPP, C. & WOTRUBA, H. 2014. Anwendung der sensorgestützten Sortierung für die Aufbereitung mineralischer Rohstoffe. *Chemie Ingenieur Technik,* 86**,** 773-783.

KOKALY, R. F., CLARK, R. N., SWAYZE, G. A., LIVO, K. E., HOEFEN, T. M., PEARSON, N. C., WISE, R. A., BENZEL, W. M., LOWERS, H. A., DRISCOLL, R. L. & KLEIN, A. J. 2017. USGS Spectral Library Version 7. *U.S. Geological Survey Data Series.*

KOUDSI, B., REFAI, H. & SLUSS, J. J. 2015. Scalable upconversion medium for static volumetric display. *Journal of Display Technology,* 11**,** 266-272.

KRÄMER, K. W., GÜDEL, H. U. & SCHWARTZ, R. N. 1998. NIR to VIS upconversion in LaCl3: 1% Er3+ one- and two-color excitations around 1000 and 800 nm. *Journal of Alloys and Compounds,* 275-277**,** 191-195.

KRIEGEL, I., JIANG, C., RODRIGUEZ-FERNANDEZ, J., SCHALLER, R. D., TALAPIN, D. V., DA COMO, E. & FELDMANN, J. 2012. Tuning the excitonic and plasmonic properties of copper chalcogenide nanocrystals. *J Am Chem Soc,* 134**,** 1583-90.

LANGHANS, K., GUILL, C., RIEPER, E., OLTMANN, K. & BAHR, D. 2003. SOLID FELIX: A static volume 3D-laser display. *Proceedings of SPIE,* 50106**,** 161-174.

LETZ, M. & PARTHIER, L. 2006. Charge centers in CaF2: Ab initio calculation of elementary physical properties. *Physical Review B,* 74.

LI, K., KANG, C. & XUE, D. 2013. Effect of electrostatic and size on dopant occupancy in lithium niobate single crystal. *Inorg Chem,* 52**,** 10206-10.

LI, X., ZHU, J., MAN, Z., AO, Y. & CHEN, H. 2014. Investigation on the structure and upconversion fluorescence of Yb(3)(+)/Ho(3)(+) co-doped fluorapatite crystals for potential biomedical applications. *Scientific Reports,* 4**,** 4446-4453.

LIAO, M.-Y., WU, C.-H., LAI, P.-S., YU, J., LIN, H.-P., LIU, T.-M. & H, -. C.-C. 2013. Surface state mediated NIR two-photon fluorescence of iron oxides for nonlinear optical microscopy. *Advanced Functional materials,* 23**,** 2044-2051.

LILLY, R. 13/06/19 2019. Type to MOFFATT, J.

LINDSTROM, R. M. & RÉVAY, Z. 2017. Prompt gamma neutron activation analysis (PGAA): recent developments and applications. *Journal of Radioanalytical and Nuclear Chemistry,* 314**,** 843-858.

LOFERSKI, J. J., SHEWCHUN, J., MITTLEMAN, S. D., DEMEO, E. A., ARNOTT, R., HWANG, H. L., BEAULIEU, R. & CHAPMAN, G. 1979. Cathodoluminescence characteristics of CuξS films produced by different methods. *Solar Energy Materials,* 1**,** 157-169.

LOREE, T. R. & RADZIEMSKI, L. J. 1981. Laser-induced breakdown spectroscopy: Time-integrated applications. *Plasma Chemistry and Plasma Processing,* 1**,** 271-279.

LUZY, E. & DUPUIS, C. 1914. *Procédé pour obtenir des projections en relief*. France patent application.

LYAPIN, A. A., RYABOCHKINA, P. A., USHAKOV, S. N. & FEDOROV, P. P. 2014. Visualiser of two-micron laser radiation based on Ho:CaF2crystals. *Quantum Electronics,* 44**,** 602-605.

MACIEL, G. S., GUIMARÃES, R. B., BARRETO, P. G., CARAVALHO, I. C. S. & RAKOV, N. 2009. The influence of Yb 3+ doping on the upconversion luminescence of Pr3+ in aluminium oxide based powders prepared by combustion synthesis. *Optical Materials,* 31**,** 1735-1740.

MACIEL, G. S., MENEZES, L. D. S., GOMES, A. S. L., ARAÚJO, C. B. D., MESSADDEQ, Y., FLOREZ, A. & AEGERTER, M. A. 1995. Temperature sensor based on frequency upconversion in Er3-doped fluoroindate glass. *IEEE Photonics Technology Letters,* 7.

MACRAE, C., WILSON, N., SMITH, J., MONTOYA, M.-J. & TORPY, A. 2016. *Luminescence Database* [Online]. CSIRO. Available: http://www.csiro.au/luminescence/default.aspx [Accessed 29/05/2019 2019].

MAES, F., STIHLER, C., PLEAU, L. P., FORTIN, V., LIMPERT, J., BERNIER, M. & VALLEE, R. 2019. 3.42 micron lasing in heavily-erbium-doped fluoride fibers. *Opt Express,* 27**,** 2170-2183.

MALOUF, A., HENDERSON-SAPIR, O., GORJAN, M. & OTTAWAY, D. J. 2016. Numerical Modeling of 3.5 μm Dual-Wavelength Pumped Erbium-Doped Mid-Infrared Fiber Lasers. *IEEE Journal of Quantum Electronics,* 52**,** 1-12.

MANDAL, S., CHANDRA, M. & NATARAJAN, S. 2007. Synthesis, structure, and upconversion studies on organically templated uranium phosphites. *Inorganic Chemistry,* 46**,** 7935-7943.

MARIN, B. C., HSU, S.-W., CHEN, L., LO, A., ZWISSLER, D. W., LIU, Z. & TAO, A. R. 2016. Plasmon-Enhanced Two-Photon Absorption in Photoluminescent Semiconductor Nanocrystals. *ACS Photonics,* 3**,** 526-531.

MCCUMBER, D. E. 1964. Theory of Phonon-Terminated Optical Masers. *Physical Review,* 134**,** A299-A306.

MENG, Z., NAGAMATSU, K., HIGASHIHATA, M., NAKATA, Y., OKADA, T., KUBOTA, Y., NISHIMURA, N., TESHIMA, T. & BUDDHUDU, S. 2004. Energy transfer mechanism in Yb3+:Er3+-ZBLAN: macro- and micro-parameters. *Journal of Luminescence,* 106**,** 187-194.

MILLAR, C. A., MILLER, I. D., AINSLIE, B. J., CRAIG, S. P. & ARMITAGE, J. R. 1987. Low-threshold CW operation of an erbium-doped fibre laser pumped at 807 nm wavelength. *Electronics Letters,* 23**,** 865-866.

MINISCALO, W. J. & QUIMBY, R. S. 1991. General procedure for the analysis of Er3+ cross sections. *Optics Letters,* 16**,** 258-260.

MONCORGÉ, R. & BENYATTOU, T. 1988. Excited-state absorption of Ni2+ in MgF2 and MgO. *Physical Review B,* 37**,** 9186-9196.

MÜHLIG, C., TRIEBEL, W., STAFAST, H. & LETZ, M. 2010. Influence of Na-related defects on ArF laser absorption in CaF2. *Applied Physics B,* 99**,** 525-533.

NGUYEN, D. C., FAULKNER, G. E. & DULICK, M. 1989. Blue-green (450-nm) upconversion Tm3+:YLF laser. *Applied Optics,* 28**,** 3553-3555.

NICHOLS, E. L. & MERRITT, E. 1911. Studies in Luminescence. XVI. The Fluorescence and Absorption of Certain Uranyl Salts. *Physical Review (Series I),* 33**,** 354-378.

OLFELT, G. S. 1962. Intensities of crystal spectra of rare-earth ions. *The Journal of Chemical Physics,* 37**,** 511-520.

OVSYANKIN, V. V. & FEOFILOV, P. P. 1966. Mechanism of summation of electronic excitations in activated crystals. *Pis'ma v ZhETF,* 3**,** 494-497.

POLLACK, S. A. & CHANG, D. B. 1988. Ion-pair upconversion pumped laser emission in Er3+ions in YAG, YLF, SrF2, and CaF2crystals. *Journal of Applied Physics,* 64**,** 2885-2893.

POLLNAU, M., GAMELIN, D. R., LÜTHI, S. R. & GÜDEL, H. U. 2000a. Power dependence of upconversion luminescence in lanthanide and transition-metal-ion systems. *Physical Review B,* 61**,** 3337-3346.

POLLNAU, M., GOLDING, P. S., JACKSON, S. D. & KING, T. A. 2000b. Energy recycling versus lifetime quenching in erbium-doped 3-µm fiber lasers. *2000 Conference on Lasers and Electro-Optics Europe***,** 107.

POLLNAU, M. & JACKSON, S. D. 2001. Erbium 3-micron fiber lasers. *IEEE Journal on Selected Topics in Quantum Electronics,* 7**,** 30-40.

POLLNAU, M. G., D. R.; LÜTHI, S. R.; GÜDEL, H. U. 2000. Power dependence of upconversion luminescence in lanthanide and transition-metal-ion systems. *Physical Review B,* 61**,** 3337-3346.

PORTER, J. F. 1961. Fluorescence excitation by the absorption of two consecutive photons. *Phys Rev Lett,* 7**,** 414-416.

QIN, W., WIN, G., CHUNG, Y., LEE, Y.-I., KIM, C. & JANG, K. 2004. Strong enhancements of infrared-to-ultraviolet upconversion emission sin Yb3+ and Tm3+ co-doped sub-micron fluoride particles prepared by using pulsed laser ablation. *Journal of the Korean Physical Society,* 44**,** 925-929.

REISFELD, R., BOEHM, L., ECKSTEIN, Y. & LIEBLICH, N. 1975. Multiphonon relaxation of rare earth ions in borate, phosphate, germanate and tellurite glasses. *Journal of Luminescence,* 10**,** 193-204.

RIEDENER, T., KRÄMER, K. & GÜDEL, H. U. 1995. Upconversion luminescence in Er3+-doped RbGd2Cl7 and RbGd2Br7. *Inorganic Chemistry,* 34**,** 2745-2752.

RIX, S. 2011. *Radiation-induced defects in calcium fluoride and their influence on material properties under 193 nm laser irradiation.* Doctor of Philosophy, Johannes Gutenberg-Universität.

ROBBEN, C. & WOTRUBA, H. 2019. Sensor-Based Ore Sorting Technology in Mining—Past, Present and Future. *Minerals,* 9.

ROBINSON, R. D., SPANIER, J. E., ZHANG, F., CHAN, S.-W. & HERMAN, I. P. 2002. Visible thermal emission from sub-band-gap laser excited cerium dioxide particles. *Journal of Applied Physics,* 92**,** 1936-1941.

RODNYĬ, P. A., KHADRO, A. K., VOLOSHINOVSKIĬ, A. S. & STRYGANYUK, G. B. 2007. Europium luminescence in fluorite upon high-energy excitation. *Optics and Spectroscopy,* 103**,** 568-572.

RYSKIN, A. I., FEDOROV, P. P., BAGRAEV, N. T., LUSHCHIK, A., VASIL'CHENKO, E., ANGERVAKS, A. E. & KUDRYAVTSEVA, I. 2017. Stabilization of high-temperature disorder of fluorine sublattice by quenching in calcium fluoride crystals. *Journal of Fluorine Chemistry,* 200**,** 109-114.

SAMBASIVAM, S., REDDY, B. K., DIVYA, A., MADHUSUDHANA RAO, N., JAYASANKAR, C. K. & SREEDHAR, B. 2009. Optical and ESR studies on Fe doped ZnS nanocrystals. *Physics Letters A,* 373**,** 1465-1468.

SAVCHUK, O. A., CARVAJAL, J. J., BRITES, C. D. S., CARLOS, L. D., AGUILO, M. & DIAZ, F. 2018. Upconversion thermometry: a new tool to measure the thermal resistance of nanoparticles. *Nanoscale,* 10**,** 6602-6610.

SCHULZE, T. F. & SCHMIDT, T. W. 2015. Photochemical upconversion: present status and prospects for its application to solar energy conversion. *Energy and Environmental Science,* 8**,** 103-125.

SHEN, Y. R. & BLOEMBERGEN, N. 1965. Theory of Stimulated Brillouin and Raman Scattering. *Physical Review,* 137**,** A1787-A1805.

SINGH, A. K., RAI, S. B. & RAI, A. 2006. Optical properties and upconversion in Er3+ and Ho3+ doping in lithium tellurite glass. *Progress in Crystal Growth and Characterization of Materials,* 52**,** 99-106.

SMART, R. G., CARTER, J. N., HANNA, D. C. & TROPPER, A. C. 1990. Erbium doped fluorozirconate fibre laser operating at 1.66 and 1.72 micron. *Electronics Letters,* 26**,** 649-650.

SRINIVASAN, B., JAIN, R. K. & MONNOM, G. 2000. Indirect measurement of the magnitude of ion clustering at high doping densities in Er:ZBLAN fibers. *Journal of the Optical Society of America,* 17**,** 178-181.

STEHR, J. E., CHEN, S. L., REDDY, N. K., TU, C. W., CHEN, W. M. & BUYANOVA, I. A. 2014. Turning ZnO into an Efficient Energy Upconversion Material by Defect Engineering. *Advanced Functional Materials,* 24**,** 3760-3764.

STOKES, G. G. 1852. On the refrangibility of light. *Philosophical Transactions of the Royal Society of London,* 142**,** 463-562.

SUN, L.-N., PENG, H., STICH, M. I. J., ACHATZ, D. & WOLFBEIS, O. S. 2009. pH sensor based on upconverting luminescent lanthanide nanorods. *Chemical Communications,* 0**,** 5000-5002.

SUYVER, J. F., AEBISCHER, A., GARCÍA-REVILLA, S., GERNER, P. & GÜDEL, H. U. 2005. Anomalous power dependence of sensitized upconversion luminescence. *Physical Review B,* 71.

SYAMCHAND, S. S. & SONY, G. 2016. Fluorescein-labeled fluoroapatite nanocrystals codoped with Yb(III) and Ho(III) for trimodal (downconversion, upconversion and magnetic resonance) imaging of cancer cells. *Microchimica Acta,* 183**,** 3209-3219.

SZELA, J. W. & MACKENZIE, J. I. 2012. Excited-state absorption measurements of Tm3+-doped crystals. *Laser Sources and Applications,* 8433.

TAN, K., LIU, S., XIE, Y. & WAGNER, G. A. 2003. The luminescence characters of pyrite and their geological significance. *He Jishu (Nuclear Techniques),* 26**,** 32-35.

TANNER, P. A., ZHOU, L., DUAN, C. & WONG, K. L. 2018. Misconceptions in electronic energy transfer: bridging the gap between chemistry and physics. *Chem Soc Rev,* 47**,** 5234-5265.

TÖBBEN, H. 1991. CW Lasing at 3.45 µm in Erbium-doped Fluorozirconate Fibres. *Frequenz,* 45.

TÖBBEN, H. 1992. Room temperature CW fibre laser at 3.5 µm in Er3+-doped ZBLAN glass. *Electronics Letters,* 28**,** 1361-1362.

TRUPKE, T., GREEN, M. A. & WÜRFEL, P. 2002. Improving solar cell efficiencies by up-conversion of sub-band-gap light. *Journal of Applied Physics,* 93**,** 4417-4122.

VAN DER STAM, W., GUDJONSDOTTIR, S., EVERS, W. H. & HOUTEPEN, A. J. 2017. Switching between Plasmonic and Fluorescent Copper Sulfide Nanocrystals. *J Am Chem Soc,* 139**,** 13208-13217.

WANG, J., MING, T., JIN, Z., WANG, J., SUN, L. D. & YAN, C. H. 2014. Photon energy upconversion through thermal radiation with the power efficiency reaching 16%. *Nat Commun,* 5**,** 5669.

WANG, Q., ZHANG, Q., ZHAO, X., LUO, X., WONG, C. P. Y., WANG, J., WAN, D., VENKATESAN, T., PENNYCOOK, S. J., LOH, K. P., EDA, G. & WEE, A. T. S. 2018. Photoluminescence Upconversion by Defects in Hexagonal Boron Nitride. *Nano Lett,* 18**,** 6898-6905.

WANG, X., KREBS, L. J., AL-NURI, M., PUDAVAR, H. E., GHOSAL, S., LIEBOW, C., NAGY, A. A., SCHALLY, A. V. & PRASAD, P. N. 1999. A chemically labeled cytotoxic agent: Two-photon fluorophore for optical tracking of cellular pathway in chemotherapy. *Proceedings of the National Academy of Science,* 96**,** 11081-11084.

WANG, X., LIU, Y., ZHAO, P., GUO, Z., LI, Y. & QU, S. 2015. Valence state change and defect centers induced by infrared femtosecond laser in Yb:YAG crystals. *Journal of Applied Physics,* 117.

WANG, X., QIU, J., SONG, J., XU, J., LIAO, Y., SUN, H., CHENG, Y. & XU, Z. 2007. Upconversion luminescence and optical power limiting effect based on two- and three-photon absorption processes of ZnO crystal. *Optics Communications,* 280**,** 197-201.

WENGER, O. S., WERMUTH, M. & GÜDEL, H. U. 2002. Chemical tuning of transition metal upconversion properties. *Journal of Alloys and Compounds,* 341**,** 342-348.

WERMUTH, M. & GÜDEL, H. U. 1997. Upconversion luminescence in a 5d transition-metal ion system: Cs2ZrCl6:Os4+. *Chemical Physics Letters,* 281**,** 81-85.

WILHELM, S. 2017. Perspectives for Upconverting Nanoparticles. *ACS Nano,* 11**,** 10644-10653.

WU, Q., LONG, Q., LI, H., ZHANG, Y. & YAO, S. 2015. An upconversion fluorescence resonance energy transfer nanosensor for one step detection of melamine in raw milk. *Talanta,* 136**,** 47-53.

XU, S., HUANG, S., LE, Q. & WANG, L. 2015. Upconversion nanophosphores for bioimaging. *Trends in Analytical Chemistry,* 66**,** 72-79.

YARIV, A. & LOUISELL, W. 1966. 5A2 - Theory of the optical parametric oscillator. *IEEE Journal of Quantum Electronics,* 2**,** 418-424.

YILDIRIM, C. & BIRER, Ö. 2014. Ultraviolet upconversion spectra of sonochemically synthesized doped NaYF4 crystals. *Chemical Physics,* 445**,** 46-52.

YOUNG, C. G. 1969. Glass Lasers. *Proceedings of the IEEE,* 57**,** 1267-1281.

YU, H. & YU, J. 2013. Inhibiting emission quenching in (Y0.1Yb0.05Er0.005Al)2O3 by Sc3+ co-doping to enhance upconversion luminescence. *Journal of Luminescence,* 137**,** 274-281.

ZHANG, P., ROGELJ, S., NGUYEN, K. & WHEELER, D. 2006. Design of a highly sensitive and specific nucleotide sensor based on photon upconverting particles. *Journal of the American Chemical Society,* 128**,** 12410-12411.

ZHENG, K., QIN, W., CAO, C., ZHAO, D. & WANG, L. 2015. NIR to VUV: Seven-Photon Upconversion Emissions from Gd(3+) Ions in Fluoride Nanocrystals. *J Phys Chem Lett,* 6**,** 556-60.

ZHOU, J., ZHANG, W., LI, J., JIANG, B., LIU, W. & PAN, Y. 2010. Upconversion luminescence of high content Er-doped YAG transparent ceramics. *Ceramics International,* 36**,** 193-197.

ZHOU, M., GAO, X., CHENG, Y., CHEN, X. & CAI, L. 2014. Structural, electronic, and elastic properties of CuFeS2: first-principles study. *Applied Physics A,* 118**,** 1145-1152.